uOttawa

L'Université canadienne
Canada's university

FACULTÉ DES ÉTUDES SUPÉRIEURES ET POSTOCTORALES

uOttawa

L'Université canadienne
Canada's university

FACULTY OF GRADUATE AND POSDOCTORAL STUDIES

Hussam Zahlan
AUTEUR DE LA THÈSE / AUTHOR OF THESIS

M.A.Sc. (Mechanical Engineering)
GRADE / DEGREE

Department of Mechanical Engineering
FACULTÉ, ÉCOLE, DÉPARTEMENT / FACULTY, SCHOOL, DEPARTMENT

Flow Obstacle Effect on Film Boiling Heat Transfer with Uniform and Non-Uniform Axial Heat Flux

TITRE DE LA THÈSE / TITLE OF THESIS

Dr. Cheng
DIRECTEUR (DIRECTRICE) DE LA THÈSE / THESIS SUPERVISOR

Dr. Groeneveld
CO-DIRECTEUR (CO-DIRECTRICE) DE LA THÈSE / THESIS CO-SUPERVISOR

EXAMINATEURS (EXAMINATRICES) DE LA THÈSE / THESIS EXAMINERS

Dr. R. Milane

Dr. M. Radulsecu

Gary W. Slater
Le Doyen de la Faculté des études supérieures et postdoctorales / Dean of the Faculty of Graduate and Postdoctoral Studies

FLOW OBSTACLE EFFECT ON FILM BOILING HEAT TRANSFER WITH UNIFORM AND NON-UNIFORM AXIAL HEAT FLUX

Hussam Zahlan

A thesis submitted to the Faculty of Graduate and Postdoctoral Studies
in partial fulfillment of the requirements for the degree of

MASTER OF APPLIED SCIENCE

in Mechanical Engineering

Ottawa-Carleton Institute for Mechanical and Aerospace Engineering
University of Ottawa
Ottawa, Canada

September 2008

Your file Votre référence
ISBN: 978-0-494-52366-7
Our file Notre référence
ISBN: 978-0-494-52366-7

ABSTRACT

An experimental investigation of the effects of axial flux distribution (AFD) and obstacles on film-boiling heat transfer was performed in a vertical tube using HFC-134a as coolant. The following parameters were examined:

- Axial flux profiles (uniform, inlet-peak and outlet-peak)
- Flow-blockage ratios (12% and 24%)
- Obstacle pitches (150 mm and 300 mm)
- Obstacle shapes (blunt and round)

Test conditions covered the pressure 1665 and 2389 kPa (water-equivalent value: 10 and 14 MPa), a mass-flux range from 1395 to 3575 $kg.m^{-2}.s^{-1}$ (water-equivalent value: 2000 to 5000 $kg.m^{-2}.s^{-1}$) and an inlet-fluid temperature range from 30 to 70°C (water-equivalent value: 229 to 324°C). Film-boiling temperature measurements were recorded for all possible heat-flux levels, up to a limiting surface temperature of 240°C to avoid Freon decomposition. Inside wall temperature distributions of the obstacle-equipped test sections were compared against those of a reference bare tube at similar flow conditions.

Flow obstacles were found to have a significant influence on film-boiling heat-transfer. Film-boiling wall temperatures along the test section were reduced significantly by decreasing the obstacle pitch, by increasing the obstacle size and by using a blunt instead of streamline-shaped obstacle.

The effect of AFD on film-boiling heat transfer is noticeable in the developing film-boiling region and can be attributed mainly to the variation in critical heat flux (CHF) occurrence. However, the AFD effect appears to be less obvious in the fully developed film-boiling region.

Since the literature suggested that the single-phase pressure-loss coefficient of the flow obstructions could be an important parameter in correlating the film-boiling heat-transfer enhancement, this parameter was also measured and correlated.

Previously derived prediction methods for obstacle-enhanced film-boiling heat transfer did not provide satisfactorily agreement with the data; therefore, a new prediction method was derived to predict the film-boiling heat-transfer augmentation for uniform AFD tubes. The new equation accounts for the enhancement in film-boiling heat transfer due to turbulence generated by (i) liquid-film termination at the dryout point and (ii) the upstream flow obstructions. The new correlation was applied to non-uniform AFD data. It was concluded that (i) this new prediction method is also applicable to non-uniform AFD tubes, (ii) the new prediction method has the correct asymptotic trends and (iii) single-phase pressure-loss coefficients cannot be used directly to predict the heat-transfer enhancement for both blunt and rounded obstacles.

ACKNOWLEDGEMENTS

I would like to express my sincere thanks to my supervisors, Professor S.C. Cheng, for his care and support, and Professor D.C. Groeneveld, for his supervision, guidance, encouragement and patience throughout this study. I also would like to express my appreciation to Dr. L.K.H. Leung of Atomic Energy of Canada Limited (AECL) for his valuable comments and advice during the course of this research.

I also sincerely thank Dr. M. El Nakla, former student of Professor S.C. Cheng and Professor D.C. Groeneveld, for advice and help. I am very grateful to my colleague and friend, Ph.D. student A. Tanase, for his advice, help and friendship.

Exceptional thanks are due to my wife, for her patience and moral support.

The financial support from the Natural Science and Engineering Research Council of Canada (NSERC) and from the Atomic Energy of Canada Ltd. (AECL) is thankfully acknowledged.

TABLE OF CONTENTS

LIST OF TABLES

LIST OF FIGURES

NOMENCLATURE

Symbol	Definition
d, D	tube inside diameter (m)
G	mass flux ($kg.m^{-2}.s^{-1}$)
h	heat-transfer coefficient ($kW.m^{-2}.K^{-1}$)
H	enthalpy ($kJ.kg^{-1}$)
H_{fg}	latent heat of vaporization = $H_g - H_f$ ($kJ.kg^{-1}$)
k	thermal conductivity ($W.m^{-1}.K^{-1}$)
K	single-phase pressure-loss coefficient (-)
L	axial location downstream from the obstacle (m)
P	pressure (kPa)
q	heat flux ($kW.m^{-2}$)
r	radius (m)
T	temperature (°C)
ΔT	temperature difference = $T_w - T_{bulk}$ (K)
x	thermodynamic quality = $(H - H_f)/H_{fg}$ (-)
x_a	actual vapor (mass) quality (-)
x_{cr}^{lim}	limiting critical quality (-)
z	axial location (m)

Greek

σ	surface tension ($N.m^{-1}$)
ε	flow-blockage ratio or obstruction ratio (cross-sectional area of obstacle to the free flow cross-sectional area) (-)
ρ	fluid density ($kg.m^{-3}$)
μ	dynamic viscosity ($N.s.m^{-2} = kg.m^{-1}.s^{-1}$)
υ	specific volume ($m^3.kg^{-1}$)

Dimensionless numbers

Nu	local Nusselt number ($= h.D.k^{-1}$)
Nu_0	bare tube local Nusselt number ($= h.D.k^{-1}$)
Gz	Graetz number ($= D.L^{-1}.Re.Pr$)
Re	Reynolds number ($= G.D.\mu^{-1}$)

Subscripts

av, avg	average
B	blunt obstacle
cr	critical
do	dryout
dev	developing film-boiling
e	equilibrium
enh	enhancement
exp	experimental
eq	water equivalent
f	saturated liquid properties
fg	difference between saturated vapour and saturated liquid properties
fd, FD	fully developed
FDFB	fully developed film-boiling
g	saturated vapour properties
hy	hydraulic diameter
i	inside
in	inlet
IP	inlet-peak AFD test section
l	subcooled liquid properties
m	step number
nb, NB	nucleate boiling
0	bare tube
ob	obstacle
pred	predicted
out	outlet
OP	outlet-peak AFD test section
rad	thermal radiation
R	streamlined obstacle
sat	saturated condition
sp	spacer
thr	threshold vapour quality
U	uniform AFD test section
v	superheated vapor properties
V	vapour
w	inside wall

Abbreviations

AFD	axial heat flux distribution
CHF	critical heat flux
DAS	data acquisition system
DNB	departure from nucleate boiling
DFFB	dispersed flow film-boiling
Eqn.	equation
FB	film boiling
HFC	hydro fluorocarbon
HTC	heat-transfer coefficient
ID	tube inside diameter
IAFB	inverted annular film boiling
LHS	left hand-side
LOCA	loss-of-coolant accident
MFB	minimum film boiling
ONB	onset of nucleate boiling
PDO	post-dryout in the dispersed flow film-boiling
Q/A	quality assurance
RHS	right hand-side
rms	root-mean squared
TC	thermocouple
TS	test section
U of O	University of Ottawa

CHAPTER 1

INTRODUCTION

1.1 Motivation

Film boiling is a boiling heat-transfer regime which is encountered at conditions where the critical heat flux (CHF) or the CHF temperature has been exceeded. It refers to the heat-transfer mode where the vapor phase is in contact with the heated surface and is characterized by a deterioration in the heat-transfer coefficient between the heated surface and vapor film. Flow film boiling may be present in many applications (e.g., steam generators, nuclear reactors, metallurgical processing and cryogenic systems). Flow film boiling is especially important in safety studies of nuclear water reactors – during a postulated loss-of-coolant accident (LOCA), flow film boiling conditions are predicted to occur. Nuclear fuel bundles are equipped with spacing devices (obstacles) such as spacers, bearing pads and endplates, designed to maintain the gap size between fuel rods and between the fuel bundle and the pressure tube wall, spacers also reduce vibration by enhanced mechanical rigidity. In general, the heat flux profile of these fuel bundles in a power reactor is not uniform; it varies axially and circumferentially, depending mainly on fuelling scheme, fuel burn up and the position of reactivity mechanisms (used to control reactor power).

In the design of rod bundles as well as in the safety analysis, the maximum fuel sheath temperature needs to be predicted. This maximum fuel temperature is affected by the heat flux profile and the presence of flow obstacles, and these effects should be considered in predicting the post-dryout heat-transfer coefficient during postulated reactor accident conditions. Relevant prediction methods as well as experimental data are scarce. A number of studies were performed focusing separately on either the effect of axial heat flux profile (e.g., Becker et al. (1992)) or the effect of appendages (e.g., Leung et al.

(2005)) in post-dryout (post-critical heat flux) heat-transfer. None of these studies have examined the combination of these two effects.

The motivation therefore for investigating this thesis topic is the lack of a reliable prediction method of flow film-boiling heat transfer for spacer-equipped nuclear fuel elements, to be used in the thermalhydraulic codes for the design and safety analysis of water-cooled nuclear reactors.

1.2 Objectives

The primary objective of this thesis is to investigate the flow obstacle effect on film boiling heat-transfer with uniform and non-uniform axial heat flux and to improve the accuracy of the current prediction methods.

The completion of the following steps was required to achieve the main objective:

- To perform experiments including the combined effect of obstacles and axial heat flux profile on post-dryout heat-transfer in tubes at Canada Deuterium Uranium (CANDU) reactor conditions of interest.

- To summarize available post-dryout prediction methods for predicting heat-transfer coefficient of test sections:
  - with different axial heat flux profiles, and
  - equipped with several types of flow obstructions.

- To analyze the experimental data obtained before and to select groups of representative data to cover the ranges of pressures and mass fluxes of interest.

- To assess the prediction methods using selected data and select the most appropriate method(s) for predicting the axial heat flux distribution effect and obstacle effect.

- To modify/update the selected method(s) based on the trends of the experimental data.

1.3 General

In flow boiling, post-dryout heat-transfer includes both flow film boiling (referred to as "film boiling" in this thesis) and the intermediate transition boiling heat-transfer. Film-boiling heat transfer can be classified according to vapour and liquid phase-distribution as (i) dispersed flow film boiling (DFFB) at void fractions higher than 80% and (ii) inverted annular flow film boiling (IAFB) at void fractions lower than 40%.

In practice, film-boiling heat-transfer in transient and steady state is encountered in various applications. This study focuses mainly on steady state film-boiling heat-transfer in presence of obstacles with uniform and non-uniform axial heat flux. It is generally assumed that steady state film-boiling prediction methods apply to transient conditions as well.

This thesis has seven chapters including an introduction and a conclusion. Chapter 2 reviews the existing literature on post-dryout and single-phase heat-transfer including the effect of axial heat flux distribution and/or obstacle. Chapter 3 describes the experiments that were performed at University of Ottawa to investigate the axial heat flux distribution and obstacle effects on post-drout heat transfer. Chapter 4 presents the test results. Chapter 5 shows the analysis of the experimental data and a comparison against prediction methods. Chapter 6 describes a new prediction method, and compares the predictions of the new correlation with the available prediction methods and with the experimental data.

CHAPTER 2

LITERATURE REVIEW

2.1 Flow Boiling

To identify the heat-transfer region of this research topic, a brief description of the boiling regimes is presented.

Flow boiling is categorized by the following three boiling regimes: (i) nucleate boiling, (ii) transition boiling and (iii) film boiling.

2.1.1 Boiling Curve

The boiling curve (Figure 2.1) shows the variation of heat flux (q) with wall superheat ($T_w - T_{sat}$) and is used to identify the various boiling heat-transfer modes. Single-phase forced convective heat-transfer to the liquid phase is the first heat-transfer mode represented on the curve. Point A is the onset of nucleate boiling (ONB); at this point, bubbles start to form and later depart from the heated surface. Nucleate boiling or forced convective evaporation is the second heat-transfer mode, path (A-B); if the temperature of the bulk fluid is below saturation, the heat-transfer regime is subcooled nucleate boiling, when bulk temperature reaches saturation, the heat-transfer mode is saturated nucleate boiling. With increasing quality, the bubble population decreases until eventually nucleation is suppressed, and the heat-transfer mode becomes forced convective evaporation. The transition between nucleate boiling or forced convective evaporation and transition boiling, point B, is referred to as the critical heat flux (CHF) point. Beyond CHF point two different paths are identified depending on the heating

method: (i) constant surface-temperature controlled systems (B-C-D) and (ii) constant heat-flux controlled systems (B-D):

- In the case (i), transition boiling (B-C) and film boiling (C-D) are encountered on the boiling curve, the transition between transition boiling and film boiling is the minimum film boiling (MFB) point, detailed description on MFB point can be found in Groeneveld and Fung (1982).
- In the case (ii), film boiling occurs (B-D).

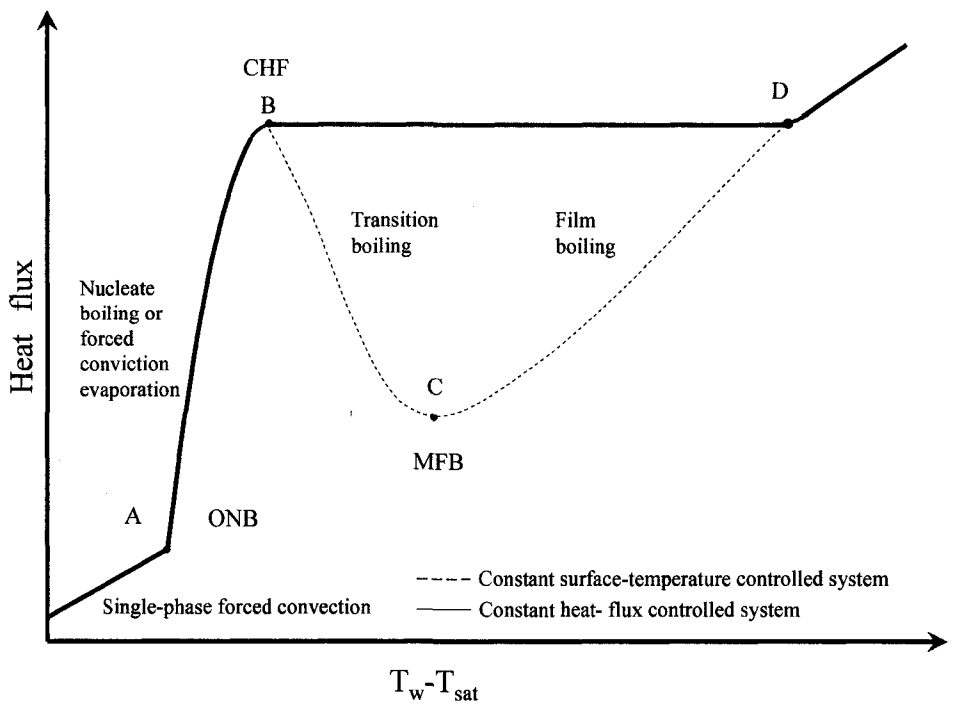

Figure 2.1 Boiling curve.

2.1.2 Heat-transfer Mechanisms

In a directly heated tube having a uniform AFD, the flow conditions change along the tube. The flow conditions determine the flow pattern and the heat-transfer mode. At low-heat fluxes and low-inlet subcoolings/high-quality flow, case A of Figure 2.2, the boiling modes encountered are: single-phase forced convective heat-transfer to fluid, nucleate

boiling, slug flow heat-transfer, forced convective boiling heat-transfer and dispersed flow film boiling (DFFB). The boiling crisis mechanism encountered at high-quality flow is due to the dryout of the thin liquid film. Beyond the dryout point, the DFFB occurs at void fractions higher than 80% and the vapour forms a continuous phase that blankets the heated surface, while a high concentration of droplets are mixed with the vapour in the core flow.

At high-heat fluxes and high-inlet subcoolings, case B of Figure 2.2, the heat-transfer modes are: single-phase forced convective heat-transfer to fluid, nucleate boiling, inverted annular film boiling (IAFB), flow transition regime (inverted slug flow film boiling) and dispersed flow film boiling (DFFB). The boiling crisis mechanism encountered at low-quality flow is the departure from nucleate boiling (DNB). Beyond DNB, the IAFB (a thin vapour film blankets the heated surface, while the liquid is in the core) occurs at void fractions below 40%. Further downstream, the IAFB transition (inverted slug film boiling) to DFFB occurs.

The present study focuses on DFFB which is encountered more often than IAFB in flow boiling equipment. Detailed description of various flow boiling regimes can be found in Collier and Thome (1994) and Groeneveld (1992).

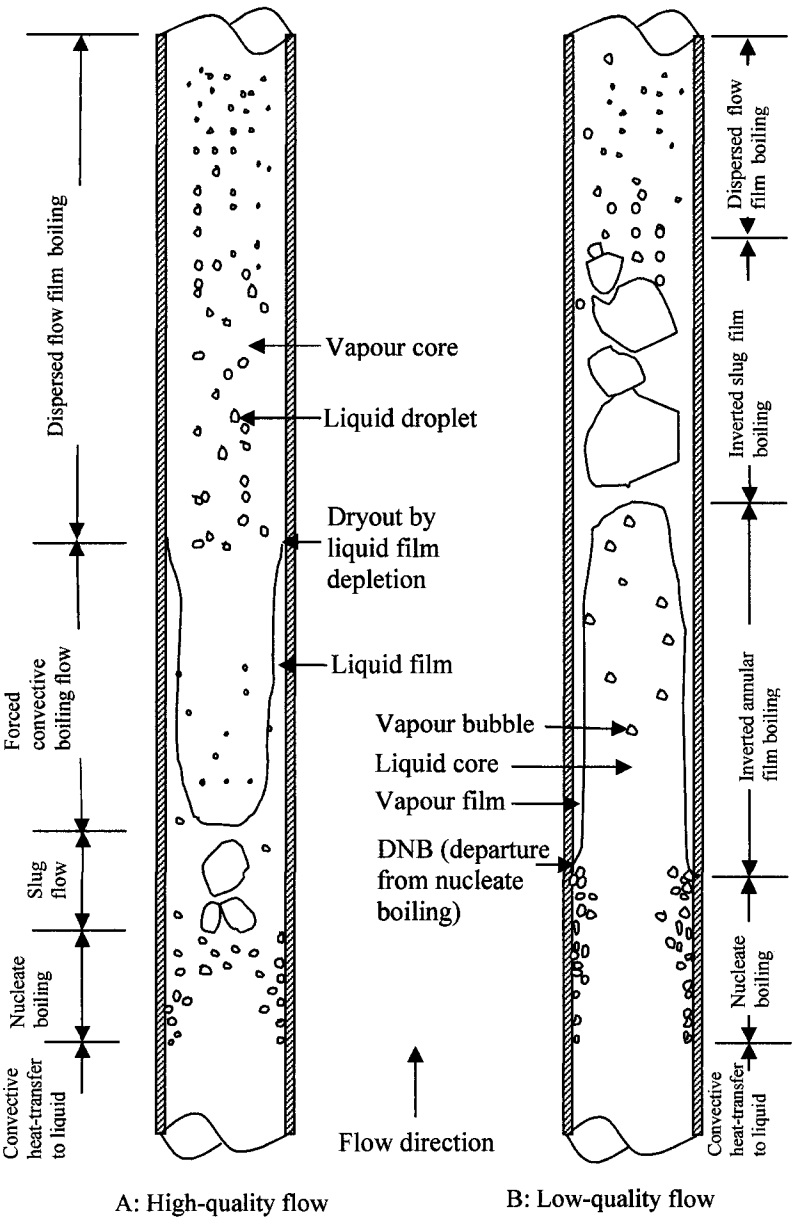

Figure 2.2 Heat-transfer regions in convective boiling.

2.2 Film Boiling

The term "developing film boiling" refers to the heat-transfer region that is located between CHF location and the fully developed film-boiling heat-transfer region, Guo and Leung (2005). In the developing film-boiling region, (downstream of the dryout and

transition boiling) rewetting no longer occurs but the heat-transfer is affected by upstream conditions and the axial surface temperature distribution has not yet leveled off, Groeneveld and Stewart (1982). The fully developed film-boiling region occurs when the axial temperature gradient has reached a plateau and is no longer affected by the distance from the CHF location or spacer location, Zahlan et al. (2008).

Figure 2.3 illustrates the pre-CHF, developing and the fully developed film-boiling heat-transfer regions expressed as surface temperature vs. axial location for a typical film boiling experiment in a uniform-AFD bare tube (without obstacles). Figure 2.4 shows pre- and post-dryout temperature profiles for uniform AFD at different heat fluxes and the asymptotic trend of the surface temperatures in the fully developed-film boiling region.

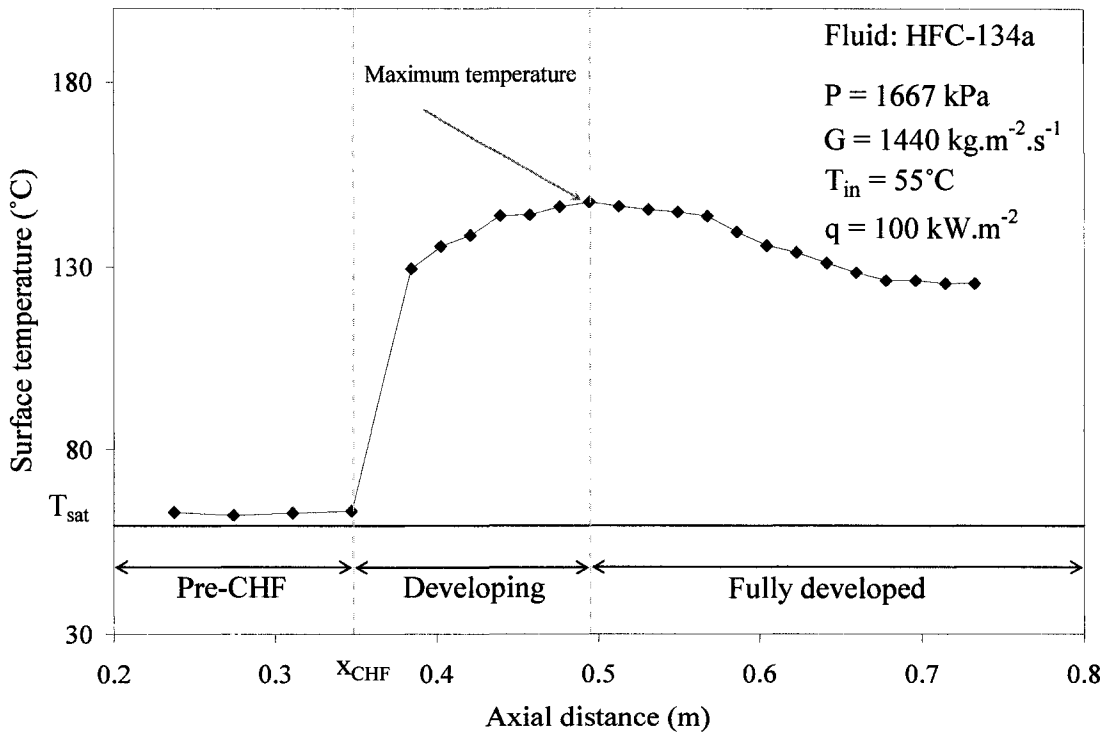

Figure 2.3 Typical surface temperature profile in film-boiling region.

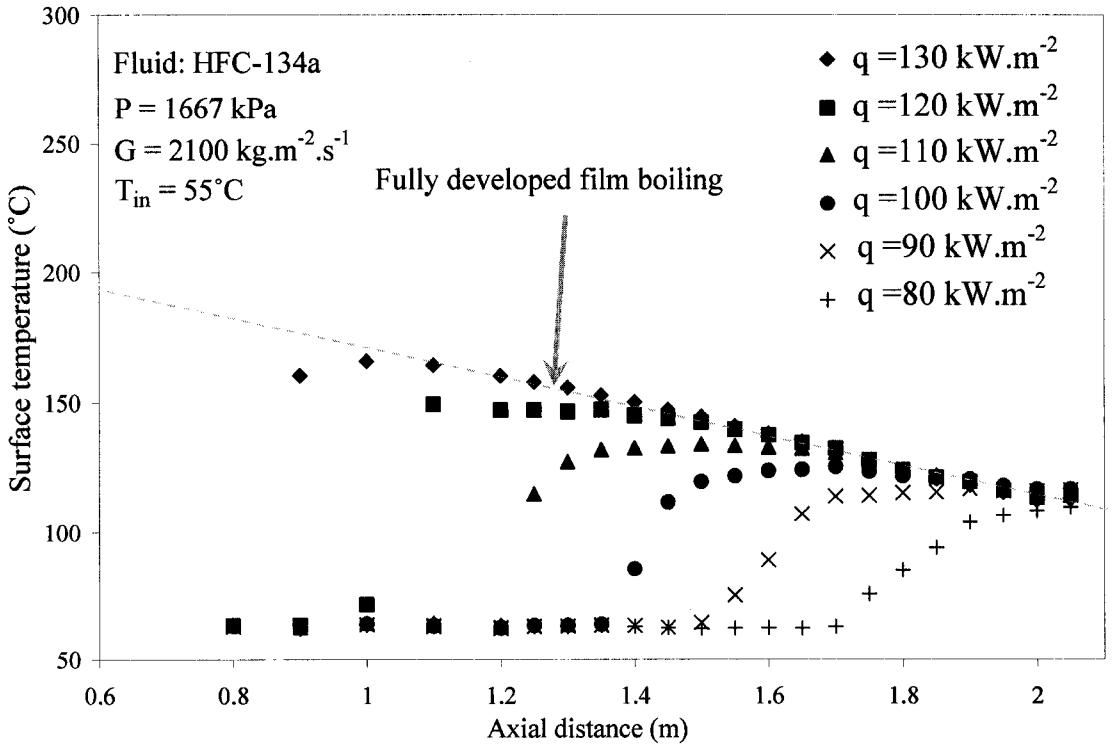

Figure 2.4 Surface temperature distributions at pre- and post-dryout conditions.

Guo and Leung (2005) have studied the developing film-boiling heat-transfer in tubes. They derived a correlation for developing film-boiling heat-transfer coefficient (h_{FB}) in tubes based on University of Ottawa-Atomic Energy of Canada Limited database and other selected datasets. The correlation is expressed as:

$$h_{FB} = h_{FDFB} K_{developing} \tag{2.1}$$

where h_{FDFB} is the fully developed film-boiling heat-transfer coefficient at the same flow conditions, $K_{developing}$ is a factor that accounts for developing film-boiling effect. Guo and Leung proposed the following equation for $K_{developing}$:

$$K_{developing} = \frac{h_{FB}}{h_{FDFB}} = 1 + \left(\frac{h_{NB}}{h_{FDFB}} - 1 \right) \exp(-a(WSR - 1)^b) \tag{2.2}$$

where h_{NB} is the nucleate-boiling heat-transfer coefficient calculated using the Chen correlation (Chen, 1963), and the numerical factors a and b were optimized using experimental data. The wall superheat ratio (WSR) is calculated from:

$$WSR = \frac{T_{w_i} - T_{sat}}{T_{CHF} - T_{sat}} \tag{2.3}$$

Equation (2.2) can be written in the form of:

$$K_{non-\dim ensional} = \frac{h_{FB}/h_{FDFB} - 1}{h_{NB}/h_{FDFB} - 1} = \frac{h_{FB} - h_{FDFB}}{h_{NB} - h_{FDFB}} = \exp(-a(WSR - 1)^b) \tag{2.4}$$

Guo and Leung (2005) used the film-boiling look-up table (2003) to predict the fully developed film-boiling heat-transfer coefficient. The predicted h_{FB} using Equation (2.1) has an average error of -2.37% and a root mean square (rms) error of 13.03% for 11163 data points.

2.3 Obstacle Effect on CHF

A brief review of literature on the obstacle effects on CHF is presented in this section. Groeneveld and Yousef (1980) performed comprehensive literature review on the effect of obstacles on CHF. They observed that obstacles can increase the CHF by more than 200%, depending on the system geometry and the flow conditions. They observed that obstacles influence the CHF by changing the phase distribution, and the CHF enhancement is more pronounced in the deposition controlled region at high-quality flows. They concluded that the enhancement is higher for short axial distances between obstacles ("obstacle pitch") and large-flow-blockage ratios (cross-sectional area of obstacle to the free flow cross-sectional area, denoted by "ε").

Guo et al. (2001), Groeneveld et al. (2001) and Pioro et al. (2002) performed experimental and analytical investigations of the obstacle effect on CHF. The

experimental investigation was performed in a vertical 6.92 mm tube using HFC-134a as a coolant. The flow conditions covered a pressure range from 0.96 to 2.39 MPa, a mass flux range from 500 to 3000 $kg.m^{-2}.s^{-1}$, and an outlet (critical) quality range from -0.05 to 0.95. Different obstacle effects were studied, e.g., the number of obstacles in series, obstacle shape, obstacle pitch, shape of leading and trailing edge, size of obstacle (flow blockage) and the location of an obstacle within a cross section. They proposed a semi-analytical model to predict the relative CHF enhancement (R_{CHF}) due to obstacles. The CHF-enhancement ratio ($\frac{CHF_{ob}}{CHF_0}$) is expressed as: $\frac{CHF_{ob}}{CHF_0} = 1+R_{CHF}$. The predictions of the model agree reasonably well with their experimental database.

Guo et al. (2001) derived an expression for the relative CHF enhancements for the lower quality entrainment-controlled region and the higher quality deposition-controlled region. They also developed a correlation for the transition between entrainment-controlled and deposition-controlled regions, which depends on the transition or "limiting critical quality", $x_{cr}^{\lim}$, given by Pioro et al. (1999). The correlations are:

$$R_{CHF} = \begin{cases} R_{CHF,E} & \text{if} \quad x_{cr} \le 0.9x_{cr}^{\lim} \\ \dfrac{x_{cr} - 0.9x_{cr}^{\lim}}{0.2x_{cr}^{\lim}} (R_{CHF,D} - R_{CHF,E}) + R_{CHF,D} & \text{if} \quad 0.9x_{cr}^{\lim} < x_{cr} < 1.1x_{cr}^{\lim} \\ R_{CHF,D} & \text{if} \quad x_{cr} \ge 1.1x_{cr}^{\lim} \end{cases} \tag{2.5}$$

where the relative CHF enhancement for entrainment-controlled region is represented by "$R_{CHF,E}$" and similarly, for deposition-controlled region, the relative CHF enhancement is represented by "$R_{CHF,D}$".

$$R_{CHF,E} = \left[b_1 \beta \frac{k_\varepsilon}{f} - b_2 \varepsilon \frac{P_{oc}}{P} (1 - x_0) \mathrm{Re}_{m0}^{-n} \right] \exp(-b_3 \frac{L}{D}) \tag{2.6}$$

where $b_1 = 0.0048$, $b_2 = 2\times10^7$, $n = 1.25$ and $b_3 = 2.45\times \mathrm{Re}_{f0}^{-0.311}$. P_{oc}/P is the ratio of the wetted perimeter contacted by obstacles (P_{oc}) to the total wetted perimeter of the channel

P, the homogenous Reynolds number (Re_{m0}) is based on the quality at obstacle location (x_0), and is expressed as $Re_{m0} = GD/\mu_m$, where $\frac{1}{\mu_m} = \frac{x_0}{\mu_g} + \frac{(1-x_0)}{\mu_f}$, μ_m is the homogenous dynamic viscosity. β is the obstacle-edge coefficient which varies from 1.0 for abrupt leading edge to 0.3 for obstacles with round leading edge, f is the friction factor for bare tube, defined from $f = 0.046\,\mathrm{Re}_{f0}^{-0.2}$, the drag coefficient k_ε is expressed as:

$$k_\varepsilon = \frac{\sqrt{\varepsilon}}{1-\varepsilon}\left[2.12 + \frac{10^4(1-\varepsilon)^2}{\mathrm{Re}_{f0}}\right] \tag{2.7}$$

and the liquid Reynolds number at obstacle location (Re_{f0}) is given by

$$\mathrm{Re}_{f0} = \frac{GD}{\mu_f}\left[(1-x_0) + \frac{\rho_f}{\rho_g}x_0\right] \tag{2.8}$$

The relative CHF enhancement of the deposition-controlled region is expressed as:

$$R_{CHF,D} = c_3\varepsilon^{0.65}\,\mathrm{Re}_V^{0.67}\exp(-c_2\frac{L}{D}) \tag{2.9}$$

where $c_2 = 1.0\times10^{-6}\,\mathrm{Re}_{mcr}^{0.8}$, and Re_{mcr} is the homogenous Reynolds number based on critical quality, and is given by $\mathrm{Re}_{mcr} = GD/\mu_m$, where $\frac{1}{\mu_m} = \frac{x_{cr}}{\mu_g} + \frac{(1-x_{cr})}{\mu_f}$, $c_3 = 1.9\times10^5$, and Re_V is the vapour Reynolds number which is given by $\mathrm{Re}_V = GD/\mu_v$.

Yang et al. (2005) performed an experimental and analytical study of the effect of axial heat flux distribution on CHF in tubes equipped with obstacles. They suggested that a limiting dryout quality region exists at low-mass fluxes for obstacle-equipped tubes. They concluded that flow obstacles enhance the local CHF especially at high dryout qualities, and reduce the AFD effect on local CHF at the location of obstacle, compared to bare tubes. The obstacle-equipped tube has a higher critical power and a stronger AFD effect on critical power than the bare tube case.

2.4 Non-Uniform AFD Effect (without Obstacles) on PDO Heat Transfer

Becker et al. (1992) investigated the AFD effect on PDO heat-transfer experimentally. They provided their PDO experimental data in graphical form for 5 non-uniform AFDs (Figure 2.5); their heat flux profiles were: inlet-peak, inlet narrow peak, middle peak, middle narrow peak and outlet-peak. The experiments were performed in vertical tubes cooled by water flowing upwards. The test sections had a 15 mm tube inside diameter and a heated length of 7 m. The flow conditions were varied over a range of pressure from 1000 to 16000 kPa, mass flux from 500 to 3000 $kg.m^{-2}.s^{-1}$, heat flux from 90 to 3060 $kW.m^{-2}$ and inlet subcooling 10 K.

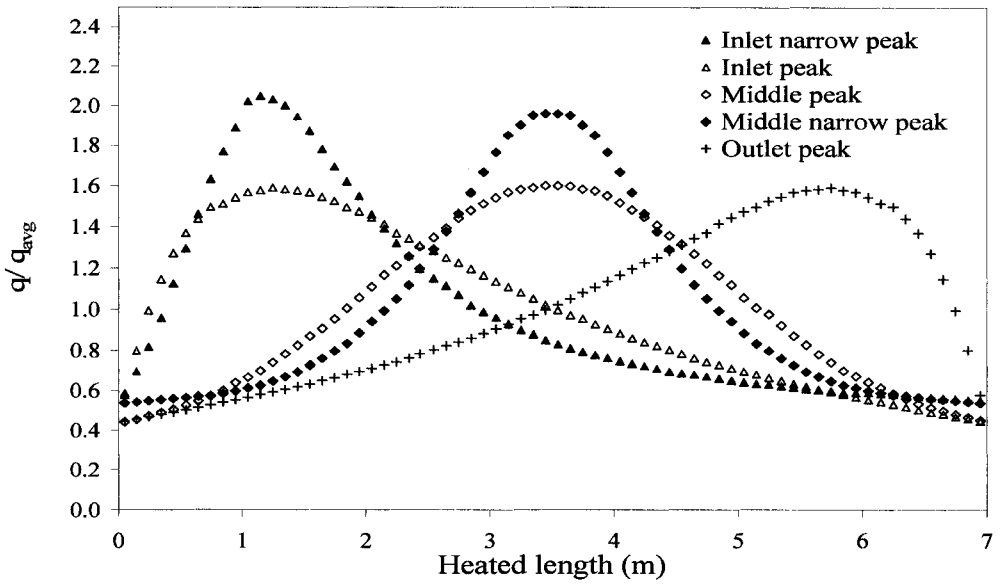

Figure 2.5 Heat flux profiles investigated by Becker et al. (1992).

The annular flow model of Whalley et al. (1974) was improved by Hewitt and Govan (1990) to predict the PDO heat-transfer. Azzopardi (1996) tested the annular flow/post-dryout model of Hewitt and Govan (1990) to predict the data of Becker et al. (1992). The model predicted the dryout location, but could not predict the location and magnitude of the maximum wall temperature.

Hoyer (1998) developed a two-phase, three-field annular flow model to predict dryout location and post-dryout heat transfer for uniform and non-uniform heated tubes. For non-uniform AFD, Hoyer (1998) used the Becker et al. (1992) data to examine his model. In the validation of his model, he used three heat flux levels (Becker data) for the inlet, middle and outlet-peak profiles. The predicted dryout location and post-dryout wall temperature profiles were in good agreement with experimental data. Minor deviation was found in the prediction.

El Nakla et al. (2006) performed an experimental and analytical investigation on the effect of AFD on PDO heat-transfer coefficient in tubes (ID = 5.46 mm) cooled by HFC-134a. The test sections were mounted vertically with upward flow. Three different axial heat flux profiles were studied: inlet-peak, middle peak and outlet-peak. Flow conditions were varied over a range of P = 1600–2800 kPa and G = 1400–4200 $kgm^{-2}.s^{-1}$. The results were compared to the reference AFD case, and the data were expressed using average heat flux and local heat flux. El Nakla et al. concluded that the AFD effect on PDO heat-transfer coefficient is not significant.

2.5 Obstacle Effects on Single-Phase Heat Transfer

Marek and Rehme (1979) performed an experimental and analytical investigation on the effect of spacers on single-phase heat-transfer in smooth and rough rod bundles. They proposed an empirical correlation for high Reynolds numbers and for smooth surfaces at spacer grids as:

$$\frac{Nu_{\max}}{Nu_0} = 1 + 5.55\varepsilon^2 \tag{2.10}$$

where Nu_0 is the fully developed Nusselt number and ε is the flow-blockage ratio. The experimental data of $(\frac{Nu_{\max}}{Nu_0} - 1)$ were plotted against ε^2, and the data points were fitted using a linear relation with a deviation of ±5% from Nu_{max}/Nu_0. The proposed correlation

was based on the assumption that heat-transfer enhancement near spacers depends on flow-blockage ratio; experimental results showed this dependency, and the analogy between pressure drop and heat-transfer supported this assumption. They found that heat-transfer augmentation could occur upstream of the leading edge of the spacer at high Reynolds number.

Hassan and Rehme (1981) performed an experimental and analytical investigation of the spacer effect on heat transfer for a gas-cooled rod-bundle test section (single-phase flow). The flow-blockage ratio was varied between 25% and 35%, and measurements were performed between $10D_{hy}$ upstream to $33D_{hy}$ downstream from the spacer grid (this was the assumed zone of influence of the spacer on heat transfer). Hassan and Rehme developed an empirical correlation to account for the influence of spacers on heat transfer. The following three parameters correlated the relationship between Nusselt number and heat-transfer enhancement:

- Reynolds number, Re,
- Graetz number, characterizes entrance effects, similar to spacer effects, since Nusselt number downstream from the spacer showed gradual decrease, when plotted against the inverse of Graetz number, Gz^{-1}, and
- flow- blockage ratio, ε.

In the development of their correlation, Hassan and Rehme assumed the same dependence of pressure drop on ε^2 for heat-transfer, since Pr $\approx$ 1 for gases, i.e. they assumed the analogy between momentum and heat is applicable. Their correlation at the spacer cross section is

$$Nu^*_{\max} = 1 + K \,\mathrm{Re}\, \varepsilon^2 \tag{2.11}$$

where $Nu^* = \frac{Nu}{Nu_0}$, and K was found from fitting Equation (2.11) to the experimental data, K depends on flow regime (Re), flow-blockage ratio (ε), and heating surface (smooth or rough).

The gradual decrease in Nusselt number from the spacer to downstream locations is similar to entrance effect. The shape of distribution of Nusselt numbers downstream from the spacer is an exponentially decaying function. The ratios of Nusselt numbers, Nu^*, downstream from the spacer were plotted against Gz^{-1} for different Re. The experimental results showed a gradual decrease of Nusselt number for every Reynolds number, and could be well approximated by a straight line at the center of each curve. The slope of the straight line (m) is the exponent of Gz number, m, which varied with Re and ε, so they assumed:

$$Nu^* = K(\mathrm{Re}, \varepsilon) Gz^{m(\mathrm{Re}, \varepsilon)} \tag{2.12}$$

The dependence of factors m and K on Re and ε was found from correlating the experimental data, and varied with types of heating surfaces, i.e., rough or smooth. The predictions of Nu^* were in good agreement with the experimental results.

Yao et al. (1982) analytically studied the effect of spacer grids on heat-transfer augmentation for rod bundles in single-phase flow and in dispersed flow film boiling (DFFB).

In single-phase flow they noticed heat-transfer enhancement upstream from the spacers over $2L/D$; their observation was based on the data obtained by other investigators. Yao et al. described the heat-transfer enhancement effects of spacers due to the local increase of velocity. In addition, if the spacer is in contact with the heated surface it can act as a fin, which cools the heated surface locally. Also the spacer can act as a heat sink, which absorbs part of thermal radiation of the rod bundles. Yao et al. neglected the thermal radiation and fin cooling of the spacers for temperatures of the heated surface below 500°C.

Yao et al. (1982) also considered analogy between momentum and heat transfer in turbulent flows as was done by Hassan and Rehme (1981). Downstream from a spacer, the flow decelerates and a turbulent wake region is established: the wake disturbs the boundary layer and enhances the heat transfer from the wall. They assumed that in this

region (downstream from the spacer) the heat-transfer augmentation caused by the wake is directly proportional to the pressure drop induced by the blockage. The overall heat-transfer enhancement due to spacers is expressed in the same form as the pressure drop increase due to the grid spacer, i.e.

$$(\frac{\Delta P}{\Delta P_0})_{sp} = \frac{f + K_{ob}\frac{D}{L}}{f} = 1 + (\frac{D}{fL})K_{ob} \tag{2.13}$$

Yao et al. used the Marek and Rehme correlation at the spacer plane (Equation (2.10)) in the form of

$$(\frac{Nu}{Nu_0})_{sp} - 1 = 5.55\varepsilon^2 \tag{2.14}$$

Yao et al. multiplied the right hand-side of Equation (2.14) by ($e^{-0.13(L/D)}$) to represent the decay of the Nusselt number ratio downstream from the grid spacer with L/D:

$$(\frac{Nu}{Nu_0})_{sp} = 1 + 5.55\varepsilon^2 e^{-0.13(L/D)}, \text{ for } \mathrm{Re} > 10^4 \tag{2.15}$$

For upstream locations, Yao et al. assumed that the effect of spacers is significant within a distance of $2L/D$, and a linear interpolation within the range of $2L/D$ was performed as an approximation to the heat-transfer enhancement measurements. When Yao et al. compared their correlations with the experimental data, they noted that the maximum enhancement (i.e., $5.55\varepsilon^2$, the correlation coefficient of Marek and Rehme in Equation (2.14)) was not well predicted.

.

Yao et al. developed a correlation to account for enhancement caused by egg-crate-type spacer grids with swirling vanes; they proposed a correlation to predict circumferential velocity, which is related to Nusselt number by a Dittus-Boelter type equation; in addition to the swirling effect, heat-transfer augmentation is influenced by the boundary layer growth:

$$(\frac{Nu}{Nu_0})_{1\Phi} = \{1 + 5.55\varepsilon^2 e^{-0.13(L/D)}\}\{1 + A^2 \tan^2 \Phi . e^{-0.034(L/D)}\}^{0.4} \tag{2.16}$$

where, A is the fraction of projected area of the vanes to the flow cross section, and Φ is the angle of the vane with respect to the axial direction.

Karoutas et al. (1995) developed a single-phase 3-D computational fluid dynamics (CFD) model (finite volume), to study velocity profiles (axial and lateral) and mass transfer near spacers. They used Laser Doppler Velocimeter to measure fluid velocity in the spacer region. They also measured the pressure drop due to spacers. Two types of spacers were examined:

- split vane design; swirling flow is generated in the subchannel.
- squeezed tube design; swirling flow is created around the rod.

Their work in the development of a two-phase model in the spacer region can be considered as a significant step forward in understanding the effect of spacers on CHF and PDO heat-transfer in pressurized water reactors (PWRs).

Holloway et al. (2004) performed an experimental and analytical investigation of the spacer effects on single-phase heat-transfer in rod bundles. They measured heat transfer and pressure drop downstream from the spacers for flow rates having Reynolds numbers (based on the hydraulic diameter of a subchannel) of 28000 and 42000. Holloway et al. developed correlations to account for heat transfer downstream from the spacers of standard support grids and of support grid with flow-enhancing features. They used several forms of correlations to represent the decaying heat-transfer enhancement with an increase in L/D. They claimed that the correlations show the tradeoff between heat-transfer enhancement downstream from the spacers and pressure drop increase resulting from the introduction of spacers. Holloway et al. (2004) observed that downstream from a split-vane grid there is a region where the local heat transfer is below that of the hydrodynamically fully developed value. Correlations for a standard grid and correlation for a grid with flow-enhancing features were derived – the local heat-transfer enhancement (local Nusselt number ratio) was correlated in terms of L/D and blockage ratio of the grid, and the normalized loss-coefficient for the support grid with flow-enhancing features.

The following correlation having an exponential form was proposed to describe heat transfer downstream from a standard support grid spacer:

$$\frac{Nu}{Nu_0} = 1 + C_1 \varepsilon^2 e^{-\alpha L / D_{hy}} \tag{2.17}$$

where C_1= 6.5, α = 0.8, L/D = 1.4 to 33

A correlation based on the following form:

$$\frac{Nu}{Nu_0} = 1 + K\left(\frac{L}{D_{hy}}\right)^{\lambda} \tag{2.18}$$

where K and λ are spacer-specific coefficients, was also proposed for disc blockage and split-vane pair:

$$\frac{Nu}{Nu_0} = 1 + \{C_1 \varepsilon^2 + C_2\left(\frac{k_{feat}}{k_g}\right)\} e^{-\alpha L/D_{hy}} \tag{2.19}$$

where C_1 = 6.5, C_2 = 3.2, α = 0.8 these coefficients were derived from curve fitting the data, and L/D = 1.4 to 33, K_{feat} is the "feature" loss-coefficient and K_g is the grid loss-coefficient.

Holloway et al. (2004) did not compare their correlations against experimental data obtained by other investigators.

The prediction methods for single-phase heat-transfer enhancement due to obstacles are presented in Table 2.1, while experiments performed on single-phase flow with obstacles are summarized in Table 2.2, and spacer pressure drop correlations in single-phase flow are tabulated in Table 2.3.

2.6 Obstacle Effects on PDO Heat Transfer

Yao et al. (1982) assumed that the prediction of single-phase heat-transfer enhancement (Equation (2.15)) can be used to predict enhancement in DFFB. They considered three mechanisms of heat-transfer augmentation: radiation, fin cooling, and vapor flow disturbance with droplets, or the total heat flux:

$$q_w = q_{w,rad} + q_{w,fin} + q_{w,2\phi} \tag{2.20}$$

where 2Φ refers to the dispersed flow at post CHF and the radiation wall heat flux ($q_{w,rad}$) can be found from:

$$q_{w,rad} = \beta F_{ws} \sigma (T_w^4 - T_s^4) \tag{2.21}$$

where β is the fraction of wall area seen by the spacer at spacer region. F_{ws} is a view factor from wall to spacer considering gray body effect. $q_{w,fin}$ is calculated with the assumption that the heat-transfer coefficient on the fin is the same as heat transfer on the wall, and $q_{w,2\phi}$ is calculated based on Equation (2.15). Yao et al. assumed that the analogy between momentum and heat transfer still exist, because for very small droplets, the two-phase dispersed flow is nearly homogenous. Equation (2.15) was considered as a first-order estimation of heat transfer near spacer grid, since other heat-transfer mechanisms such as rewetting of the heating surface are not considered.

Gonin and Sergeev[1] performed an analytical and experimental investigation of steam-water mixtures in tubes (2 and 5 m length), ID = 10 mm. The test section was equipped with spacer simulators having a flow-blockage ratio of 15.4 and 32.6% and a spacer pitch of 0.1 and 0.5 m. The flow conditions were varied over a pressure range of 9.8–17.8 MPa, a mass flux range of 500–1500 $kg.m^{-2}.s^{-1}$, and a heat flux range of 170–1500 $kW.m^{-2}$. Gonin and Sergeev developed a one-dimensional procedure of PDO heat-

[1] Year of publication is unknown

transfer in channels with spacers. The predictions agreed with experimental data obtained from annuli and rod bundles with obstacles.

Gonin and Sergeev found that rewetting was observed more frequently in test sections with higher flow-blockage ratios – the enhancement was more pronounced when pressure was decreased from 17.8 to 13.7 MPa or mass flux was increased. Because of decreasing pressure, vapour density decreases and therefore the vapour-droplet mixture velocity increases, but when the pressure was decreased to 9.8 MPa, at low-mass fluxes, the effect became less significant. One finding, that seems unrealistic, is that for a spacer pitch of 0.1 m the temperature drop downstream from the spacers was less significant than the temperature drop with a pitch of 0.5 m.

Gonin and Sergeev developed a 1-D method of predicting heat transfer downstream from the obstacles based on the classical 2-step PDO model – convective heat removal from heated surface to vapour (non-thermodynamic equilibrium), and from vapour to dispersed liquid droplets at saturation temperature. The prediction method for heat-transfer augmentation divides heat-transfer region near spacers into separate regions, based on the heat-transfer mode. The rewetting zone is considered by using flow-boiling heat-transfer correlations – at the end of rewetting zone, the heat-transfer coefficient is calculated by the correlation of Isachenko (1969). The augmentation of single-phase heat transfer is also considered. The actual quality is predicted by integrating numerically Sergeev's Energy Equation (discussed below), consequently, the enthalpy of superheated vapor is calculated and wall temperature is defined as:

$$T_w = T_V + q/h_V \tag{2.22}$$

Sergeev's vapour-droplet flow energy equation (Sergeev, 1987), in differential form, is approximated by the following equation where the actual quality (vapour-weight quality) is the unknown variable.

$$\frac{dx_a}{dx_e} = Cm\frac{k_v}{\sigma(\rho_f)}\frac{P_W G^2}{\sum_j (qP_h)_j} x_a(1-x_a)\left(\frac{x_e - x_a}{x_a}\right)^n \tag{2.23}$$

where C is an empirical factor = 1.0 or 1.5, m and n are pressure-dependent parameters, P_h and P_w are the heated and wetted perimeters, respectively, and q_j is the local heat flux. The amount of liquid droplets evaporated as a result of interaction with obstacles is assumed to be proportional to liquid flow rate and flow-blockage ratio, and is predicted by:

$$\Delta G = -G(1-x_a)k\varepsilon \tag{2.24}$$

where k is the spacer efficiency factor.

The actual vapor mass quality is predicted from the numerical integration of the energy differential equation starting from x_{do}, where $x_a = x_{do} = x_e$, and $T_V = T_{sat}$. At the cross section of a spacer, the change (addition) of quality can be found from:

$$\Delta x_a = (1-x_a)k\varepsilon \tag{2.25}$$

and consequently, by integrating the energy equation, any x_a can be found. Enthalpy may be calculated from an energy balance equation – once x_a, enthalpy and P are known, T_V is also defined, and $T_w = T_V + q/h_V$. Rewetting is taken into account by considering the difference between x_a and x_e at the spacer cross section – if the difference is > 0, it is expected that the additional vapour is due to liquid evaporation as a result of interaction of droplets with spacers. The length of rewetting region can be calculated from:

$$\Delta Z = \frac{GH_{fg}(x_a - x_e)}{\sum_j (qP_h)_j} \tag{2.26}$$

In this rewetting region, correlations for boiling heat transfer are considered. The Gonin and Sergeev model considered the enhancement of single-phase heat transfer correlated by Yao et al. (1982). The model also considered the heat transfer to vapour at the end of

rewetting length, as well as near dryout point, where the heat-transfer coefficient is calculated from:

$$\frac{h}{h_0} = 1.38\,(D_{hy} / \Delta z) \tag{2.27}$$

where, Δz is the distance downstream from the dryout point.

Sergeev et al. (1990) performed an experimental and analytical investigation of the effect of spacers on post-dryout heat transfer. The same flow conditions as in Gonin and Sergeev experiments apply. Sergeev's energy equation is limited by $G \leq 1000$ kg.m^{-2}.s^{-1} (Kirrilov and Groeneveld, 1999). Sergeev et al. (1990) also studied the global and local effects of spacer, i.e., global decrease of temperature distribution, and local or downstream temperature drop. Both effects are related to flow-blockage ratio – the global and local effects are more pronounced for large ε values. The local temperature drop is related to quality, the temperature drop is less at high qualities. Rewetting has a similar dependence of local temperature drop on quality. As expected, Sergeev et al. (1990) noticed that rewetting occurred more frequently with large flow-blockage ratios.

Sergeev (2005) proposed a phenomenological 1-D model for film boiling heat-transfer based on the following assumptions:

- two mechanisms of heat transfer exist (from wall to vapour and from vapour to liquid droplets),
- the two-phase flow has a uniform distribution of droplets within the vapour core, and
- a constant Nusselt number is assumed for droplets.

Sergeev (2005) showed that his model can be applied to uniform and non-uniform AFD profiles. The model also considered spacer effects and different channel geometries. An ordinary differential equation relating mass quality and equilibrium quality was derived based on the energy equation of heat flux from vapour to droplets. The equation is the same as Equation (2.23) and has the final form of:

$$\frac{dx_a}{dx_e} = Cm \frac{k_v}{\sigma(\rho_f)} \frac{P_w G^2}{\sum_j (qP_h)_j} x_a (1 - x_a) \left(\frac{x_e - x_a}{x_a} \right)^n \tag{2.28}$$

and can be approximated by:

$$\frac{dx_a}{dx_e} = A(1 - x_a)(x_e - x_a) \tag{2.29}$$

where $A = Cm$.

The heat-transfer effect of spacers is considered in the same way as in Gonin and Sergeev and Sergeev et al. (1990).

Kim and Korol'kov (1991) proposed an empirical correlation to account for the separation of droplets from the film boiling:

$$\frac{Nu}{Nu_0} = 1 + K_e \varepsilon^2_e \left(-0.13 \frac{L}{D_{hy}} \right) \tag{2.30}$$

where

$$K_e = A(x - x_{thr})(1 - x) \tag{2.31}$$

x_{thr} is the dryout quality, which is predicted by Galchenko (1984), and does not account for CHF enhancement due to obstacles, A is a heat-transfer enhancement factor, which is a numerical factor determined experimentally, for a given design and specific conditions in which the spacer operates (for each obstacle, parameter A is defined separately).

Kim and Korol'kov's correlation was developed based on Yao et al. (1982) single-phase heat-transfer augmentation correlation, where the factor 5.55 was replaced by the heat-transfer enhancement factor (K_e). The correlation overpredicts heat-transfer enhancement and is in poor agreement with its experimental data at high x_{thr}. It does not predict rewetting downstream from the obstacles.

Stosic (1995) analyzed the spacer effect on PDO heat transfer in rod bundles using the HECHAN 2.1 model. He considered the model as non-homogenous. The droplets in the film flow were also considered in some cases in order to validate the analogy between momentum and heat transfer. Stosic found that the enhancement of heat-transfer coefficient near spacers increased by about 20 to 25%, and spacer effects are present up to 20 to 30*L/D* downstream from a spacer. Different types of spacers were considered, honey comb grid spacer and egg-crate grid spacer. Spacers improved heat transfer, however they also increased pressure drop (form drag and skin friction). Some spacer designs were equipped with swirling vanes (e.g., mixing vane grids). Grid spacers with swirling vanes enhance sub-channel mixing and increase velocities, which in turn increase heat transfer between the fluid and the heated surface downstream from the spacer. The mixing vanes are designed in such a way that they create swirling in the adjacent sub-channels in opposite directions, to avoid swirling flow against each other.

The HECHAN model considers a channel with average hydraulic values and boundary conditions. PDO regime is modeled as one dimensional, non-homogenous, and non-equilibrium flow of a two-phase mixture. It assumes no droplet break-up at the dryout location, if the diameter of droplet is less than the critical one. Two-phase pressure-loss is calculated with the single-phase pressure-loss multiplied by a two-phase multiplier, Φ.

$$\Delta P_{2\Phi(local)} = K_{ob}\frac{G^2}{2\rho_{2\Phi}} = K_{ob}\frac{G^2}{2\rho_{l,sat}}\Phi \tag{2.32}$$

where Φ is the two-phase local-loss multiplier, K_{ob} is the local single-phase pressure-loss coefficient. Based on experimental data, Equation (2.32) was approximated using the homogenous multiplier, thus Equation (2.32) becomes:

$$\Delta P_{spacer} = K_{ob}\frac{G^2}{2\rho_{l,sat}}\left[1+\frac{v_{fg}}{v_{l,sat}}(x)\right] \tag{2.33}$$

where v_{fg} is the difference between specific volume of saturated vapor and liquid. Stosic (1995) adopted single-phase flow prediction correlation of Marek and Rehme (1979) and

Yao et al. (1982) correlations for the model HECHAN, the only difference from Yao et al. correlation is that, for spacers with swirling vanes, the term which represents straight spacer effect is summed to the term which considers the swirling augmentation (Yao et al. multiplied the two terms). A comparison between predictions of the model and experimental data obtained by Stosic (1995) showed an overprediction of surface temperatures for the steady state experiments. The overprediction is caused by (i) neglecting the enhancement of droplets break-up (the droplet flux was assumed to be constant), when they hit the spacer, and (ii) the sensitivity of droplet diameter to critical Weber number. However, for the transient tests, a better agreement was found.

Leung et al. (2005) performed analytical and experimental study of the effect of obstacles on post-dryout heat transfer. They developed a correlation for fully-developed-film-boiling heat transfer to predict heat-transfer enhancement near obstacle, expressed as:

$$Nu^* = \frac{Nu}{Nu_0} = 1 + (0.47 + 0.481 x_e (1 - x_e)^{0.105}) \times K_{ob} \exp(-0.13 \frac{L}{D_{hy}}) \tag{2.34}$$

where K_{ob} is the single-phase pressure-loss coefficient of the obstacle, which in addition to flow-blockage ratio includes other obstacle parameters like obstacle shape and location, and x_e is the equilibrium quality.

Leung et al. (2005) also derived a correlation for developing film-boiling heat-transfer enhancement:

$$\frac{Nu_{dev}}{Nu_{fd}} = 1 + (\frac{Nu_{nb}}{Nu_{fd}} \frac{k_f}{k_g} - 1) \exp\left[-10.83 \left(\frac{q}{CHF_{ob}} - 1 \right)^{0.37} \psi_{tp}^{-0.08} \left(\frac{\rho_f}{\rho_g} \right)^{0.28} \right] \tag{2.35}$$

where Nu_{fd} is the fully developed film-boiling Nusselt number, Nu_{nb} is the nucleate boiling Nusselt number predicted by Chen correlation (1963), ψ_{tp} is the two-phase Weber number:

$$\psi_{tp} = \frac{G^2 D(x_e/\rho_g + (1-x_e)/\rho_f)}{\sigma} \tag{2.36}$$

q is the local heat flux, CHF_{ob} is the enhanced value of CHF due to presence of flow blockages, and can be predicted using equations given by Guo (2001), Groeneveld (2001) and Pioro et al. (2002).

Equation (2.34) features the single-phase pressure-loss coefficient; this implies an analogy between momentum and heat transfer. For single-phase heat-transfer, Equation (2.34) shows good agreement with six data sets with an *rms* error of 4.71%. For film boiling data, it has the correct asymptotic trends but with an *rms* error of 20.05 %, as it underpredicts the enhancement of higher flow blockage and it does not consider possible rewetting of the heated surface downstream from an obstacle.

Leung et al. (2005) improved the prediction of heat-transfer enhancement by considering the enhancement of CHF due to obstacles as predicted by Equation (2.35). For a location downstream from an obstacle, the value of critical heat flux (CHF_{ob}) is compared with the local heat flux (q): if $q < CHF_{ob}$, nucleate boiling is assumed, otherwise film boiling is assumed. Leung et al. (2005) also improved the prediction accuracy of the correlation by considering enhancement effect of developing film-boiling downstream from an obstacle.

Anglart et al. (2005) experimentally investigated the PDO heat transfer for an annulus with spacers. The experimental results suggested the importance of dryout and PDO local equilibrium qualities as correlating parameters. With decreasing mass flux, dryout and PDO equilibrium qualities increase, and the PDO wall superheats also increase. This increase of wall superheat was attributed to the relative decrease in the concentration of droplets. The effect of heat flux was also shown at specific flow conditions. The dryout location moved from downstream to upstream from the spacer, when heat flux was increased by 10 to 12%.

Uchida et al. (1999) investigated the effect of spacers on post DNB heat transfer in rod bundles cooled by Freon-123. The effect of simple support grid, non-mixing grid, and grid with mixing vanes on post DNB heat-transfer was studied. Uchida et al. (1999) found that the enhancement of heat-transfer coefficient is higher for both spacers with or without swirling vanes than for simple support grid spacer. They examined the correlations of Groeneveld (1973), Condie-Bengston/RELAP5, Kuo (1981) and Groeneveld and Delorme (1976). The correlation of Groeneveld and Delorme (1976) gave better prediction of post-DNB temperatures than other correlations for the simple support grids.

Prediction methods for PDO heat-transfer enhancement due to obstacle can be found in Table 2.1, experiments performed on DFFB flow and obstacles are summarized in Table 2.2, and spacer pressure drop correlations in DFFB are tabulated (Table 2.3).

2.7 Spacer Effects at Reflooding

Analytical and experimental studies were performed by Cluss (1978) on spacer effects in a vertical tube with constant temperature, representing PDO heat-transfer conditions during the reflood-phase of a LOCA. Cluss (1978) applied a single-phase heat-transfer correlation (Dittus-Boelter) to DFFB by considering the increase of velocity of vapor at the spacer entrance, where the void fraction is assumed 100%. The radial (deposition) velocity is predicted by the Ganic and Rohsenow (1976) correlation, which is a function of vapor velocity and vapor Reynolds number. The flow-blockage ratio was not considered as a correlating parameter in his study.

Cluss (1978) described the possible mechanisms of enhancement as follows:
The flow area reduction at the spacer increases flow velocity and forms an effect similar to the entrance effect, which increases wall-to-vapor convection and wall-to-droplet conduction, droplets colliding with the spacer can form a saturated liquid film, which can cool the superheated vapor and the heated surface, by providing extra heat-transfer

surface as a fin, also this layer absorbs part of radiative heat flux from the hot wall and splashes droplets onto the heated surface downstream from the spacer.

Nagler (2000) performed Lagrangian/Eulerian simulation (unsteady droplets conservation equations in a Lagrangian form were transferred into Eulerian system) of a DFFB regime during reflood including spacer effects; he assumed the following heat-transfer enhancement effects of spacers:

Effect on heat transfer to droplets:

- droplets in DFFB have two competing effects: (i) droplets in the core suppress turbulence, which will tend to decrease HTC at high vapor Reynolds number and (ii) droplets can disturb the boundary layer and produce additional turbulence as they are close to the wall.
- droplet breakup between spacers is negligible (low droplet Weber number and high void fraction), probability of droplet breakup at the spacer increases with increasing the spacer cross section.
- droplets which hit the spacer are shattered; and the collision probability of droplets which may hit the spacer is a function of flow- blockage obstruction and flow area (flow-blockage ratio).
- the population distribution of droplets which may collide with spacer is doubled at the entrance of each spacer grid.
- the drag coefficient has a significant influence on droplet velocity. Droplet motion is caused by the drag force acting on droplet by the momentum of the vapor.

Effect on wall-to-vapor heat transfer:

- the reduction of the flow area at obstacle leads to increase in flow velocity and sudden decrease in hydraulic diameter.
- the radiation heat transfer is minor.

Ergun (2006) modeled the PDO heat transfer with a two-fluid Eulerian approach. He considered the effects of spacers during the reflood phase of a LOCA for a pressurized

water reactor (PWR), including heat-transfer enhancement upstream from the spacers at reflood conditions. Ergun (2006) modeled all aspects of spacer effects on heat and mass transfer; he summarized the literature pertinent to droplet hydrodynamics, and also described the spacer effects on heat-transfer enhancement as:

(i) Single-phase heat-transfer enhancements:

spacers constrict flow area, and hence disrupt momentum and thermal boundary layers; the flow accelerates within the spacer and expands downstream. This region of developing boundary layer is similar to the entrance region, so the heat-transfer enhancement can be modeled as an entrance effect. Spacer structures provide a surface for radiation heat transfer from rods, and they help to cool the fuel rods and de-superheat the vapor.

(ii) Two-phase heat-transfer enhancements:

- spacers are colder than the fuel rods, and they rewet easier than the hotter rods, thus enabling the formation of liquid film which provides additional interfacial heat transfer between vapor and liquid film. This contact also results in an evaporation of the liquid film which causes vapor velocity to increase.
- spacers break-up entrained droplets into smaller ones, which have more heat-transfer area and when evaporating, they increase vapor velocity and convective heat transfer.
- Re-entrainment of droplets from the spacers increases the convective heat-transfer.

2.8 Research Work in Related Areas

Windecker and Gu (1999) studied annular flow in rod bundles (numerical study and simulation using Eulerian/Lagrangian approach). In order to separate the parameters influencing the deposition rate in Boiling Water Reactors (BWR), they simulated saturated steam water flow with and without spacers (ring type).

The primary parameters investigated were: total mass flux, vapour quality, vapour-phase turbulence intensity, droplet mean diameter as well as spacer width and height. They proposed a correlation of droplet deposition rate, based on two assumptions:

1. no entrainment from wall to core.
2. no change of vapor quality by evaporation.

The correlation is:

$$\frac{\dot{D}}{\sqrt{tke}\,\rho_g} = k^* C^* \tag{2.37}$$

where,

$\dot{D}$ - deposition flux, referred to unit wall area

C^* - dimensionless droplet core concentration

k^* - dimensionless deposition rate

tke- turbulent kinetic energy of the gas phase (two-way coupled)

They concluded that:

- for fuel rod bundles without spacers, an increase in vapor Reynolds number results in a proportional increase of droplet deposition rate, however an increase in droplet mean diameter results in a decrease in droplet deposition rate.
- in rod bundles without spacers, they did not observe any dependency of deposition rate on droplet core concentration.

They confirmed that the increase of turbulent kinetic energy downstream of a ring-type spacer is correlated to the spacer flow-blockage ratio.

2.9 Discussion of the Obstacle Effects on Single-Phase and PDO Heat Transfer

The findings of the literature review are summarized in the following subsections.

2.9.1 Single-Phase Heat-Transfer Studies

Marek and Rehme (1979), Hassan and Rehme (1981), and Yao et al. (1982) investigated the effect of spacers on single-phase heat transfer. Yao et al. (1982) also investigated the effect of spacers on PDO heat transfer.

Initially, the maximum heat-transfer enhancement, due to spacers, was correlated by Marek and Rehme (1979). Based on their experimental results, they proposed correlations for smooth and rough surfaces based on the analogy between pressure drop (momentum transfer) and heat-transfer. Hassan and Rehme (1981) proposed correlations to account for the obstacle effect upstream and downstream from the spacer. The equations of Yao et al. (1982) were also based on the analogy between momentum and heat transfer; they correlated the distribution of relative enhancement downstream from the spacer as an exponentially decaying function of L/D.

Holloway et al. (2004) performed experimental and analytical investigations on single-phase heat transfer in rod bundles. The correlations were developed to account for the heat transfer downstream from standard support grids and downstream from support grid with flow-enhancing features. Holloway et al. (2004) did not test their correlations against the experimental data of others.

2.9.2 PDO Heat-Transfer Studies

Papers authored by (i) Gonin and Sergeev, (ii) Sergeev et al. (1990), (iii) Kim and Korol'kov (1991), and (iv) Sergeev (2005) investigated the effect of obstacles on PDO heat transfer. Papers (i), (ii), and (iv) used a similar approach in considering the mechanisms of heat-transfer augmentation, which focused mainly on the prediction of the actual mass quality, and the application of appropriate heat-transfer correlations to certain regions upstream and downstream from the spacer – the Yao et al. (1982) correlation was used to predict spacer heat-transfer enhancement.

Kim and Korol'kov (1991) used a similar phenomenological approach to Marek and Rehme (1979), and Yao and Hochreiter (1982); the methodology is based on analogy between pressure drop (momentum) and heat transfer.

Stosic (1995) analyzed the spacer effect in rod bundles. Spacer effects in PDO heat transfer during steady-state and transient conditions were investigated by his model (HECHAN). In his model, Stosic assumed non-equilibrium, non-homogenous 1-D two-phase flow. Spacers improved the downstream heat transfer, but also increased pressure drop (form drag and skin friction). The Stosic model overestimated surface temperature for steady state experiments. Different types of spacers were considered. The obstacle effects started upstream from the first spacer, however for the second spacer, at $G < 1000$ $kg.m^{-2}.s^{-1}$, the effects were considered to start downstream from the spacer. The overall spacer effects were treated by assuming that the PDO spacer effects consist of: (i) single-phase (homogenous) flow effect; where the correlation of Yao et al. (1982) is used, and (ii) two-phase-flow-effect, where non-homogenous flow is assumed.

Leung et al. (2005) performed an experimental and analytical study, where they introduced correlations for developing and fully developed PDO heat transfer. The correlation for fully developed PDO flow features the single-phase pressure-loss coefficient as a correlating parameter, which replaced flow-blockage ratio. The pressure loss-coefficient includes other effects such as obstacle location and shape, which influences the PDO heat transfer. The prediction accuracy of the correlations are in good agreement with the experimental data for single-phase heat transfer; for PDO heat transfer the model underpredicted the enhancement.

Uchida et al. (1999), Anglart et al. (2005), and Peng et al. (2003) performed experiments on post CHF heat transfer near obstacles on rod bundles, annuli, and tubes, respectively.

2.9.3 Prediction Methods and PDO Heat-Transfer Mechanisms

2.9.3.1 Prediction methods in single-phase and PDO heat transfer

- There is no specific prediction method available that predicts the combined effect of axial heat flux profile and flow obstacle on post-dryout heat-transfer coefficient. None of the existing studies have examined the combination of these two effects.

- Marek and Rehme (1979) correlated heat-transfer enhancement at the spacer plane in single-phase; they considered Reynolds analogy between momentum transfer (pressure drop) and heat transfer. Yao et al. (1982) correlated the distribution of enhancement downstream from a spacer in single-phase flow as an exponentially decaying function of *L/D*. Sergeev et al. (1990) used the correlation of Yao et al. (1982) in their vapor generation model to predict spacer enhancement in PDO heat transfer, they also calculated the actual quality. Kim and Korol'kov (1991) introduced the quality to account for spacer enhancement in PDO heat transfer; they replaced the spacer loss-coefficient ($5.55\varepsilon^2$) with a numerical factor determined from experiments. Leung et al. (2005) introduced the single-phase pressure-loss coefficient which replaced the numerical factor of Kim and Korol'kov (1991) to account for the obstacle shape and location in the flow-cross section; they also introduced the effect of CHF and developing film-boiling on PDO heat transfer in presence of obstacles.

- The prediction methods of Nusselt number ratio (Nu/Nu_0) in single-phase flow have the basic form of Equation (2.15) of Yao et al. (1982): $\frac{Nu}{Nu_0} = 1 + a_1 \times \varepsilon^2 \times \exp(-a_2 \frac{L}{D})$, where the coefficient a_1 is optimized to fit data of specific spacer designs, and a_2 represents the decaying rate of (Nu/Nu_0) and usually has the value of 0.13 as in the Yao et al. (1982) correlation. In PDO heat transfer, the analogy between momentum and heat transfer is assumed valid on the

basis that the droplets are uniformly distributed in the flow – this assumption seems to be more realistic for highly turbulent flows. Similar to single-phase flow, the overall form of the PDO heat transfer correlations remained unchanged, except that an effect of quality was introduced into the correlating parameters. The PDO Nusselt number ratio had the form: $\frac{Nu}{Nu_0} = 1 + a_3 \times B \times f(x) \times \exp(-a_4 \frac{L}{D})$, where a_3 is a numerical constant for specific design of spacer, and a_4 represents the decaying rate of (Nu/Nu_0), and usually has a value of 0.13. B is the single-phase pressure-loss coefficient, or the square of flow-blockage ratio, and $f(x)$ is a function that has a weak dependence on x. Obstacle effects on CHF and the developing film-boiling effect on PDO heat-transfer enhancement were also considered.

2.9.3.2 PDO heat-transfer enhancement mechanisms

Obstacles block off a fraction of the channel free flow-area; hence the flow distribution, the heat-transfer characteristics of the two-phase flow and the surface-temperature distribution are changed. In film boiling, the heat-transfer enhancement can be attributed to:

(i) Turbulence enhancement:

- Obstacle induced: due to an increase in turbulence at the obstacle location which enhances the heat transfer between vapour and heated surface and between vapour and droplets.
- Rewetting: because of the sudden local contraction and expansion of the flow area, the fluid flow accelerates in the axial and radial directions causing an increase in turbulence of the two-phase flow and forcing entrained droplets in the core flow to change their trajectories. Depending on the flow blockage and quality, these droplets have a greater probability of impinging on the heated surface and cause rewetting close to obstacle location. Rewetting will lead to an increase in vapour generation.

- Enhancement of heat-transfer rate downstream of an obstacle: beyond the obstacles, the flow expands and decelerates, and turbulent wakes are generated. Overall, the relative velocity between the vapor and the droplets is increased compared to fully developed flow at upstream locations, and the interfacial heat transfer is also increased. The developing film boiling heat transfer leads to a decrease in vapor superheat.

(ii) Droplet break-up: as a result of droplet collision on the obstacle surface and depending on the flow blockage and quality, large droplets shatter into smaller sizes, so that the heat-transfer area of droplets is increased. Droplets break-up results also in an increase in vapour generation and an increase in interfacial heat transfer between vapour and droplets and between droplets and heated surface.

(iii) Fin effect: the presence of an obstacle increases the heat-transfer area conducting heat from the surface to the coolant.

Table 2.1 Prediction methods of spacer effect on single-phase and PDO heat transfer.

Author	Prediction method	Flow regime	Comments
Marek and Rehme (1979)	$\frac{Nu_{max}}{Nu_0} = 1 + 5.55\varepsilon^2$, at the spacer plane (the maximum enhancement), ε is the flow-blockage ratio.	Single-phase Gas	Predicts only the maximum enhancement
Hassan and Rehme (1981)	At spacer leading edge: $\frac{Nu_{max}}{Nu_0} = 1 + K(\mathrm{Re})\varepsilon^2$, and $\frac{Nu}{Nu_0} = K(\mathrm{Re},\varepsilon)Gz^{m(\mathrm{Re},\varepsilon)}$ For downstream from the spacers, Gz is Graetz number, and K is a factor depends on Re, ε and heating surface (rough or smooth).	Single-phase Gas	Smooth and rough surfaces
Yao et al (1982)	Upstream from spacer, linear interpolation from $2L/D$ to the location of Nu_{max} (cross section of spacer). Downstream from spacer: $(\frac{Nu}{Nu_0})_{sp} = 1 + 5.55\varepsilon^2 e^{-0.13(L/D)}$	Single-phase (different) and PDO (re-flood conditions)	• $\mathrm{Re} > 10^4$ • Smooth surfaces • For bundles equipped with straight egg crate spacer
Holloway et al. (2004)	Downstream from spacers $\frac{Nu}{Nu_0} = 1 + C_1\varepsilon^2 e^{-\alpha L/D_{hy}}$, where $C_1 = 6.5$, $\alpha = 0.8$	Single-phase Water	• Re: 28000 and 42000 • L/D = 1.4 to 33 • Smooth surfaces • Bundles • Support grid (standard without flow enhancing features like swirling vanes)

Table 2.1 Prediction methods of spacer effect on single-phase and PDO heat transfer (continued).

Author	Prediction method	Flow regime	Comments
Sergeev et al. (1990)	Complex calculation procedure	PDO Water	Tube, bundle, and annulus
Gonin and Sergeev	Complex calculation procedure	PDO Water	Tube, bundle, and annulus
Kim and Korol'kov (1991)	$\frac{Nu}{Nu_0} = 1 + K_e \varepsilon 2_e^{\left(-0.13\frac{L}{D_{hy}}\right)}$, where $K_e = A(x - x_{thr})(1 - x)$, A is a numerical factor defined experimentally, x_{thr} is the dryout quality	PDO Water	Annulus, the constant, A, needs to be derived from obstacle data.
Leung et al. (2005)	Eqn. (2.34): $Nu^* = \frac{Nu}{Nu_0} = 1 + (0.47 + 0.48 \mathrm{lx}_e (1 - x_e)^{0.105}) \times K_{ob} \exp(-0.13\frac{L}{D_{hy}})$ where K_{ob} is the obstacle single-phase-pressure loss coefficient and x_e is the equilibrium quality. Eqn. (2.35) considers enhancement of developing film boiling downstream from the obstacles and includes CHF enhancement due to obstacles, CHF_{ob}: $\frac{Nu_{dev}}{Nu_{fd}} = 1 + (\frac{Nu_{nb}}{Nu_{fd}} \frac{k_f}{k_g} - 1) \exp\left[-10.83\left(\frac{q}{CHF_{ob}} - 1\right)^{0.37} \psi_{tp}^{-0.08} \left(\frac{\rho_f}{\rho_g}\right)^{0.28}\right]$ Nu_{fd} is the fully developed film-boiling Nu, Nu_{nb} is nucleate boiling Nu number predicted by Chen correlation (1963), and ψ_{tp} is the two-phase Weber number.	PDO HFC-134a	K_{ob} takes into account obstacle shape and location.

Table 2.1 Prediction methods of spacer effect on single-phase and PDO heat transfer (concluded).

Author	Prediction method	Flow regime	Comments
Sergeev (2005) PDO Model with a correction for spacers	Calculation procedure similar to Sergeev (1990)	PDO Water	Considers AFD Different flow geometries: tube, bundle, and annulus

Table 2.2 Experiments performed on obstacle effect on single-phase and PDO heat transfer.

Table Reference	Flow regime/ Flow conditions	Test Section (TS)	Spacer/obstacle details	Comments
Marek and Rehme (1979)	Single-phase, Re = 1.26×10^5 q = 30 kW.m^{-2}	TS with 3 electrically heated tubes, OD = 21.2 mm each, and length = 2002 mm	ε = 25–35%, honeycomb-type, 30 mm long	Gas
Hassan and Rehme (1981)	Single-phase, Re = 6×10^2–2×10^5 q = 0.5–50 kW.m^{-2}	TS with 3 electrically heated tubes, OD = 21.2 mm each, and length = 2002 mm	ε = 25–35%, honeycomb-type, 30 mm long	• Gas • Uniform AFD • Measurements at $10D_{hy}$ upstream and $33D_{hy}$ downstream from the spacer
Holloway et al. (2004)	Single-phase, Re = 28000 and 42000	5×5 rod bundle, OD = 9.5 mm	Different grid designs with and without mixing vanes	Water
Karoutas et al. (1995)	Single-phase, P = 4.83 bar, T_{water} = 26.67°C, average velocity = 6.79 m.s^{-1}	5×5 rod bundle	Two grid designs were investigated.	Water, measurements of velocity components as well as pressure drop measurements

Table 2.2 Experiments performed on obstacle effect on single-phase and PDO heat transfer (concluded).

Reference	Flow regime/ Flow conditions	TS	Spacer/obstacle details	Comments
Gonin and Sergeev	PDO, P = 9.8–17.8 MPa, G = 500–1500 $kg.m^{-2}.s^{-1}$, q = 170–1500 $kW.m^{-2}$	Upflow, tube ID = 10 mm, length= 2 and 5 m	ε = 0.154 and 0.326% Pitch = 0.1 and 0.5 m	Water, figures plotted with G = 500 and 1000 $kg.m^{-2}.s^{-1}$
Sergeev et al. (1990)	PDO, P = 9.8–17.8 MPa, G = 500–1500 $kg.m^{-2}.s^{-1}$, q = 170–1500 $kW.m^{-2}$	Upflow, tube ID = 14 mm, and length = 2 and 5 m	ε = 0.154 and 0.326% Pitch = 0.1 and 0.5 m	Water, figures plotted with G = 500 and 1000 $kg.m^{-2}.s^{-1}$
Kim and Korol'kov (1991)	PDO, P = 2.65 and 3.3–6.4 MPa, G = 420, 847, and 1200 $kg.m^{-2}.s^{-1}$, x_{in} = 0.38–0.45 and 0.795	Upflow, annulus, internal tube is heated	ε = 0.1% 3 spacers, box-shape Pitch = 0.5 m	Water
Peng et al. (2003)	PDO, P = 1.67 MPa, G = 1000, 2000, and 3000 $kg.m^{-2}.s^{-1}$, T_{in} = 37, 47, and 57°C	Upflow, tube ID = 6.92 mm	ε = 12%, long cylinder, OD = 2.4 mm, length = 10 mm	• HFC-134a • Experiment included the change of circumferential position of obstacle
Leung et al. (2005)	PDO, P = 1.13 MPa, G = 2000 and 3000 $kg.m^{-2}.s^{-1}$, T_{in} = 27°C, q = 203–222 $kW.m^{-2}$	Upflow, tube ID = 4.1 mm, and length= 100 cm	Ring, cube, and hexagon-shape ε = 0.37%	HFC-134a
Anglart et al. (2005)	PDO, P = 70 bar, inlet subcooling = 10 and 40 K, G = 500–2000 $kg.m^{-2}.s^{-1}$	Upflow, annulus 22.1×10 mm, two-side heating	ε is not specified, similar to BWR spacers	Water, uniform AFD
Uchida et al. (1999)	Post DNB, P = 1.42–2.60 MPa, G = 560–3060 $kg.m^{-2}.s^{-1}$, inlet-subcooling = 5–15°C	Upflow, 3×3 rod bundles, OD = 9.5 mm	Standard, non-mixing, and grid with mixing vanes, pitch = 12.6 mm	HFC-123

Table 2.3 Spacer (obstacle) pressure drop correlations.

Reference	Prediction method	Flow regime	TS/ spacer	Comments
Groeneveld and Yousef (1980)	$\Delta P_{sp} = K_{ob}\frac{\rho V_0^2}{2} + f_{sp}\frac{t}{De_{sp}}\frac{\rho V_{sp}^2}{2} - f_o\frac{t}{De}\frac{\rho V_0^{sp}}{2}$ Where, f_{sp}, f_0 are the friction factors for spacer and for tube wall without spacer over the spacer length, respectively, t is the spacer length, V_0 is the bulk velocity without the influence of the spacer, D_e is the equivalent diameter	Single-phase	Rod bundles	First term on the right- hand side of the equation represents pressure drop due to spacer, second term, skin friction pressure drop of the spacer and the third term, skin friction of the bare bundle over the spacer length
Groeneveld and Yousef (1980)	$\frac{\Delta P_{TP}}{\Delta P_{LO}} = 1 + x\frac{v_{fg}}{v_{l,sat}}$, where ΔP_{TP} and ΔP_{LO} are the pressure drop of the spacer in two-phase and single-phase flows, respectively	PDO	Rod bundles	The homogeneous two-phase multiplier is recommended by the authors
Rehme and Trippe (1981)	$K_{ob} = C_v\,\varepsilon^2$	Single-phase	Rod bundles/ four different shapes and blockage-area ratios	The modified drag coefficient, C_v= 6–7, for Re > 5×10^4, round leading edges, short spacers and 0.2 > ε > 0.45
Stosic (1995)	$\Delta P_{sp} = K_{ob}\frac{G^2}{2\rho_{l,sat}}\left(1+\frac{v_{fg}}{v_{l,sat}}(x)\right)$ where, $K_{ob}= C_v\varepsilon^2$	PDO	Rod bundles, different types of grid spacers	The homogeneous multiplier is used: $1+\frac{v_{fg}}{v_{l,sat}}(x)$
Leung and Hotte (1997)	$K_{ob} = 9.3797\left(\tan(\frac{\pi}{2}(\varepsilon)^2)\right)^{1.088}$	Single-phase	For central-segment flow obstacle	-
Yao et al. (1982)	$(\frac{\Delta p}{\Delta p_0})_{sp} = \frac{f + K_{ob}\frac{D}{L}}{f} = 1 + (\frac{D}{fL})K_{ob}$	Single-phase and PDO	Grid spacers	-

CHAPTER 3

DESCRIPTION OF EXPERIMENT

3.1 Experimental Loop

The experiment has been conducted in the multi-fluid test loop at the University of Ottawa (Figure 3.1) using HFC-134a as the working fluid. The main components of the loop are test section, condenser, pressurizer, pumps, pre-heaters, power supply, and related instrumentation.

Two pumps connected in series with a bypass discharge a constant flow rate of HFC134a (or Freon 134a). The Freon circulates from the pumps to Coriolis flow meter and heats up while passing through an electric pre-heater and the test section. A 12-kW DC power supply (40V, 300A) provides direct heating to the vertical test section. Leaving the test section, the Freon passes through the condenser (coaxial heat exchanger), where Freon vapour is condensed and the fluid flows back to the suction side of the pumps. Details of the University of Ottawa multi-fluid test loop can be found in Yang (2003).

3.2 Test Sections

Two test sections are used in this investigation: (i) uniform AFD tube, and (ii) a non-uniform AFD tube having a peak heat flux either near the inlet or outlet. These test sections are made of Inconel-600 tubes with an inside diameter of 5.46 mm. Each test section is oriented vertically and heated by direct current (DC), electric power supplied through copper electrodes clamped tightly to the tube. The outer wall temperature of the test section is measured by attaching K-type self-adhesive miniature thermocouples.

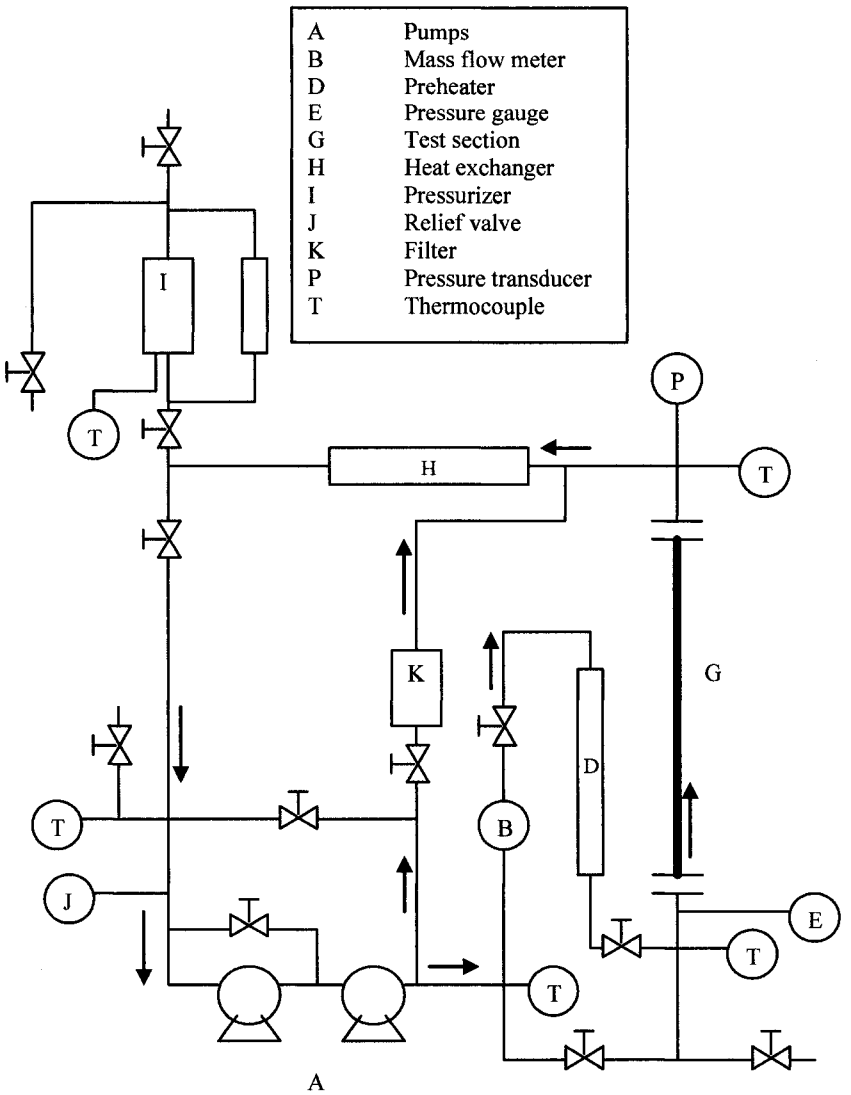

Figure 3.1 Schematic diagram of the experimental multi-fluid loop.

The temperature distribution around the periphery is checked during the single-phase tests. A new uniform AFD tube was installed to obtain a uniform temperature distribution around the periphery. It had a more uniform circumferential wall thickness distribution. The flow direction in the test section is up-wards. Figure 3.2 shows the schematic of the uniform test section with obstacle locations along the heated length; a schematic of the blunt and rounded shape obstacle (ε = 24%) is also shown on this figure. Figure 3.3 displays details of axial positions of thermocouples for the uniform AFD TS. Figure 3.4

presents obstacle positions for inlet-peak and outlet-peak test sections, while Figures 3.5 and 3.6 show axial positions of thermocouples and heat flux profiles for inlet-peak and outlet-peak test sections. A detailed description of the heat flux profiles was given by Yang et al. (2003); the profile is achieved by varying the outside diameter, resulting in a variable electrical resistance at different locations along the test section length.

Mild steel flow obstacles with either 12% or 24% flow-blockage ratios are introduced inside these test sections. The uniform test section is equipped with four obstacles (300-mm pitch) or seven obstacles (150-mm pitch) having a cylindrical shape. The obstacles had either a blunt or rounded (i.e., streamlined) leading and trailing edges. The 24% and 12% obstruction-ratio obstacles have diameters of 2.7 mm and 1.9 mm, respectively. Each obstacle has a10-mm length. The obstacles were held at the required locations with ring-shaped ceramic magnets.

Both inlet-peak and outlet-peak test sections are equipped with 5 or 9 obstacles of the same flow-blockage ratio, pitch and shape as those of the uniform test section. Compared to that of the uniform AFD tube, the number of obstacles was increased to extend the fully developed PDO region at locations downstream from the obstacles (the power increase, as will be discussed in Section 3.4, was limited by CHF occurrence which resulted in high wall temperatures at locations upstream of the first obstacle — especially for blunt obstacles and a 150-mm obstacle pitch).

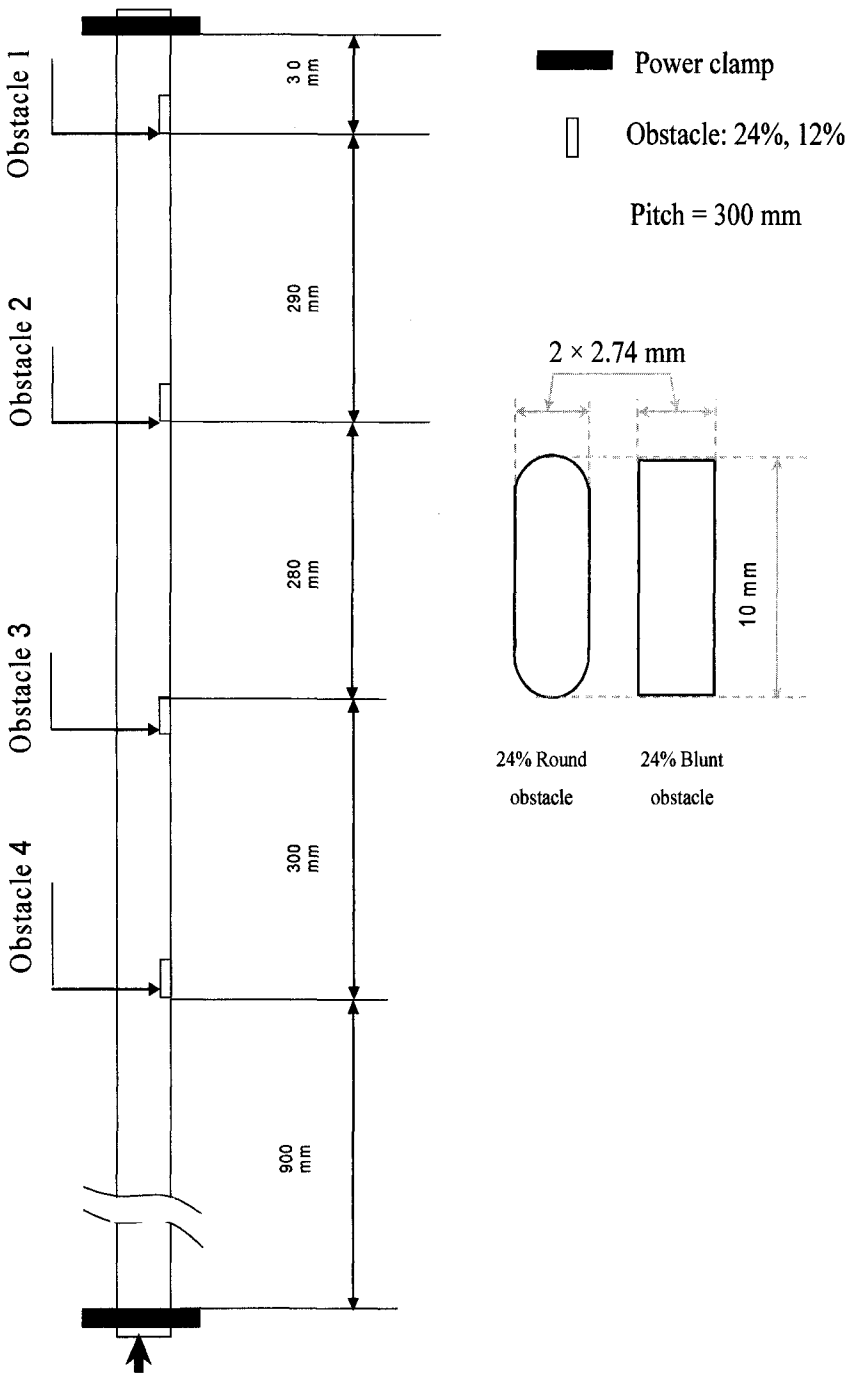

Figure 3.2 Axial positions of obstacles for the uniform AFD test section and a schematic of blunt and rounded obstacle having $\varepsilon = 24\%$.

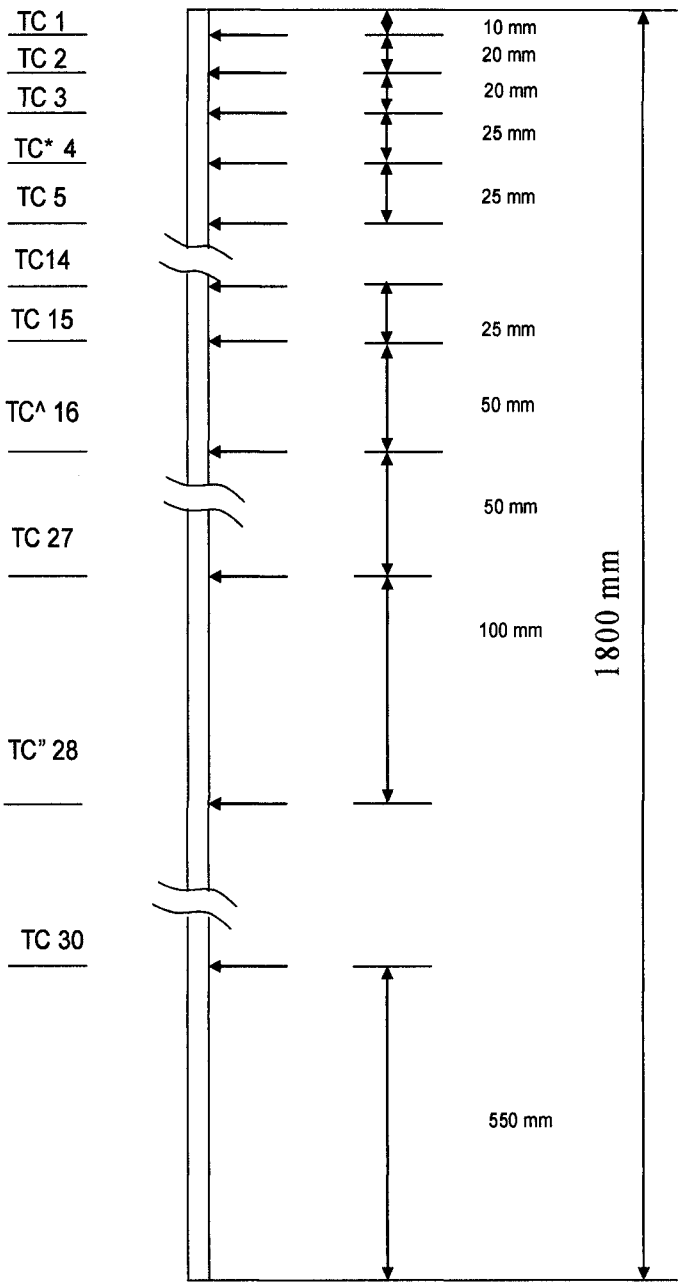

Figure 3.3 Axial positions of thermocouples for the uniform AFD test section.

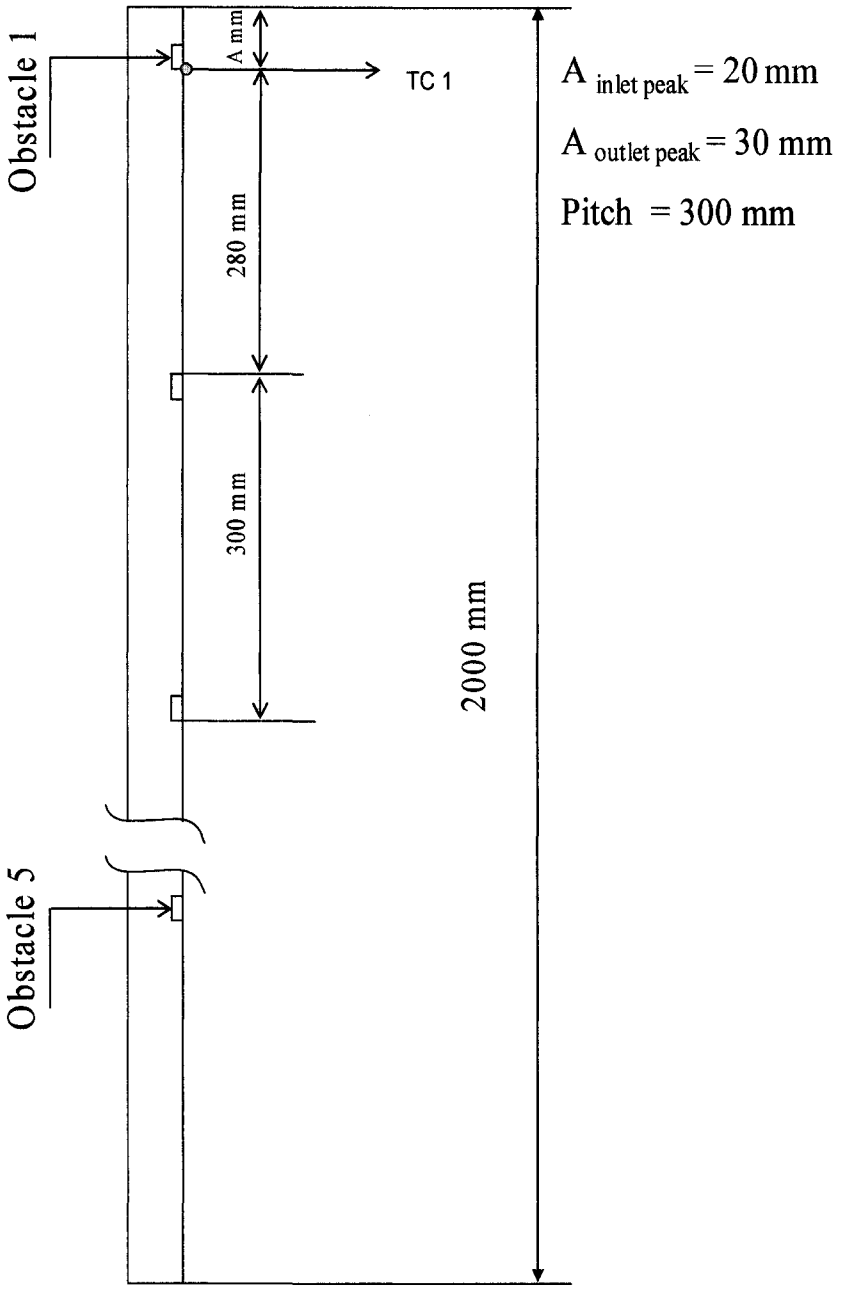

Figure 3.4 Axial positions of obstacles for the inlet and outlet-peak AFD test section..

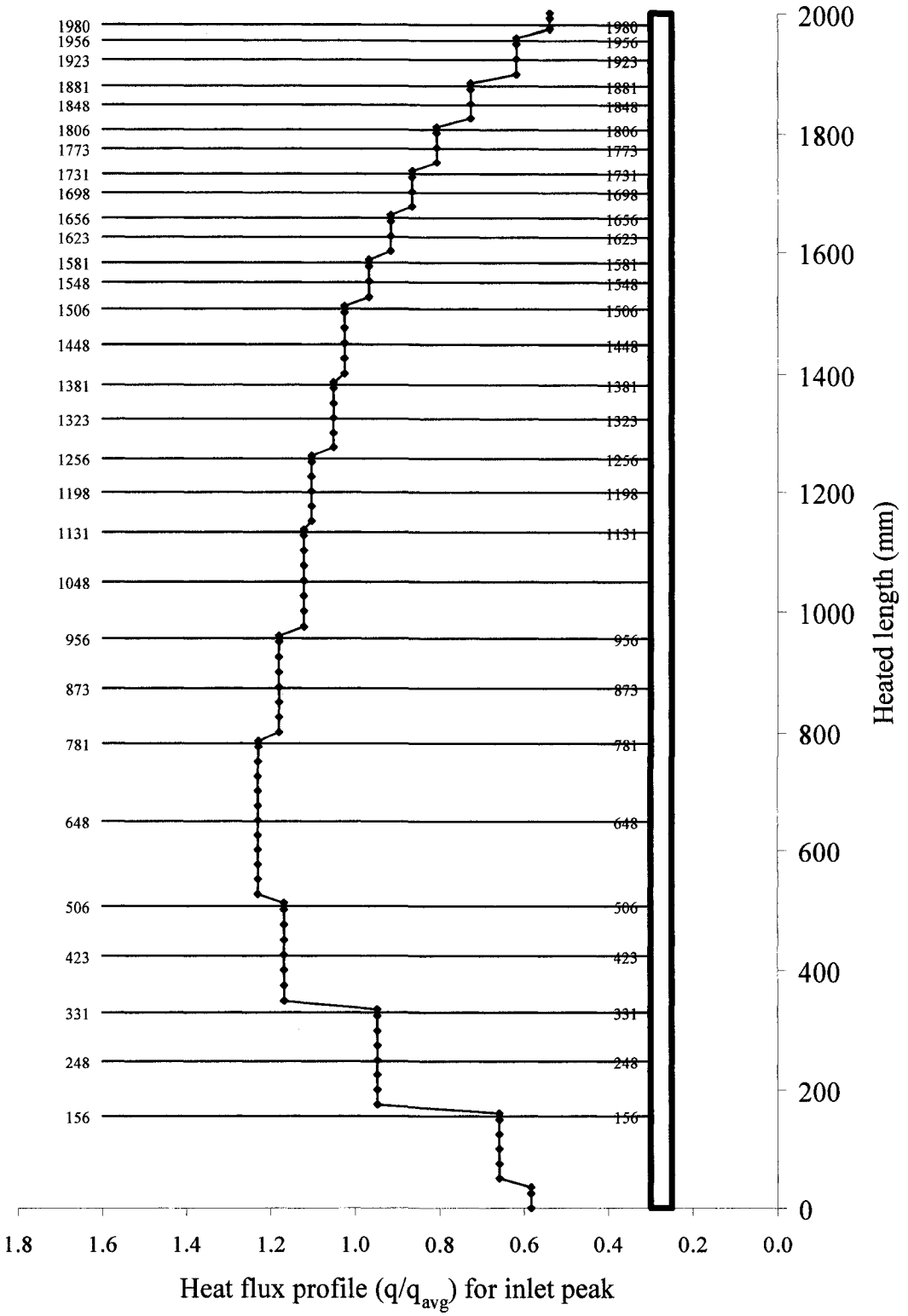

Figure 3.5 Heat flux profile and thermocouples locations for the inlet-peak AFD test section.

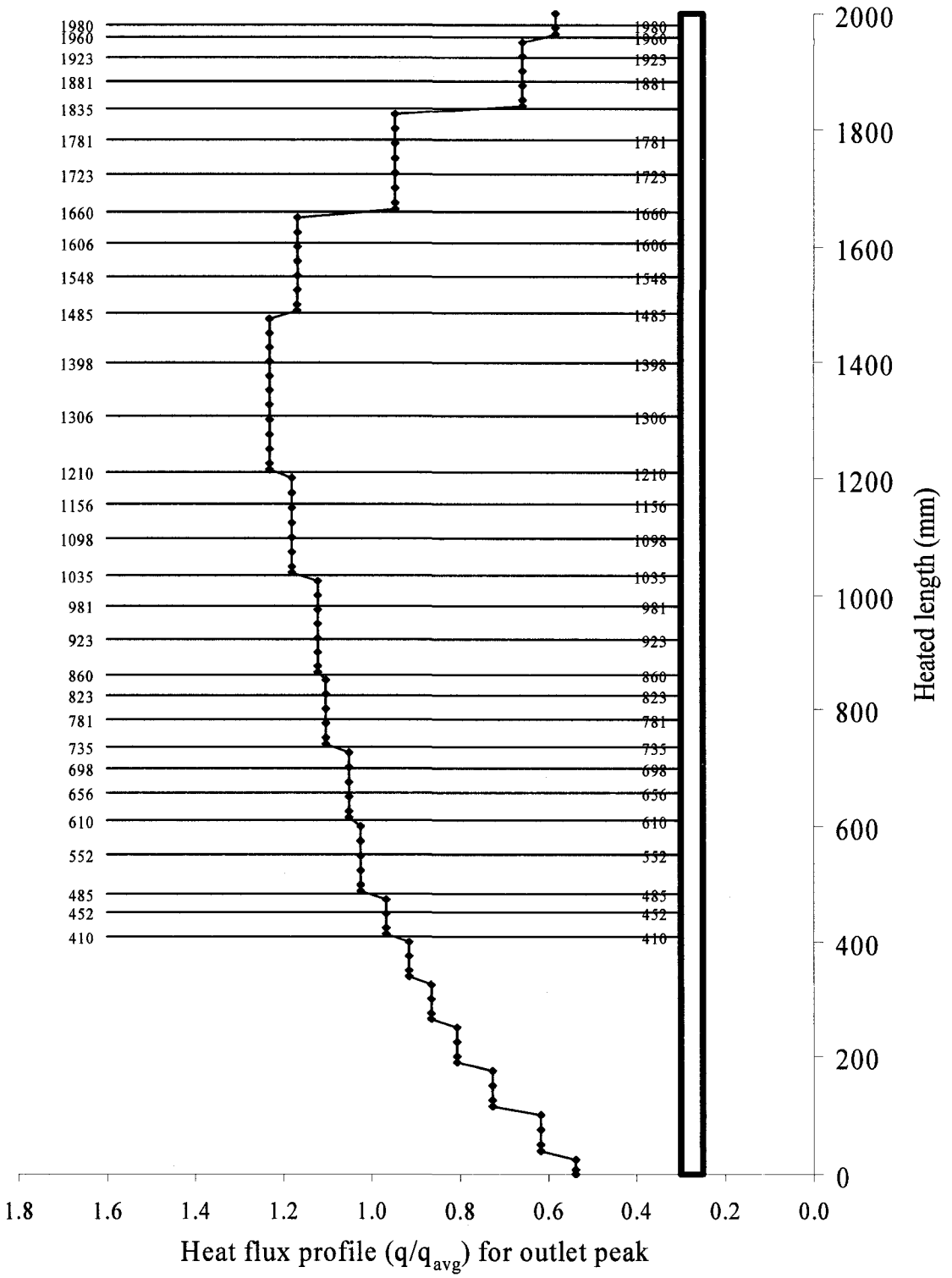

Figure 3.6 Heat flux profile and thermocouples locations for the outlet-peak AFD test section.

3.3 Test Matrix

Table 3.1 shows the test matrix. The HFC-134a conditions (1st and 3rd columns) were determined from equivalent water values, based on respectively the same density ratio (for pressure) and the same Reynolds number (for mass flux). The various test section configurations for the experiment are shown in Table 3.2.

Table 3.1 Experimental test matrix.

p (kPa)	p_{eq}^{+} (kPa)	G ($kg.m^{-2}.s^{-1}$)	G_{eq}^{-} ($kg.m^{-2}.s^{-1}$)	T_{sat} (°C)	T_{in}* (°C)								
					70	65	60	55	50	45	40	35	30
1665	10000	1395	2000	60				X	X	X	X	X	X
		2090	3000	60				X	X	X	X	X	
		2780	4000	60				X	X	X	X		
		3533	5000	60				X	X	X			
2389	14000	1410	2000	75	X	X	X	X	X	X	X	X	
		2110	3000	75	X	X	X	X	X	X	X		
		2861	4000	75	X	X	X	X	X				
		3576	5000	75	X	X	X	X					

* Four heat flux levels for each inlet temperature.
+Water-equivalent pressure is based on equal density ratio for both water and HFC-134a.
-Water-equivalent mass flux is based on equal Reynolds numbers and equal tube diameter.

Table 3.2 Details of test configurations.

AFD	Flow-blockage ratio	Pitch, mm		Leading edge	
		150	300	Round	Blunt
Uniform	12%		X	X	
Uniform	24%	X	X	X	X
Inlet-peak	12%		X	X	
Inlet-peak	24%	X	X	X	X
Outlet-peak	12%		X	X	
Outlet-peak	24%	X	X	X	X

3.4 Experimental Procedure

Commissioning runs were performed prior to the start of the PDO experiment. These runs included leakage detection, heat loss test, heat balance test, thermocouple calibration, pressure calibration, voltage calibration, and current calibration. Detailed descriptions of all tests, performed before the start of the PDO test program, are provided in Appendix A.

Following a change in test conditions or power level, the data acquisition system (DAS) readings were recorded after steady-state conditions had been reached. A preliminary check on flow stability, thermocouple readings, current and voltage readings was performed.

For every test matrix point, the required pressure and flow conditions were first established. The power to the pre-heater was then adjusted to obtain the required inlet temperature. After this step, the power to the test section was gradually increased, until CHF occurred. With increasing power to the test section, the mass flux and preheater power were adjusted as required to maintain steady conditions. Pressure was maintained usually within $\pm$ 1psi (6.9 kPa) from the set point. Inlet subcooling was kept usually within $\pm$ 0.3K. The maximum power applied to the test section corresponded to either the limit of the power supply or a maximum surface temperature of 240°C (to avoid decomposition of Freon). Post-dryout temperature distributions were recorded at typically 5 to 6 power levels for a given set of flow conditions.Tests were performed first at the maximum power level. A scan of flow conditions and temperature distributions was taken. The power was then reduced in steps of 5 or 10 $kW.m^{-2}$. After each power step, and after reaching steady-state conditions, a scan of all instruments were taken. The test run was terminated when the tube was completely rewetted.

El Nakla et al. (2006) performed bare-tube experiments with uniform, inlet-peak and outlet-peak axial power profiles. To permit a direct comparison with these bare-tube results, thermocouple locations and heated lengths of the obstacle-equipped test sections

with inlet-peak and outlet-peak axial power profiles were identical to those of El Nakla's bare-tube test sections.

3.5 Repeatability Tests

Repeatability tests were performed for obstacle-equipped test sections of uniform, inlet-peak and outlet-peak axial power profiles. Measurements of outside wall temperatures (as presented in Appendix A) along the test section showed good agreement between original and repeat runs. For the outlet-peak test section, distributions of the inverse HTC (h^{-1}) vs. quality and the outside wall temperature at the thermocouple positions along the test section are compared in Figures A6a to A6k. Note that the original and repeat runs are in excellent agreement.

CHAPTER 4

EXPERIMENTAL RESULTS AND DISCUSSION

4.1 General

This chapter describes the experimental data processing, the observed parametric trends and the AFD effect for obstacle-equipped test sections with uniform and non-uniform AFDs.

The following notation system is used to identify the axial heat flux profile and obstacle configuration: *AbbCddd* where *A* corresponds to either "U", "IP" or "OP" denoting the uniform, inlet-peak, or outlet-peak axial heat flux profile, *bb* corresponds to either "12" or "24" denoting the 12% or 24% flow-blockage ratio, *C* corresponds to "B" or "R" denoting the blunt or round (streamlined) obstacle, and *ddd* corresponds to either "150" or "300" denoting either 150-mm or 300-mm obstacle pitch. For example: U24B300 refers to the uniformly heated test section equipped with blunt obstacles having a 24% flow-blockage ratio at the 300-mm pitch.

The calculated inside-wall temperatures are presented as a function of axial distance along the test section; obstacle positions are shown on the horizontal axis in the figures. In addition, variations of the inverse heat-transfer coefficient (i.e., h^{-1}) are also plotted against local quality for some cases. To illustrate the obstacle (or obstacle-related) effect at similar flow conditions in either the bare or obstacle-equipped test section with a non-uniform axial heat flux profile, the average heat flux (calculated with the total test-section power averaged over the entire heated area) is shown.

Examples of the inside wall-temperature distribution along the test section are shown and discussed in this chapter. The data presentation covers high pressure (P = 2389 kPa and

P_{eq} = 14 MPa) and low-pressure (P = 1665 kPa and P_{eq} = 10 MPa), and all mass fluxes, except some cases for uniform and inlet-peak AFDs at high-mass fluxes, for which no corresponding bare-tube case having the same inlet temperature and/or heat flux could be found.

4.2 Data Processing

The outside wall-temperature (T_o) was measured in the experiment. The corresponding inside-wall temperature (T_{wi}) is calculated using heat diffusion equation (HDE) applied in cylindrical coordinates with internal heat generation:

$$T_{w_i} = T_o + \frac{2 q_{loss} r_o - q_v r_o^2}{2k} \ln \frac{r_o}{r_i} + (r_o^2 - r_i^2) \frac{q_v}{4k} \tag{4.1}$$

where q_{loss} is the loss heat flux from the wall to outside atmosphere ($W.m^{-2}$) which was very small, and was therefore neglected (see Appendix A), q_v is the heat generated per unit volume ($W.m^{-3}$), k is the wall thermal conductivity of Inconel 600 ($W.m^{-1}.K^{-1}$), and r_o and r_i are the outside and inside tube radii (m), respectively. Equation (4.1) is applied in the evaluation of the heat-transfer coefficient, which is expressed as:

$$h = \frac{q}{(T_{w_i} - T_{sat})} \tag{4.2}$$

where the temperature at saturation, T_{sat}, corresponds to pressure at the exit of the test section (it was found that the pressure drop over the film-boiling length is negligible). For test sections with the non-uniform axial heat flux profile, the local heat-transfer coefficient is calculated at each thermocouple location based on the local heat flux. The local heat flux is calculated with power fractions corresponding to 17 steps of the test section by:

$$q(m) = \frac{U \times I \times power_r(m)}{(\pi \times 2 \times r_i \times step_l(m))} \tag{4.3}$$

where U is the voltage drop along the test section, I is the electric current, and $power_r(m)$ *and* $step_l(m)$ are power fraction and step length for the m^{th} step, respectively. Yang et al. (2003) described details for establishing power steps of the non-uniform AFD test sections. The local thermodynamic quality corresponding to the thermocouple location is calculated with the energy-balance equation:

$$x(i) = 4\frac{q(m) \times step_l(m)}{G \times H_{fg} \times D_i} + x_{in} \tag{4.4}$$

The thermodynamic properties of HFC-134a are obtained using International Standard Formulation (Tillner-Roth and Baehr, 1994) and transport properties are based on equations of Krauss et al. (1993).

An uncertainty analysis of the measurements has been performed and is presented in Appendix B.

4.3 Observed Parametric Trends on PDO Heat Transfer in Uniform AFD Tube

4.3.1 Pitch Effect

Figure 4.1 illustrates the effect of obstacle pitch on wall-temperature distributions in the uniform-heated tube, which was equipped with either four rounded obstacles at a 300-mm pitch (obstacle numbers 1, 3, 5 and 7) or seven rounded obstacles at a 150-mm pitch (obstacle numbers from 1 to 7). All obstacles had a 24% blockage-area ratio. The reference temperature distribution for a bare tube is also shown in Figure 4.1 for comparison. Dryout occurs at the same locations upstream of all obstacles for both pitches. The location differs slightly from that in the bare tube and is probably due to

slight differences in flow conditions. A comparison of wall-temperature distributions of tubes with 150-mm and 300-mm obstacle pitches against those of the bare tube shows that the obstacles have a strong effect on delaying dryout occurrence and lowering the post-dryout wall temperature. For the bare tube, the developing-flow region extends up to the axial location of about 1 m (line with circles), while fully developed film boiling conditions are present at locations beyond 1 m in the plain tube (line with diamonds). The developing film-boiling is caused by the disturbance of droplets impinging on the heated surface and the development of vapour superheat, Guo and Leung (2005). Developing film-boiling corresponds to cases downstream of the dryout and transition boiling points where rewetting no longer occurs but where the heat transfer is affected by upstream conditions (dryout and/or spacer) and the axial surface temperature distribution has not yet leveled off, Groeneveld and Stewart (1982). The fully developed film-boiling region is reached when the axial temperature gradient reaches a plateau and the wall temperatures are no longer affected by the distance from the CHF location or obstacle location.

Rewetting has been observed at locations just downstream of the obstacle for the 300-mm pitch (only four obstacles were installed for this case: at obstacle location 1, 3, 5 and 7 shown in Figure 4.1). Dryout was re-established at locations further downstream of the most upstream obstacle until the next obstacle at the downstream location, where rewetting re-occurred due to the increased turbulence. The length of the post-dryout region appears to be longer at the downstream obstacle location than the upstream obstacle location. This is probably due to the reduction in CHF at the higher qualities. Dryout has been suppressed beyond the first upstream obstacle for the 150-mm pitch, and re-established at locations slightly upstream of the last obstacle. This results in lower wall temperatures than the obstacle-equipped tube of 300-mm pitch and the bare tube. A drop in wall temperature has been observed at the last thermocouple location of the obstacle-equipped tubes and is due to the axial heat conduction, since the thermocouple is located close to the upper power clamp (1 cm).

Figure 4.2 shows the effect of obstacle pitch on the inside wall-temperature distributions at high-pressure and low-mass flux ($G = 1410$ kg.m^{-2}.s^{-1} and $G_{eq} = 2000$ kg.m^{-2}.s^{-1}). The uniform test section is equipped with 4 streamlined obstacles having a 24% flow-blockage ratio at the 300-mm pitch or 7 streamlined obstacles having the same obstruction ratio at the 150-mm pitch. For the test section with the 300-mm pitch at the heat-flux level of 110 kW.m^{-2} and inlet temperature of 55°C, the PDO region starts at z = 1.3 m, while for the test section with a 150-mm pitch, the PDO region begins at z = 1.45 m. As expected, the test section with the 150-mm pitch has lower PDO wall temperatures than that with the 300-mm pitch. A comparison of the wall-temperature distributions of both configurations (150 mm and 300 mm) against those of bare tube, shows that the obstacles have a strong effect on delaying CHF occurrence and lowering the PDO wall temperature. The difference in inside wall temperatures for both pitches diminishes at the exit of the test section. A drop in wall temperature has been observed at the last thermocouple location of the obstacle-equipped test section for both pitches and is due to the axial heat conduction since the thermocouple is located 1 cm from the upper power clamp (Figure 3.3).

4.3.2 Effect of Flow-Blockage Ratio

Figure 4.3 compares wall temperatures in tubes equipped with streamlined obstacles of two different sizes (flow-blockage ratios of 24% and 12%) at the 300-mm pitch at high-pressure and high-mass flux ($G = 2861$ kg.m^{-2}.s^{-1} and $G_{eq} = 4000$ kg.m^{-2}.s^{-1}). The larger obstacle (24%) suppresses the dryout occurrence over a longer distance than the small obstacle (12%). This is due to the increase in turbulence decay distance downstream of the larger obstacle. The difference becomes small with increasing axial location and dryout occurs at the same location beyond 1.5 m.

Figure 4.4 shows the effect of varying the flow obstruction ratios (24% and 12%) of the streamlined obstacle on the inside wall temperature distribution at high-pressure and moderate-mass flux ($G = 2110$ kg.m^{-2}.s^{-1} and $G_{eq} = 3000$ kg.m^{-2}.s^{-1}). The PDO

temperatures of the obstacle-equipped tubes are significantly lower than those of the bare tubes. For $1.3 < z < 1.5$ m, the inside wall temperature difference between test section configuration (U24R300) and test section (U12R300) decreases with increasing z. For $z >$ 1.5 m, the points of the two configurations are almost the same. This suggests that the obstacle-size effect on CHF diminishes with increasing quality (at downstream locations). As expected, at locations upstream of the first obstacle (first CHF location), all three configurations indicate approximately the same temperature.

4.3.3 Effect of Streamlining Obstacle-Edges (Obstacle Shape)

All obstacles used in this experiment have the same cylindrical shape, but the leading and trailing edges of some obstacles were rounded to provide a more streamlined shape than blunt obstacles. Figure 4.5 compares wall temperatures obtained for these two obstacle types. Overall, temperature variations are similar for blunt and rounded obstacles. The blunt obstacle, however, appears to suppress dryout re-occurrence over a longer distance than the rounded obstacle. The difference is attributed to the higher turbulence generated from a blunt object.

Figure 4.6 shows the obstacle leading and trailing edge shape effect (rounded vs. blunt) for a 150 mm pitch uniform-AFD test section at high-pressure and low-mass flux. In general the effect is more significant at low z or at low quality. Blunt obstacles have a stronger CHF enhancement effect; they delay the onset of CHF occurrence and provide a slightly lower wall temperature distribution than the rounded obstacles for the same flow conditions and the same obstruction ratio. It appears that the differences in temperature profiles between the obstacle-equipped test sections diminish as z increases.

4.3.4 Mass Flux Effect

Figure 4.7 shows the mass flux effect for the U24R300 uniform test section configuration at high-pressure. As expected, CHF occurs further downstream for higher flows. The

upper-bound temperatures for the obstacle-equipped test section and $z > 1.5$ m at G = 2123 $kg.m^{-2}.s^{-1}$ is slightly lower than those at G = 1431 $kg.m^{-2}.s^{-1}$, and the corresponding temperature difference between bare and obstacle-equipped tubes for those points is higher for 2123 $kg.m^{-2}.s^{-1}$. Figure 4.8 presents the same data re-plotted as the inverse heat-transfer coefficient vs. thermodynamic quality (see Section 4.1 for description). Because of the different mass flux values, local quality differs also at a given axial location. In this figure PDO conditions at G = 2123 $kg.m^{-2}.s^{-1}$ are established at $x = 0.33$ and are maintained to $x = 0.35$ where rewetting occurred due to the presence of an obstacle. At G = 1431 $kg.m^{-2}.s^{-1}$, first dryout occurs at $x = 0.4$ and the surface rewets at the next obstacle location ($x = 0.49$), further downstream from this point PDO conditions are maintained.

4.3.5 Pressure Effect

Figure 4.9 shows the effect of pressure on the U24R300 test section at low-mass flux and at $x_{in} \approx -0.22$. At P = 2389 kPa, first dryout occurs earlier than at P = 1667 kPa . Variation of pressure changes the physical properties of vapour.

For $z > 1.7$ m, bare tube wall temperatures at P = 2389 kPa are lower than those at P = 1667 kPa. This is thought to be due to the enhanced vapour thermal conductivity as the pressure increases (El Nakla, 2007). Stewart and Groeneveld (1982) also found that the HTC increases with increasing pressure. Because of different saturation temperatures and enthalpies, the local quality is not the same for obstacle-equipped test sections for a given axial location, and the pre-CHF temperatures also differ. Therefore the results are re-plotted in Figure 4.10 as inverse of HTC distributions vs. local quality.

The effect of increasing vapour thermal conductivity does not apply to the whole range of thermodynamic quality on Figure 4.10, because the upstream conditions (i.e. the developing film-boiling effect) are more significant.

4.3.6 Inlet Temperature Effect

Figures 4.11 and 4.12 show the effect of inlet temperature on the wall temperature profiles for the U12R300 test section at high-pressure and high-mass flux. Figure 4.12 is the same as Figure 4.11, except that the wall temperature is plotted against local quality. As expected, when re-plotting the wall temperatures based on the same local conditions results in better agreement between the bare-tube temperature profiles. The temperature profiles for the obstacle-equipped test section do not coincide on the T vs. x plot, because the obstacle locations for different inlet temperatures are at different qualities; however the maximum temperatures line up very well. A variation in inlet subcooling has almost no effect on the heat-transfer coefficient for the bare tube.

4.3.7 Heat Flux Effect

Figures 4.13 and 4.14 show the heat flux effect for U12R300 test section at high-pressure and high-mass flux. Both figures are for the same data, but the second one is plotted as the inverse heat-transfer coefficient vs. x. For obstacle-equipped tubes the upper bound points coincide for the two heat flux levels (Figure 4.13). For $z > 1.6$ m, the temperature difference between the obstacle-equipped test section and the bare tube for q = 150 $kW.m^{-2}$ is slightly lower compared to that for q = 130 $kW.m^{-2}$ (Figure 4.13).

The shape of the inverse HTC profile is somewhat similar when the results are plotted as in Figure 4.14 compared to Figure 4.13. A variation in heat flux has almost no effect on the heat-transfer coefficient for the obstacle-equipped tubes. However, the variation in heat flux was relatively small (15%).

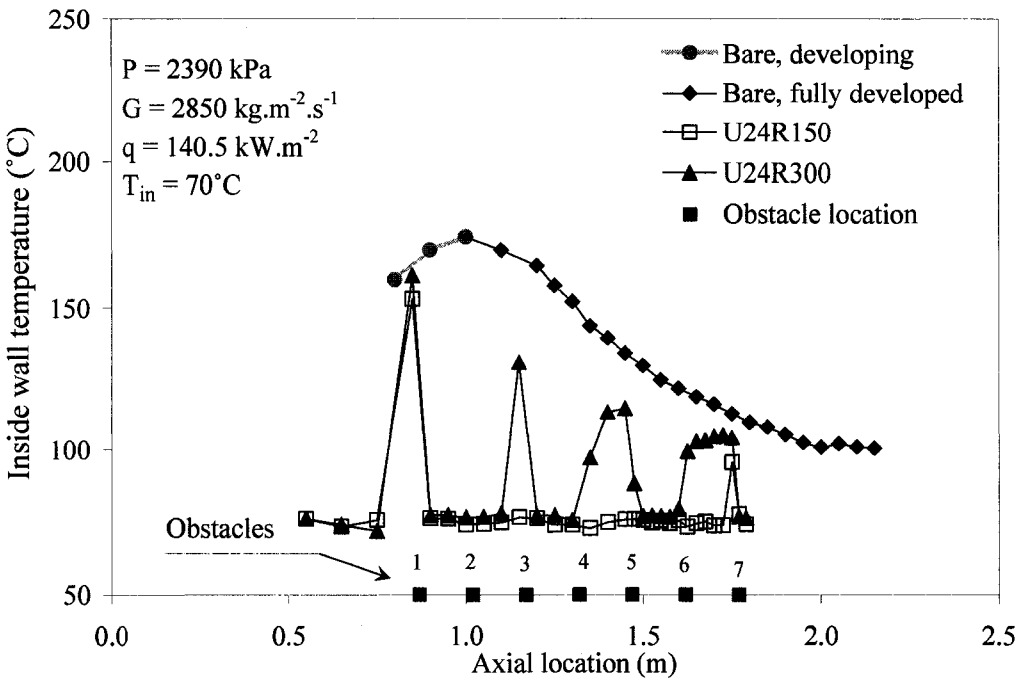

Figure 4.1 Effect of obstacle pitch on the temperature distribution for streamlined obstacles (uniform profile, high-pressure and high-mass flux).

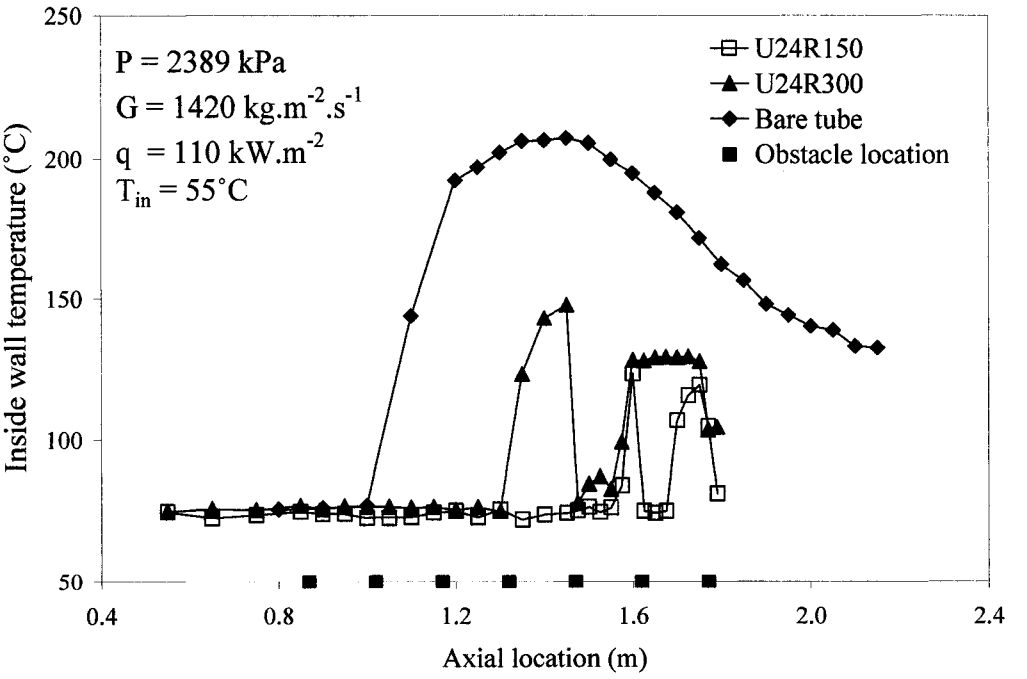

Figure 4.2 Effect of obstacle pitch on the temperature distribution for streamlined obstacles (uniform profile, high-pressure and low-mass flux).

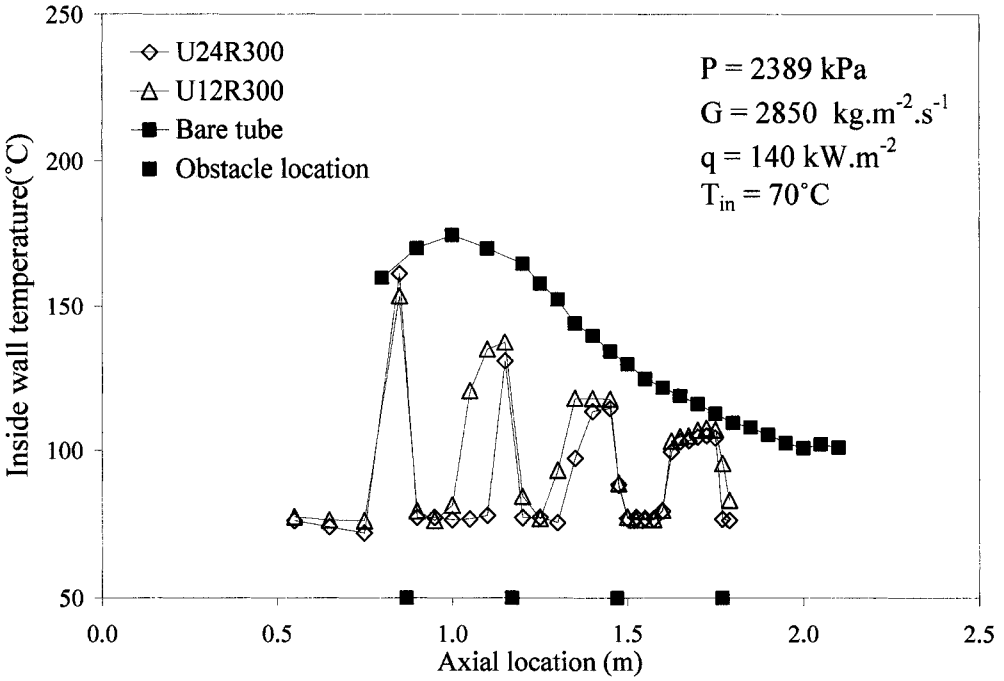

Figure 4.3 Effect of flow-blockage ratio on the temperature distribution for streamlined obstacles (uniform profile, high-pressure and high-mass flux).

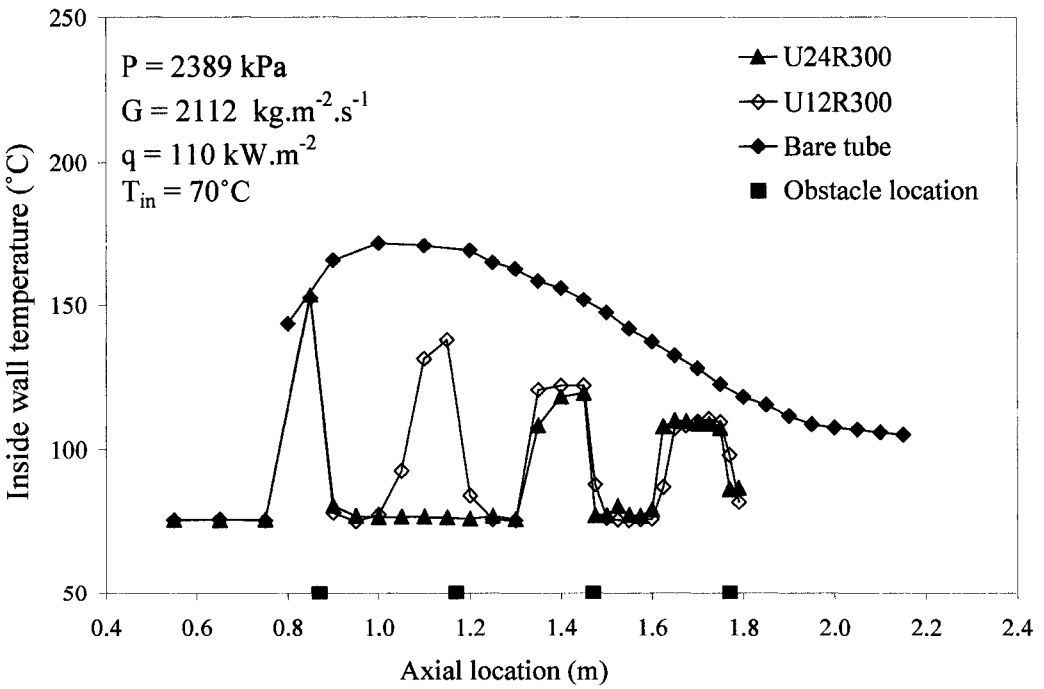

Figure 4.4 Effect of flow-blockage ratio on the temperature distribution for streamlined obstacles (uniform profile, high-pressure and moderate-mass flux).

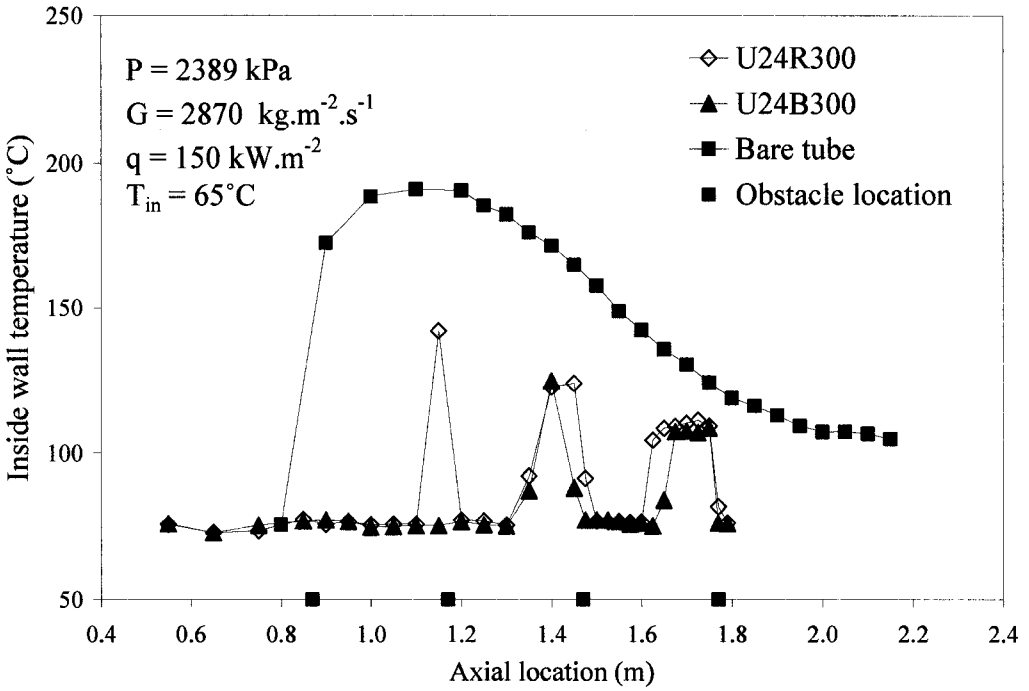

Figure 4.5 Effect of obstacle shape on the temperature distribution for streamlined and blunt obstacles (uniform profile, high-pressure and high-mass flux).

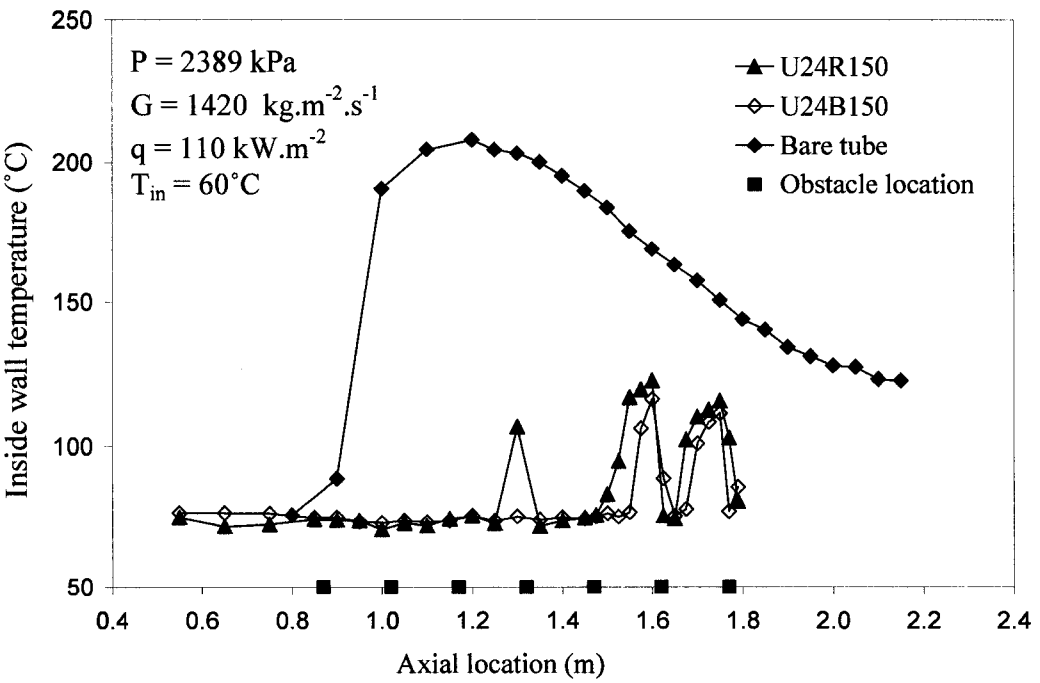

Figure 4.6 Effect of obstacle shape on the temperature distribution for streamlined and blunt obstacles (uniform AFD, high-pressure and low-mass flux).

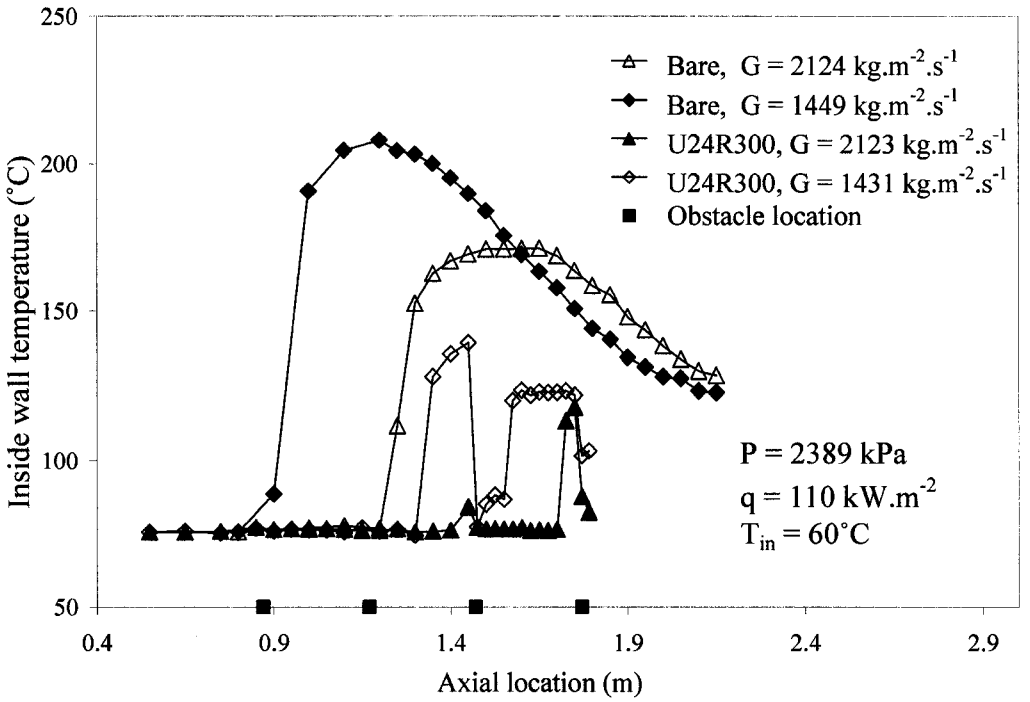

Figure 4.7 Effect of mass flux on the temperature distribution for streamlined obstacles (uniform AFD, high-pressure).

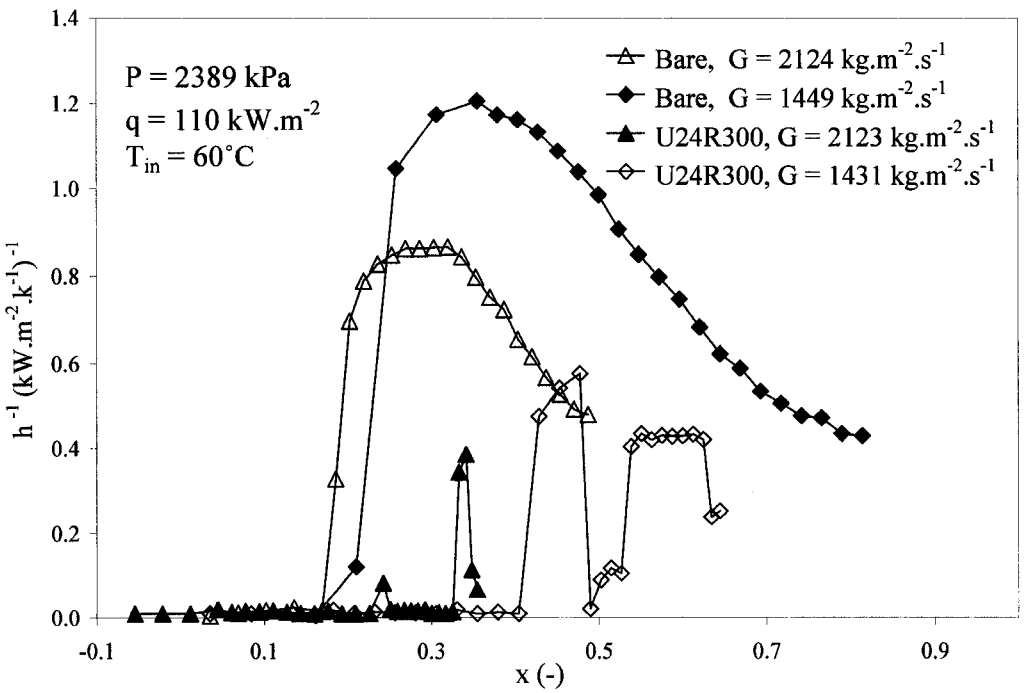

Figure 4.8 Effect of mass flux on the inverse HTC vs. local quality for streamlined obstacles (uniform AFD, high-pressure).

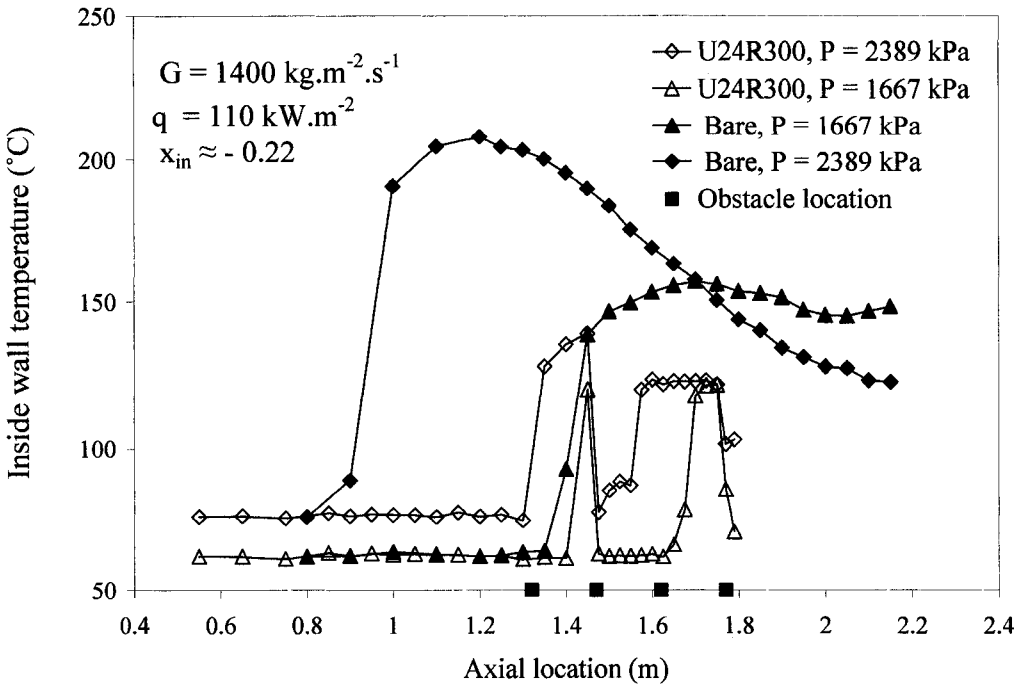

Figure 4.9 Effect of pressure on the temperature distribution for streamlined obstacles (uniform AFD, low-mass flux).

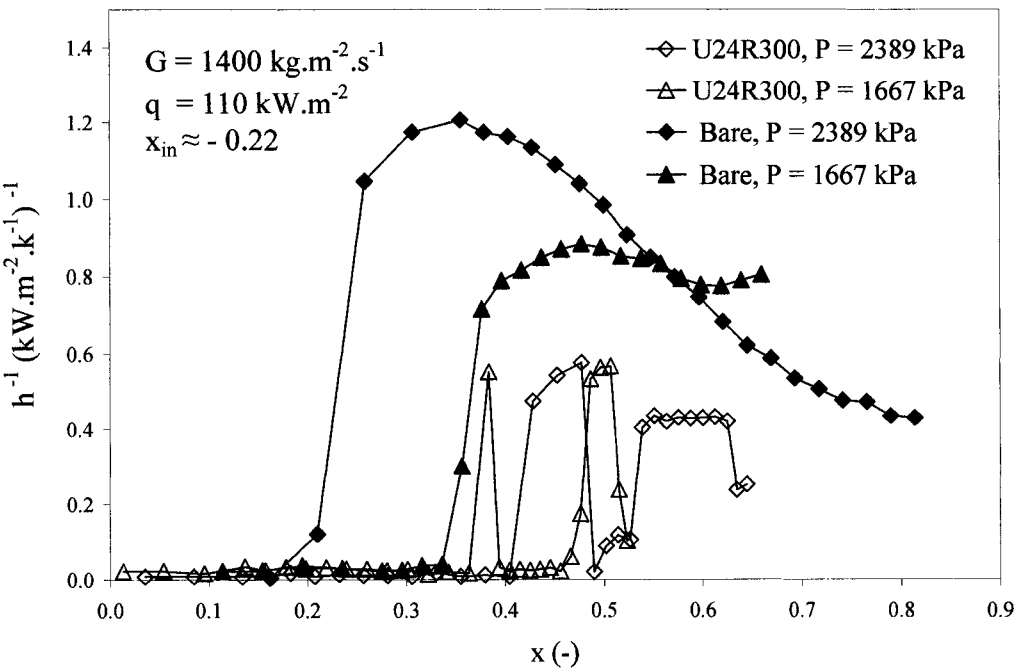

Figure 4.10 Effect of pressure on the inverse HTC vs. local quality for streamlined obstacles (uniform AFD, low-mass flux).

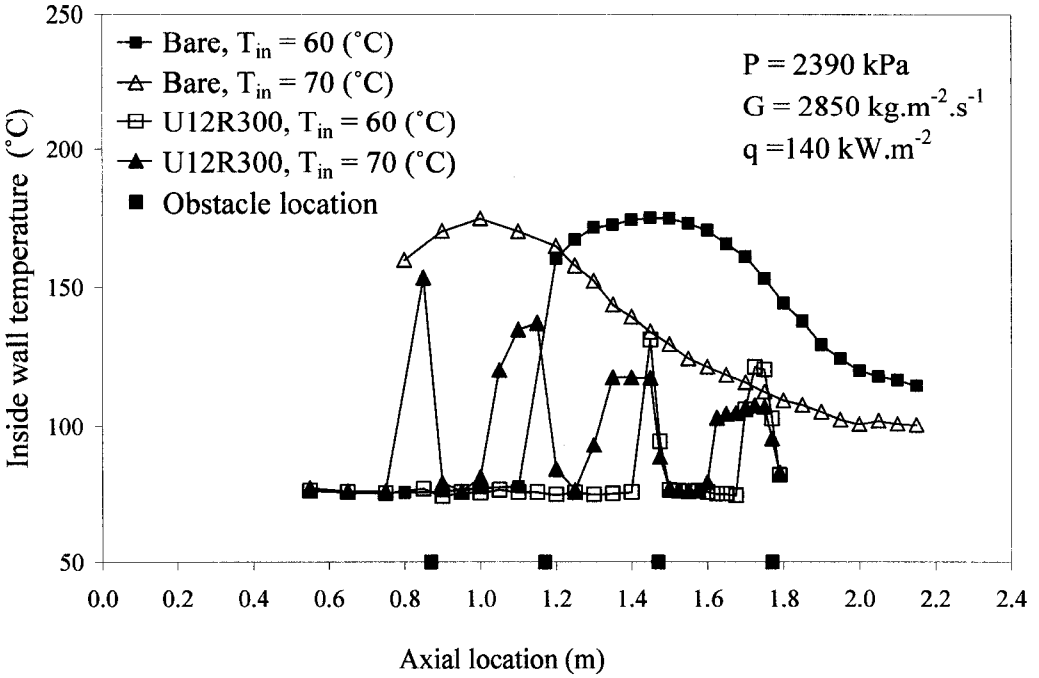

Figure 4.11 Effect of inlet temperature on the temperature distribution for streamlined obstacles (uniform AFD, high-pressure and high-mass flux).

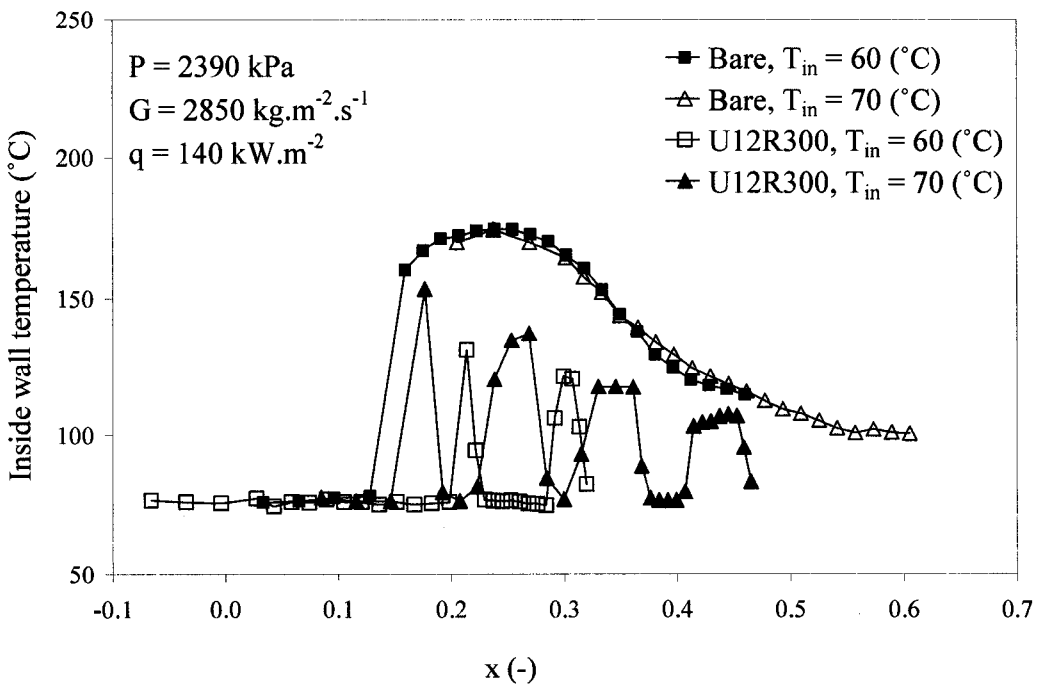

Figure 4.12 Effect of inlet temperature on the temperature distribution vs. local quality for streamlined obstacles (uniform AFD, high-pressure and high-mass flux).

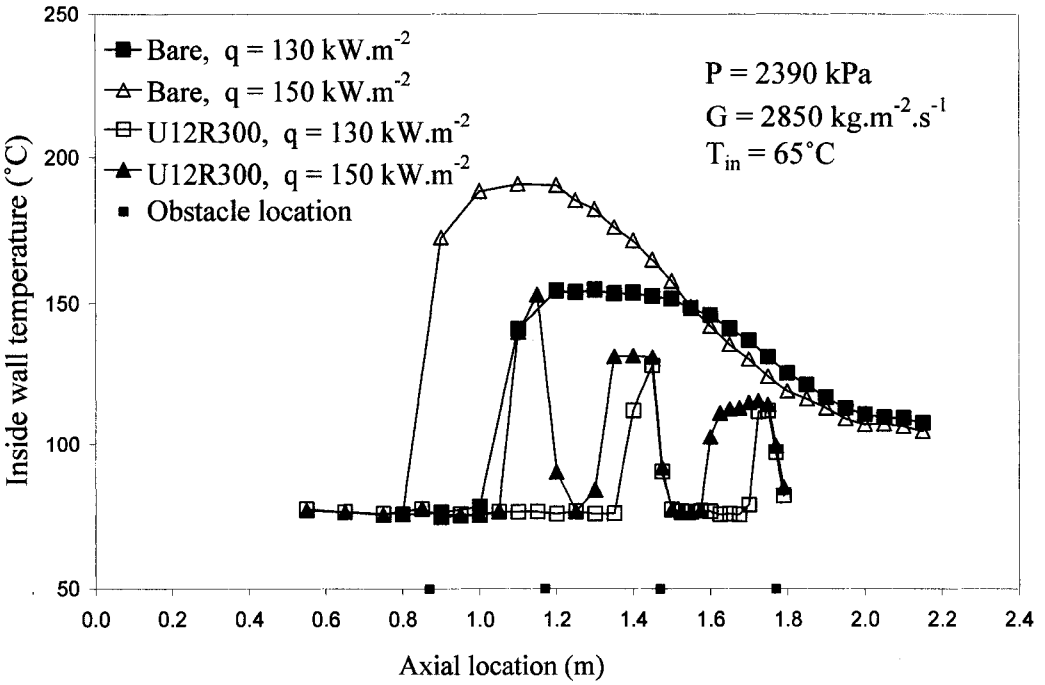

Figure 4.13 Effect of heat flux on the temperature distribution for streamlined obstacles (uniform AFD, high-pressure and high-mass flux).

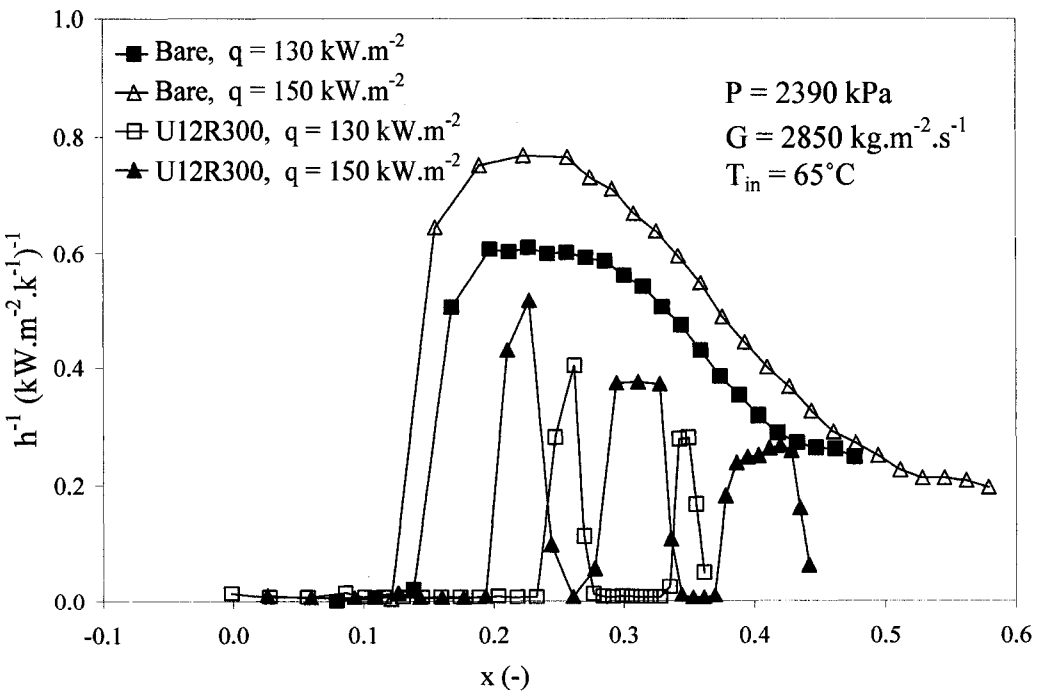

Figure 4.14 Effect of heat flux on the inverse HTC vs. local quality for streamlined obstacles (uniform AFD, high-pressure and high-mass flux).

4.4 Observed Parametric Trends on PDO Heat Transfer in Non-Uniform AFD Tubes

4.4.1 Pitch Effect

Figure 4.15 shows the pitch effect on wall-temperature distributions for blunt-shaped obstacles in the tube with an inlet-peak flux profile. The distribution for the plain (bare) tube is also shown for comparison. A reduction in wall temperature has been observed for the obstacle-equipped tubes as compared to the plain tube. Dryout occurrences were suppressed by the first upstream obstacle at the 300-mm pitch for locations prior to 0.95 m (only five obstacles were installed in this case), and two upstream obstacles at the 150-mm pitch for locations prior to 1.05 m. The surface appears to rewet at each obstacle location of the 150-mm pitch. Rewetting was observed only at the first three locations of the 300-mm pitch, while post-dryout conditions appear to be maintained at locations downstream of the last two obstacles. Note that rewetting could well have occurred downstream all obstacles. However, due to the limited number of thermocouples used, rewetting occurrence at the trailing edge of the 4^{th} obstacle may not have been detected, since no thermocouple was attached to this location. Note also that the axial position of the 5^{th} obstacle coincides with the location of the last thermocouple (2 cm from the upper power clamp); this implies that the thermocouple reading could have been influenced by the axial heat conduction to the unheated surface of the tube), resulting in a lower heat flux and rewetting occurrence at the last thermocouple. The decreasing trend of wall temperature with increasing axial location suggests the presence of fully developed film boiling conditions at two downstream sections between obstacles of the 300-mm pitch. No fully developed film-boiling conditions were achieved at locations between obstacles for the 150-mm pitch. However, the difference in peak wall temperature between obstacle pitches diminishes at these locations. A peculiar surface-temperature reduction is observed upstream of the last obstacle; the reduction is probably due to measurement uncertainty of the thermocouples or obstacle location.

Figure 4.16 shows the pitch effect for the rounded obstacles in the test section having an inlet-peak AFD at high-pressure and moderate-mass flux. Only limited measurements

were obtained at similar flow conditions in both bare and obstacle-equipped test sections. This is because the bare test section reached the maximum wall temperature while the streamlined-obstacle-equipped test section could barely get into dryout. At high-mass fluxes and a 150-mm pitch, no CHF conditions could be reached for the test section with either blunt or streamlined obstacles at conditions where CHF could be obtained in the bare test section.

4.4.2 Flow-Blockage Effect

4.4.2 1 Inlet-peak AFD

Figure 4.17 compares wall temperatures along tubes having the inlet-peak axial heat flux profile equipped with streamlined obstacles of 24% and 12% flow-blockage ratios at a pitch of 300 mm. Peak temperatures of the tube equipped with obstacles of the 12% flow-blockage ratio approach those of the bare tube, while peak temperatures of the tube equipped with the 24% flow-blockage obstacles remain lower. For $z > 1.1$ m, the difference in PDO wall temperatures between bare tube case and obstacle-equipped tubes decreases with increasing z. The surface rewets downstream of the 24% flow blockage obstacles, but not for the 12% flow-blockage obstacles. The reduction in wall temperature for the obstacle with 12% flow-blockage ratio is steeper at the location of 1.4 m where rewetting has occurred.

Figure 4.18 shows flow blockage effect at high-pressure and high-mass flux. Only two PDO points are obtained in the configuration IP24R300 at $z = 1.923$ and 1.956 m, which correspond to TC 28 and TC 29 respectively.

4.4.2.2 Outlet-peak AFD

A similar effect of obstacle size on post-dryout wall temperature has been observed in tubes having an outlet-peak axial power profile (Figure 4.19 and 4.20). The wall

temperatures for both 24% and 12% obstruction ratios are lower than those of the bare tube, but the difference between the 24% and 12% PDO temperatures is not significant. The 24% obstacles tend to suppress dryout re-occurrences over a longer distance downstream of the obstacle than the 12% obstacles. Close to the end, the 12% flow blockage wall temperatures seem to converge to the bare tube wall temperatures, while the 24% flow blockage has either noticeably lower PDO temperatures or suppresses CHF occurrence completely.

4.4.3 Effect of Streamlining Obstacle-Edges (Obstacle Shape)

Figure 4.21 shows the obstacle shape effect at high-pressure and high-mass flux. Wall temperatures for the blunt-obstacle-equipped test section are always lower than those for the streamlined-obstacle-equipped TS.

Figure 4.22 presents the shape effect for the inlet-peak profile at high-pressure and low-mass flux. The PDO temperatures of the obstacle-equipped tubes are significantly lower than those of the bare tube. For the blunt-obstacle-equipped test section (IP24B300) the wall temperatures are slightly lower than the temperatures for the streamlined-obstacle-equipped TS.

4.4.4 Mass Flux Effect

4.4.4.1 Inlet-peak AFD

Figure 4.23 and 4.24 present the mass flux effect for inlet-peak axial power profile at low and moderate-mass fluxes. The inlet-peak AFD tube is equipped with 5 streamlined obstacles at a 300 mm pitch. The comparison between the two mass fluxes is expressed as wall temperature distribution versus axial location (Figure 4.23) and inverse heat-transfer coefficient against thermodynamic quality (Figure 4.24). As expected the mass flux effect for the inlet-peak AFD tube is similar to that for the uniform AFD – for the

same locations the wall temperatures at the higher mass velocities are lower. A pronounced effect can be seen when comparing the two temperature profiles of the obstacle-equipped tubes against the corresponding temperatures of the bare tubes. Close to the exit of the test section, the tube (IP12R300) at G = 2124 $kg.m^{-2}.s^{-1}$ shows slightly larger temperature difference than the tube at G = 1431 $kg.m^{-2}.s^{-1}$.

4.4.4.2 Outlet-peak AFD

Figure 4.25 shows the mass flux effect at low-pressure for the OP12R300 test section. Again, the PDO temperatures for the obstacle-equipped tube at G = 2772 $kg.m^{-2}.s^{-1}$ are lower than those at the lower flow. When comparing PDO temperatures for the obstacle-equipped test sections to the bare tube PDO temperatures, it can be seen that the maximum temperatures approach each other, especially at the downstream end of the test section. In Figure 4.26 there are steep jumps of the inverse HTC (more pronounced in bare tubes), for bare and obstacle equipped tubes, the corresponding axial locations of these jumps are: z = 1.66 and 1.835 m (Figure 3.6). These steps were not observed for the bare tubes having a uniform AFD (see Figure 4.7 and 4.8) and are thought to be due to: (i) the large step in heat flux (q/q_{av} dropped from 1.17 to 0.947 for z = 1.66 m, and from 0.947 to 0.658 for z = 1.835 m), and (ii) the proximity of the measurement locations to the heat flux step locations. The corresponding thermocouples are located at $z \approx$ 1.66 and 1.835 m, respectively.

4.4.5 Pressure Effect

4.4.5.1 Inlet-peak AFD

The effect of pressure on PDO heat transfer is similar as that observed for the uniform-AFD tube, discussed in Section 4.3.5. Figure 4.27 and 4.28 present the pressure effect on PDO heat transfer for the inlet-peak AFD tube. The tube is equipped with five-streamlined obstacles having 12% flow-blockage ratio at 300 mm pitch. PDO conditions

for the obstacle-equipped tube at P = 2389 kPa are established at z = 1.3 m (Figure 4.27); and downstream of the 3rd and 4th obstacles, where rewetting and subsequent dryout occurred. However for P = 1667 kPa, PDO conditions are established close to the exit of the test section, where all temperature profiles converge.

4.4.5.2 Outlet peak AFD

Figure 4.29 and Figure 4.30 present the effect of pressure on PDO heat transfer for the outlet-peak AFD tube. Two pressures were tested (1667 and 2389 kPa). At P = 2389 kPa and z = 1.6 to 1.66 m (Figure 4.29) the film boiling wall temperature differences between the bare and the obstacle equipped tube are clearly larger than the corresponding wall temperature differences at P = 1667 kPa. The same finding can be seen in Figure 4.30, at P = 2389 kPa and $x \approx 0.35$, the difference between the bare and the obstacle-equipped tube PDO wall temperature is larger than that at P = 1667 kPa. In Figure 4.30, as discussed earlier, there are severe jumps of the inverse HTC for the bare and obstacle-equipped tube cases. This is thought to be due to the proximity of the thermocouples to the step location.

4.4.6 Inlet Temperature Effect

4.4.6.1 Inlet-peak AFD

Figures 4.31 and 4.32 show the effect of inlet temperature on PDO heat transfer for the inlet-peak AFD tube. As noted for the uniform AFD tube, almost no effect of inlet temperature could be noticed for the inlet-peak AFD tube results .

4.4.6.2 Outlet-peak AFD

The inlet temperature effect on PDO heat transfer for the outlet-peak AFD is presented in Figure 4.33 and 4.34. The outlet-peak tube has 5-streamlined obstacles with 24% flow-blockage ratio at a 300-mm pitch. Temperature profiles (Figure 4.33) of the two configurations with obstacles are below the bare-tube temperatures. Beyond z = 1.45 m, the surface temperatures of the bare tube at T_{in} = 65°C are slightly higher than the surface temperatures of the bare tube at T_{in} = 70°C. For the obstacle equipped tube at T_{in} = 65°C, surface temperatures are slightly higher than of tube at T_{in} = 70°C.

4.4.7 Heat Flux Effect

4.4.7.1 Inlet-peak AFD

In Figure 4.35 and 4.36 the wall temperature profiles of the bare tubes are quite close. Also the surface temperatures of the obstacle-equipped tubes are close. The heat flux was varied from q = 140 to 150 kW.m^{-2}, this variation does not show any significant influence on PDO heat transfer. The heat flux effect for the inlet-peak tube (Figures 4.35 and 4.36) is weak and is similar to the effect of heat flux for the uniform-AFD tube.

4.4.7.2 Outlet-peak AFD

A minor heat flux effect for outlet-peak AFD tube can be noticed close to the exit of the test section – the bare tube temperature profiles almost coincide, while surface temperatures of the obstacle-equipped tube at q = 120 kW.m^{-2} appear below that of the same configuration at 140 kW.m^{-2} (Figure 4.37 and 4.38).

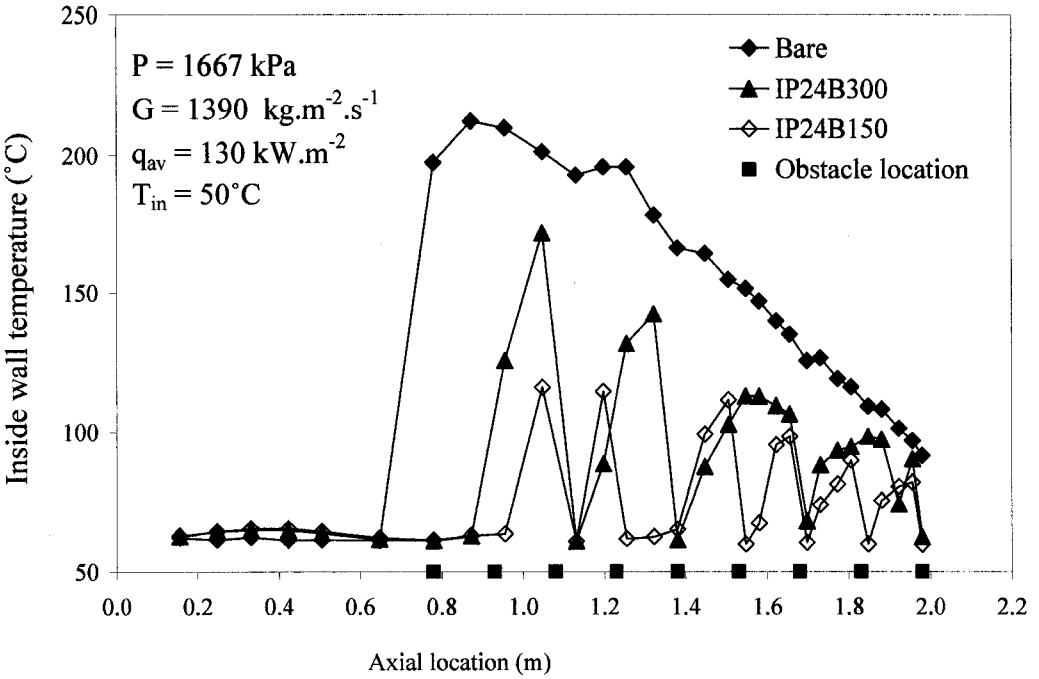

Figure 4.15 Effect of obstacle pitch on the temperature distribution for blunt obstacles (inlet-peak profile, low-pressure and low-mass flux).

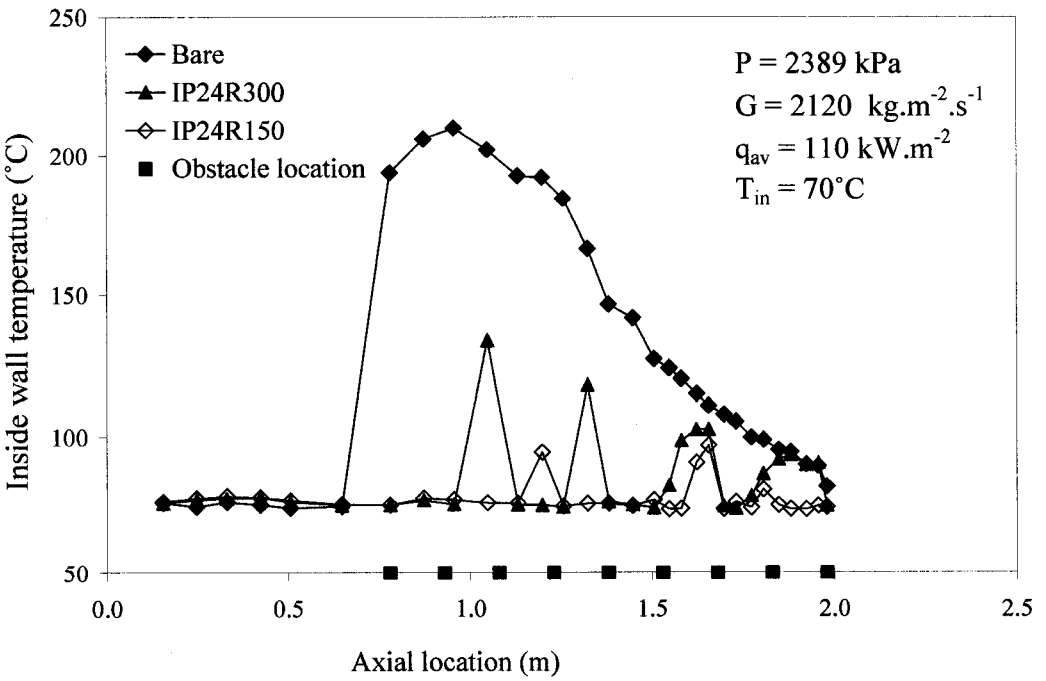

Figure 4.16 Effect of obstacle pitch on the temperature distribution for streamlined obstacles (inlet-peak profile, high-pressure and moderate-mass flux).

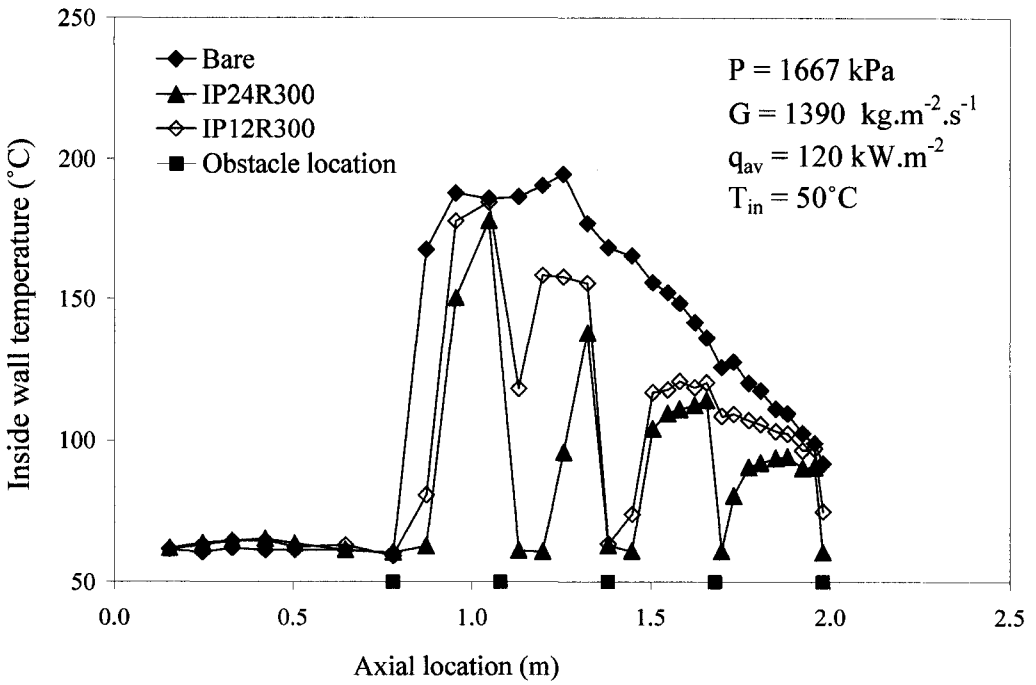

Figure 4.17 Effect of flow-blockage ratio on the temperature distribution for streamlined obstacles (inlet-peak profile, low-pressure and low-mass flux).

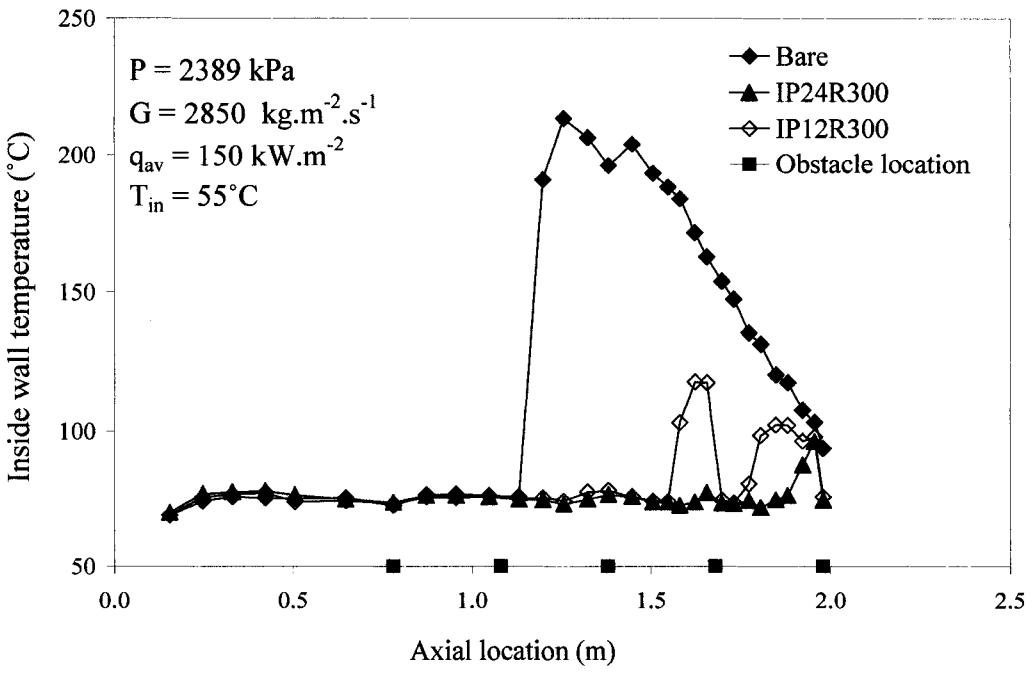

Figure 4.18 Effect of flow-blockage ratio on the temperature distribution for streamlined obstacles (inlet-peak profile, high-pressure and high-mass flux).

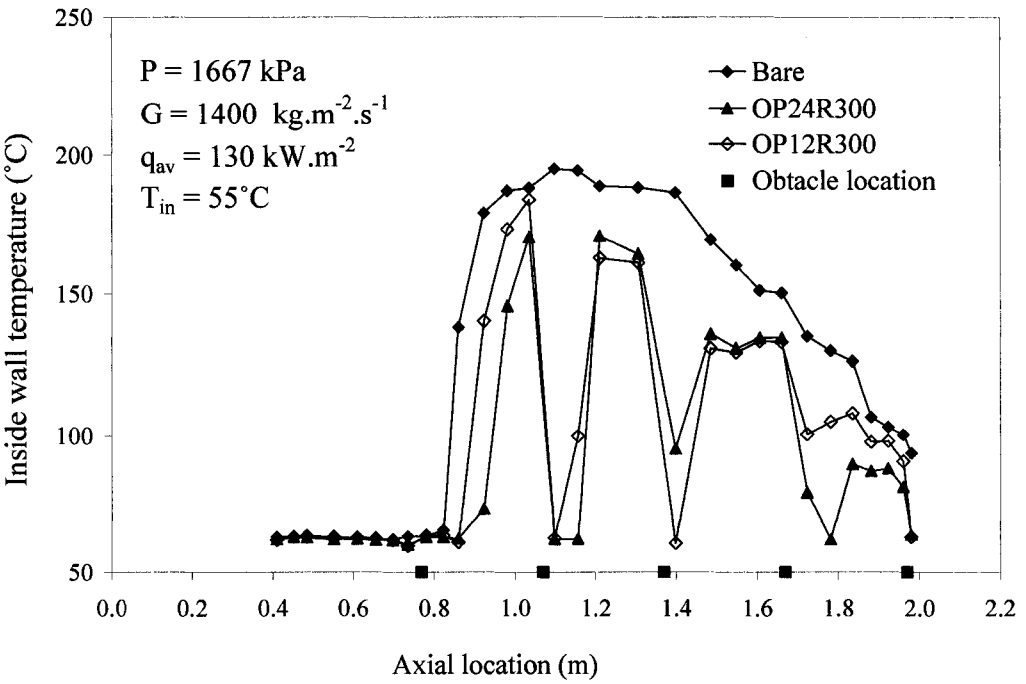

Figure 4.19 Effect of flow-blockage ratio on the temperature distribution for streamlined obstacles (outlet-peak profile, low-pressure and low-mass flux).

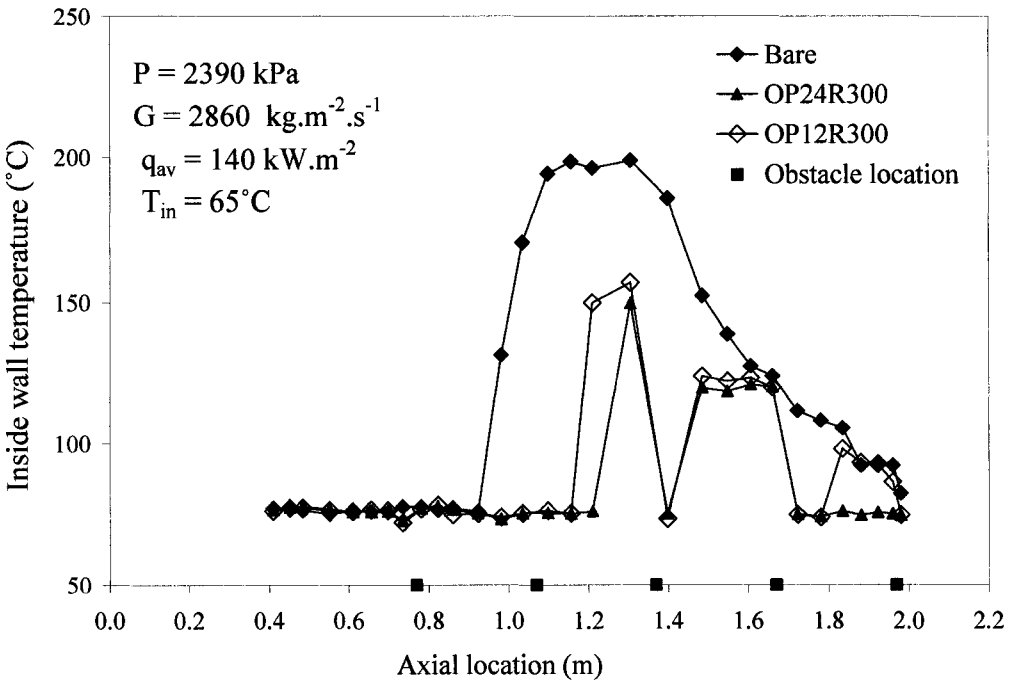

Figure 4.20 Effect of flow-blockage ratio on the temperature distribution for streamlined obstacles (outlet-peak profile, high-pressure and high-mass flux).

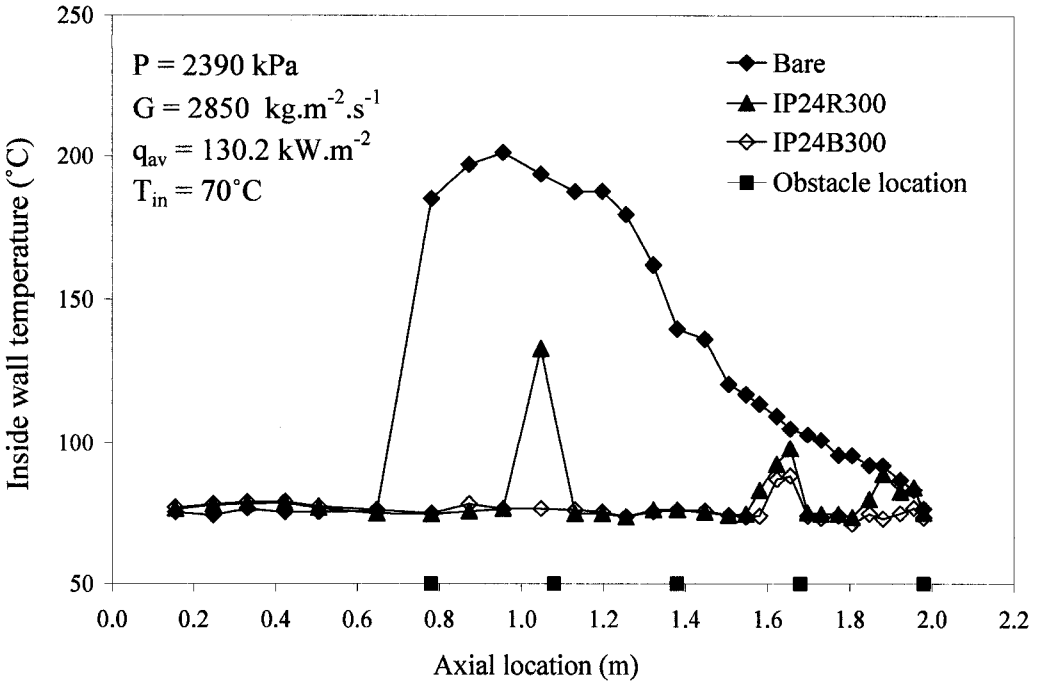

Figure 4.21 Effect of obstacle shape on the temperature distribution for streamlined and blunt obstacles (inlet-peak profile, high-pressure and high-mass flux).

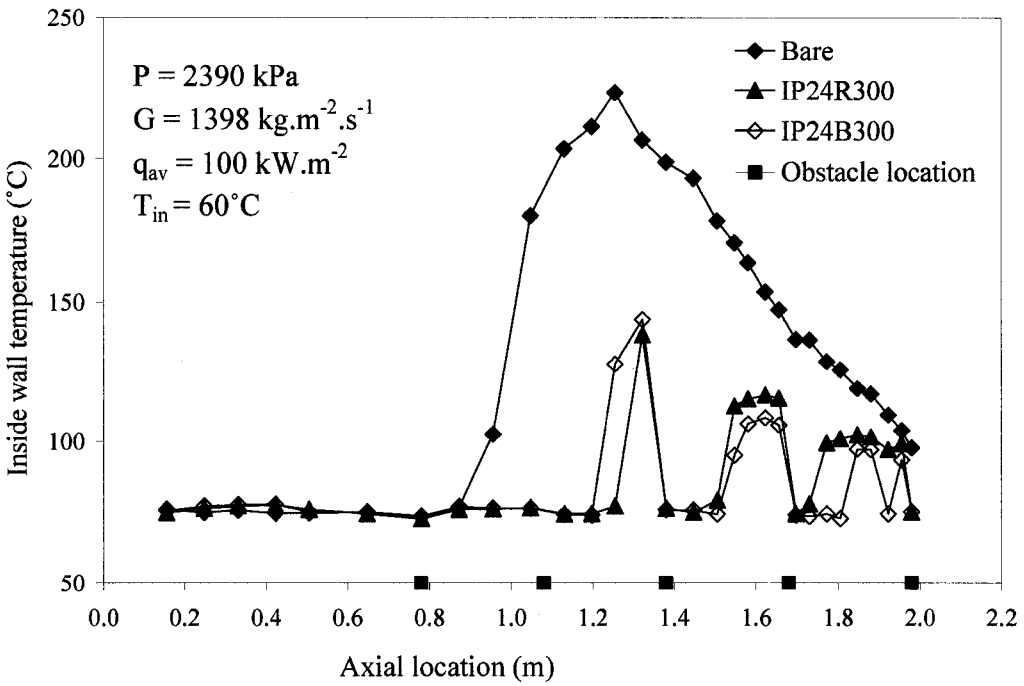

Figure 4.22 Effect of obstacle shape on the temperature distribution for streamlined and blunt obstacles (inlet-peak profile, high-pressure and low-mass flux).

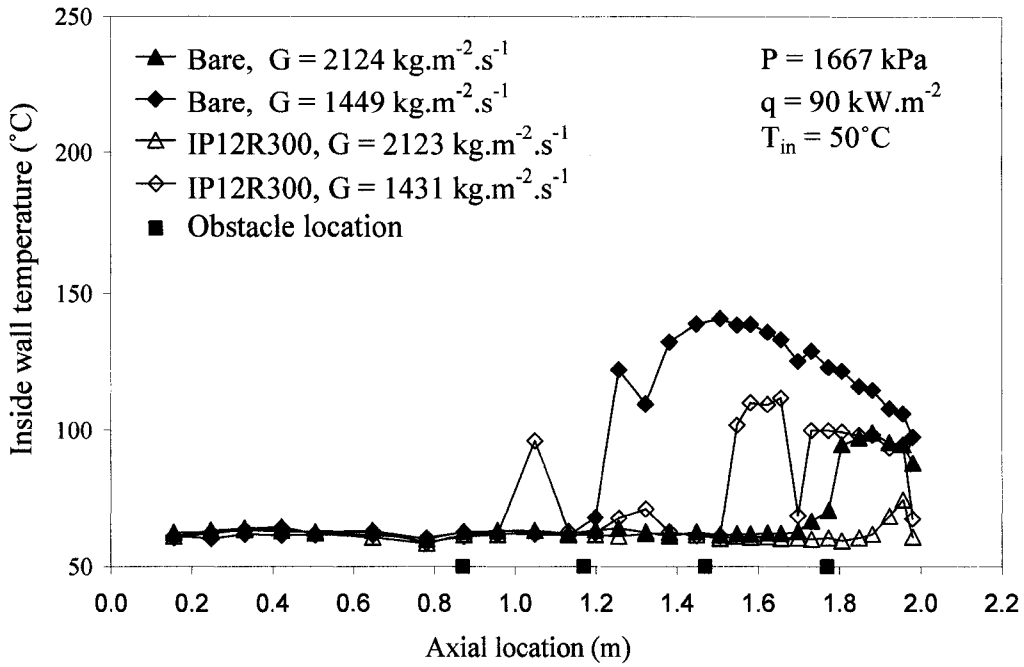

Figure 4.23 Effect of mass flux on the temperature distribution for streamlined obstacles (inlet-peak profile, low-pressure).

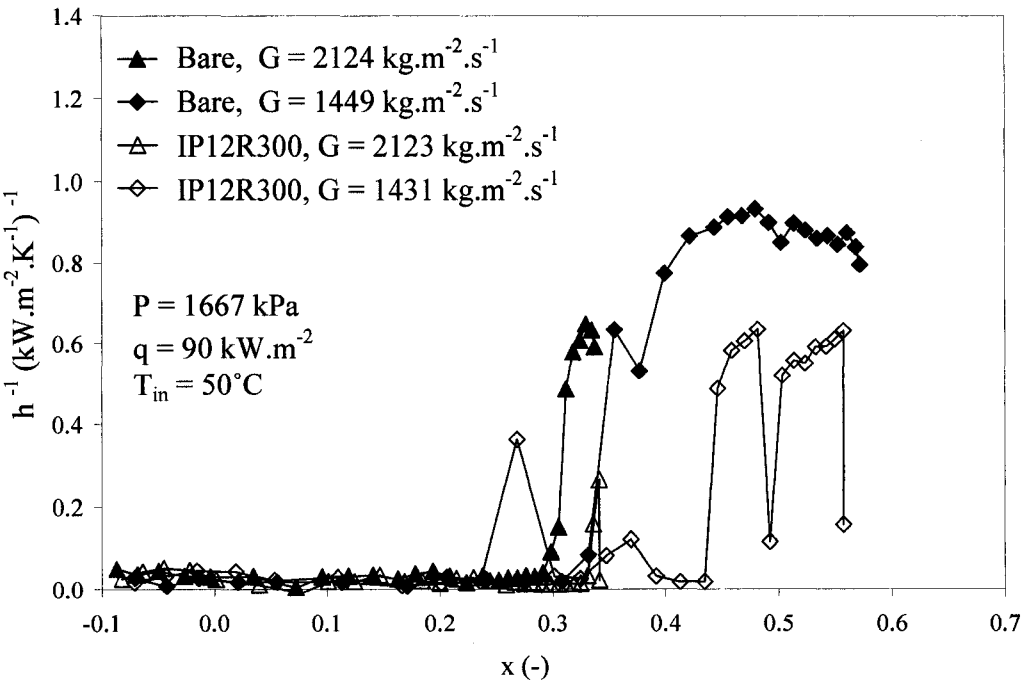

Figure 4.24 Effect of mass flux on the inverse HTC vs. local quality for streamlined obstacles (inlet-peak AFD, low-pressure).

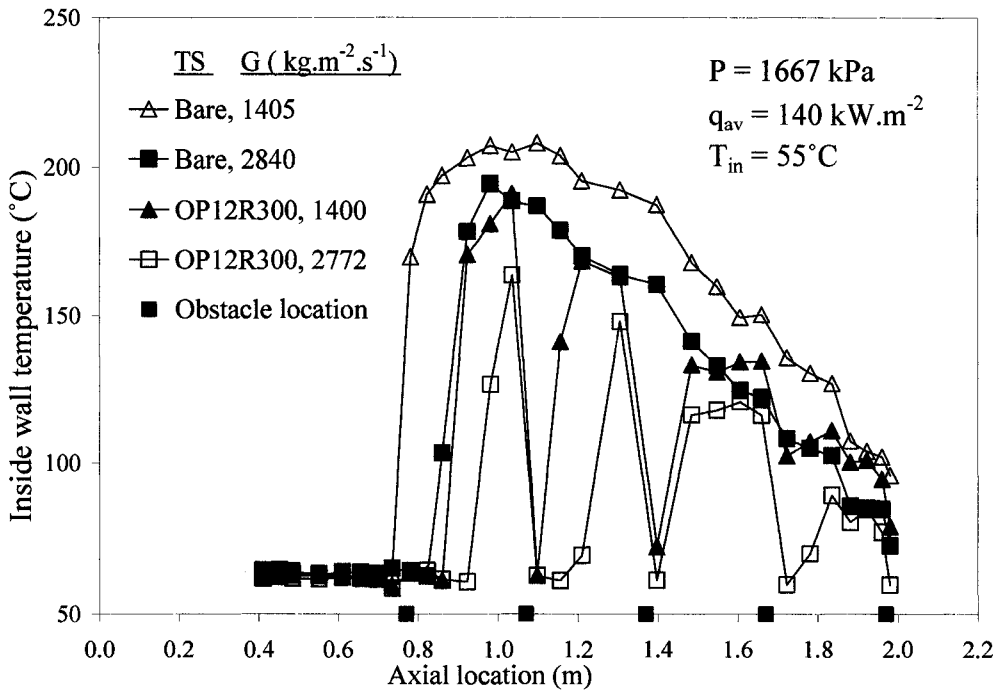

Figure 4.25 Effect of mass flux on the temperature distribution for streamlined obstacles (outlet-peak AFD, low-pressure).

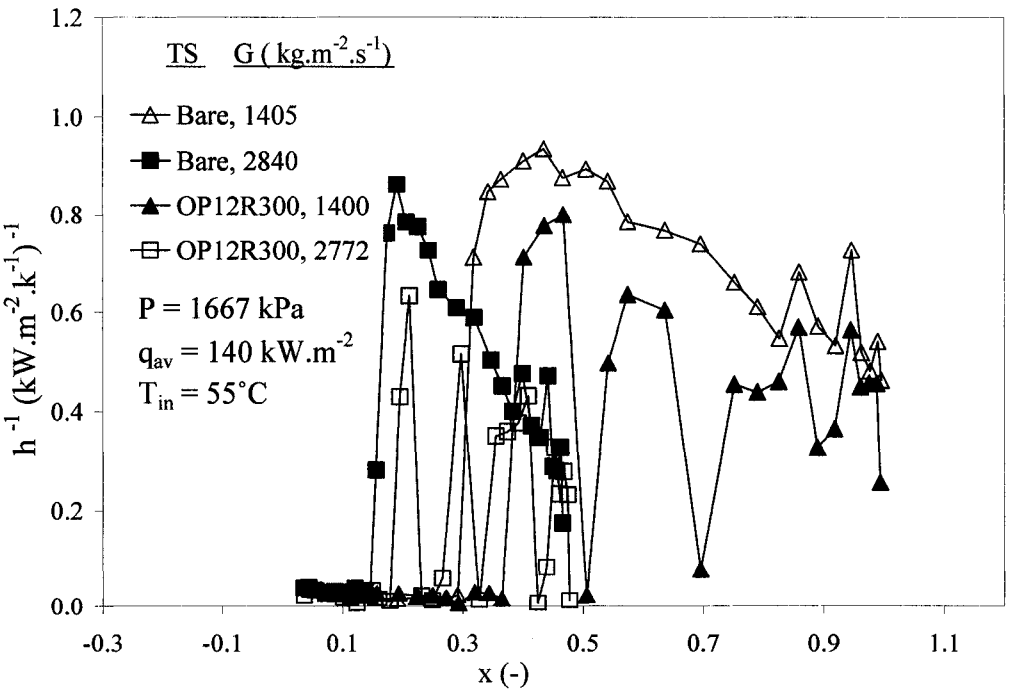

Figure 4.26 Effect of mass flux on the inverse HTC vs. local quality for streamlined obstacles (outlet-peak AFD, low-pressure).

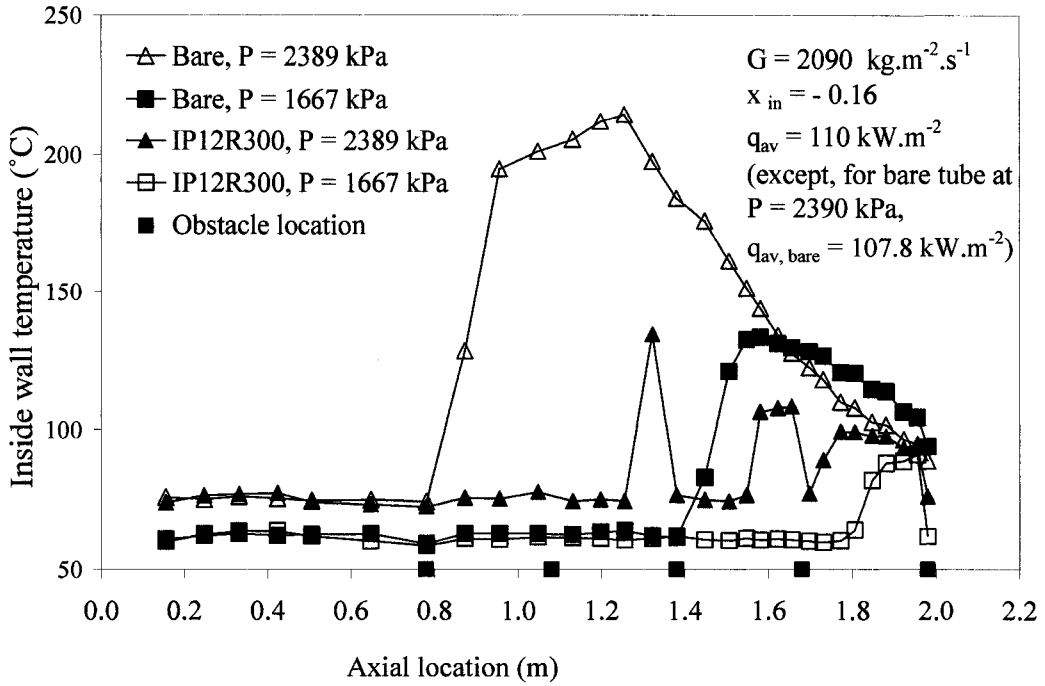

Figure 4.27 Effect of pressure on the temperature distribution for streamlined obstacles (inlet-peak AFD, moderate-mass flux).

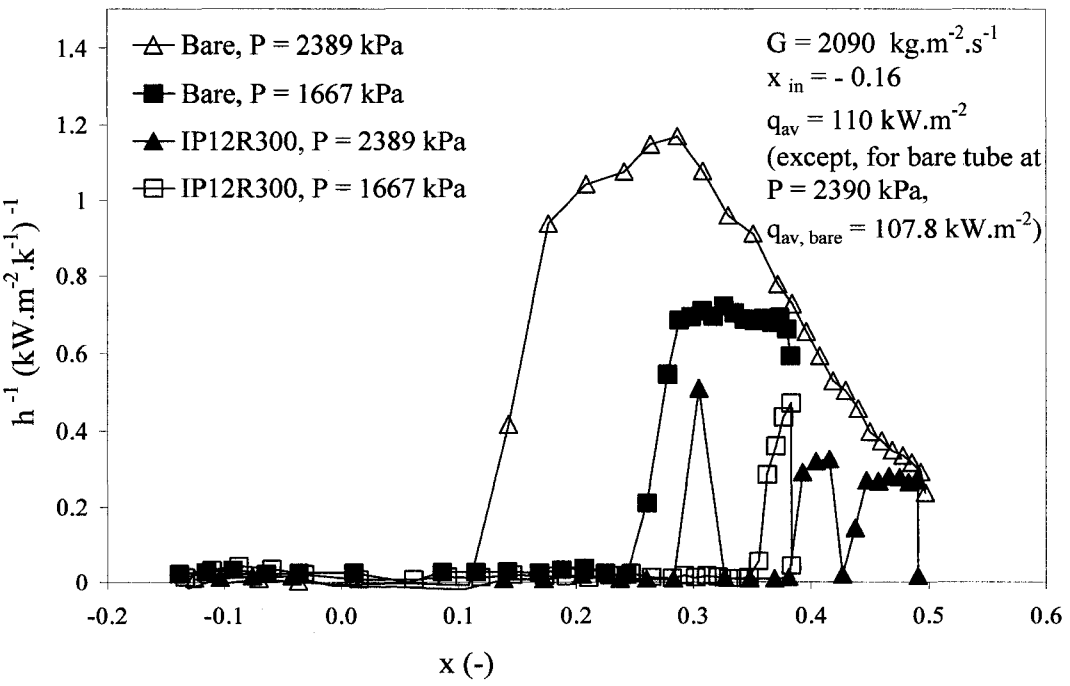

Figure 4.28 Effect of pressure on the inverse HTC vs. local quality for streamlined obstacles (inlet-peak AFD, moderate-mass flux).

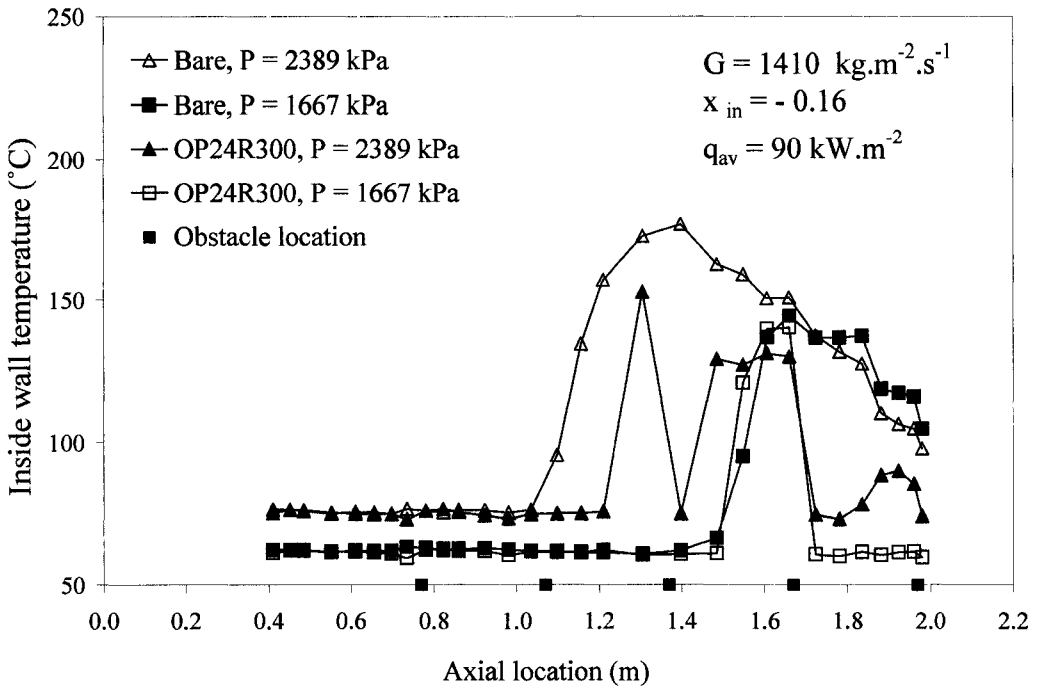

Figure 4.29 Effect of pressure on the temperature distribution for streamlined obstacles (outlet-peak AFD, low-mass flux).

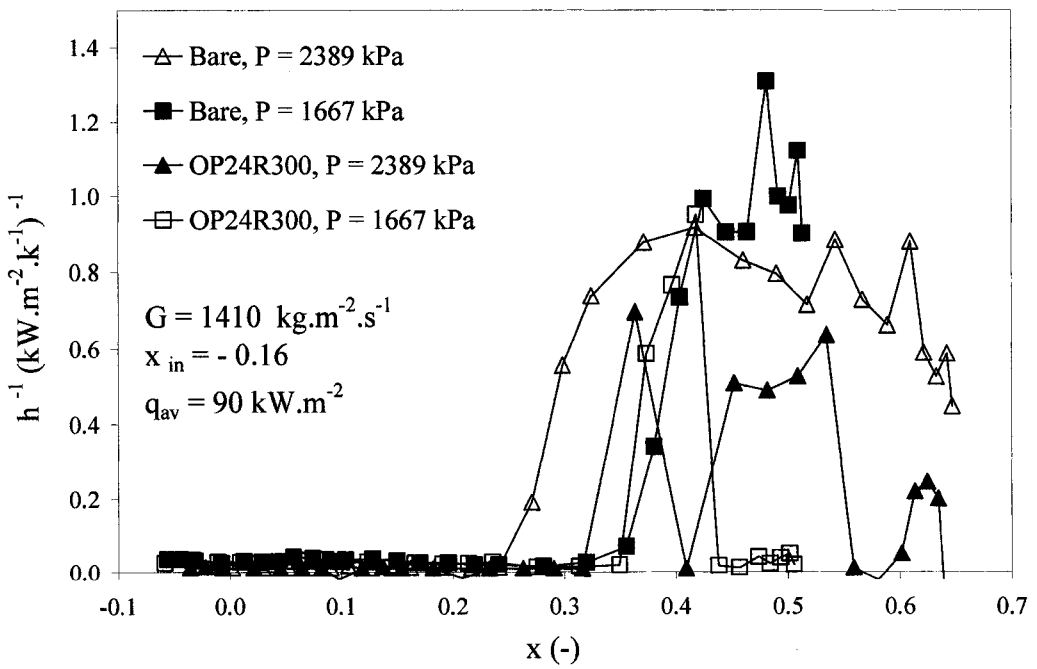

Figure 4.30 Effect of pressure on the inverse HTC vs. local quality for streamlined obstacles (outlet-peak AFD, low-mass flux).

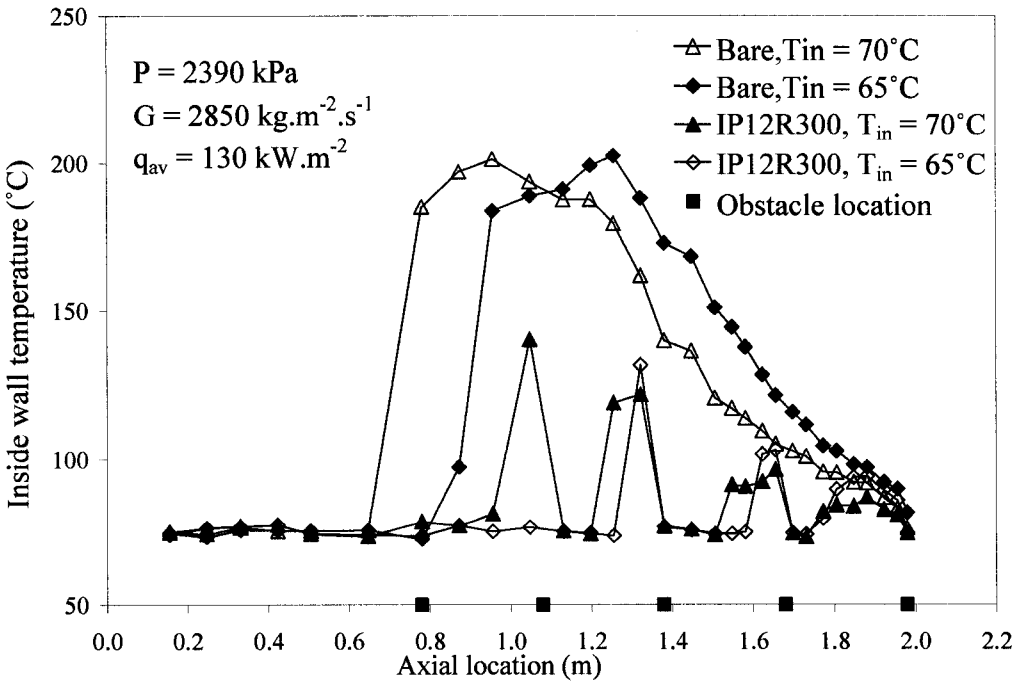

Figure 4.31 Effect of inlet temperature on the temperature distribution for streamlined obstacles (inlet-peak AFD, high-pressure and high-mass flux).

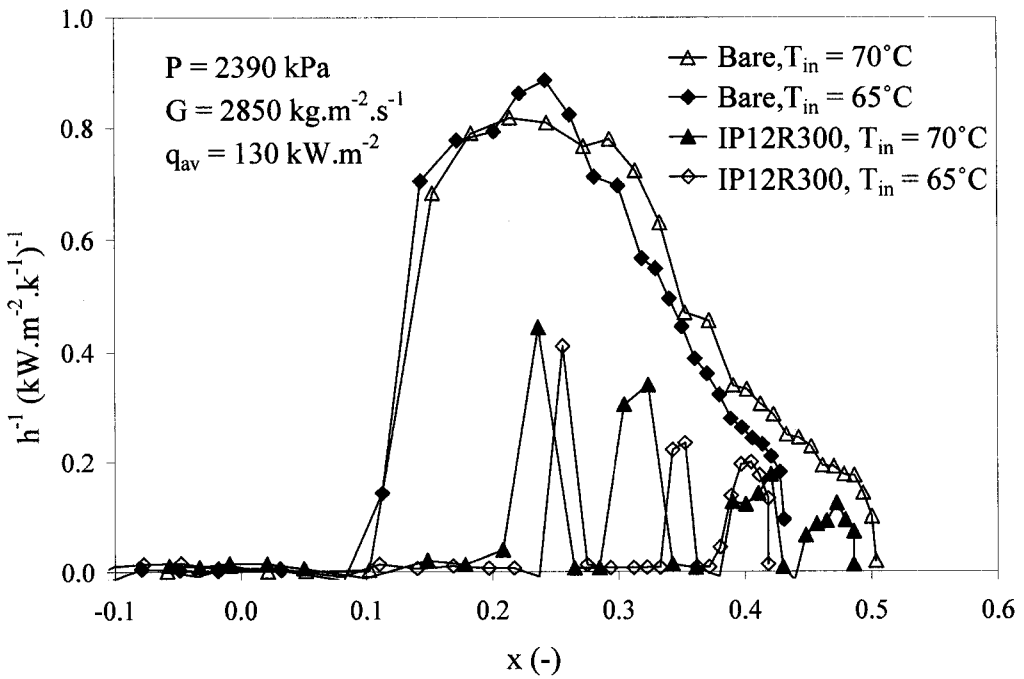

Figure 4.32 Effect of inlet temperature on the inverse HTC vs. local quality for streamlined obstacles (inlet-peak profile, high-pressure and high-mass flux).

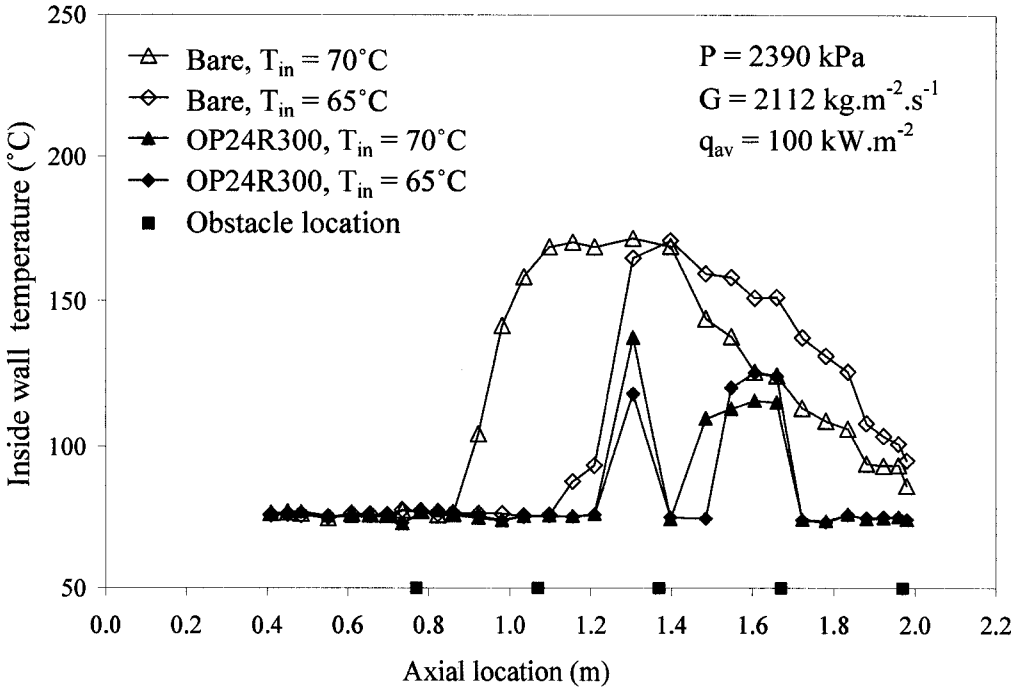

Figure 4.33 Effect of inlet temperature on the temperature distribution for streamlined obstacles (outlet-peak AFD, high-pressure and moderate-mass flux).

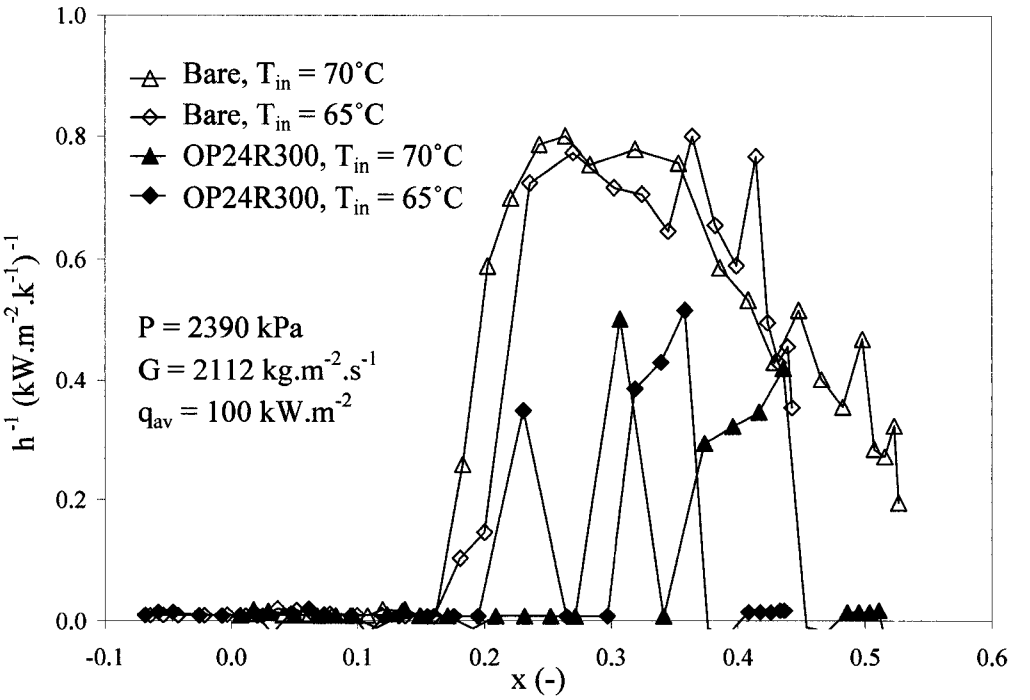

Figure 4.34 Effect of inlet temperature on the inverse HTC vs. local quality for streamlined obstacles (outlet-peak profile, high-pressure and moderate-mass flux).

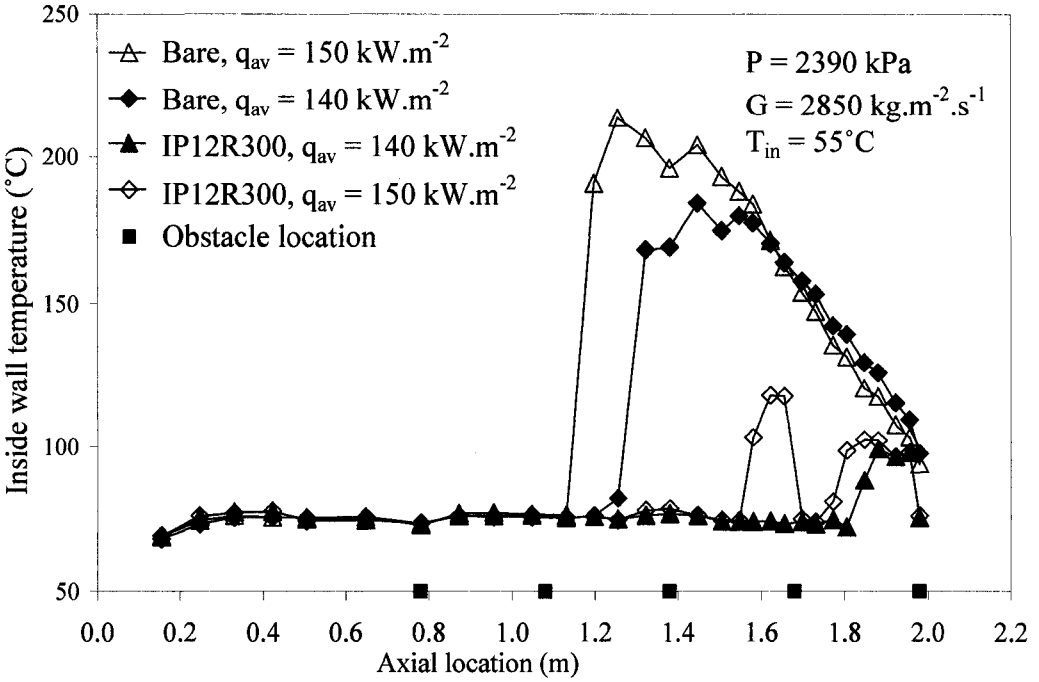

Figure 4.35 Effect of heat flux on the temperature distribution for streamlined obstacles (inlet-peak profile, high-pressure and high-mass flux).

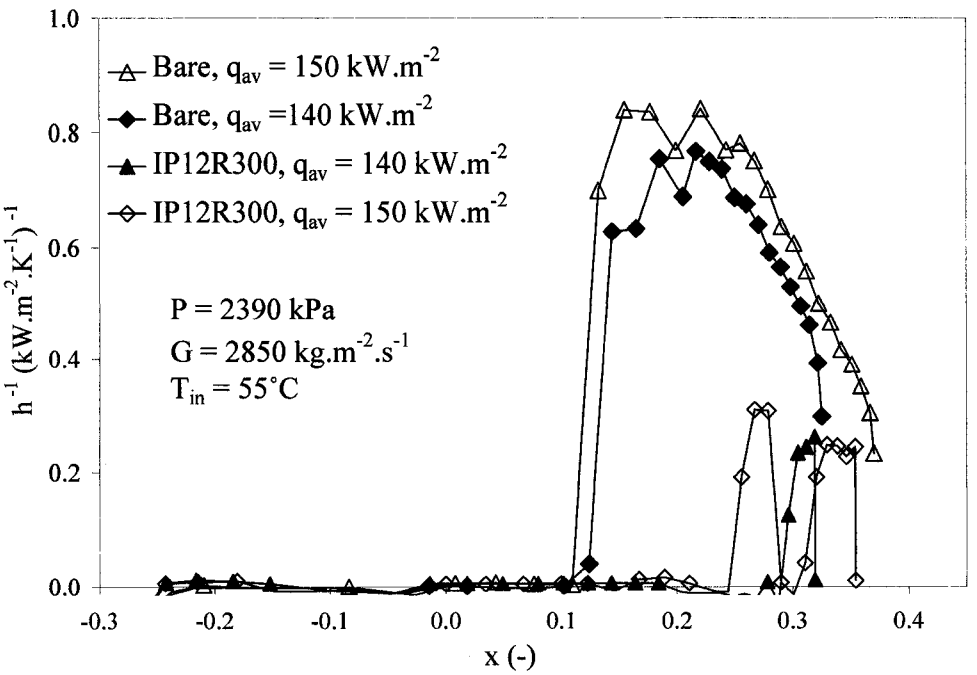

Figure 4.36 Effect of heat flux on the inverse HTC vs. local quality for streamlined obstacles (inlet-peak profile, high-pressure and high-mass flux).

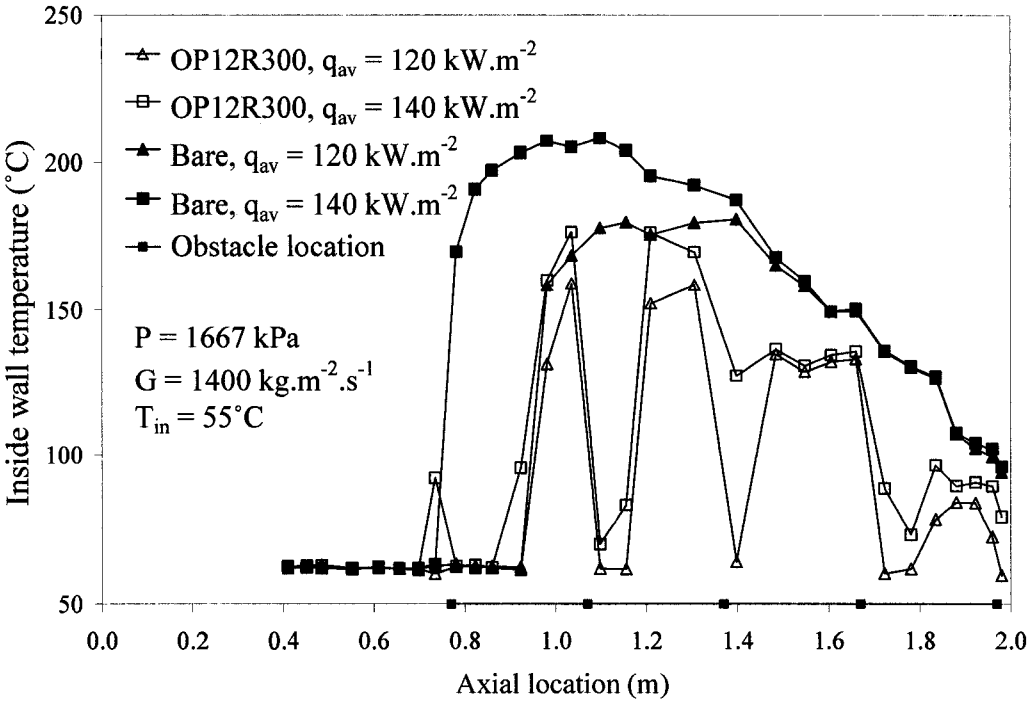

Figure 4.37 Effect of heat flux on the temperature distribution for streamlined obstacles (outlet-peak profile, low-pressure and low-mass flux).

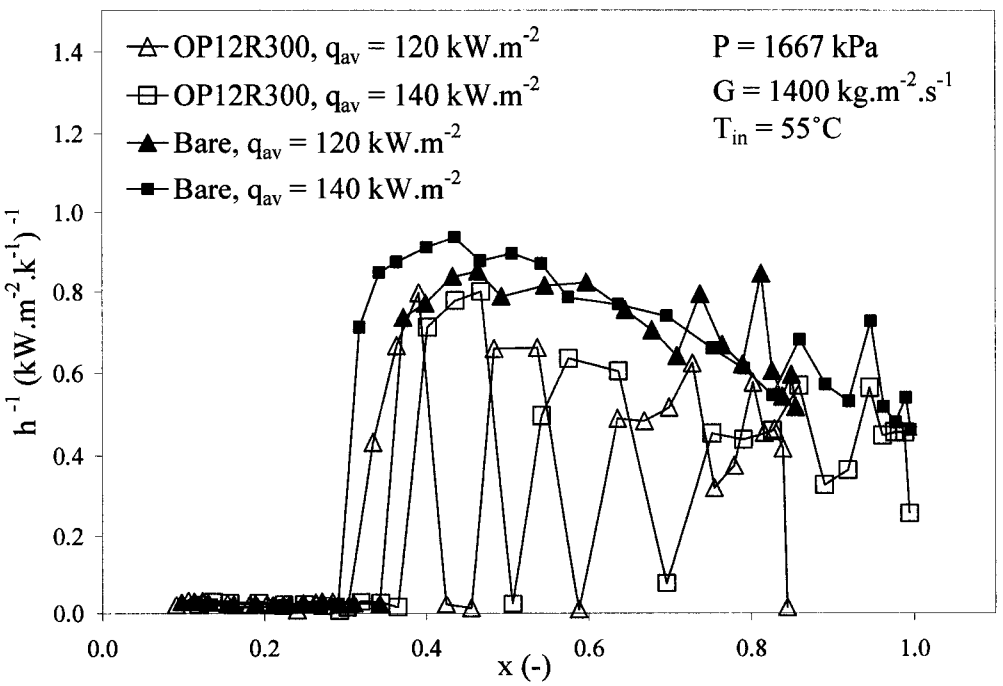

Figure 4.38 Effect of heat flux on the inverse HTC vs. local quality for streamlined obstacles (outlet-peak profile, low-pressure and low-mass flux).

4.5 Observed AFD Effect on PDO Heat Transfer

Figure 4.39 shows the impact of the axial heat flux profile on the post-dryout wall temperatures for streamlined obstacles having a 12% flow-blockage ratio and a 300-mm pitch. Five obstacles are positioned at different locations and the local heat flux varies in tubes having different axial heat flux profiles. Therefore, the comparison of wall temperatures at various locations may not be representative. Overall, bare tube PDO wall temperatures for the inlet-peak profile are higher than those of other profiles at upstream locations, while bare tube PDO wall temperatures for the uniform profile are higher at downstream locations. A similar trend appears to be present when comparing the AFDs for bare tubes on an inverse HTC vs. quality basis as shown in Figure 4.40.

The PDO wall temperatures for obstacle-equipped tubes do not appear to vary considerably for these profiles. This is mainly due to the suppression of dryout by the presence of an upstream obstacle, which minimizes the difference in vapour superheat. As indicated above, comparisons of wall temperatures at various locations is difficult due to different obstacle locations in these tubes, as well as different local heat fluxes. Therefore, the inverse of heat-transfer coefficient is also presented for tubes of various axial heat flux profiles as a function of the local thermodynamic quality. Figure 4.40 illustrates the variations of inverse HTC for tubes of various heat flux profiles with rounded obstacles. The differences in inverse HTC between tubes of various axial heat flux profiles appear to be small. For the inlet-peak and uniform AFD tube, rewetting has been observed to occur at similar local thermodynamic qualities. However, for the outlet peak profile, post-dryout conditions could be maintained at the high local heat-flux section (thermodynamic qualities between 0.25 and 0.35).

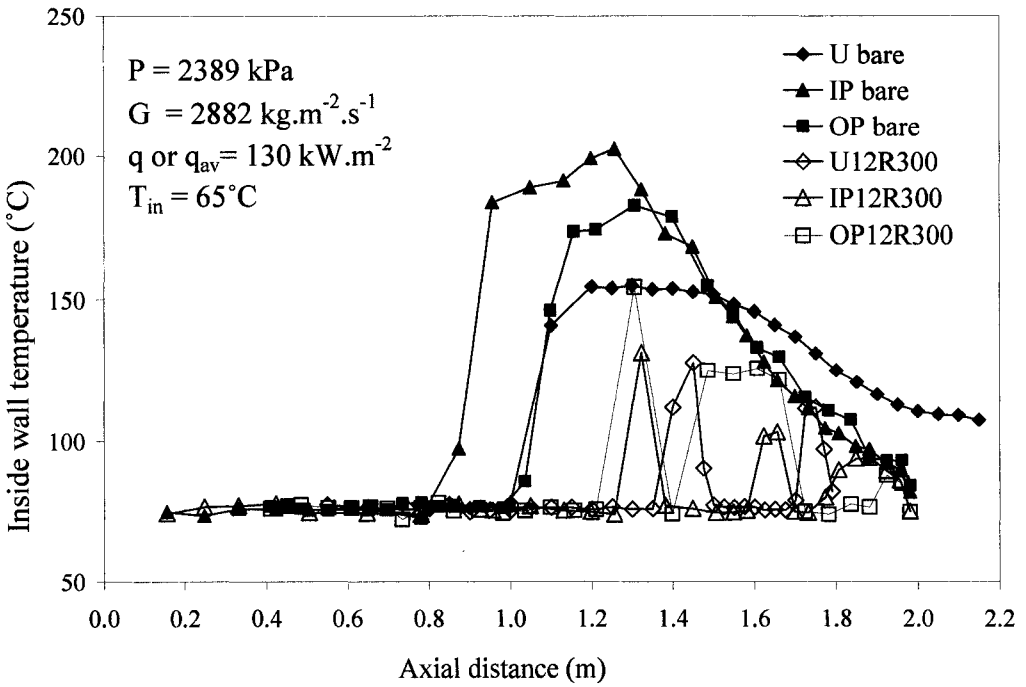

Figure 4.39 Effect of AFD on the temperature distribution for streamlined obstacles (uniform, inlet-peak and outlet-peak profiles, high-pressure and high-mass flux).

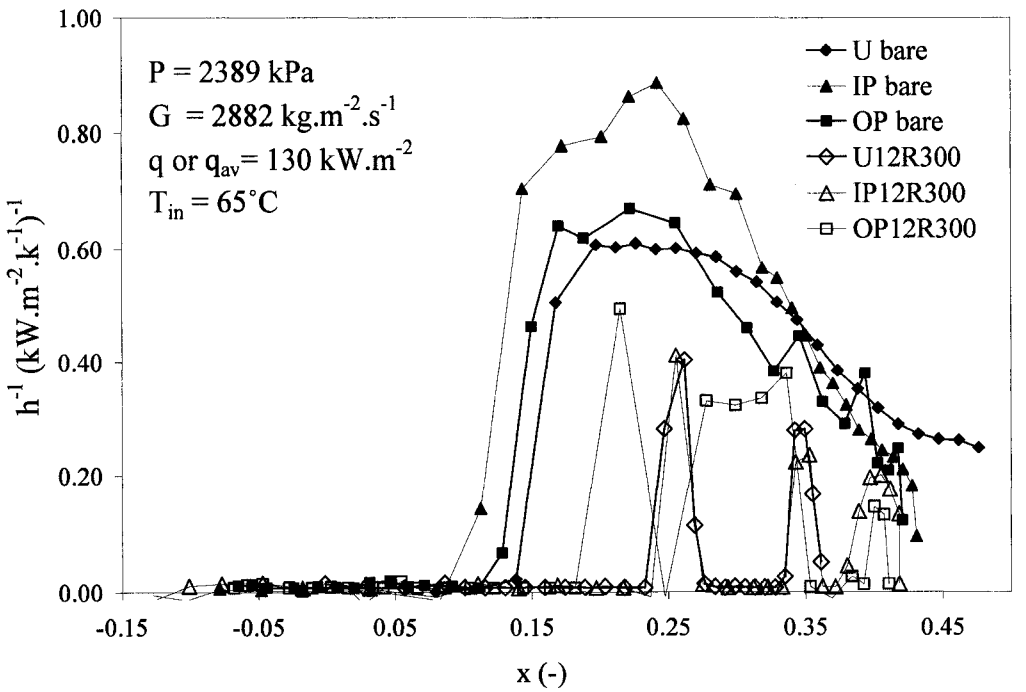

Figure 4.40 Effect of AFD on the inverse HTC distribution vs. local quality for streamlined obstacles (uniform, inlet-peak and outlet-peak profiles, high-pressure and high-mass flux).

CHAPTER 5

ANALYSIS OF EXPERIMENTAL DATA AND COMPARISON AGAINST PREDICTION METHODS

5.1 Selection of PDO Heat-Transfer Enhancement Data and Discussion

The experimental data showing clear evidence of film boiling (data with minimum rewetting points, longer-film boiling regions and high PDO temperatures) were selected from the bare-tube and obstacle-equipped-tube databases for further processing. These data were plotted as (1/h vs. x) and (T_w vs. axial location). The data processing included tabulation of the relative heat-transfer enhancement, expressed as $(h_{ob}-h_{bare})\times 100/h_{bare}$, for the maximum measured wall temperatures in the developing film-boiling region.

Table 5.1 (high-mass flux) and Table 5.2 (low-mass flux) present the selected PDO heat-transfer enhancement data expressed as $(h_{ob}-h_{bare})\times 100/h_{bare}$ as a function of quality, for cases where the flow conditions (P, G, q, x and T_{in}) are the same for the bare and obstacle-equipped test sections.

Table 5.1 Compilation of selected PDO heat-transfer enhancement data: uniform AFD test section, high-mass flux.

Obstacle parameter/AFD	Flow conditions	Quality, x (-)		$(h_{ob}-h_{bare})\times 100/h_{bare}$ (%)	
Flow-blockage ratio/ uniform AFD TS	P = 2389 kPa G = 2850 kg.m^{-2}.s^{-1} q = 140 kW.m^{-2} T_{in} = 70°C	U12R300	U24R300	U12R300	U24R300
		0.4454	0.4496	30.2*	37.7*
		0.3611	0.3644	55.4*	63.9+
		0.2691	0.2714	61.8+	78.6-
Obstacle shape/ uniform AFD TS	P = 2389 kPa G =2870 kg.m^{-2}.s^{-1} q =150 kW.m^{-2} T_{in} = 65°C	U24R300	U24B300	U24R300	U24B300
		0.4165	0.4169	55.6*	67.6+
		0.3247	0.3004	95.0+	118.5 -
		0.2245		90.1-	

- Transition boiling points - correspond to data obtained close to CHF location, where intermittent dryout and rewetting can occur, and the axial temperature gradient is very steep.

+ developing film-boiling points - correspond to cases downstream of the CHF and transition boiling points where rewetting no longer occurs but the heat transfer is affected by upstream conditions and the axial surface temperature distribution has not yet levelled off.

** fully developed film-boiling points - correspond to cases where the axial temperature gradient has reached a plateau and appears to be no longer affected by the distance from the CHF location or spacer location, Groeneveld and Stewart (1982).*

Table 5.2 Compilation of selected PDO heat-transfer enhancement data: uniform, inlet-peak and outlet-peak AFD test section, low-mass flux.

Obstacle parameter/AFD	Flow conditions	Quality, x (-)		$(h_{ob}-h_{bare})\times 100/h_{bare}$ (%)	
Obstacle pitch/ inlet-peak AFD TS	P = 1665 kPa G = 1409 kg.m^{-2}.s^{-1} q_{av} = 130 kW.m^{-2} T_{in} = 50°C	IP24R300	IP24R150	IP24R300	IP24R150
		0.8289	0.8586	42.9*	84.4$^-$
		0.7539	0.7949	35.5$^+$	60.6$^-$
		0.5894	0.7486	44.1$^+$	71.9$^+$
		0.4412	0.6799	14.3$^+$	58. 0$^+$
			0.5201		111.8$^-$
			0.4388		178.0$^-$
Flow-blockage ratio/ inlet-peak AFD TS	Same as above	IP12R300	IP24R300	IP12R300	IP24R300
		0.7404	0.8289	17.5*	42.9*
		0.5134	0.7539	33.1*	35.5$^+$
		0.3852	0.5894	10.7*	44.1$^+$
			0.4412		14.3$^+$
Obstacle shape/ inlet-peak AFD TS	Same as above	IP24R300	IP24B300	IP24R300	IP24B300
		0.8289	0.8315	42.9*	28.2*
		0.7539	0.7229	35.5$^+$	64.2*
		0.5894	0.5923	44.1$^+$	43.6$^+$
		0.4412	0.4443	14.3$^+$	26.7$^+$
Obstacle pitch/ uniform AFD TS	P = 2389 kPa G = 1420 kg.m^{-2}.s^{-1} q = 110 kW.m^{-2} T_{in} = 60°C	U24R300	U24R150	U24R300	U24R150
		0.6128	0.6244	58.9*	81.1$^+$
		0.4777	0.5512	78.3$^+$	92.7$^+$
			0.4048		317.2$^-$
	P = 1667 kPa G = 1400 kg.m^{-2}.s^{-1} q = 140 kW.m^{-2} T_{in} = 45°C	U24R300	U24R150	U24R300	U24R150
		0.7377	0.7625	49.6*	78.9$^+$
		0.5946	0.6832	43.8$^+$	62.5$^+$
		0.4385	0.6039	35.0$^+$	114.3$^-$
			0.5246		125.1$^-$
Flow-blockage ratio/ uniform AFD TS	P = 2389 kPa G = 1420 kg.m^{-2}.s^{-1} q = 110 kW.m^{-2} T_{in} = 60 °C	U12R300	U24R300	U12R300	U24R300
		0.6183	0.6128	43.5*	58.9*
		0.4826	0.4777	55.8$^+$	78.3$^+$
		0.3345		22.2$^+$	
	P = 1667 kPa G = 1400 kg.m^{-2}.s^{-1} q = 140 kW.m^{-2} T_{in} = 45°C	U12R300	U24R300	U12R300	U24R300
		0.7445	0.7377	32.8*	49.6*
		0.6000	0.5946	30.7$^+$	43.8$^+$
		0.4424	0.4385	9.3$^+$	35.0$^+$
Obstacle shape/ uniform AFD TS	P = 2389 kPa G =1420 kg.m^{-2}.s^{-1} q =110 kW.m^{-2} T_{in} = 60°C	U24R300	U24B300	U24R300	U24B300
		0.6128	0.6315	58.9*	52.8$^+$
		0.4777	0.4590	78.3$^+$	100.0$^+$
			0.3112		116.4$^+$
	P = 1667 kPa G = 1400 kg.m^{-2}.s^{-1} q = 140 kW.m^{-2} T_{in} = 45°C	U24R300	U24B300	U24R300	U24B300
		0.7377	0.7512	49.6*	61.7$^+$
		0.5946	0.5689	43.8$^+$	57.2$^+$
		0.4385	0.4126	35.0$^+$	43.8$^+$
Flow-blockage ratio/ outlet-peak AFD TS	P = 2390 kPa G =2120 kg.m^{-2}.s^{-1} q =130 kW.m^{-2} T_{in} = 70°C	OP12R300	OP24R300	OP12R300	OP24R300
		0.6599	0.6627	18*	189$^+$
		0.5145	0.5178	34.5$^+$	34$^+$
		0.3815	0.3853	58$^+$	48.5$^+$
		0.3000	0.3045	74$^+$	94$^-$

The selection of the fully developed film boiling data in the above tables is not perfect as some residual developing-film-boiling effects may still be present. If all these residual effects were to be removed, then insufficient data would have been available for further analysis.

Figure 5.1-(a) shows the effect of flow-blockage ratio (12% vs. 24%) on PDO heat transfer, expressed by T_w vs. axial location. The inlet-peak AFD tube was equipped with 5 obstacles having a 300-mm pitch. Film boiling started at z = 0.78 m for the IP12R300 configuration, while it started at z = 0.87 m for the IP24R300 configuration. For the tube with the 12% flow-blockage obstacles, the maximum wall temperature was reached downstream from first obstacle at z = 0.956 m and q/q_{av} = 1.18, after which the inverse heat-transfer coefficient tends to level off until the second obstacle (Figure 5.1-(b)), this leveling off is considered typical of reaching fully developed film-boiling conditions. Downstream from the second and third obstacles, the next two points with maximum temperatures were encountered at z =1.198 and 1.656 m; just downstream from these points, the heat-transfer coefficient was increasing, and these downstream data were therefore considered fully-developed film-boiling points.

A similar approach was applied in the data analysis for the configuration IP24R300 (Figure 5.1-(a) and 5.1-(b)). The tabulated maximum wall temperatures (4 points) are considered as developing film-boiling points, except one point (downstream fourth obstacle at z = 1.848 m), this point was considered as a fully developed-film-boiling point.

Figure 5.2-(a) presents the effect of flow-blockage ratio (12% vs. 24%) on PDO surface temperatures for the outlet-peak AFD test section at high-pressure and moderate-mass flux. The outlet-peak tube was equipped with 5 rounded obstacles having either 12 or 24% flow-blockage ratio at a 300-mm pitch. Upstream from the 1st obstacle, first dryout occurs at the same location (z = 0.656 m) for the bare- and obstacle-equipped test section, also the three runs show the same surface-peak temperature at the same axial location (z = 0.735 m). Downstream from the first three obstacles, both obstacle-configurations show

rewetting at the same axial location, but the rewetting region (downstream from the first two obstacles) is longer for the obstacles with ε = 24%, also the surface encountered the maximum PDO wall temperatures at identical axial locations, for the two obstacle-equipped tubes. The tube with obstacles having ε = 12% experienced 1st maximum wall temperature at z = 1.035 m, this point was considered as a developing film-boiling point. The next two points with maximum PDO wall temperatures (z = 1.21 and 1.485 m) were considered also developing film-boiling points, while the point downstream from 4th obstacle at z = 1.835 m was considered a fully developed film-boiling point, since the surface temperature decreases or the heat transfer coefficient increases downstream from this point. At this point (start of the step number 16, x = 0.66 and q/q_{av} = 0.658), it was observed that there is a jump in the inverse HTC (Figure 5.2-(b)) which is caused by the significant decrease in the axial heat flux distribution, as was discussed in Chapter 4, since the previous step has a much larger local to average heat-flux ratio (q/q_{av} = 0.946), and is due to the proximity of the measurement locations to the step of the heat flux locations.

For the second configuration (OP24R300), four points with maximum wall temperature were identified; the first point was considered as a transition boiling point, while for the other three points, the surface was assumed to encounter developing film-boiling.

Figures 5.3-(a) and 5.3-(b), below, illustrate the obstacle pitch effect (150 mm vs. 300 mm) on PDO heat transfer. The uniform test section was equipped with 7 or 4 streamlined obstacles having a flow-blockage ratio of 24% at low-pressure and low-mass flux. A reduction in wall temperature has been observed for the obstacle-equipped tubes as compared to the bare tube. Dryout occurrences were suppressed by the first 3 upstream obstacles at the 150-mm pitch for locations prior to 1.25 m (seven obstacles were installed in this case), and by the two upstream obstacles at the 300-mm pitch for locations prior to 1.05 m.

For the tube with a 150-mm pitch, the surface appears to rewet at each obstacle location. The first two-maximum wall temperatures were located at z = 1.3 and 1.45 m

downstream from the third and fourth obstacle, respectively. Downstream from these points the surface rewetted within a short distance downstream from the next thermocouple locations (z =1.35 and 1.475 m). The surface at these points is considered to experience transition boiling. Downstream from the two subsequent obstacles the surface with maximum temperatures was considered to be experiencing developing film-boiling. These developing regions started downstream from the fifth and sixth obstacle and did not rewet at the next thermocouple locations, and the increase in surface temperature is not very steep. With increasing L/D downstream from the obstacles, the surface temperature increase is less steep.

For the tube with the 300-mm pitch, a similar analysis was performed, where three locations with maximum surface temperatures were identified, for the first two points the surface is considered to exhibit developing film-boiling and for the third point at z = 1.725 m the surface is considered to experience fully developed film-boiling.

Figures 5.4 to 5.6 (1/h vs. x, and T_w vs. axial location) show the selected enhancement data (Table 5.2) for both the uniform and non-uniform AFD test sections. Figure 5.4 shows plots of the selected and compiled data for the pitch effect (Figure 5.4-(a) and (c)) and flow-blockage ratio effect (Figure 5.4-(b) and (d)) on PDO heat transfer for a uniform AFD tube at high-pressure and low-mass flux. Figure 5.5 presents the effect of obstacle shape on PDO heat transfer for uniform AFD tube: the figures on the left hand-side (LHS) show the shape effect at high-pressure and low-mass-flux and the right hand-side (RHS) figures present the shape effect at low-pressure and low-mass-flux. Figure 5.6 displays the effect of obstacle pitch (LHS figures) and shape (RHS figures) on PDO heat transfer for the inlet-peak AFD tube. The heat-transfer enhancement data at the locations of maximum wall temperatures in Figures 5.4 to 5.6 were compiled in a similar manner as discussed earlier in this section, and the results were summarized in Table 5.2.

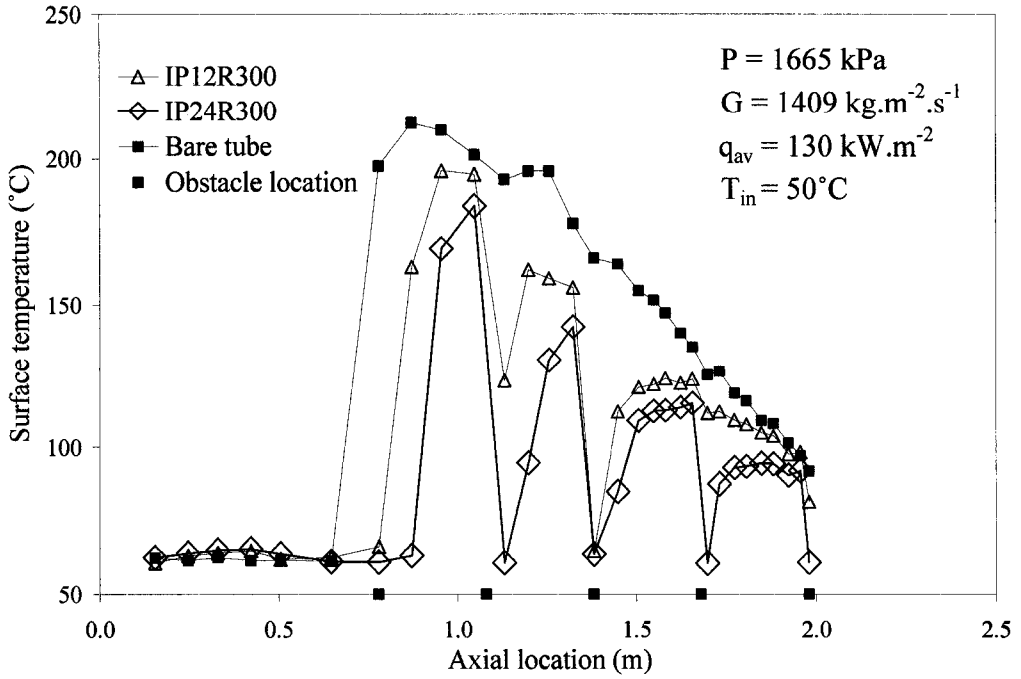

(a)

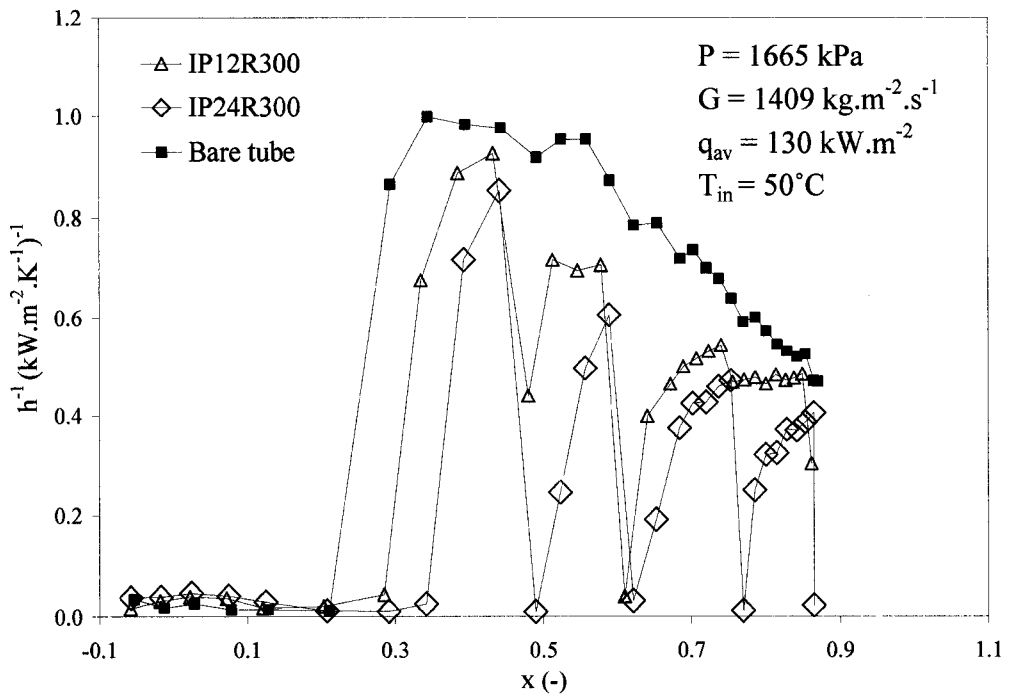

(b)

Figure 5.1 Effect of flow-blockage ratio on the temperature distribution (a) and on the inverse HTC distribution (b) for streamlined obstacles and inlet-peak AFD.

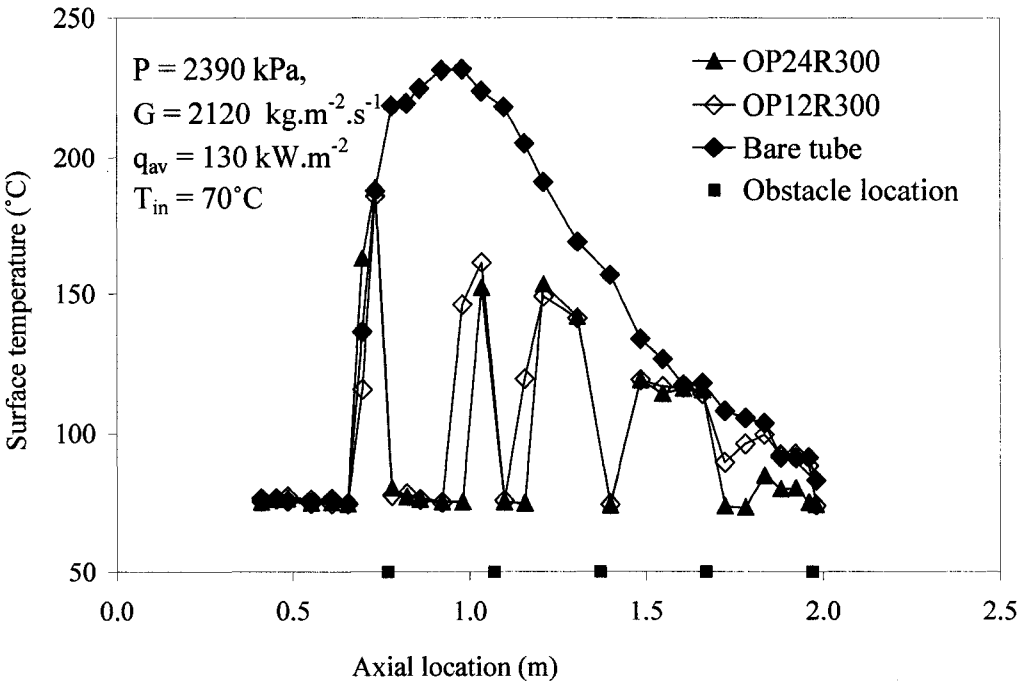

(a)

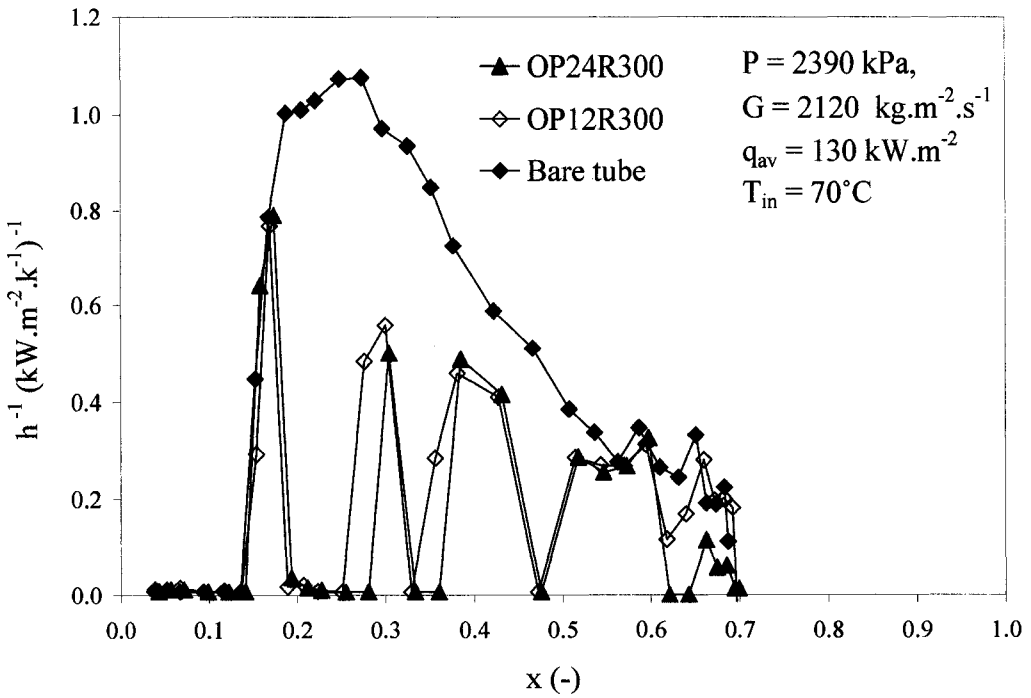

(b)

Figure 5.2 Effect of flow-blockage ratio on the temperature distribution (a) and on the inverse HTC distribution (b) for streamlined obstacles and outlet-peak AFD.

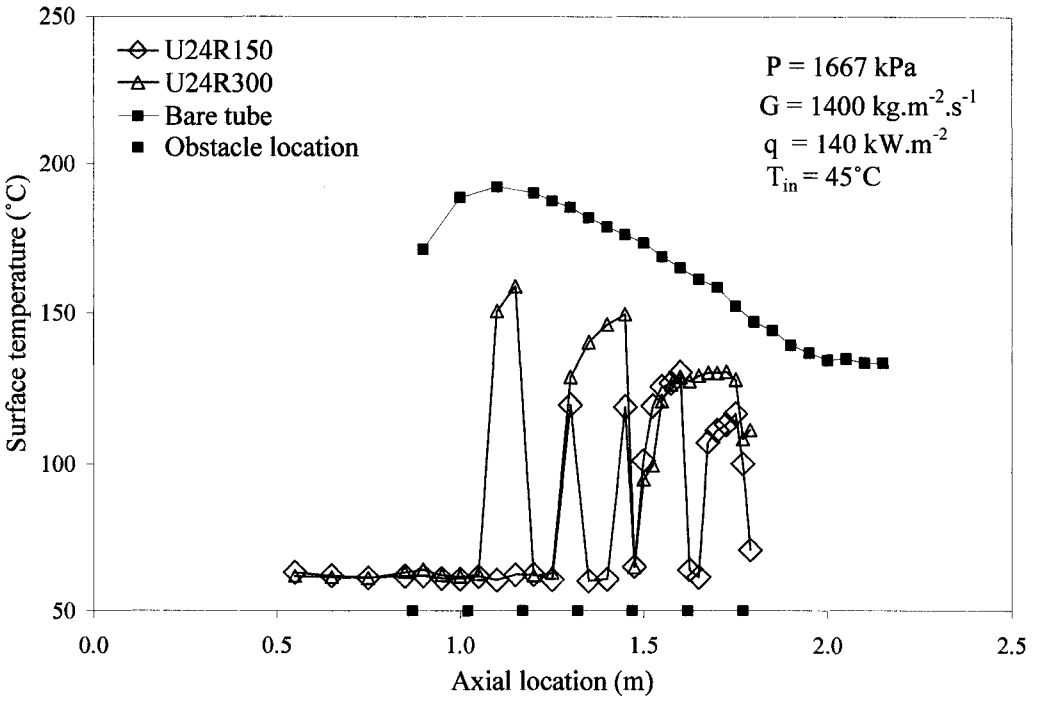

(a)

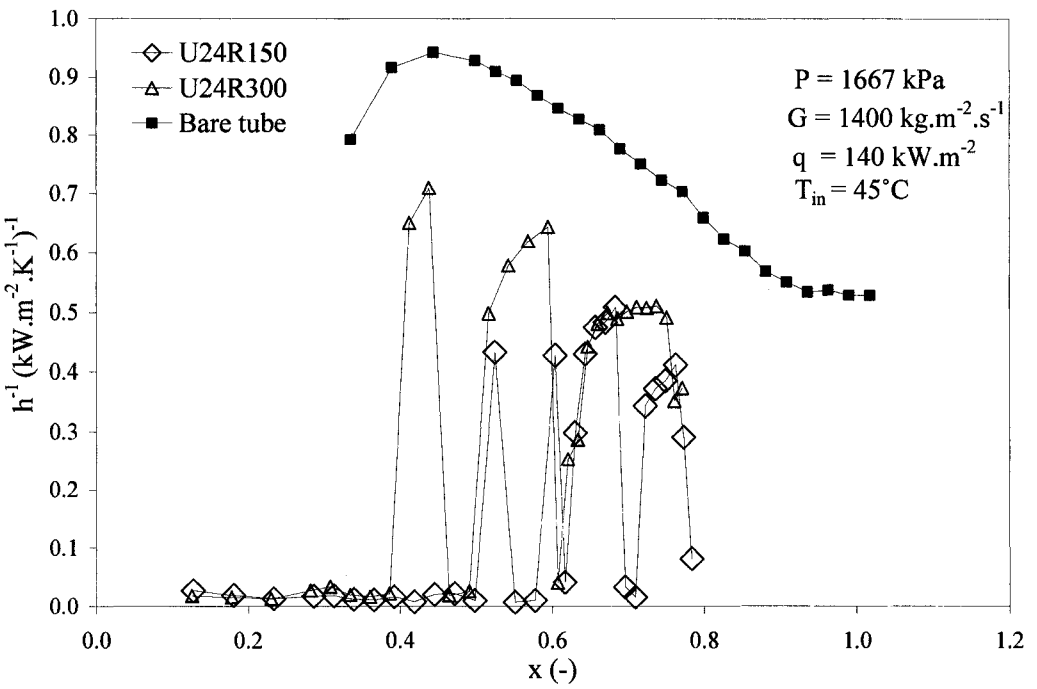

(b)

Figure 5.3 Effect of obstacle pitch on the temperature distribution (a) and on the inverse HTC distribution (b) for streamlined obstacles and uniform AFD.

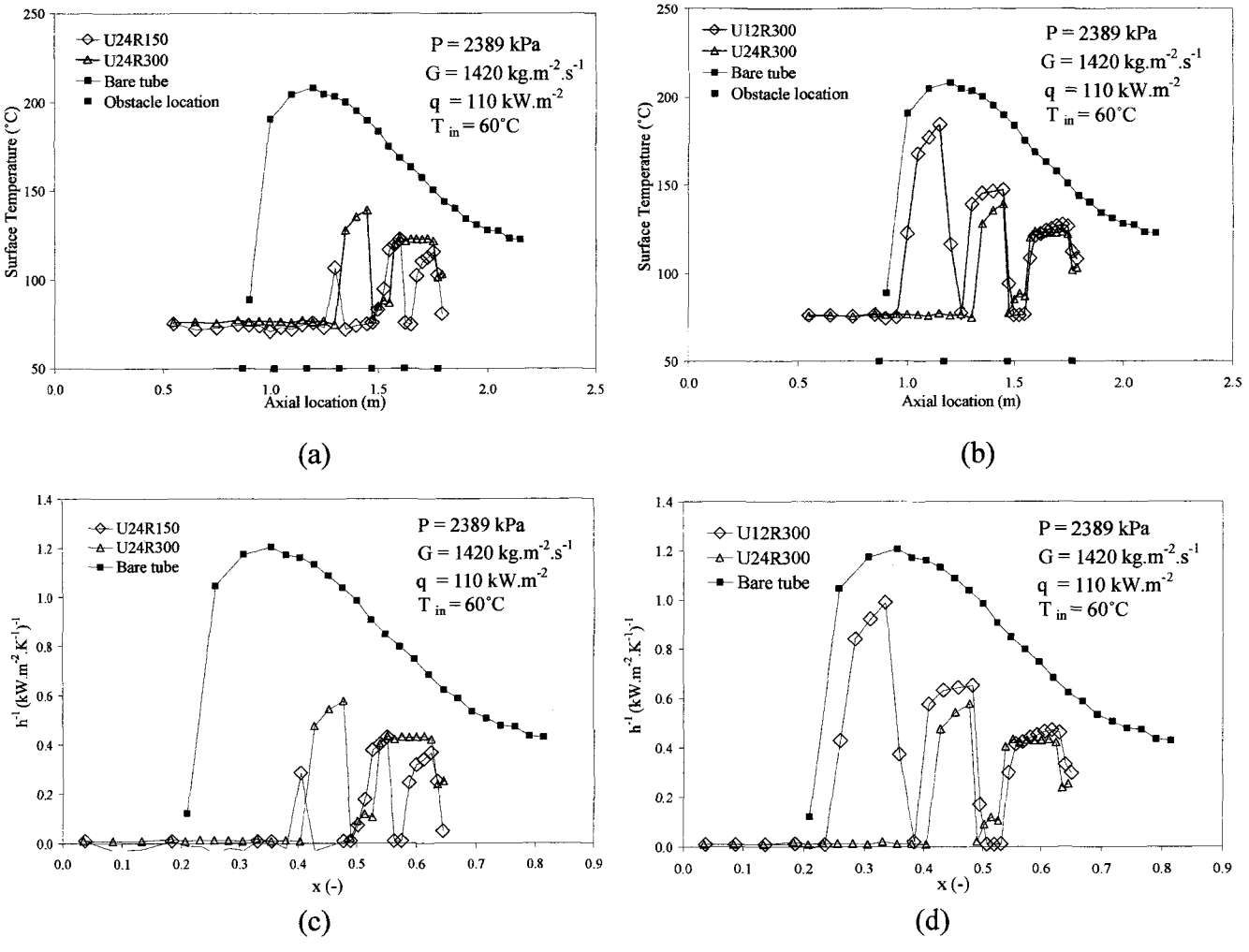

Figure 5.4 Flow obstacle effects on PDO heat transfer for uniform AFD tube; pitch effect (LHS Figures: (a) and (c)) and flow-blockage ratio effect (RHS: (b) and (d)).

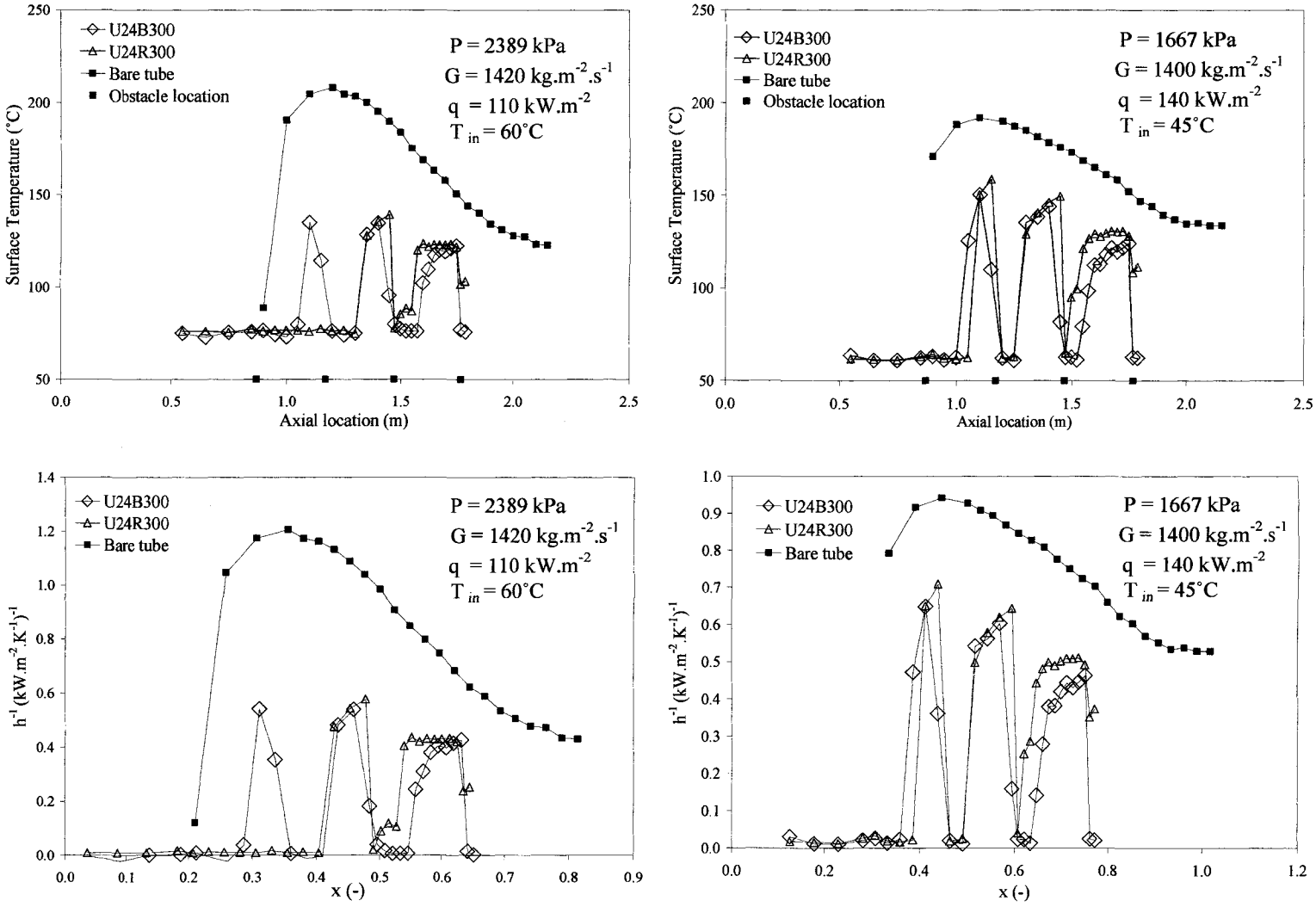

Figure 5.5 Effect of obstacle shape on PDO heat transfer for uniform AFD tube; at high P (LHS Figures) and at low P (RHS).

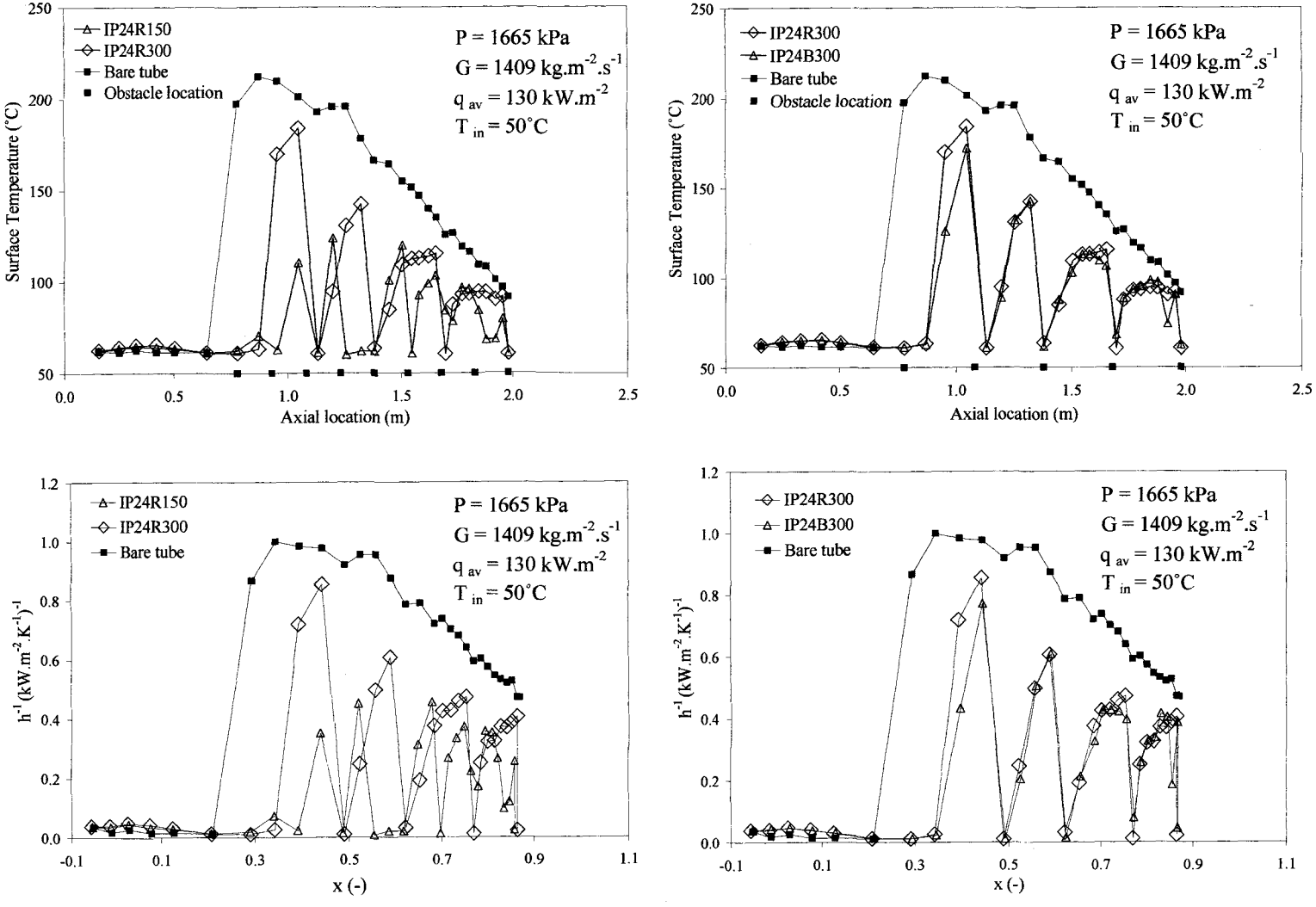

Figure 5.6 Effect of obstacle pitch (LHS) and shape (RHS) on PDO heat transfer for inlet-peak AFD tube.

5.2 Comparison of Experimental Results with Available Freon Data

As discussed in Chapter 2, experimental investigations of the obstacle effect on PDO heat-transfer in tubes are very scarce, while experiments investigating the combined AFD and obstacle effect in DFFB are not available.

5.2.1 Effect of Quality and Axial Location

Figure 5.7 presents the effect of variation of local quality at the obstacle location (x_{ob} = 0.14, 0.24 and 0.34) on the PDO heat-transfer coefficient ratio expressed by h_{bare}/h_{ob} vs. *L/D*. Note that h_{bare}/h_{ob} is equivalent to $(T_w-T_{sat})_{ob}/(T_w-T_{sat})_{bare}$. For the uniform-AFD tube equipped with 5-streamlined obstacles, the lowest local quality exhibited the higher heat-transfer enhancement ratio (h_{ob}/h_{bare}). Figure 5.7 also shows that the longest pre-dryout region occurred at $x_{ob} = 0.14$.

A similar effect was also found for the inlet-peak AFD tube (Figure 5.8). The quality at the flow obstruction was 0.28, 0.45, 0.61 and 0.75. With decreasing quality, h_{ob}/h_{bare} increased, except at x_{ob} = 0.28 and *L/D* = 32 or 49, the curve of h_{bare}/h_{ob} at x_{ob} = 0.28 shows a higher heat-transfer coefficient ratio (h_{bare}/h_{ob}) or lower heat-transfer enhancement ratio (h_{ob}/h_{bare}), since the bare tube HTC was obtained during developing-film boiling.

Peng et al. (2003) observed a similar effect of thermodynamic quality on PDO heat-transfer coefficient ratio (Figure 5.9). Details regarding their experimental investigation were presented in Chapter 2.

Zhang (1997) and Leung et al. (2005) also performed an experimental study on the effect of obstacles on PDO heat transfer. They observed that rewetting occurred just downstream of the obstacles and covered a narrow region, beyond which the dry zone was re-established. Figure 5.10 shows the effect of ring-shaped obstacle on wall

temperature distributions and the effect of axial location on surface-temperatures for developing film-boiling. The obstacle was initially located upstream from the thermocouple region at $x_{ob} = 0.11$. As the obstacle was moved from $z = 0.73$ m to $z = 0.89$ m, the rewetting location also moved downstream (it always occurred just downstream from the obstacles).

5.2.2 Effect of *L/D*

Figure 5.11 displays the well known effect of *L/D* on PDO heat transfer. The temperature profile of the obstacle-equipped tube increases as the *L/D* increases until the fully developed film-boiling region is reached. Generally, in the fully developed region, surface temperature decreases with increasing *L/D*.

5.2.3 Effect of Obstacle Shape

Leung et al. (2005) investigated the effect of obstacle shape (cube, hexagon and ring) on PDO heat transfer (Figure 5.12). Although the comparison was based on slightly different values of heat flux for the three obstacle shapes, they found that the establishment of PDO region downstream from the ring-shaped obstacle starts at a much lower quality than for the cube and hexagon, and the surface temperature for the test section with ring-shaped obstacle is higher than those of the other obstacles, while the surface temperature for the test section with the cube-shaped is the lowest. They attributed the differences in the temperature distributions to (i) low CHF enhancement-ratio ($\frac{CHF_{ob}}{CHF_0}$) for the ring-shaped obstacle (Pioro et al., 2000), and (ii) the higher turbulence level generated downstream from the cube-shaped obstacle.

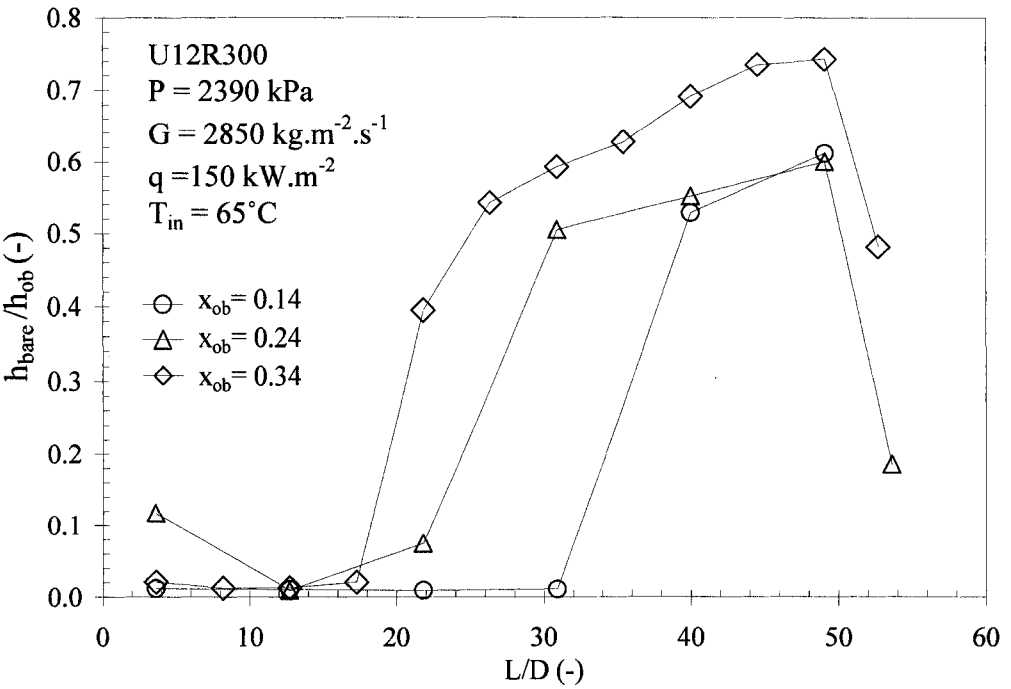

Figure 5.7 Quality effect on heat-transfer coefficient ratio (h_{bare}/h_{ob}), uniform AFD test section at high-pressure and high-mass flux.

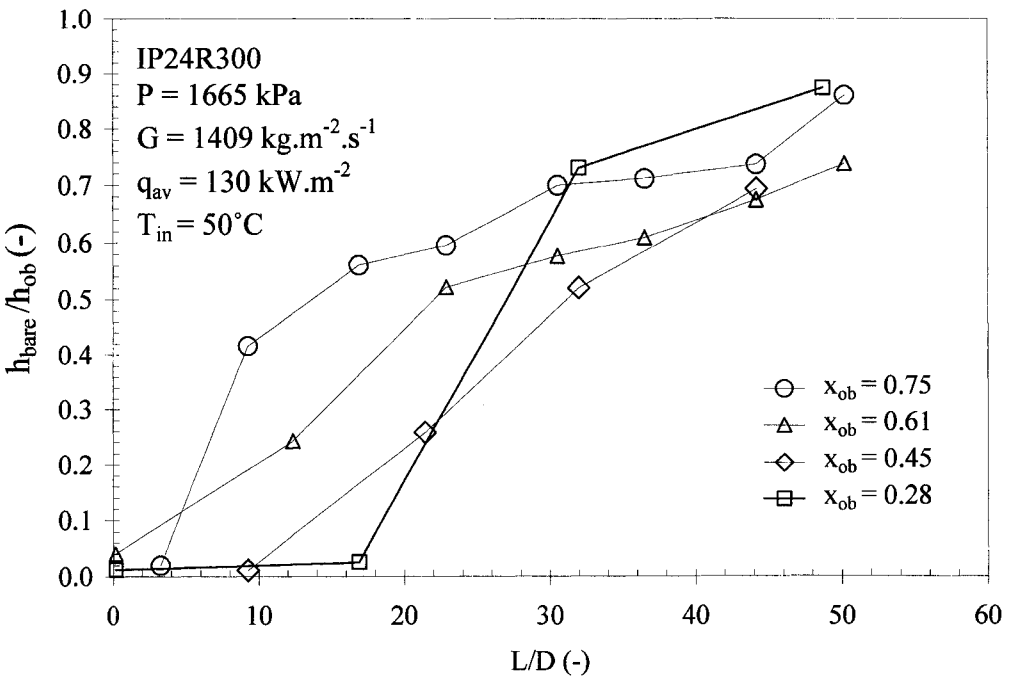

Figure 5.8 Quality effect on heat-transfer coefficient ratio (h_{bare}/h_{ob}), inlet-peak AFD test section at low-pressure and low-mass flux.

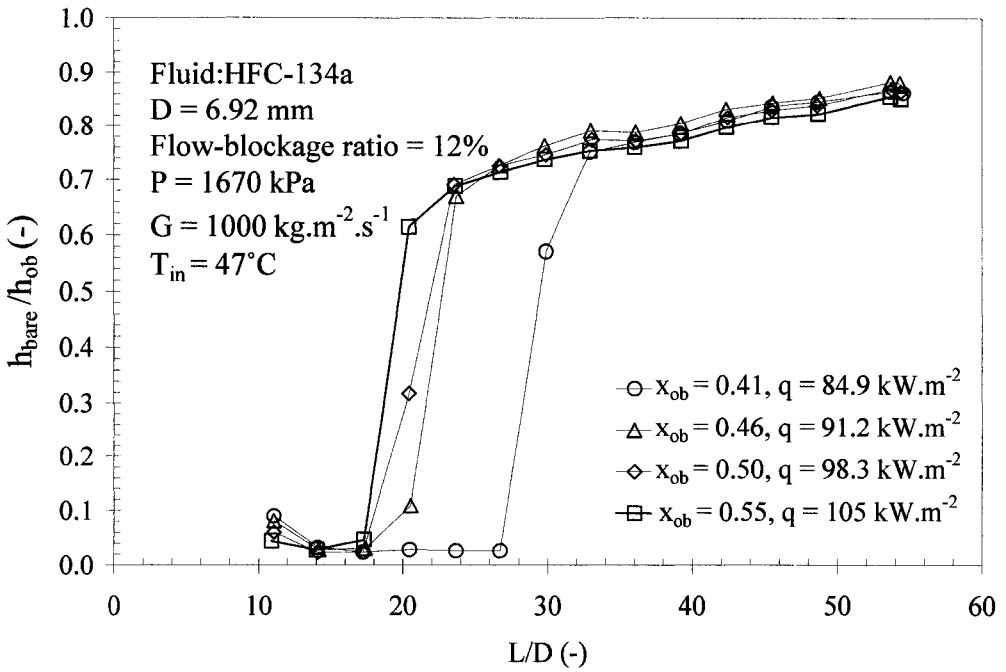

Figure 5.9 Quality effect on heat-transfer coefficient ratio (h_{bare}/h_{ob}), uniform AFD test section, reproduced from (Peng et al., 2003).

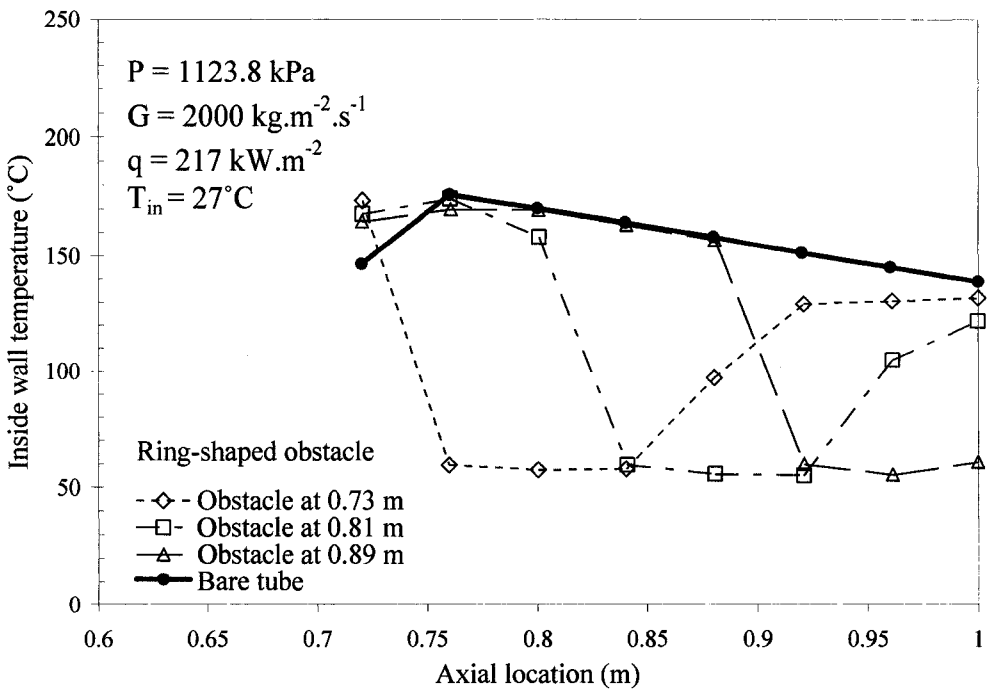

Figure 5.10 Wall temperature distributions for ring-shaped obstacle at different locations in the thermocouple region, reproduced from (Leung et al., 2005).

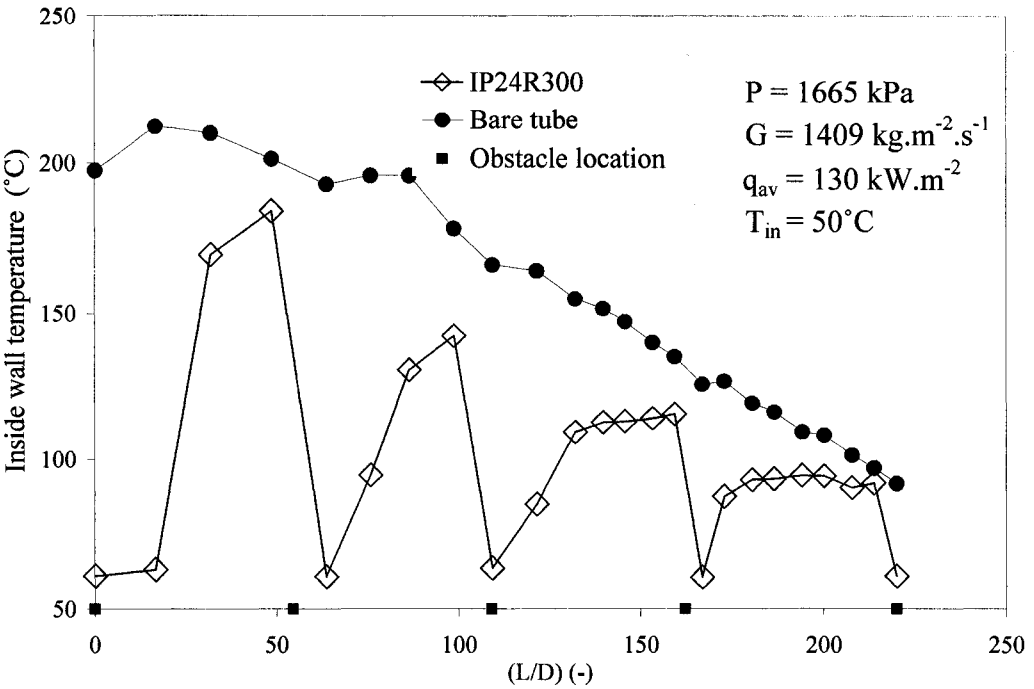

Figure 5.11 Typical *L/D* effect on surface temperature vs. *L/D* from first upstream obstacle, inlet-peak AFD test section at low-pressure and low-mass flux.

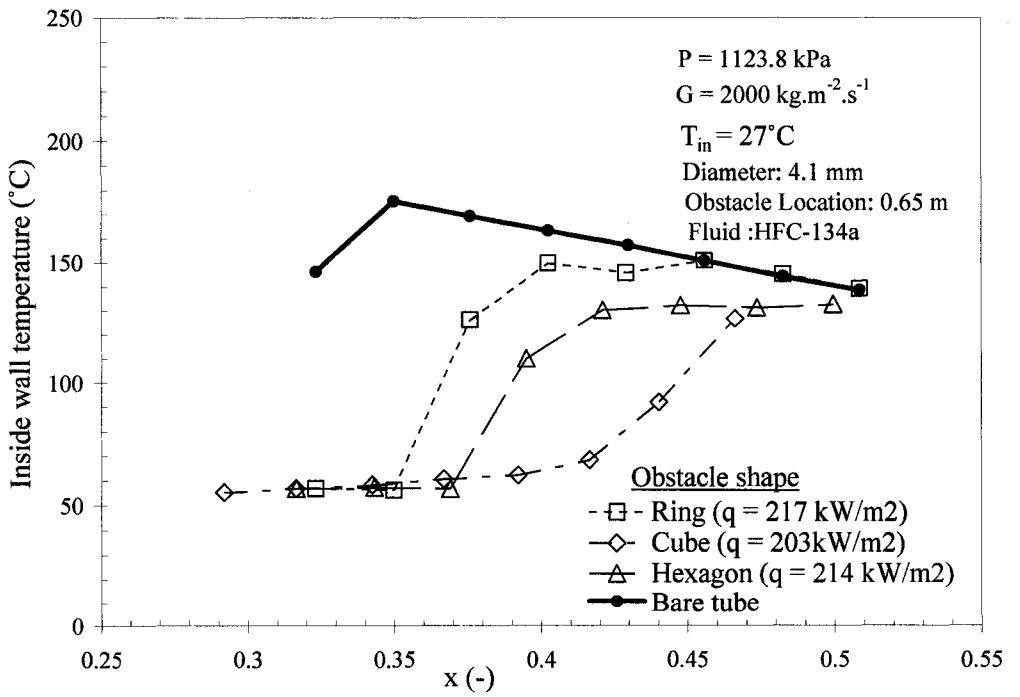

Figure 5.12 Comparison of surface-temperature distributions for different-shaped obstacles located upstream thermocouple region, reproduced from (Leung et al., 2005).

5.3 Mechanistic Description of Flow Obstacle Effect and AFD Effect

Following the discussion in Section *2.9.3.2*: Incropera et al. (2005), considering boundary layer approximations, described Reynolds analogy of the conservation equations (applied to boundary layer) in single-phase, (e.g., typical flow over a flat plate). For specified values of Prandtl number and pressure gradient, it is well known that an analogy exists between heat transfer and turbulent momentum (friction): the conservation equations have a similar form (i.e., similar boundary conditions and similar normalized dimensionless parameters). In the following equations, the dimensionless independent variables are indexed with "*". Because of the above Reynolds analogy, the velocity distribution (momentum equation) and the temperature distribution (energy equation) must have the same functional form of the solution, in other words,

$$C_f = \frac{\tau_s}{\rho V^2/2} = \left(\frac{2}{\mathrm{Re}}\right)\frac{\partial u^*}{\partial y^*}\Big|_{y^*=0}$$

$$Nu \equiv \frac{hl}{k_f} = +\frac{\partial T^*}{\partial y^*}\Big|_{y^*=0}$$

$$\Rightarrow Nu = \mathrm{Re}\frac{C_f}{2}$$

where C_f is the coefficient of friction (or the fanning factor), τ_s is the surface shear stress, V is the bulk velocity, u is the boundary layer axial velocity, l is the characteristic length, $u^* = u/V, y^* = y/l$ *and* $T^* = \frac{T - T_w}{T_\infty - T_w}$, where $T_\infty = T_{bulk}$.

Colburn-Chilton (1933 and 1934) showed that the above prescribed analogy is applicable for fully developed turbulent internal flows, and over a range of Pr number (confirmed experimentally); $0.7 < \mathrm{Pr} < 160$. The Colburn J factor is

$$\frac{C_f}{2} = St\,\mathrm{Pr}^{2/3} \equiv J$$

where St is the Stanton number $= \frac{Nu}{\mathrm{Re\,Pr}}$.

The analogy between momentum and heat transfer is assumed valid[2] for dispersed flow film-boiling, because in film boiling, the primary heat transfer mechanism is the convective component from wall to the continuous vapour phase, which includes very small droplets; therefore the two-phase DFFB region may be considered as nearly homogenous, and the heat transfer mechanisms are thus similar to the convective heat transfer from the wall to the single-phase fluid.

The physical properties variation due to temperature gradient can be accounted for (Kreith, 1973) by considering the average film temperature of the fluid, $T_{film} = 0.5\times(T_w + T_{bulk})$.

Rehme (1973) evaluated the pressure drop due to grid spacers of rod bundles by correlating the pressure-loss coefficient (K_{ob}) as a function of flow-blockage ratio, $K_{ob} = C_v \varepsilon^2$, the coefficient C_v has a weak dependence on Re. Yao et al. (1982) assumed that the overall heat-transfer enhancement due to spacers has the same form as the pressure drop increase due to the grid spacer, Eqn. (2.13).

In the entry region of a pipe flow, the axial velocity as well as the bulk temperature depend on axial and radial location. The dimensionless Graetz number, $Gz = \frac{D}{L}\mathrm{Re}\,\mathrm{Pr}$, characterizes the effect of entry region on heat transfer ($Nu_{entry} = f(Gz)$). The distribution of Nu number downstream from entrance of a pipe flow decreases gradually with increasing Gz^{-1} up to the fully developed region. Downstream from the obstacles, the Nusselt number ratio (Nusselt number for the tube with obstacles to the bare tube Nusselt number at similar flow conditions (Nu/Nu_0)) also decreases gradually with an increase in the inverse of Gz (Hassan and Rehme, 1981) or with an increase in L/D (Yao et al., 1982). This exponential decay in the Nusselt number ratio (Nu/Nu_0) is similar to the entry effect on heat transfer.

.

[2] Strictly speaking, the modified Reynolds analogy was derived for fully developed turbulent flows

A similar mechanism is expected to take place during film-boiling heat transfer. Obstacles influence film-boiling heat transfer significantly, and with increasing flow-blockage ratio, film-boiling heat transfer increases. The presence of obstacle in the DFFB region suppresses dryout occurrence and at locations downstream from the dryout front, developing film-boiling starts (see Section 2.2 and footnotes of Table 5.1). The maximum heat-transfer enhancement effect of the obstacle occurs at the trailing edge of an obstacle (L/D = 0). The obstacle effects on film boiling heat transfer decays with distance (L/D) downstream from the obstacle – which is similar to the entrance effect.

This decreasing obstacle effect can be expressed as a decaying film boiling heat-transfer enhancement (Nu/Nu_0) and is due to the following three effects that decrease with the increase in L/D from the obstacle: (i) impingement of droplets on the heated surface and/or rewetting, (ii) the droplet break-up effect, and (iii) the increased turbulence. This decay function for film-boiling heat-transfer enhancement (Nu/Nu_0) downstream from an obstacle is similar to that for single-phase heat transfer enhancement for the same obstacle. The differences (Yao et al., 1982) are attributed to the presence of droplets in the DFFB and their interaction with the obstacle causing rewetting and/or providing additional turbulence and additional heat-transfer area with the continuous vapour phase.

The length of the enhanced heat-transfer region downstream from an obstacle depends on the flow conditions and the flow blockage. When the film boiling becomes fully developed (i.e., surface temperature is no longer affected by the upstream conditions, which occurs when the vapour film reaches fully developed conditions and is no longer disturbed by the obstacle, or in other words the vapour superheat becomes fully established), then the obstacle effect disappears.

Although the AFD effect on film-boiling temperatures in bare tubes (mainly caused by the variations of heat flux along the test section) can be significant (El Nakla et al., 2006; Zahlan et al., 2008), particularly for developing film boiling, the presence of obstacle in the test section diminishes the AFD effect; since the additional turbulence generated by obstacle tends to suppress any effects originating upstream from the obstacle including

the AFD. A similar finding was reported by Yang et al. (2005) for the AFD effect on CHF in the presence of obstacles. Obstacles suppress dryout occurrence, cause rewetting and/or cause the film boiling to be "under-development". Hence, obstacles decrease the wall superheat, and reduce the variation in PDO HTC for different AFDs.

5.4 Single-Phase Pressure-Loss Coefficient

As was shown in the literature review, the single-phase obstacle pressure-loss coefficient, K_{ob} can be an important parameter in predicting the heat transfer enhancement. K_{ob} has been determined experimentally (Tanase et al., 2008) for 5 and 9 obstacles. Table 5.3 shows the measured variation of K_{ob} for different configurations and mass velocities. The experiments and repeat tests do not show a significant dependence of obstacle pressure drop on obstacle pitch. The dependence of K_{ob} on Re is weak: K_{ob} decreases slightly with increasing Re. The measurements are generally up to 50% higher than the predicted values of K_{ob} by Idel'chik (1994) and Leung et al. (2005).

A correlation was developed from the single-phase measurements for rounded obstacles (Figure 5.13). The correlation is expressed as:

$$K_{ob} = E_1 \varepsilon \mathrm{Re}^{-E_2} \tag{5.1}$$

where $E_1 = 2.835$, $E_2 = 0.07$.

Figure 5.13 shows a comparison between predicted single-phase-pressure loss coefficient for streamlined obstacles as a function of Re and flow-blockage ratio, and experimental values, this figure shows a weak dependence of K_{ob} on Re, so with increasing Re, K_{ob} decreases slightly.

Generally, the correlations for PDO heat-transfer enhancement express the spacer or obstacle effect as a function of flow-blockage ratio or single-phase pressure-loss

coefficient K_{ob}, assuming that the analogy between pressure drop (momentum transfer) and heat transfer applies. This works reasonably well for rounded obstacles, but for blunt obstacles, it is found that K_{ob} does not represent the shape effect on PDO heat-transfer enhancement. Tanase (2008), showed also a slight effect of shape on single-phase heat-transfer enhancement (Figures 5.14 and 5.15), expressed as $((h/h_{bare}) - 1)$. The average heat-transfer enhancement ratio between blunt and round obstacles having the same flow-blockage ratio calculated as average $(Nu/Nu_0 - 1)_{blunt}$/average $(Nu/Nu_0 - 1)_{round}$ at G = 1000 $kg.m^{-2}.s^{-1}$ was 1.195. Similarly for PDO heat transfer, the ratio was found 1.31 at G = 1420 $kg.m^{-2}.s^{-1}$. The obstacle shape strongly affects K_{ob}; for blunt obstacles (5 obstacles in series having 24% flow-blockage ratio and 300-mm pitch at low-mass fluxes), the measured K_{ob} is 0.84, while the experimental K_{ob} for 5 streamlined obstacles with similar flow-blockage ratio and pitch is 0.34.

Table 5.3 Single-phase-pressure-loss coefficient K_{ob} for different configurations of obstacles.

Obstacle shape and flow-blockage ratio	No. of obstacles	Pitch, (mm)	Mass flux, G ($kg.m^{-2}s^{-1}$)			
			1410	2110	2860	3576
			Single-phase pressure-loss coefficient, K_{ob} (-)			
Blunt, 24%	5	300	0.84	0.84	0.83	0.81
	9	150	0.81	0.77	0.75	0.72
Round, 24%	5	300	0.34	0.33	0.32	0.31
	9	150	0.36	0.34	0.34	0.34
Round, 12%	5	300	0.14	0.14	0.15	0.16
	9	150	0.16	0.14	0.15	0.15

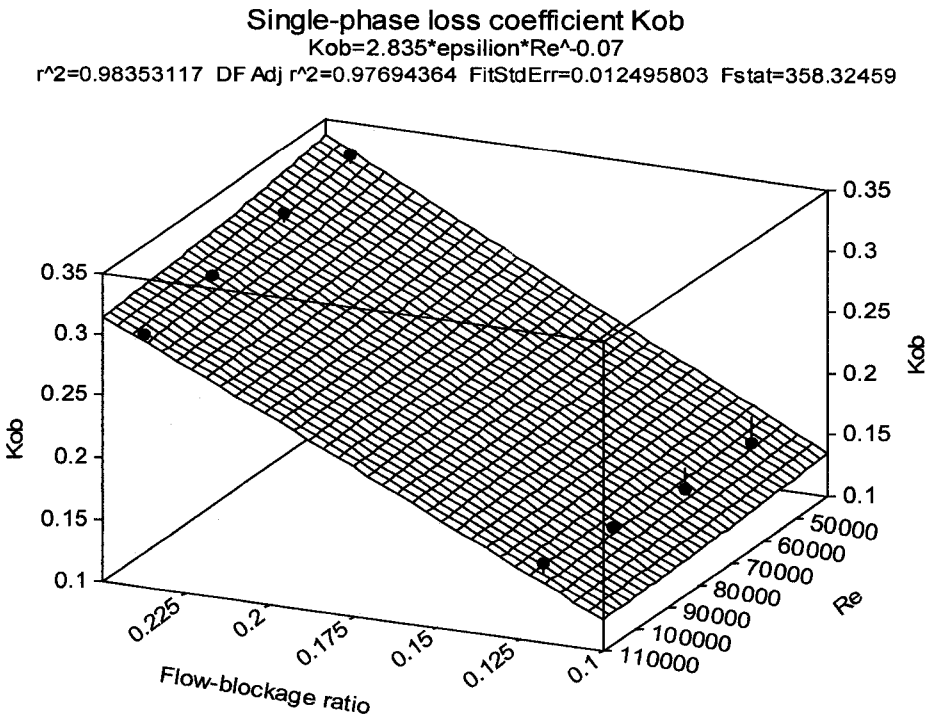

Figure 5.13 Comparison between measured single-phase pressure-loss coefficients with predictions of Equation (5.1) for round obstacles.

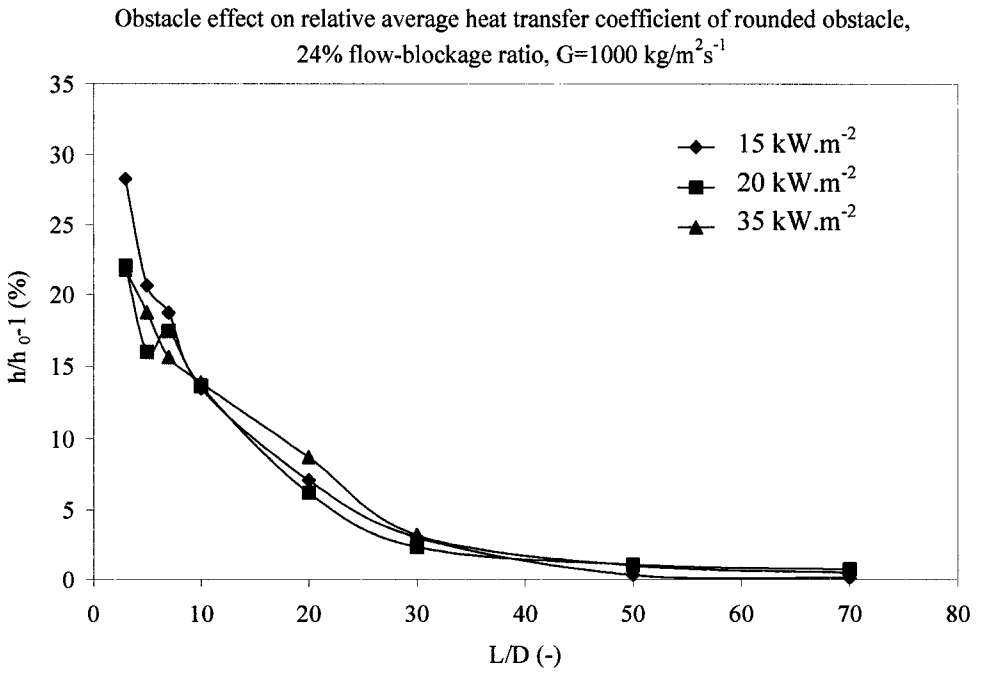

Figure 5.14 Single-phase heat-transfer enhancement for uniform test section and rounded obstacles with ε = 24%, reproduced from Tanase (2008).

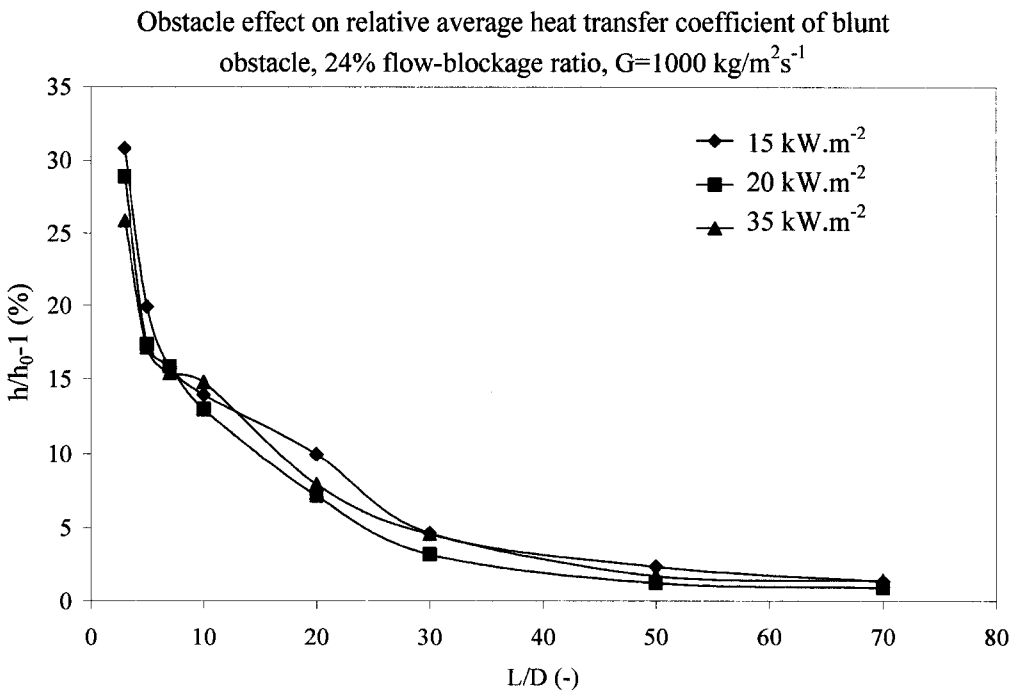

Figure 5.15 Single-phase heat-transfer enhancement for uniform test section and blunt obstacles with ε = 24%, reproduced from Tanase (2008).

5.5 Application of Prediction Methods to Data

This section discusses the comparison of the predicted and measured PDO heat-transfer enhancements (Nu/Nu_0) in obstacle-equipped test sections. The PDO correlation of Yao et al. (1982) and Leung et al. (2005) were applied to selected experimental data obtained in the developing FB region. They do not predict the effect of non-uniform AFD on Nu/Nu_0. Kim and Korol'kov (1991) correlations could not be applied due to the unavailability of the coefficient K_e. The correlations are described below.

5.5.1 Prediction Method of Yao et al. (1982)

The Yao et al. correlation is based on single- phase flow data. The correlation is:

$$(\frac{Nu}{Nu_0})_{sp} = 1 + 5.55\varepsilon^2 e^{-0.13(L/D)} \tag{2.15}$$

Yao et al. assumed that Eqn. (2.15) can also be applied to PDO heat transfer conditions. Figure 5.16 and 5.17 compare the predictions of the Yao et al. correlation and the measured heat-transfer enhancement (Nu/Nu_0), for a uniform AFD test section having 4 streamlined obstacles at a 300-mm pitch with 12% or 24% flow-blockage ratio, respectively. These figures show that the Yao et al. correlation underpredicts the measured Nu/Nu_0 significantly. The reason may be because the correlation does not properly predict the much stronger effect of spacers on PDO heat-transfer enhancement (because of the impact of the flow obstructions on the droplet trajectories and therefore enhanced droplet-wall interaction) compared with the weaker spacer effect on single-phase heat transfer.

5.5.2 Prediction Method of Kim and Korol'kov (1991)

Kim and Korol'kov's heat transfer enhancement equation,

$$\frac{Nu}{Nu_0} = 1 + K_e\varepsilon^2 e^{\left(-0.13\frac{L}{D_{hy}}\right)} \tag{2.30}$$

is similar to that of Yao et al.'s Eqn. (2.15), except for that, their constant (5.55) was replaced by the parameter K_e.

$$K_e = A(x - x_{thr})(1 - x) \tag{2.31}$$

where $x_{thr} = x_{do}$.

These equations are based on water data and its application to our Freon results is questionable because of the following reasons:

(i) Equation (2.31) requires a new value of A for each obstacle in a multi-obstacle tube. However, the A value is not constant for a given spacer, the location of spacer for determining the empirical factor, A, is not specified, since A varies (data analysis) from one obstacle cross section to another depending on the quality (location). They found that K_e can be 10 to 100 times greater than 5.55, but at some obstacle locations K_e is close to the 5.55 value for fully developed film boiling.

(ii) x_{thr} is from Galchenko, $x_{thr} = 1 - 0.86\exp(\frac{-19}{\psi})$, where $\psi = G(\frac{D_{hy}}{\sigma\rho_f})^{0.5}$

This correlation does not consider the effect of obstacles on the CHF location, and is not corrected for obstacle-equipped test sections. An experimental x_{do} can be used in this analysis, instead.

(iii) Equation (2.30) is superseded by Leung et al. (2005), i.e., Equation (2.34).

Because of the above concerns this equation could not be applied directly to our Freon data. However the final form of the proposed equation in Chapter 6 has some similarity to this equation as will be shown later.

5.5.3 Prediction Method of Leung et al. (2005)

Leung et al. (2005) presented the obstacle-enhanced film boiling correlation:

$$Nu^* = \frac{Nu}{Nu_0} = 1 + (0.47 + 0.48\,\text{lx}_e(1 - x_e).^{0.105}) \times K_{ob}\exp(-0.13\frac{L}{D_{hy}}) \qquad (2.34)$$

Leung et al. (2005) included in their model the effect of critical heat flux and the developing film-boiling effect on PDO heat transfer. The developing film-boiling effect is predicted by:

$$\frac{Nu_{dev}}{Nu_{fd}} = 1 + \left(\frac{Nu_{nb}}{Nu_{fd}}\frac{k_f}{k_g} - 1\right)\exp\left[-10.83\left(\frac{q}{CHF_{ob}} - 1\right)^{0.37} \psi_{tp}^{-0.08}\left(\frac{\rho_f}{\rho_g}\right)^{0.28}\right] \tag{2.35}$$

This correlation could not be applied to a wide range of data, since the correlation for predicting CHF_{ob} did not adequately represent the observed CHF enhancement. The correlations of Guo et al. (2001) were applied to predict x_{do} and length in dryout with multiple obstacles. The difficulties in obtaining adequate predictions for dryout lengths are illustrated in the figures of Section 6.5 and will be discussed later. To resolve the CHF_{ob} prediction concern, the approach taken in applying Leung's Equation (i.e., Equation (2.35)) is to extract CHF_{ob} values from selected experiments. Section *5.5.3.1* shows the methodology performed to extract CHF_{ob} from experimental data. However not all CHF_{ob} values of the two runs (see Section *5.5.3.1*) could be extracted, due to limited range of CHF_{ob} qualities in the experimental data.

Correlations (2.34) and (2.35) were applied to the selected data (Section 5.1). The results are shown in Figures 5.16–5.19. Figure 5.16 and 5.17 show a comparison between measured and predicted enhancement ratios expressed as Nu/Nu_0 for uniform AFD tube for the test section equipped with 4 streamlined obstacles of 12% or 24% flow-blockage ratio at the 300-mm pitch. The results show that the predictions of Leung et al. (2005) are clearly below the measured Nu/Nu_0. This correlation is sensitive to the value of CHF_{ob}.

Figures 5.18 and 5.19 are similar to Figures 5.16 and 5.17, except that a correction factor was applied to the Nu_{nb} because of the large difference between measured and predicted nucleate boiling Nusselt number (Chen 1963). This improved the prediction somewhat as will be discussed in Section 5.5.4.

The wall temperature predictions corresponding to these figures will be shown in Section 6.6.

Looking at Equations (2.15), (2.30) and (2.34), it can be seen that all these equations are identical, except for the function $K = (Nu/Nu_0 - 1)/(\varepsilon^2 \times \exp(-0.13 \times L/D))$. In Eqn.

(2.15), Yao et al. (1982) considered a constant value of K = 5.55 for single-phase or DFFB; this results in similar obstacle effect on single-phase and PDO heat-transfer. In addition, for different obstacle locations in the film boiling tests, the PDO heat-transfer enhancement is the same, because the effect of quality and droplets are not considered in the Eqn. (2.15) – this explains the significant underpredictions of the experimental data shown in Figures 5.16 and 5.17. In Kim and Korol'kov's Eqn. (2.30), $K = K_e$, the effect of droplets and quality are taken into account by the parameter x and x_{thr}, but x_{thr} does not consider the effect of obstacle on CHF. In addition Eqn. (2.30) does not provide any predictions at x = 0 or 1. In Eqn. (2.34), $K = (K_{ob}/\varepsilon^2)\times f(x)$, and $K_{ob} = f(\varepsilon^2)$. In Leung et al's model, K_{ob} takes into account the effect of quality, obstacle shape and obstacle location in a cross section; in addition, the developing film boiling effect and CHF enhancement are also considered.

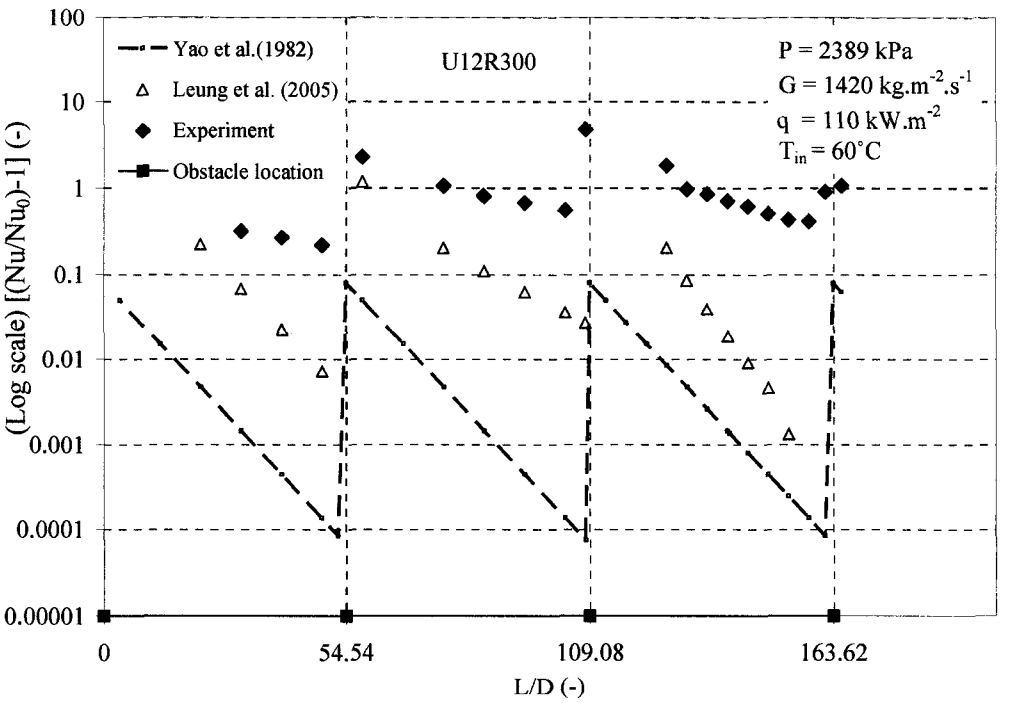

Figure 5.16 Comparison between predicted and experimental heat-transfer enhancements for U12R300.

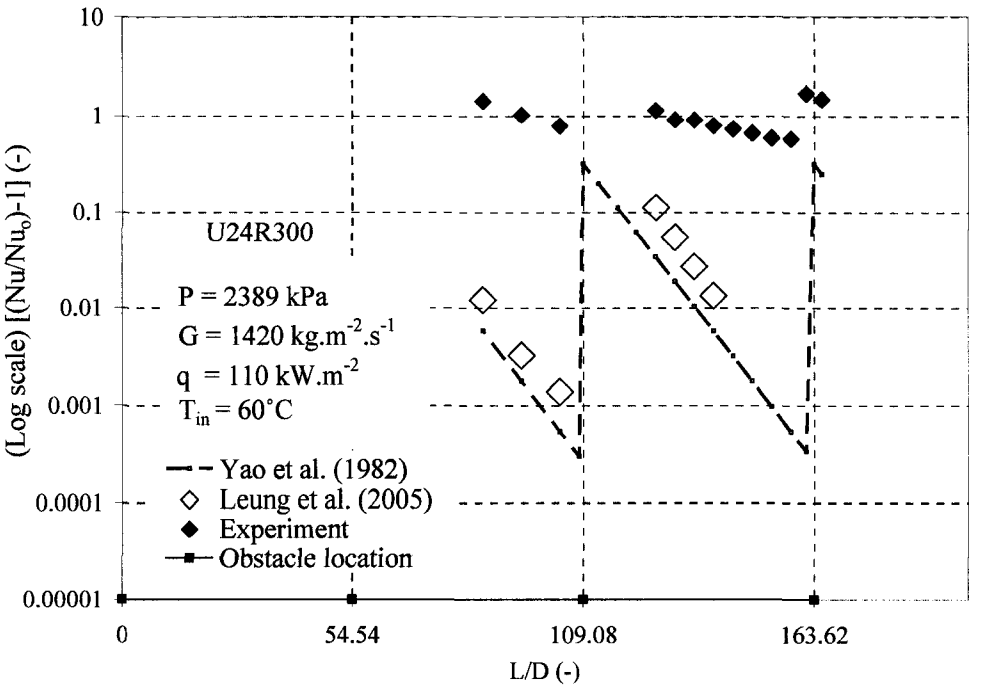

Figure 5.17 Comparison between predicted and experimental heat-transfer enhancements for U24R300.

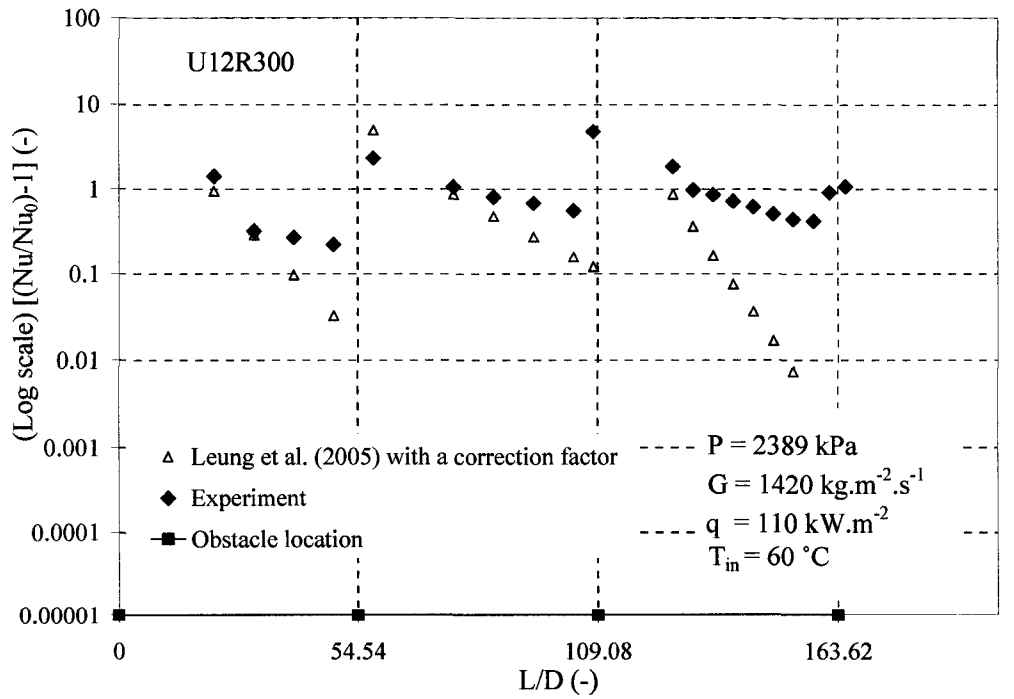

Figure 5.18 Comparison between predicted (Leung et al. with a correction factor) and experimental heat-transfer enhancements for U12R300.

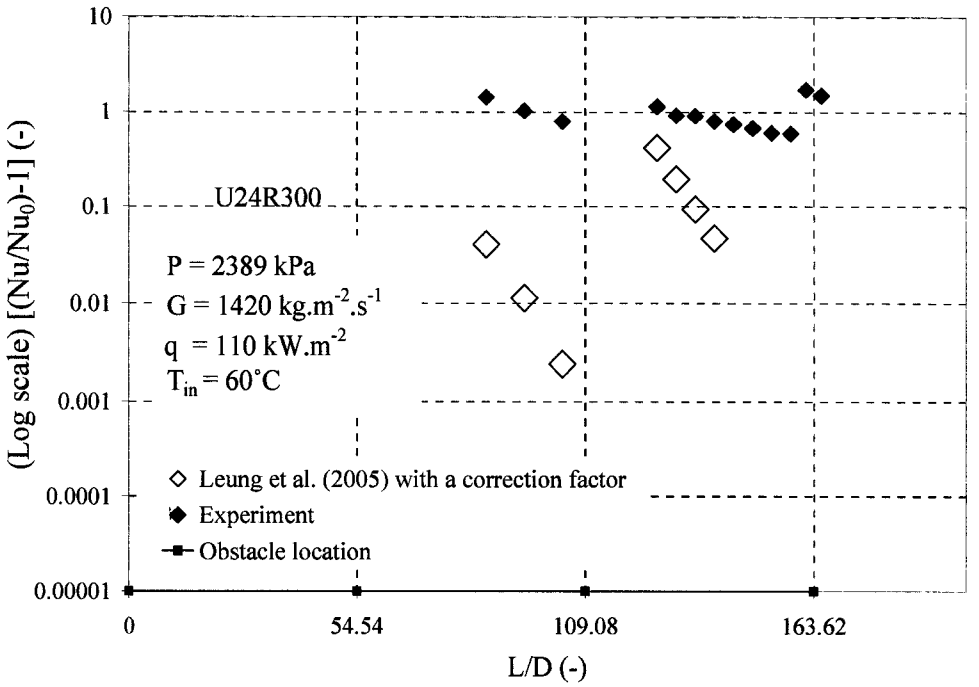

Figure 5.19 Comparison between predicted (Leung et al. with a correction factor) and experimental heat-transfer enhancements for U24R300.

5.5.3.1 Extraction of CHF values from obstacle-equipped data

Two sets of data obtained in obstacle-equipped test sections (uniform tube with streamlined obstacles having either 12 or 24% flow-blockage ratio) were selected. The test pressure and mass flux were: P = 2389 kPa and G = 1410 $kg.m^{-2}s^{-1}$.

The experimental data (23 runs) of the U12R300 configuration have an inlet temperature range of 55 to 70°C and a heat flux range of 70 to 130 $kW.m^{-2}$. For the U24R300 configuration, the data (18 runs) have the same range of inlet temperature and heat flux. The dryout locations of interest are within the obstacle region.

Data were tabulated as CHF_{ob} = f(x, L/D), and grouped by quality, x (a narrow range of quality, i.e. : $x \pm 0.02$ was chosen). For each obstacle region of interest, the extracted CHF_{ob} data were correlated by a linear curve fit (Figure 5.20 and 5.21). A few points that did not have the required range of L/D or had a very narrow ranges of x were excluded

from the curve fitting. Fitting functions were applied to all points to find CHF_{ob} values at locations of interest; the predicted values were then compared to the extracted values in order to verify the accuracy of the predictions (Table 5.4 and 5.5). This methodology provided a reasonably accurate prediction of CHF_{ob} (CHF_{ob} vs. quality) for uniform test section configurations U12R300 and U24R300. This can be seen in Figure 5.22 and 5.23.

Table 5.4 Comparison between measured CHF_{ob} and curve fit values, U12R300.

Point no.	x (-)	L/D (-)	Measured CHF_{ob} ($kW.m^{-2}$)	CHF_{ob} predicted from curve fit ($kW.m^{-2}$)
Obstacle no.3				
1*	0.618	44.54	57.72	52.22
2*	0.606	40.00	64.59	59.69
3*	0.594	35.45	64.36	67.23
4	0.581	30.91	74.22	74.70
5	0.569	26.36	86.42	82.23
6	0.557	21.82	82.80	89.71
7	0.544	17.27	100.39	97.18
Obstacle no.2				
8	0.495	53.64	78.77	78.00
9	0.483	49.1	79.95	80.53
10	0.458	40.00	83.99	85.58
11*	0.433	30.91	98.94	90.64
12	0.4085	21.82	98.19	95.69
13	0.359	3.64	104.70	105.8
Obstacle no.1				
14*	0.335	49.09	25.33	63.38
15	0.310	40.00	74.67	73.68
16	0.285	30.91	82.00	83.97
17	0.260	21.82	95.26	94.27

Point no. with italics is a measured CHF_{ob} point with sufficient range of quality and wide range of L/D.

** Point that has insufficient range of L/D or x.*

Table 5.5 Comparison between measured CHF_{ob} and curve fit values, U24R300.

Point no.	x (-)	L/D (-)	Measured CHF_{ob} ($kW.m^{-2}$)	CHF_{ob} predicted from curve fit ($kW.m^{-2}$)
Obstacle no.3				
1*	0.576	30.91	72.54	68.98
2	0.564	26.36	75.60	76.07
3	0.551	21.82	84.14	83.22
4	0.539	17.27	89.88	90.35
Obstacle no.2				
5	0.478	49.09	41.81	41.81
6*	0.453	40.00	26.78	53.63
7	0.427	29.64	65.49	65.49

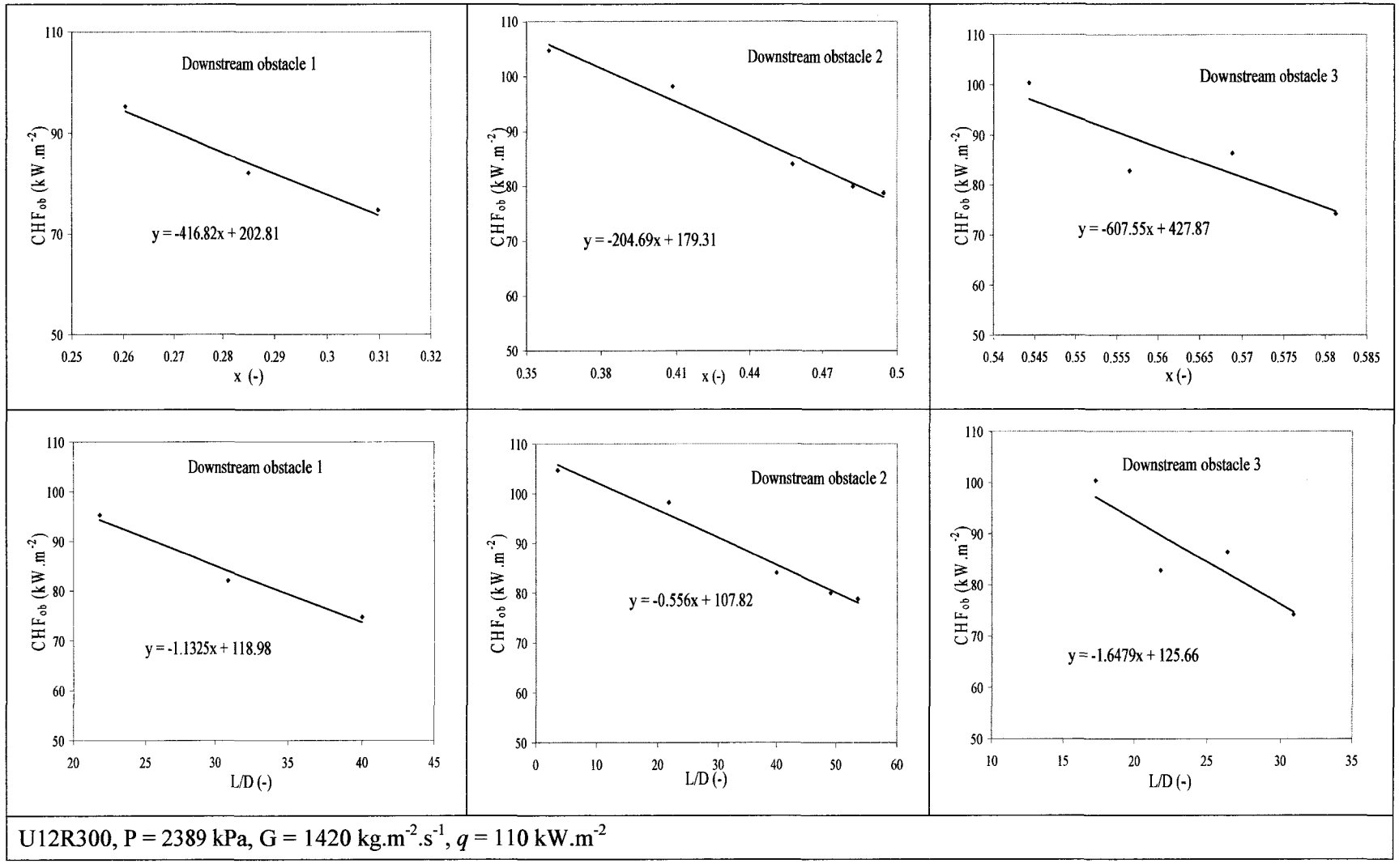

Figure 5.20 Linear curve fit for extracted representative CHF_{ob} values downstream from the 1st, 2nd, and 3rd obstacles.

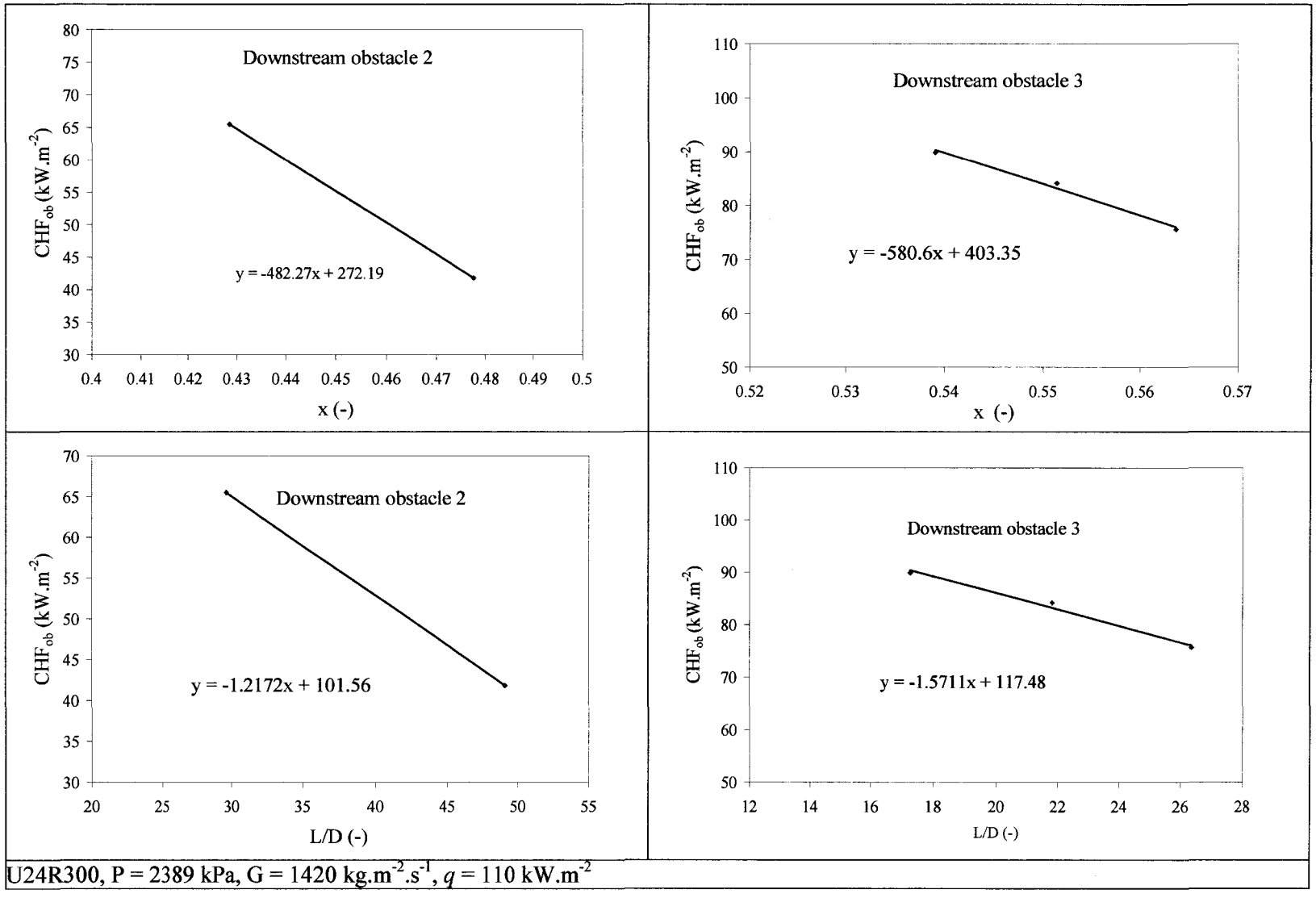

Figure 5.21 Linear curve fit for extracted representative CHF_{ob} values downstream from 2nd and 3rd obstacles.

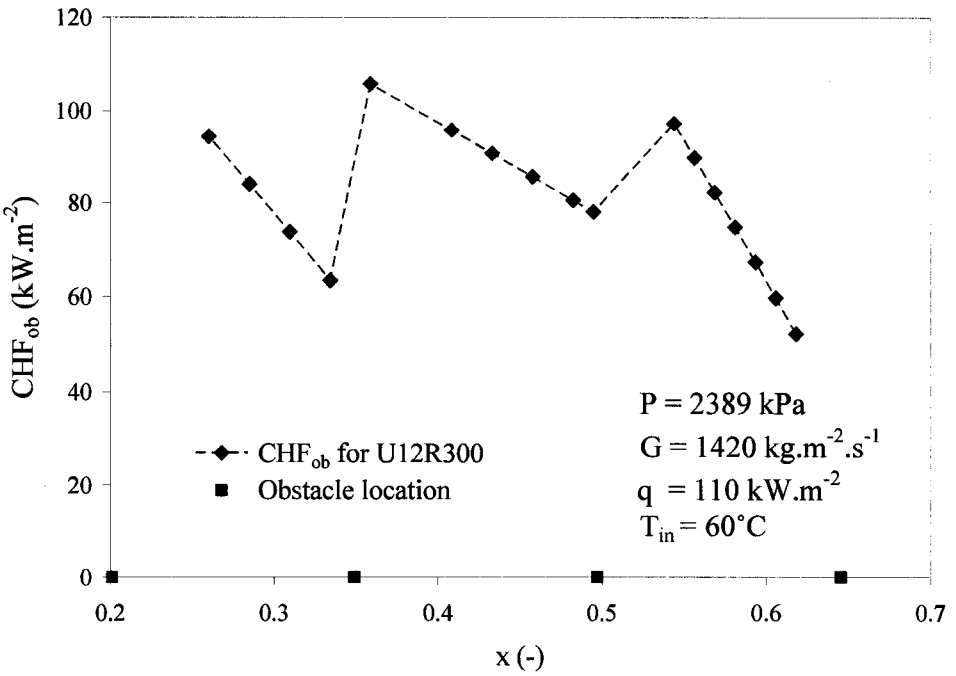

Figure 5.22 Extracted *CHF_{ob}* values vs. quality for U12R300 at high P and Low G.

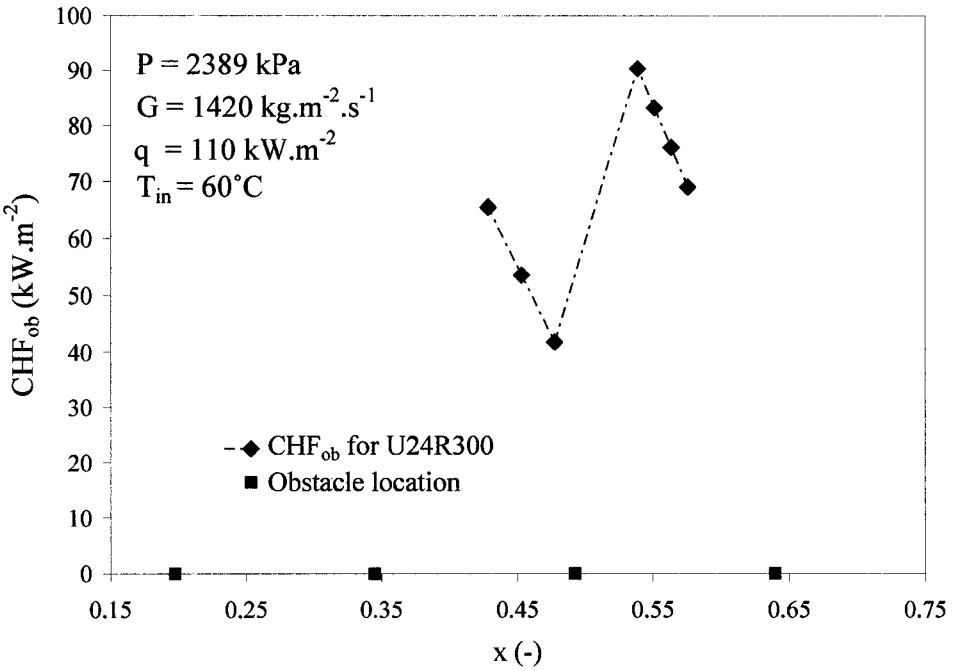

Figure 5.23 Extracted *CHF_{ob}* values vs. quality for U24R300 at high P and Low G.

5.5.4 Discussion

The Yao et al. (1982) Equation (2.15) underpredicts the PDO heat-transfer enhancement significantly and therefore is unacceptable for predicting the axial temperature profile. PDO enhancement includes, in addition to single-phase heat-transfer enhancement mechanisms (correlated by Yao et al. (1982), Eqn.(2.15)), the more significant effect of droplets – thus equations that consider only the single-phase effects or based primarily on single-phase data will result in a significant underprediction of PDO enhancement. As discussed in Section 5.5.3, the parameter K (K = 5.55) in Eqn. (2.15) has a constant value for single-phase and PDO heat transfer, while in Eqn. (2.34), $K = (K_{ob}/\varepsilon^2)\times f(x)$. This provides an additional effect of shape and quality in Leung's et al. (2005) prediction method, which will be discussed next.

The application of Leung et al. correlations to the experimental data, for developing film-boiling (Equations (2.34) and (2.35)), resulted also in an underprediction of the heat-transfer enhancement. One input parameter of Equation (2.35) is the nucleate boiling Nusselt number. Applying Chen correlation (1963) to predict the nucleate boiling heat-transfer coefficient resulted in an underprediction of h_{nb} by more than 75% when compared with the measured heat-transfer coefficient at the dryout point. The calculation of $h_{Chen,nb}$ involves evaluating the pool boiling heat-transfer coefficient and includes an iteration procedure to estimate T_w; the resulting wall superheat from the calculated T_w is approximately 10K compared to an experimental value of around 2K.

After the application of a correction to $h_{Chen,nb}$, to enhance the agreement with the measured values of h_{nb}, the predicted enhancement ratios are still significantly below the measured enhancement ratios. Therefore a new method for predicting the obstacle effect was required. The next Chapter describes the derivation of the new prediction method.

CHAPTER 6

A NEW PREDICTION METHOD FOR THE OBSTACLE EFFECT ON DEVELOPING FILM BOILING

6.1 Introduction

The previous chapter has shown that only a few prediction methods for PDO heat-transfer enhancement downstream from flow obstacles are available. Those that are available were found to have a limited range of application and cannot satisfactorily predict the observed experimental trends of this study. Therefore, an improved prediction method was derived as described in this chapter.

When dryout occurs in the presence of obstacles, two types of heat-transfer enhancement are present: (a) heat-transfer enhancement due to the developing FB heat transfer, as observed downstream of a dryout front in bare test sections ("dryout-enhanced film boiling" or "developing FB effect" denoted by subscript "$_{do}$") and (b) heat transfer downstream of obstacles caused by the obstacle-induced turbulence in the vapor stream containing entrained droplets ("obstacle-enhanced film boiling" denoted by subscript "$_{ob}$").

The measured combined effect of obstacles and developing film boiling on the heat transfer rate is expressed by the ratio $(Nu/Nu_0)_{exp}$.

Section 6.2 describes the derivation of the prediction equations for developing film-boiling effect and their parametric trends, while Section 6.3 discusses the development of the obstacle-enhanced FB equations and their parametric trends. Section 6.4 explains the approaches applied to combine these two effects. In Section 6.5, the prediction of dryout and rewetting location is described. Section 6.6 compares predicted and measured temperature profiles for uniform and non-uniform AFD test sections. Finally in Section

6.7, a comparison of the measured temperature profiles with the predicted profiles from the new prediction method and from other prediction methods is presented and the asymptotic trends of the new equations are discussed.

6.2 Dryout-Enhanced Film Boiling

6.2.1 Introduction

Heat-transfer enhancement due to the dryout-enhanced film boiling is due to several mechanisms including (i) turbulence created by the liquid film dryout, (ii) the development of the vapour film boundary layer (iii) change in intensity of droplet impingement on the heated wall, and (iv) developing vapor superheat. Compared to fully developed film-boiling HTC, the developing film-boiling HTC is much higher.

A good prediction method must have the correct asymptotic and parametric trends (the asymptotic trends of the dryout- and obstacle-enhanced FB will be discussed in Section 6.7). These trends for the dryout-enhanced FB equation will be examined (next subsection) by comparing graphically the predicted trends with the experimental trends based on the test data of the U12R300 configuration at P = 1665 and 2389 kPa and for the configuration U24R300 at the high-pressure.

6.2.2 Development of the Equation for Dryout-Enhanced Film Boiling

The current experimental database and the bare tube data (El Nakla et al., (2006)) suggest that the FB heat-transfer effect downstream from a dryout location decreases with an increase in quality (x) and the ratio of distance from dryout location to diameter $(L/D)_{do}$. Figure 6.1 shows the Nu/Nu_0 variation for developing film-boiling data obtained in a uniform AFD bare tube downstream from the dryout location. The $(Nu/Nu_0)_{do}$ variation is presented as a function of $(L/D)_{do}$ and quality at P = 2389 kPa and G = 1410 $kg.m^{-2}.s^{-1}$.

From this figure it can be seen that $(Nu/Nu_0)_{do}$ decays exponentially with an increase in both $(L/D)_{do}$ and quality. Figure 6.2 presents the best-fit surface and shows a similar decaying trend as was shown by the experimental data in Figure 6.1. Figure 6.3 displays how the equation of the surface-fit in Figure 6.2 was applied to obstacle-data (U12R300) expressed by the measured Nu/Nu_0. The results (Figure 6.3) show a reasonable agreement at low $(L/D)_{do}$ and for qualities between 0.3 and 0.8. Note that the predicted $(Nu/Nu_0)_{do}$ shows also a very weak enhancement effect on $(Nu/Nu_0)_{do}$ for $(L/D)_{do} > 25$ — the predicted enhancement $(Nu/Nu_0)_{do} = 1.015$ at $(L/D)_{do} = 30$ and $x = 1.0$.

Figure 6.3 shows that when the dryout effect is combined with the obstacle effect, then the overall effect on FB heat transfer can be significantly higher than the dryout effect in bare tubes.

Figures 6.4 and 6.5 compare the decaying trends with $(L/D)_{do}$ of the experimental Nu/Nu_0 and the predicted dryout heat-transfer enhancement expressed as $(Nu/Nu_0)_{do}$ using the equation shown in Figure 6.2, for a range of qualities for the U12R300 and U24R300 test section configurations, at high-pressures and low-mass fluxes.

The equation representing the heat-transfer enhancement due to the developing film-boiling effect is based on the U of O bare tube database for HFC-134a (Uniform AFD, from El Nakla et al. (2006)). The data for P = 2389 kPa and G = 1410 $kg.m^{-2}.s^{-1}$ are correlated as:

$$(Nu_{dev}/Nu_0)_{do} = 1 + A_1 \exp(-B_1 (L/D)_{do} - C_1 x) \tag{6.1}$$

where $A_1 = 20.68$, $B_1 = 0.035$ and $C_1 = 6.2$, and Nu_0 is the bare tube fully developed Nusselt number, Nu_0 is calculated for P = 1665 kPa from:

$$Nu_0 = 0.016\,\mathrm{Re}_V^{\,0.7864}\,\mathrm{Pr}_V^{\,0.1} \tag{6.2}$$

Equation (6.2) predicts the U of O bare-tube database, (El Nakla et al., 2006) with an average error of -0.46% and a root-mean squared (*rms*) error of 4.6%.

A similar correlation was derived for the fully developed bare-tube film boiling data at P = 2389 kPa, and is expressed as:

$$Nu_0 = 5.495.10^{-6}\,\mathrm{Re}_V^{\,1.838}\,\mathrm{Pr}_V^{\,-26.73} \tag{6.3}$$

Equation (6.3) predicts the same database with an average error of -1.89% and an *rms* error of 7.46%. The average error of Eqn.(6.1) expressed in the ratio of $(Nu_{dev}/Nu_0)_{do}$ is -2.95% and the *rms* error is 12.3%. The average error and *rms* error are defined as:

$$\begin{aligned} average \quad error &= \frac{1}{n}\sum_{i=1}^{n}(error)_i \\ rms \quad error &= \sqrt{\frac{1}{n}\sum_{i=1}^{n}(error)^2{}_i} \\ error &= \frac{(Nu_{dev}/Nu_0)_{do,predicted}}{(Nu_{dev}/Nu_0)_{do,measured}} - 1 \end{aligned} \tag{6.4}$$

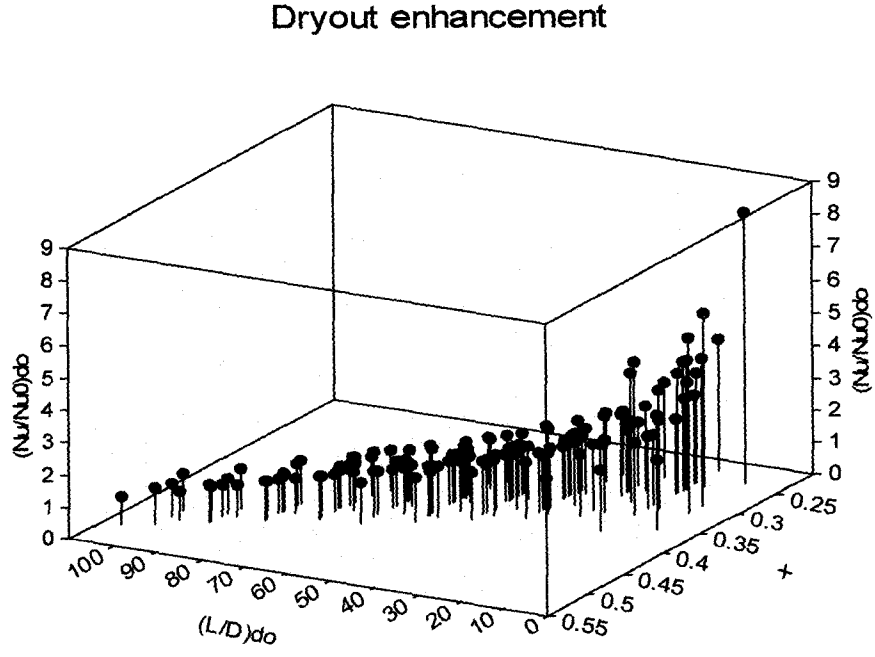

Figure 6.1 Uniform AFD bare tube developing FB data, expressed as $(Nu/Nu_0)_{do}$ at high-pressure and low-mass flux.

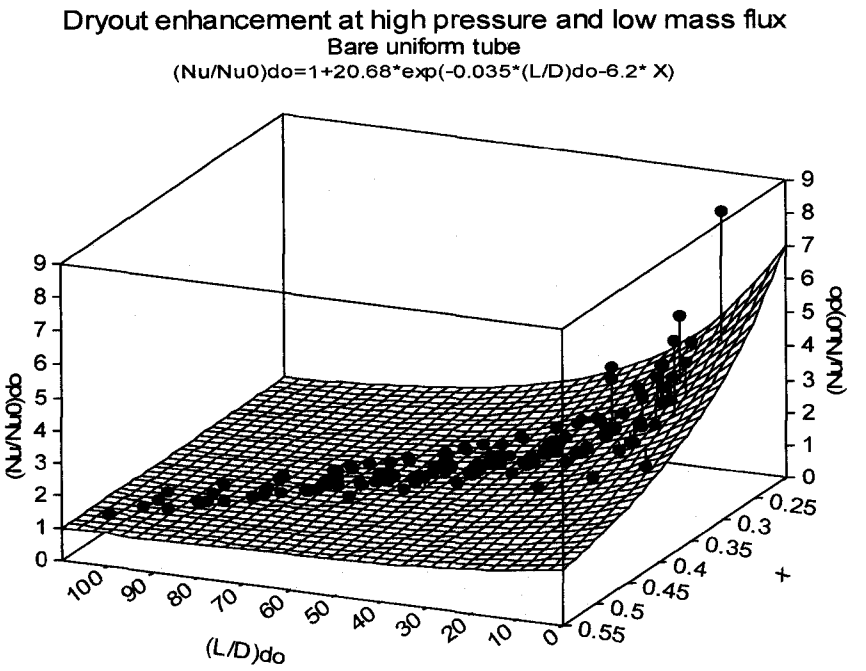

Figure 6.2 Comparison between predictions (surface) and measurements of the dryout-enhanced FB, expressed as $(Nu/Nu_0)_{do} = f(x, (L/D)_{do})$ for bare uniform AFD test section at low-mass flux and high-pressure.

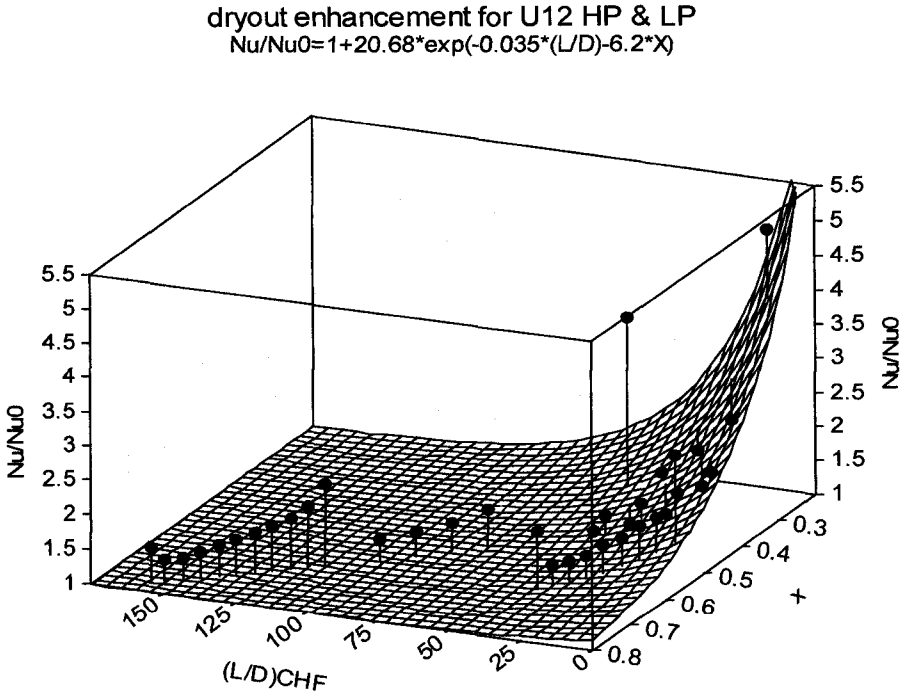

Figure 6.3 Comparison between predicted dryout-enhanced FB (surface) and measured obstacle effect, expressed as Nu/Nu_0, for U12R300 at low-mass flux and high-and low-pressures.

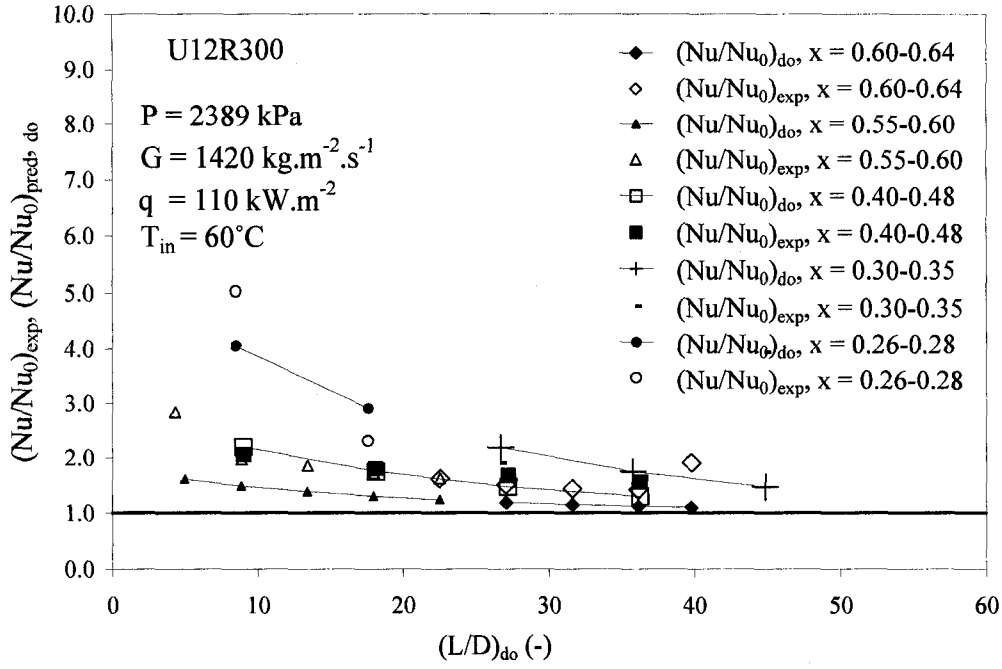

Figure 6.4 Comparison of predicted $(Nu/Nu_0)_{do}$ and $(Nu/Nu_0)_{exp}$ for U12R300.

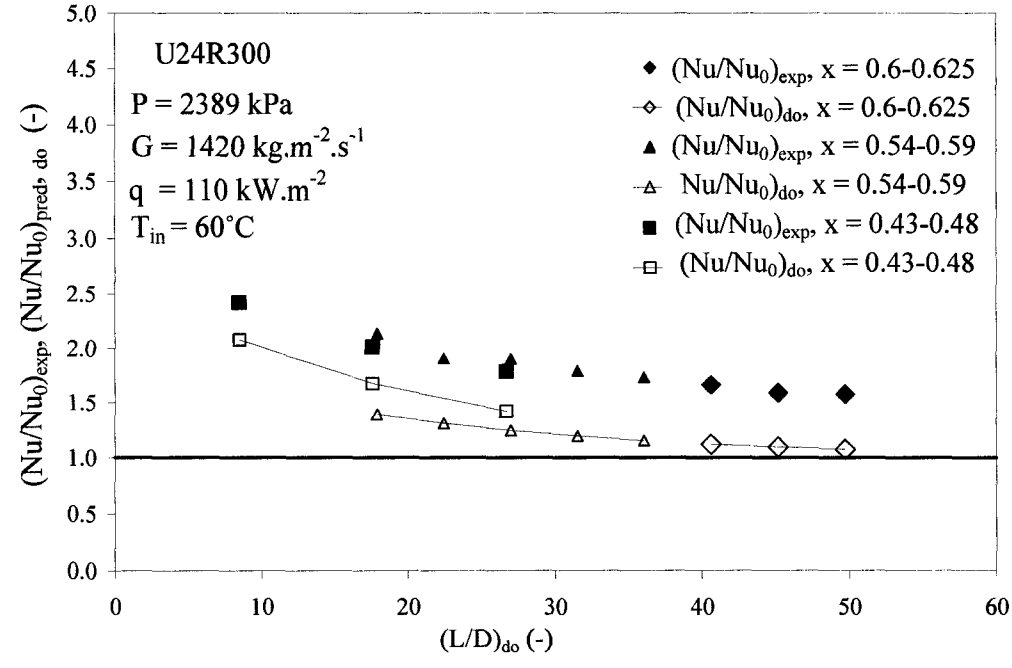

Figure 6.5 Comparison of predicted $(Nu/Nu_0)_{do}$ and $(Nu/Nu_0)_{exp}$ for U24R300.

6.3 Obstacle-Enhanced Film Boiling

6.3.1 Introduction

In Section *2.9.3.1*, the main parameters that affect PDO heat-transfer enhancement in presence of obstacle have already been identified (K_{ob}, x, x_{do}, exp(L/D)). Using a similar approach, the following section will show how the experimental data were correlated to represent the measured trends.

The parametric trends for the obstacle-enhanced FB will be examined by comparing graphically the predicted and the experimental trends based on the experimental data of the U12R300 configuration at different pressures (1665 and 2389 kPa) and for the configuration U24R300 at the high-pressure.

6.3.2 Development of the Equation for the Obstacle-Enhanced Film Boiling

The current database shows that the experimental data (Nu/Nu_0) can best be represented by the following parameters: (K_{ob}, Re_V, exp-(L/D)). Figure 6.6 shows the experimental obstacle heat-transfer enhancement (Nu/Nu_0) as a function of L/D and Re_V for the uniform tube equipped with 4 streamlined obstacles having 300 mm pitch and a flow-blockage ratio of 12%. Nu/Nu_0 increases with decreasing L/D from obstacle; this increase is especially strong for $L/D < 30$. Figure 6.6 also shows that the effect of Re_V on Nu/Nu_0 is weaker than the L/D effect; Nu/Nu_0 increases slightly with decreasing Re_V.

The obstacle enhancement component $(Nu_{dev}/Nu_0)_{ob}$ was empirically correlated as a function of $(L/D)_{ob}$ and Re_V, based on the selected (Section 5.1) PDO heat-transfer enhancement data. Figure 6.7 displays the best-fit surface (obstacle-enhanced FB equation) of the same experimental data as in Figure 6.6. The Figure 6.7 displays the same experimental trends discussed earlier, so with decreasing L/D, the predicted (Nu/Nu_0 -1) increases exponentially. The Re_V effect is weak: Nu/Nu_0 increases slightly

with decreasing Re_V from 450000 to 150000. Nu/Nu_0 reaches its maximum value of 2.55 at L/D = 0 and Re_V = 150000. The data to be used for deriving an equation for the obstacle-enhanced FB were selected from the database for conditions where the obstacle effects dominate. Generally, the obstacle-enhanced FB dominates at high qualities. Table 6.1 presents a comparison between predictions of the derived equation (obstacle-enhanced FB expressed as $(Nu/Nu_0)_{ob}$), predictions of the Eqn. (6.1) (dryout-enhanced FB heat transfer expressed as $(Nu/Nu_0)_{do}$) and the measured $(Nu/Nu_0)_{exp}$ for the uniform tube equipped with 4 rounded obstacles at a 300-mm pitch having ε = 12 and 24%; this table shows that the obstacle-enhanced FB dominates over the dryout-enhanced FB heat transfer for the 12 and 24% test section configurations. Figure 6.8 and 6.9 compare experimental and predicted obstacle effect expressed as $(Nu/Nu_0)_{ob}$ using the derived obstacle-enhanced FB equation for the U12R300 and U24R300 configurations, at high-pressures and low-mass fluxes. The derived obstacle-enhanced FB heat-transfer equation is:

$$(Nu_{dev}/Nu_0)_{ob} = 1 + A_2(\mathrm{Re}_V)^{B_2} K_{ob} \exp(-C_2 \frac{L}{D}) \tag{6.5}$$

where A_2 = 25, B_2 = -0.08, C_2 = 0.035, K_{ob} is the single-phase pressure-loss coefficient calculated from Eqn. (5.1). For blunt obstacles (see Section 5.4), K_{ob} is calculated for round obstacles and a heat-transfer correction factor "R" is applied; R represents the ratio of the average measured heat-transfer enhancement of blunt obstacle to the average measured heat-transfer enhancement of the round obstacle for same ε, and is calculated by R_{blunt} = average $(Nu/Nu_0 - 1)_{blunt}$/average $(Nu/Nu_0 - 1)_{round}$. The best fit was R_{blunt} = 1.2. R_{blunt} is applied to account for the obstacle blunt shape effect on FB heat transfer.

Table 6.1 Data for obstacle-enhanced FB equation.

x	$(L/D)_{ob}$	$(L/D)_{do}$	$(Nu/Nu_0)_{exp}$	$(Nu/Nu_0)_{ob}$	$(Nu/Nu_0)_{do}$
U24R300					
0.625	50.9	49.7	1.58	1.5	1.075
0.613	46.4	45.2	1.59	1.59	1.095
0.601	41.8	40.6	1.66	1.69	1.12
0.588	37.3	36.1	1.73	1.81	1.15
0.576	32.7	31.5	1.79	1.95	1.19
0.564	28.2	27	1.9	2.11	1.24
0.551	23.6	22.4	1.91	2.31	1.31
0.539	19.1	17.9	2.13	2.54	1.39
0.478	50.9	26.7	1.78	1.51	1.42
0.453	41.8	17.6	2.01	1.7	1.67
U12R300					
0.641	0	39.8	1.912	2.26	1.1
0.631	50.9	36.2	1.42	1.21	1.12
0.618	46.4	31.6	1.44	1.25	1.15
0.606	41.8	27.1	1.51	1.29	1.19
0.594	37.3	22.5	1.62	1.34	1.24
0.581	32.7	18	1.71	1.4	1.3
0.569	28.2	13.4	1.86	1.47	1.38
0.557	23.6	8.9	1.97	1.56	1.48
0.544	19.1	4.3	2.83	1.65	1.61

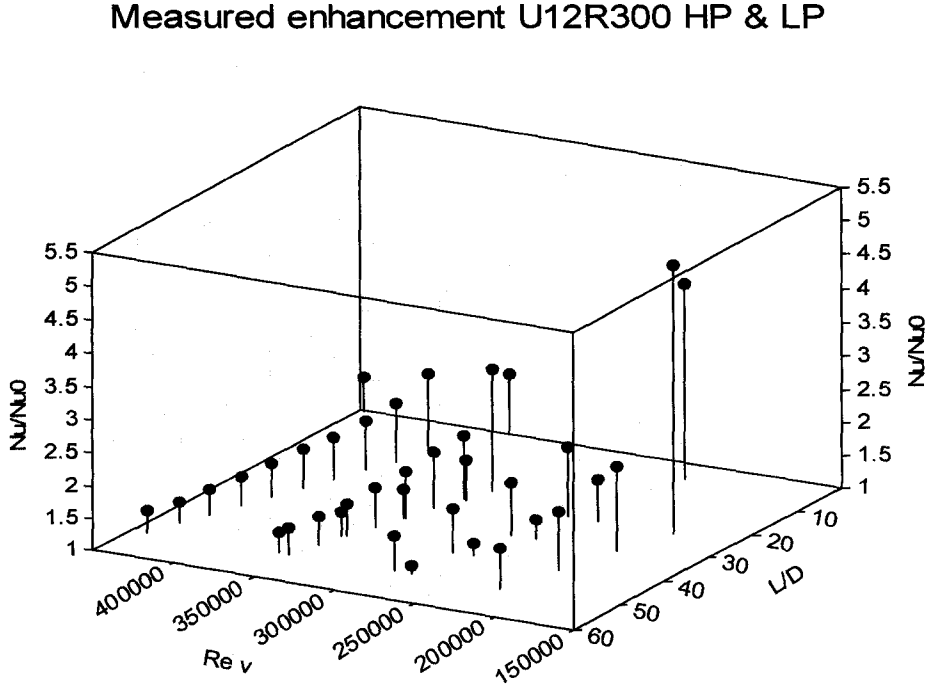

Figure 6.6 Experimental Nu/Nu_0 for U12R300 at high-and low-pressures and at low-mass flux, data for obstacle-enhanced FB heat transfer.

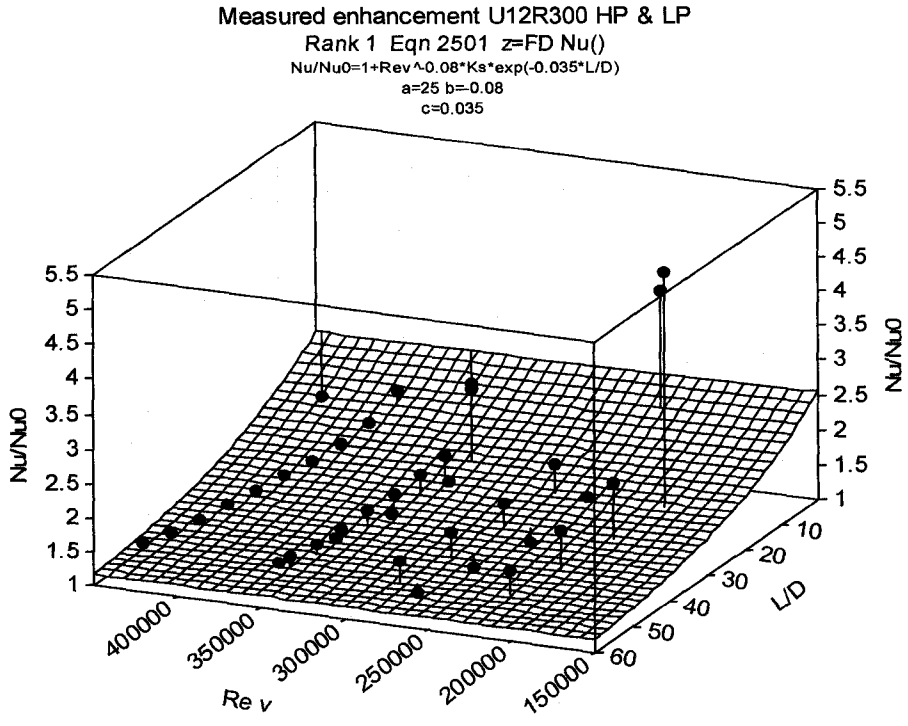

Figure 6.7 Comparison of predicted (surface) and measured obstacle effect (Nu/Nu_0) for U12R300 at high-and low-pressures and at low-mass fluxes.

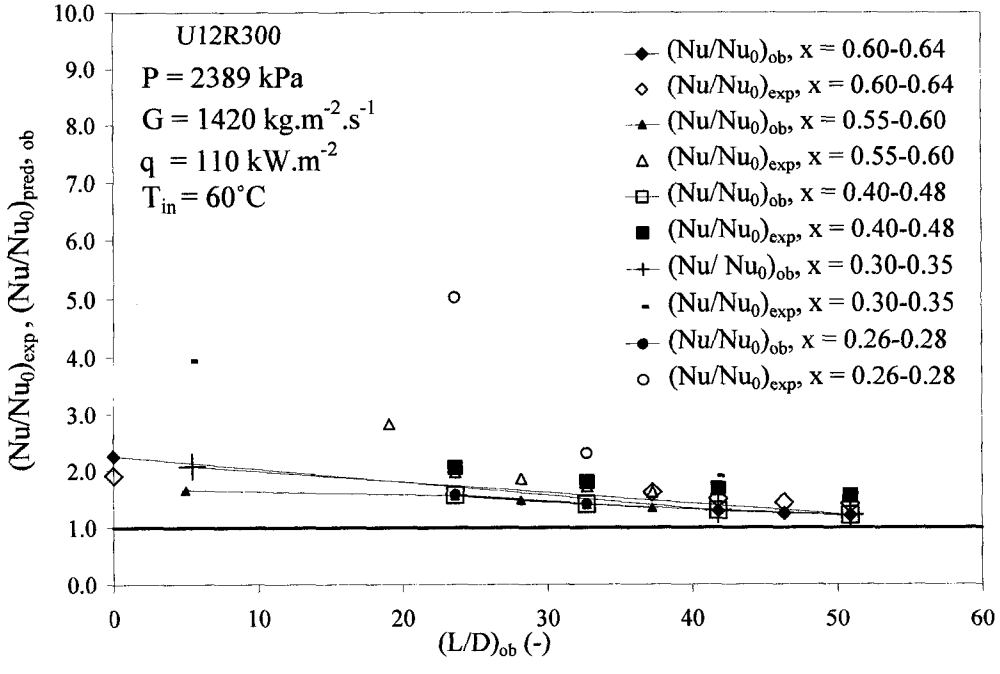

Figure 6.8 Comparison of predicted $(Nu/Nu_0)_{ob}$ and measured obstacle effect expressed as $(Nu/Nu_0)_{exp}$ for U12R300.

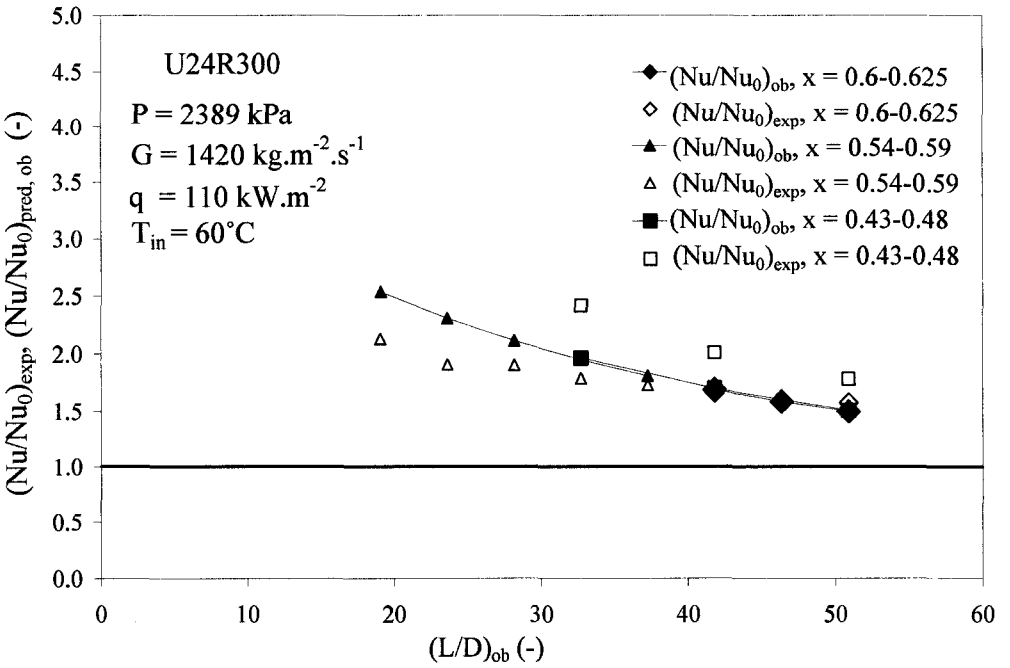

Figure 6.9 Comparison of predicted $(Nu/Nu_0)_{ob}$ and measured obstacle effect expressed as $(Nu/Nu_0)_{exp}$ for U24R300.

6.4 Approaches for Combining the Dryout and Obstacle Effect

Section 6.2 and 6.3 demonstrated the development of the new equations for both the dryout and obstacle effect for enhancing FB heat transfer. The mechanisms representing these two effects occur separately from each other. It is concluded from this study that their contribution to the overall effect on FB heat transfer differs from the approach used for combining them in the previous study of Leung et al. (2005), because the primary contributor to FB heat-transfer enhancement (obstacle-enhanced FB) tends to suppress the upstream effects including the developing film boiling effect. Various approaches can be applied to combine these two FB enhancement components, e.g.:

(i) addition, $$(\frac{Nu}{Nu_0})_{overall} = ((Nu_{dev}/Nu_0)_{do} + (Nu_{dev}/Nu_0)_{ob} - 1) \quad (6.6)$$

(ii) multiplication, $$(\frac{Nu}{Nu_0})_{overall} = (Nu_{dev} / Nu_0)_{do} (Nu_{dev} / Nu_0)_{ob} \quad (6.7)$$

(iii) taking the maximum: $(\frac{Nu}{Nu_0})_{overall} = Maximum\left((\frac{Nu_{dev}}{Nu_0})_{do}, (\frac{Nu_{dev}}{Nu_0})_{ob}\right)$ (6.8)

(iv) in addition to the above mentioned forms of equations, dryout and obstacle effects on FB were correlated initially as a function of thermodynamic quality, and in some cases, Eqn. (6.1) was raised to a power of n ($n \leq 1$):

$$(\frac{Nu}{Nu_0})_{overall} = ([(Nu_{dev}/Nu_0)_{do}]^n + (Nu_{dev}/Nu_0)_{ob} - 1) \quad (6.9)$$

where $[(Nu_{dev}/Nu_0)_{do}]^n = [1 + a_1 \exp(-b_1 (L/D)_{do} - c_1 x)]^n$, where a_1, b_1 *and* c_1 are empirical constants optimized based on the data, and $(Nu_{dev}/Nu_0)_{ob} = f(x, (L/D)_{ob})$.

Typically at the lower qualities (x = 0.25–0.4), it was found that the dryout-enhanced FB heat transfer is larger than the obstacle-enhanced FB, while at higher qualities, the obstacle enhanced FB dominates. It was noted from the data that, the combined effect (PDO enhancement due to dryout and obstacle) does not vary linearly or nearly linearly with either of the components (Eqn.(6.1) or (6.5)) as would have been implied by using either Eqn. (6.6) or (6.7). This may be explained by the fact that the obstacle suppresses any upstream effects, i.e. turbulence generated by the obstacle tends to suppress the upstream effects including the developing film boiling effect, or, in other words, when dryout occurs upstream from the obstacle, the turbulence generated by the obstacle can be assumed to have dampened out any residual effects of an upstream dryout location.

Based on extensive data analysis, it was found that the observed film boiling heat-transfer enhancement (i.e. in the developing film-boiling region) could best be represented by the maximum of these two heat-transfer enhancement components, i.e. approach (iii). The data analysis showed that either the sum of the two effects (approach (i) and (iv)) or a multiplication of them (approach (ii)) provided an inferior representation of the overall heat-transfer enhancement. At lower x, the developing FB effect dominates the obstacle-enhanced FB (e.g., Table 6.2 which will be discussed below). The data analysis (Subsection 6.2.2) showed that the overall effect of developing film-boiling and obstacle-

enhanced FB heat transfer is much higher than the developing film-boiling effect in bare tubes.

Table 6.2 shows a comparison of the predictions of Eqn. (6.1) and (6.5) and the measured Nusselt number ratio, for the uniform AFD tube, equipped with 4 streamlined obstacles having a 12% flow-blockage ratio and a pitch of 300 mm. The test was performed at low-pressure and low-mass flux. For x = 0.36 to 0.44, Eqn. (6.1) (developing FB heat transfer due to upstream dryout location) is dominant and predicts the higher Nusselt number ratio, beyond x = 0.44, Eqn. (6.5) (the obstacle-enhanced FB) is dominant and predicts the higher Nusselt number ratio.

The current experimental database suggests that

(i) dryout-enhanced FB heat transfer data can be best represented by an exponentially decaying function of quality (x) and $(L/D)_{do}$,

(ii) as discussed above, the obstacle and dryout effects do not significantly reinforce each other, i.e. they should not be combined by addition or multiplication, (e.g., for the test section configuration (U24R300), Table 6.3 shows that for a range of thermodynamic qualities and $(L/D)_{do}$ from dryout ($(L/D)_{do} = (z - z_{do})/D$) and $(L/D)_{ob}$ from obstacle ($(L/D)_{ob} = (z-z_{ob})/D$), the measured Nusselt number ratio is overpredicted significantly, when multiplication or summation of the two effects was performed),

(iii) generally, obstacle effects (single-phase and droplet related mechanisms) are dominant over dryout-enhanced FB, and

(iv) at certain locations with low x, low $(L/D)_{do}$ and high $(L/D)_{ob}$, dryout-enhanced FB heat transfer dominates the obstacle-enhanced FB. Section 6.6 will show the experimental trends and compare these trends to the predicted trend of PDO heat-transfer enhancement (Eqn.(6.8)) due to the dryout-induced turbulence and due to the obstacle-inducted turbulence.

From the above discussion of the experimental data trends, it is concluded that the maximum enhancement (approach (iii)) of these two competing effects (dryout and

obstacle effects on FB) provides the optimum prediction of the obstacle effect. The derived correlation is:

$$(\frac{Nu}{Nu_0})_{overall} = Maximum \left((\frac{Nu_{dev}}{Nu_0})_{do}, (\frac{Nu_{dev}}{Nu_0})_{ob} \right) \quad (6.8)$$

Table 6.2 Comparison between predictions of Equation (6.1) and (6.5) with measured Nu/Nu_0.

x	$(L/D)_{ob}$	$(L/D)_{do}$	$(Nu/Nu_0)_{pred,\ do}$	$(Nu/Nu_0)_{pred,\ ob}$	$(Nu/Nu_0)_{exp}$
0.77	52.7	158.2	1.001	1.225	1.501
0.76	49.1	154.6	1.001	1.256	1.326
0.74	44.5	150.0	1.001	1.300	1.328
0.73	40.0	145.5	1.001	1.353	1.376
0.72	35.5	141.0	1.002	1.414	1.456
0.71	30.9	136.4	1.002	1.486	1.498
0.69	26.4	131.9	1.003	1.570	1.582
0.68	21.8	127.3	1.004	1.670	1.630
0.67	17.3	122.8	1.005	1.786	1.735
0.65	12.7	118.2	1.006	1.923	1.874
0.64	8.2	113.7	1.007	2.084	2.170
0.60	49.1	100.0	1.015	1.260	1.307
0.57	40.0	91.0	1.024	1.359	1.373
0.55	30.9	81.9	1.040	1.495	1.431
0.52	21.8	72.8	1.064	1.682	1.602
0.47	3.6	54.6	1.167	2.298	6.059
0.44	49.1	45.5	1.271	1.266	1.122
0.42	40.0	36.4	1.438	1.366	1.192
0.39	30.9	27.3	1.709	1.506	1.288
0.36	21.8	18.2	2.147	1.699	1.640

Table 6.3 Comparison of $(Nu/Nu_0)_{exp}$ and the predictions of overall enhancement by different combinations of $(Nu/Nu_0)_{do}$ and $(Nu/Nu_0)_{ob}$.

x	$(L/D)_{ob}$	$(L/D)_{do}$	Predicted $(Nu/Nu_0)_{do}$	Predicted $(Nu/Nu_0)_{ob}$	Overall, $(Nu/Nu_0)_{pred}$ (multiplication)	Overall, $(Nu/Nu_0)_{pred}$ (summation)	$(Nu/Nu_0)_{exp}$
0.58	32.7	31.5	1.2	1.95	2.3	2.15	1.8
0.56	28.2	27.0	1.2	2.1	2.5	2.3	1.9
0.55	23.6	22.5	1.3	2.3	3.0	2.6	1.9
0.54	19.0	17.9	1.4	2.5	3.5	2.9	2.1

6.5 Prediction of Dryout and Rewetting Location

6.5.1. Methodology for Predicting the CHF Location

In order to predict the dryout and rewetting locations, the correlation of Guo et al. (2001) (Equation (2.5)) was applied to uniform and non-uniform AFD tubes. The application of Eqn. (2.5) involved the determination of CHF-enhancement ratios (CHF_{ob}/CHF_0) in the presence of obstacles. The methodology used is:

- Assume quality, $x = x_{do}$ in obstacle regions.
- The obstacle-heated length is divided into 1 cm length intervals for uniform AFD tube and 0.5 and 1 cm intervals for the non-uniform AFD tube.
- Apply the fluid- to-fluid modeling of Groeneveld et al. (1997) and the CHF look-up table (Groeneveld et al., 2005) for bare tube; find the predicted relative CHF enhancement [3] (Equation (2.5)) at each location.
- Where the predicted CHF_{ob} equals or intersects with the local heat flux, then dryout or rewetting is predicted to occur: when q_{local} becomes greater than CHF_{pred}, then the intersection point is assumed as a dryout point, and when $q_{local} > CHF_{pred}$ PDO conditions prevail, while for $CHF_{ob} > q_{local}$, the pre-CHF or rewetting region is present.

6.5.2 Guo CHF_{ob} Prediction Method

6.5.2.1 Uniform AFD tube

The equation of Guo et al. (2001) for predicting CHF enhancement was applied to the uniform AFD tube at high-pressure and low-mass flux. The results for the U12R300 configuration (4 rounded obstacles, ε = 12% and 300 mm pitch) are presented in Figure

[3] $R_{CHF} = \frac{CHF_{ob}}{CHF_0} - 1$

6.10, where the distribution of CHF in the obstacle region vs. thermodynamic quality is shown, the predicted CHF locations are also presented on the Figure 6.10. The results show that the experiment measured three dryout points and two rewetting points, (Figure 5.4-(d)) from tabulated data of Section 5.1). The first 2 dryout points are predicted with an error of -5.1% and -2.98%, while the third CHF point could not be predicted, Figure 6.11 shows a comparison of the predicted and measured quality at CHF for U12R300 configuration. Figure 6.12 presents the predicted temperature profile based on predicted dryout and rewetting points, this will be discussed in Section *6.5.2.3*.

For the U24R300 configuration (4 rounded obstacles, ε = 24% and 300 mm pitch), two dryout points and one rewetting point were measured (Figure 5.4-(d)), while three dryout points and two rewetting points were predicted (Figure 6.13), the two dryout points were predicted successfully with an error of 1.64% and 1.79%.

6.5.2.2 Inlet-peak AFD tube

The local conditions approach was applied to predict the bare tube CHF for non-uniform AFD tubes; the employment of the BLA concept (boiling length average heat flux) for predicting the CHF in an obstacle-equipped tube is questionable except for the first dryout point, since the upstream history is very different for subsequent dryout points when an upstream CHF has occurred. The results show that for inlet-peak test section (Figure 6.14) with 5 rounded obstacles having 12% flow-blockage ratio and 300 mm pitch, there are two experimental dryout points (Figure 5.1-(b)), while the predictions show three; the first predicted point has an error of -4.5%, while the other point is poorly predicted. For the test section with a 24% flow-blockage ratio, the predicted and measured dryout locations do not agree (Figure 6.15). The predicted dryout and rewetting points using Guo et al. (2001) approach do not represent the measured points, the best agreement with the experimental data was found for the predictions of U12R300 configuration of the uniform tube (Figure 6.10).

6.5.2.3 Modified CHF_{ob} prediction method of Guo

Equation (6.8) was applied to predict the full temperature profile using the predicted (Guo et al., 2001) dryout and rewetting points (Figure 6.12). It can be seen that the first predicted rewetting point (x = 0.30) is shifted back from the measured (x = 0.39), while the second measured rewetting point is not predicted. This also affected the predicted temperature profile. Attempts made to modify the Guo et al. Equation (2.5) are discussed below.

Equation (2.5) of Guo et al. (2001) is adjusted to fit the experimental data of Table 5.2. The modified Guo et al. correlations are:

- for $(x_{cr} < 0.75\, x_{cr}^{lim})$:

$$\frac{CHF_{ob}}{CHF_{bare}} = 1 + \frac{7K_{ob}{}^{2}}{(1-x_{cr})^{0.1}} \exp(-0.05(L/D)) \tag{6.10}$$

and

- for $((x_{cr} \geq (0.75\, x_{cr}^{lim}))$ and $(x_{cr.} \leq x_{cr}^{lim}))$, then:

$$\frac{CHF_{ob}}{CHF_{bare}} = 1 + 8K_{ob}{}^{1.9} \left(\frac{(1-x_{cr})}{x_{cr}}\right)^{0.85} \exp(-0.01(L/D)) \tag{6.11}$$

and

- for $(x_{cr} > x_{cr}^{lim})$:

$$\frac{CHF_{ob}}{CHF_{bare}} = 1 + 17K_{ob}{}^{0.5} \left(\frac{(1-0.9x_{cr})}{x_{cr}}\right)^{0.6} \exp(-0.02(L/D)) \tag{6.12}$$

The modified Guo et al. (2001) correlations were employed to predict dryout and rewetting points of the same uniform AFD data used in Subsection *6.5.2.1* (Figure 5.4-

(d)).The results (Figure 6.16 and 6.18) show a better agreement with the measured dryout and rewetting points than the earlier predicted CHF points by Guo et al. (2001). A comparison between measured surface temperatures with the predicted temperature profiles (Equation (6.8)) including predictions of dryout and rewetting points is presented in Figure 6.17 and 6.19.

Guo et al. (2001) prediction method can be improved, as discussed earlier, but ideally we need more CHF data in obstacle-equipped tubes to get the optimum prediction. Alternatively, the measured CHF points may be used in the application of the Equation (6.8), and this approach (which provides the best prediction of the measured temperature distribution) will be discussed in Section 6.6.

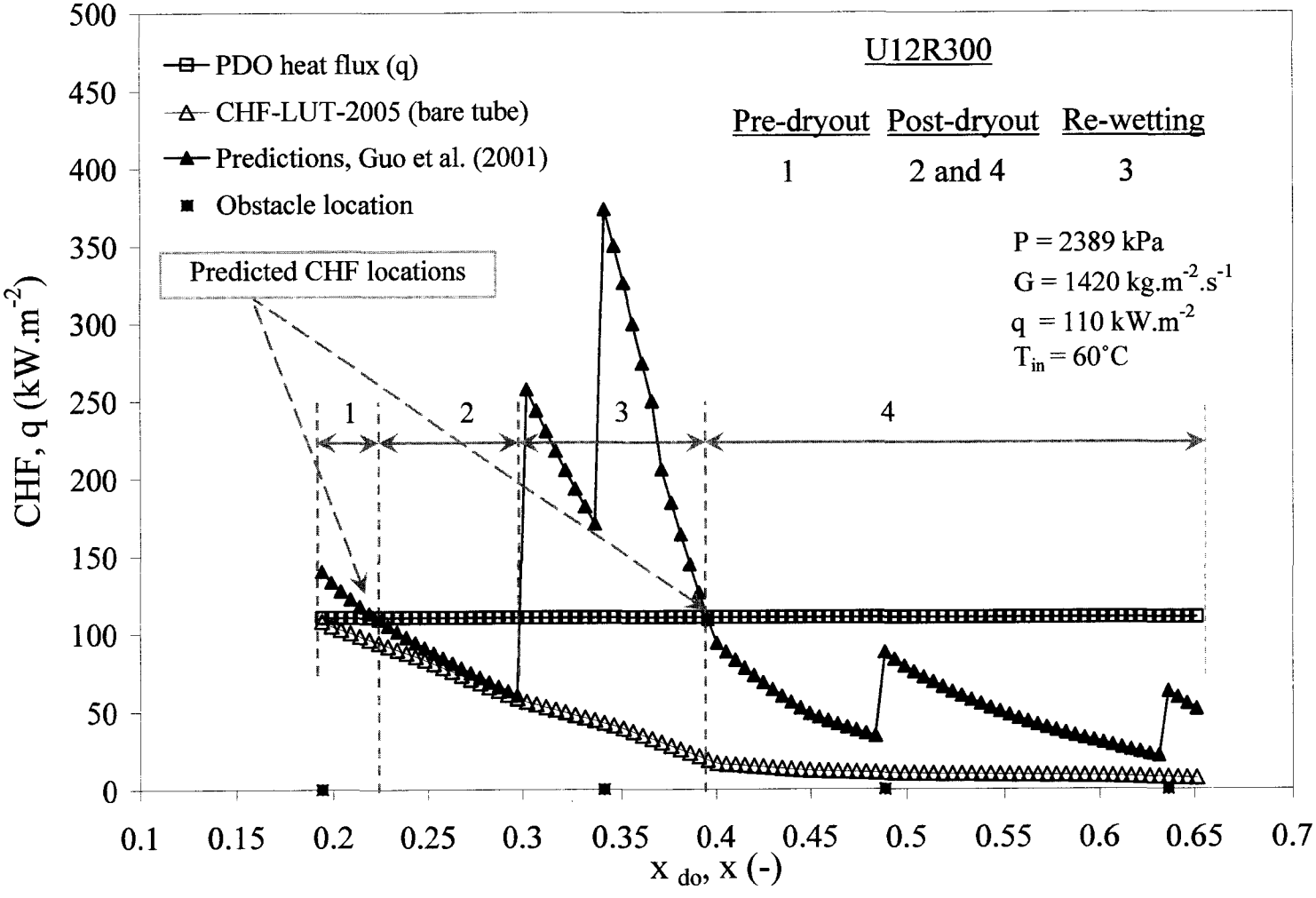

Figure 6.10 Predictions of CHF locations in the obstacle region (Guo et al., 2001) for uniform AFD test section, rounded obstacles with ε = 12% and 300 mm pitch.

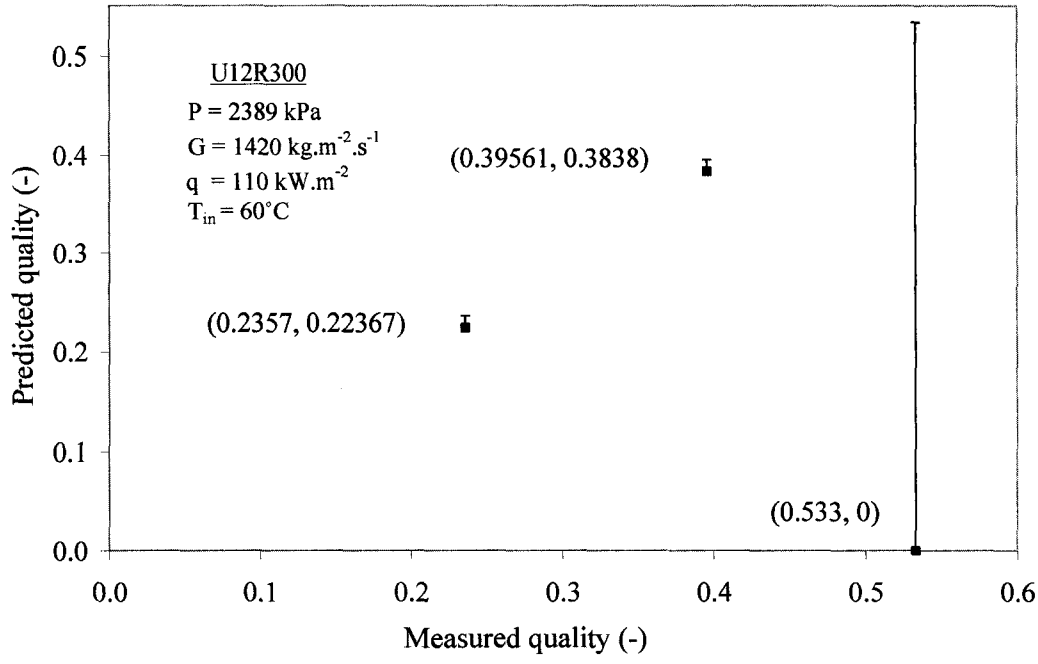

Figure 6.11 Comparison of the predicted (Guo et al., 2001) and measured quality at CHF for U12R300 at high P and low G.

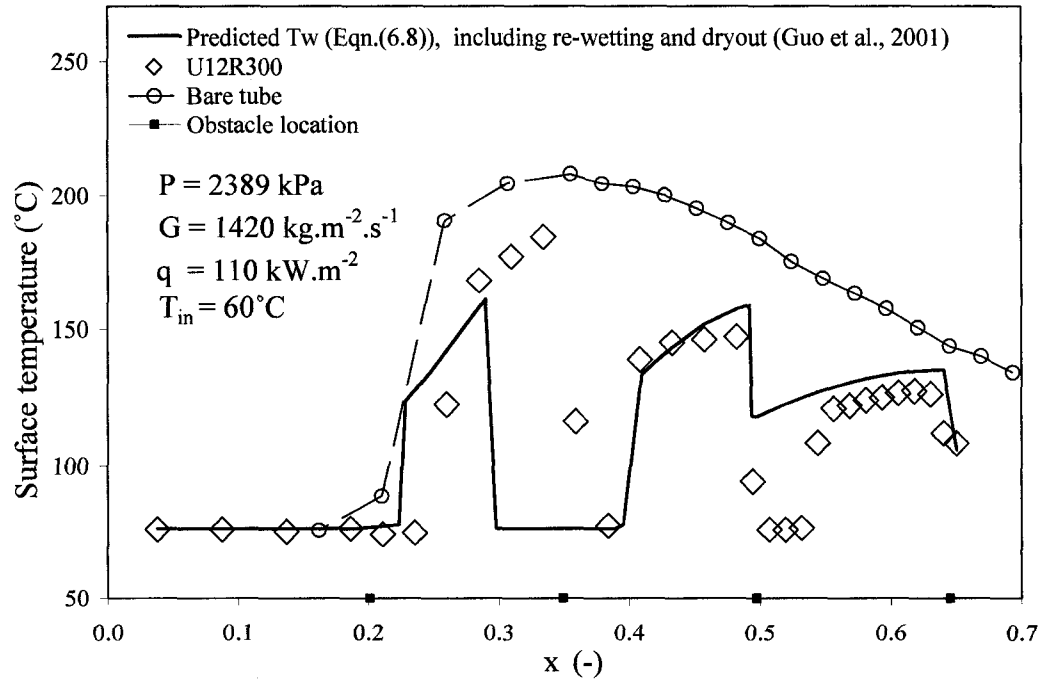

Figure 6.12 Predictions of surface temperatures based on Guo et al. (2001) correlations for uniform AFD tube, rounded obstacles with ε = 12%.

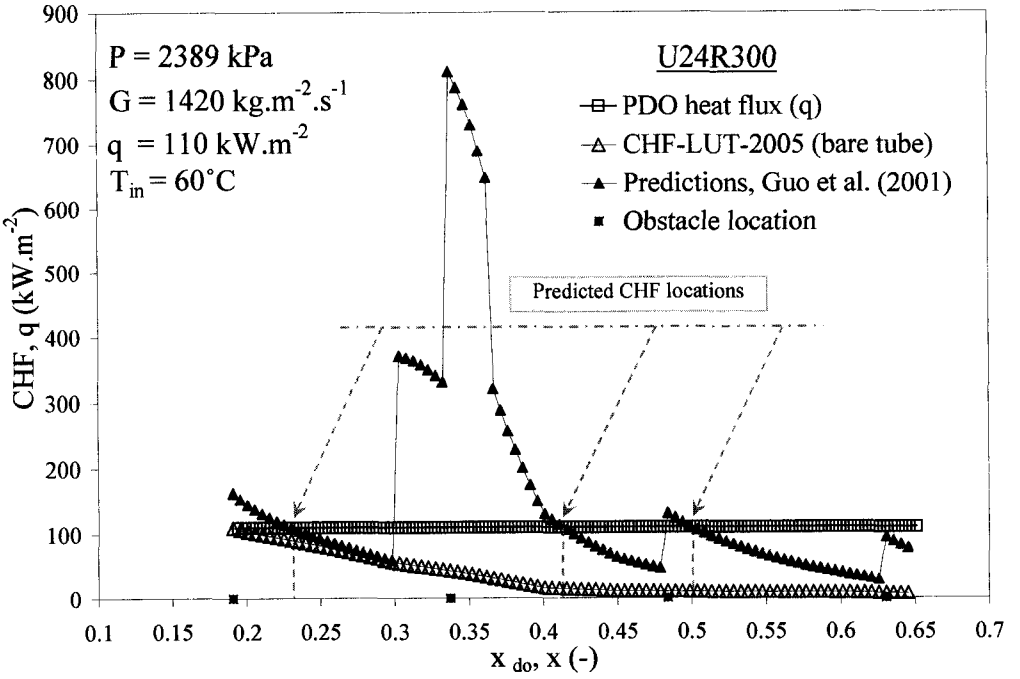

Figure 6.13 Predictions of CHF locations in the obstacle region (Guo et al., 2001) for uniform AFD test section, rounded obstacles with ε = 24% and 300 mm pitch.

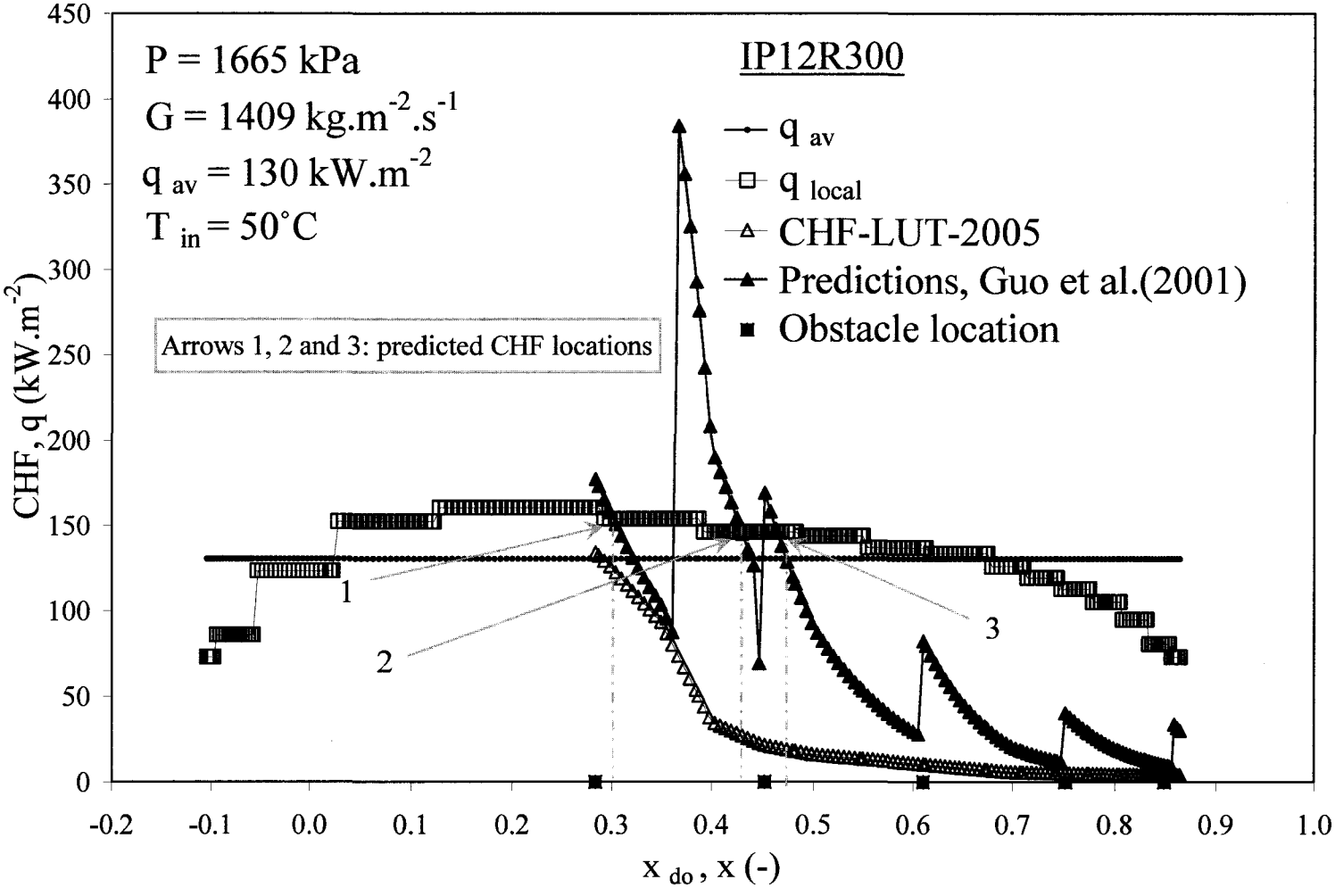

Figure 6.14 Predictions of CHF points in the obstacle region (Guo et al., 2001) for inlet-peak AFD test section, rounded obstacles with ε = 12% and 300 mm pitch.

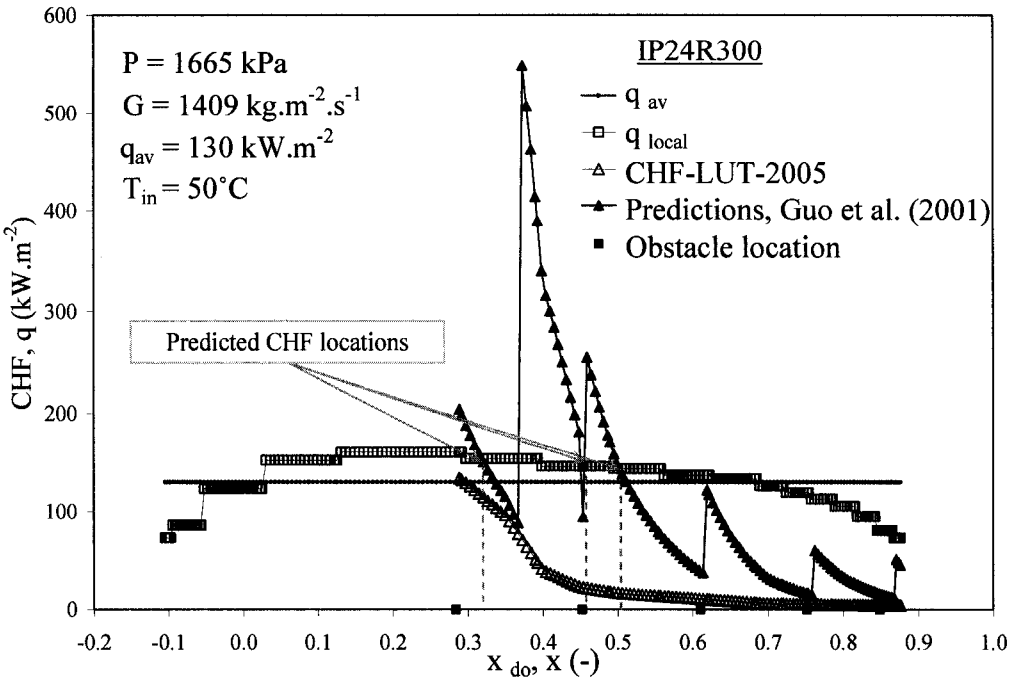

Figure 6.15 Predictions of CHF points in the obstacle region (Guo et al., 2001) for inlet-peak AFD test section, rounded obstacles with ε = 24% and 300 mm pitch.

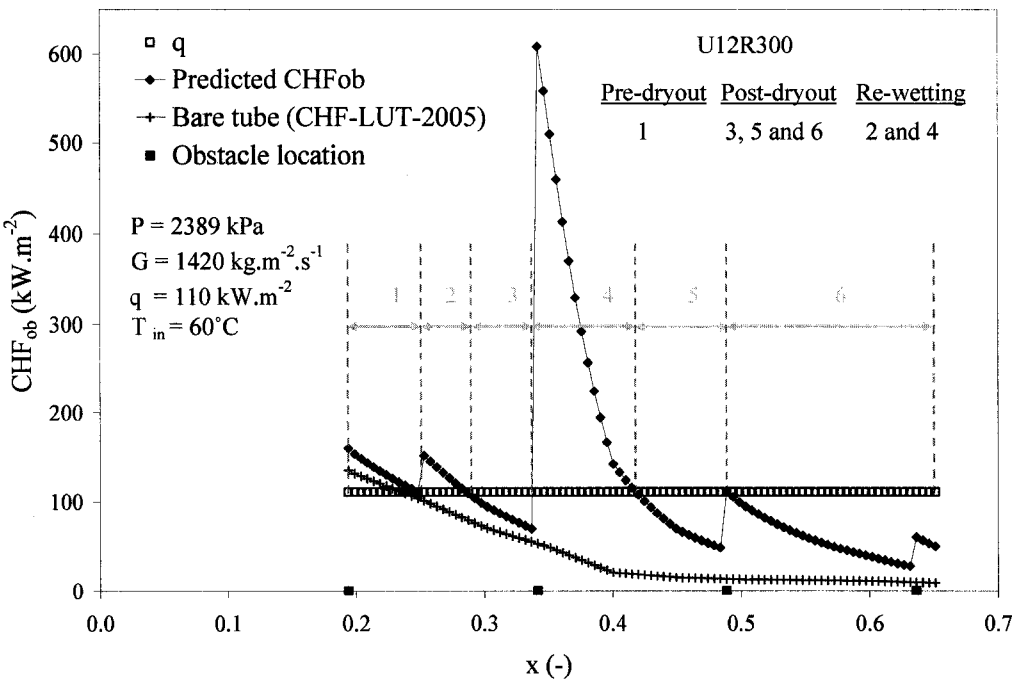

Figure 6.16 Predictions (modified Guo) of CHF points in the obstacle region for uniform AFD test section, rounded obstacles with ε = 12% and 300 mm pitch.

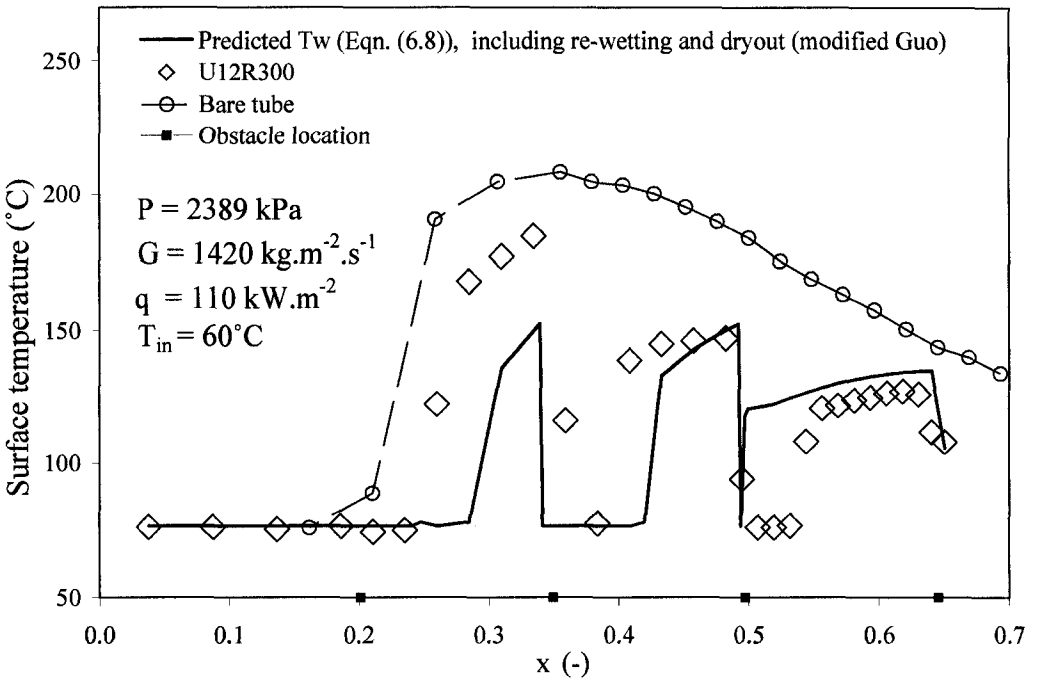

Figure 6.17 Predictions of surface temperature based on modified Guo correlations for uniform AFD tube, rounded obstacles with $\varepsilon = 12\%$.

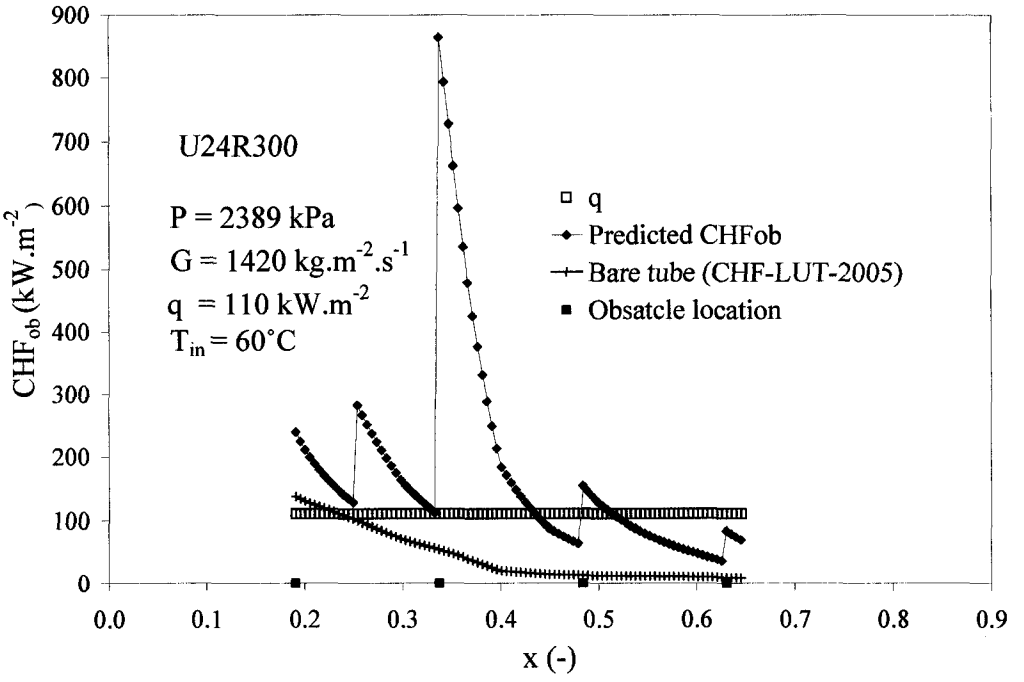

Figure 6.18 Predictions (modified Guo) of CHF points in the obstacle region for uniform AFD test section, rounded obstacles with $\varepsilon = 24$ and 300 mm pitch

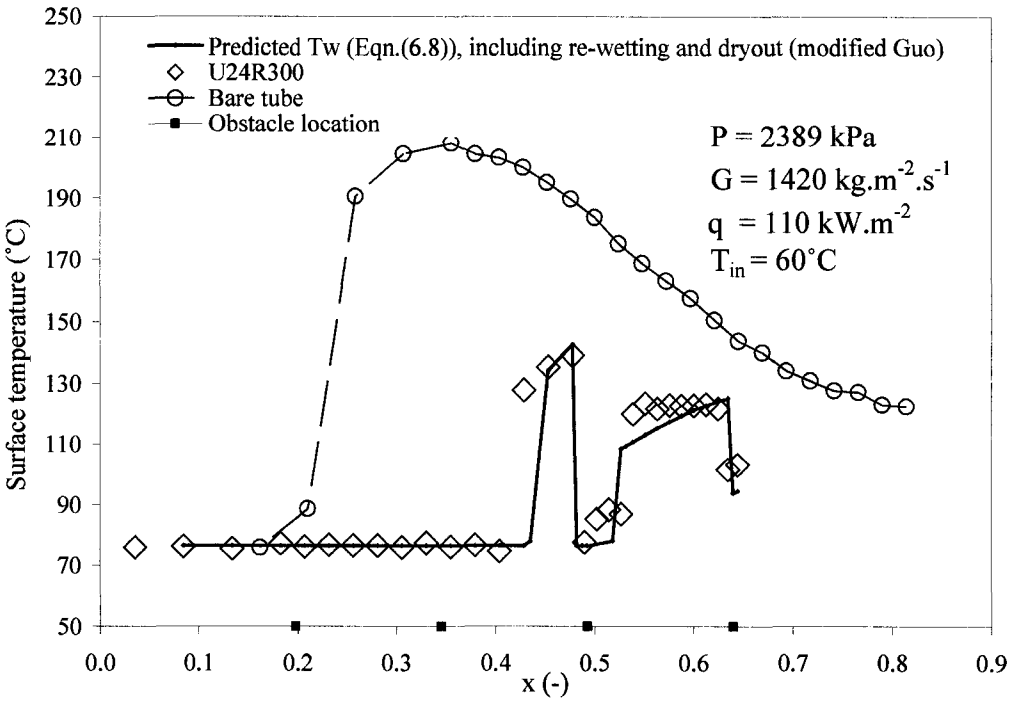

Figure 6.19 Predictions of surface temperature based on modified Guo correlations for uniform AFD tube, rounded obstacles with $\varepsilon = 24\%$.

6.6 Comparison between the Proposed Equation and the Experimental Data

In this section the wall temperature distributions predicted using Equation (6.8) are compared to the experimental data from Section 5.1. The dryout and rewetting locations are taken from the measurements. For a particular case, the inverse HTC distribution is presented as an additional figure in Section 6.6.2.

The nearly vertical black line on the figures indicates the predicted change in overall FB heat-transfer enhancement from leading to trailing edge of an obstacle[4], while the nearly vertical gray line shows the transition from/to nucleate boiling

[4] Note that this predicted drop in temperature at the obstacle location corresponds to an increase in the local FB heat transfer because of the enhancement effect of the obstacle

6.6.1 Uniform AFD Tube

Figure 6.20 shows a comparison of the predicted and measured temperature profiles, for the uniform AFD tube, equipped with 4 streamlined obstacles having a 12% flow-blockage ratio with a pitch of 300 mm. The test was performed at high-pressure and low-mass flux. From the inlet to first dryout occurrence downstream from the first obstacle, the test section experiences nucleate boiling and the wall temperature can be predicted from either a nucleate boiling or a saturated boiling correlation. The developing film-boiling region starts downstream from the dryout location. After the first two flow obstacles, the dryout-enhanced FB heat transfer is dominant (non-continuous line indicated by arrows), and Eqn. (6.1) applies. However after the third obstacle, heat-transfer enhancement due to the upstream obstacle (continuous line, Eqn. (6.5)) becomes the dominant developing heat-transfer mode. The temperatures in the first developing film-boiling region are slightly underpredicted. With increasing thermodynamic quality, the agreement between predicted and measured wall temperature profiles is improved. The measurements show that rewetting generally occurs at the obstacle, close to the trailing edge. This is due to the higher turbulence downstream of the obstacle, which increases the axial and lateral velocities and also increases the deposition rate of the droplets, thus increasing the local CHF significantly. As the quality increases, the concentration of droplets in the PDO flow decreases, and therefore the heat-transfer enhancement due to droplet-wall interaction becomes weak.

Figure 6.21 shows a similar temperature profiles for the same test section configuration as for Figure 6.20, except for a lower pressure. Here, Eqn. (6.1) (developing FB heat transfer due to the upstream dryout location) is dominant and predicts the lower wall temperatures in the first obstacle span. However, beyond the second obstacle, Eqn. (6.5) (obstacle-enhanced FB) becomes dominant. At the second and third obstacles, the heated surface does not appear to have been rewetted completely (although rewetting may have occurred between the thermocouple locations). Here the step change in wall temperature corresponds to the predicted transition in heat-transfer enhancement that occurs at the

flow obstacle plane. The predicted wall temperature distributions are slightly lower than the measured wall temperature.

Figures 6.22 and 6.23 show the predicted wall temperatures for a uniform AFD test section with 7 or 4 streamlined obstacles having a 24% flow-blockage ratio and 150 or 300 mm pitch, respectively. In Figure 6.22 downstream from the first dryout a sudden temperature jump and immediate rewetting is observed to occur: this probably represents transition boiling (see footnotes of Table 5.1); the wall temperature appears to be over-predicted for this point but this may be due to not accounting for local axial conduction that will lower the local heat flux and hence the local temperature spikes. Figure 6.23 shows a better agreement. A similar predicted profile can be seen in Figure 6.24 for blunt obstacles with a 24% flow-blockage ratio. The increased in slope in T_w downstream from the second obstacle is due to switch from dryout-enhanced FB to obstacle-enhanced FB heat transfer.

The new correlation was applied to the uniform AFD test sections equipped with either rounded or blunt obstacles at high-pressure and high-mass flux. The results (Figures 6.25 and 6.26) show significant underpredictions except for the downstream developing film-boiling region, where the predicted temperature profile is slightly lower than the measured wall temperatures. Figure 6.25 does not show a temperature drop at the second obstacle, because the predicted dryout-enhanced FB exceeded slightly the obstacle-enhanced FB at the trailing edge of this obstacle. This seems to correspond to a very narrow FB region that rewets at the next obstacle in the experimental test section.

6.6.2 Non-Uniform AFD Tube

Figure 6.27 and 6.29 show changes in slope for the predicted temperature profiles caused by changes in local q due to heat flux profile at the corresponding locations, these changes are particularly evident in figure 6.29 and will be discussed later.

The proposed correlation, which is derived for uniform AFD tubes and is based on bare tube PDO correlations for the fully developed FB, was applied to non-uniform AFD (inlet and outlet-peak) test section at different flow conditions. Figures 6.27 and 6.28 show a comparison of the predicted and measured wall temperatures for non-uniform inlet-peak AFD test section. The results for an inlet-peak AFD tube, equipped with 5 streamlined obstacles having a 12% flow-blockage ratio and a 300-mm pitch, at low-pressure and low-mass flux are presented in Figure 6.27. The corresponding results obtained at high-pressure and high-mass fluxes are shown in Figure 6.28.

In Figure 6.27, downstream from the first and second obstacles, the predicted PDO wall temperatures are lower than the experimental wall temperatures, but for the next developing region (downstream from the third obstacle) the predictions are in excellent agreement with the measured wall temperatures, and downstream from the fourth obstacle, the predicted wall temperature profile is slightly lower than the experimental profile. The furthest downstream region approaches the fully developed film-boiling (the temperatures for the obstacle-equipped test section converge with those of the bare tube).

Figure 6.28 presents similar trends – underpredictions are noticed downstream from the first and second obstacles, but downstream from the third obstacle the agreement between the predicted and measured temperatures is good, while downstream fourth obstacle a slight overprediction is observed. The predicted temperature drop at the second obstacle cannot be observed, since upstream from the second obstacle, the predicted dryout-enhanced FB heat transfer exceeds the predicted obstacle-enhanced FB heat transfer until the trailing edge of the obstacle, where the obstacle-enhanced FB shows a slightly higher heat-transfer prediction.

Figure 6.29 shows the results for an outlet-peak AFD test section, equipped with 5 streamlined obstacles, at low-pressure and low-mass flux. The results are similar to those of the inlet-peak AFD test section. At $x = 0.84$, this point (maximum) belongs to step no. 15 of the outlet-peak AFD ($z = 1.781$ m, $q/q_{av} = 0.946$) and the next minimum point has a different flux shape ($q/q_{av} = 0.658$). These changes in the slope disappear when the

predictions of the proposed correlation for the same data are plotted as the inverse of HTC vs. quality (Figure 6.30). In Figure 6.29 the obstacle-enhanced FB is much greater than the dryout–enhanced FB at locations downstream from the 4th obstacle, because the upstream dryout location is far away ($(L/D)_{do} \geq 59$). The absence of rewetting at the location of the 4th obstacle ($x = 0.8$) is probably due to (i) the concentration of droplets in the DFFB is low and the enhancement effect caused by the 12% round obstacles appears to be insufficient to rewet the surface at the 4th obstacle location, and (ii) the reduction in heat flux because of the non-uniform AFD profile. Note that the observed rewetting of the obstacle-equipped tube at the 5th obstacle is due to the axial heat conduction, since the thermocouple is located close to the upper power clamp (2 cm). Figure 6.29 shows again good agreement between predicted and measured film boiling temperature profiles.

The average error in wall temperature = -2.88% and an *rms* error = 12.28%, for all developing FB data used.

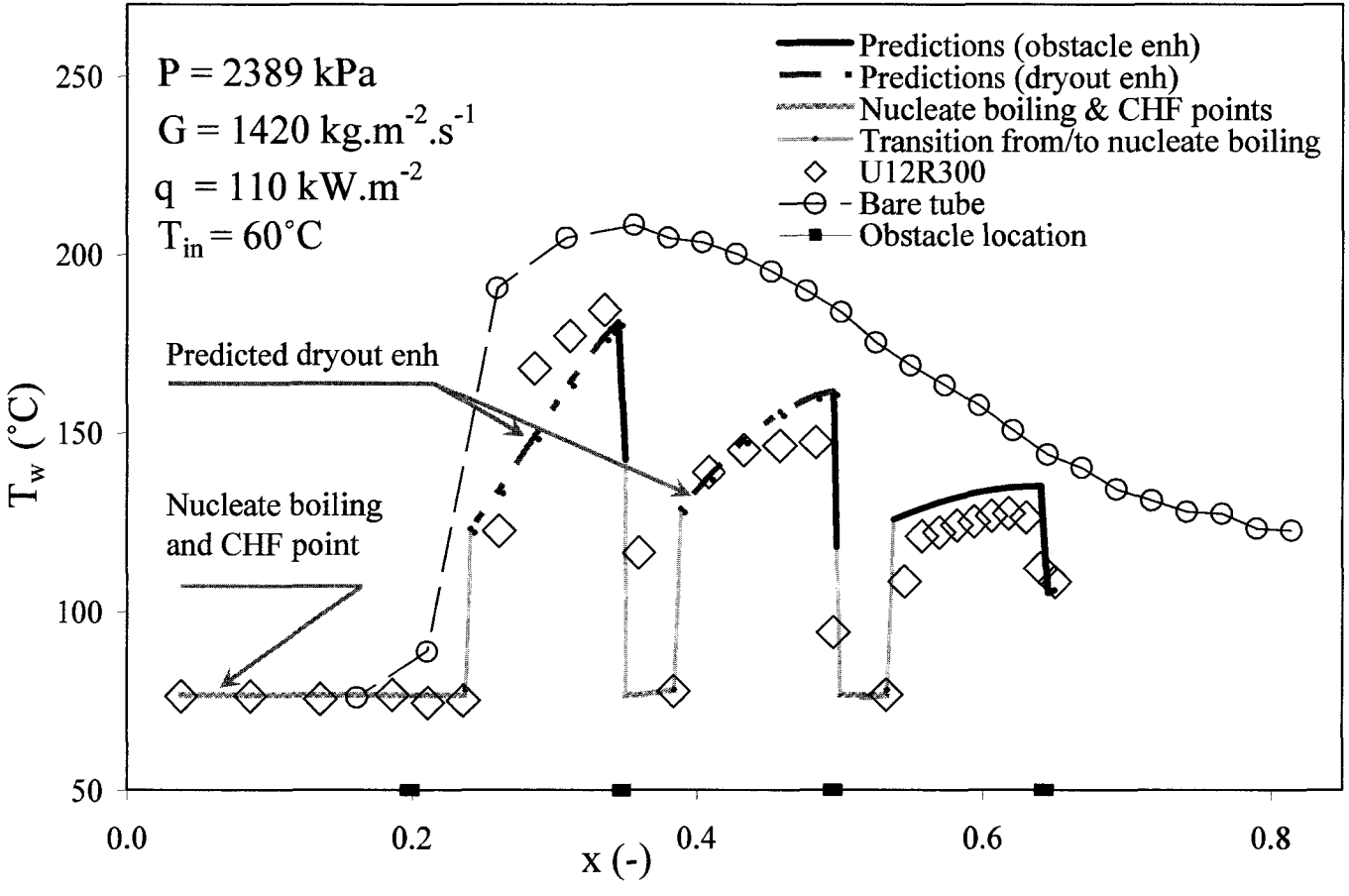

Figure 6.20 Comparison of predicted and measured temperature profiles for U12R300 at high P and low G.

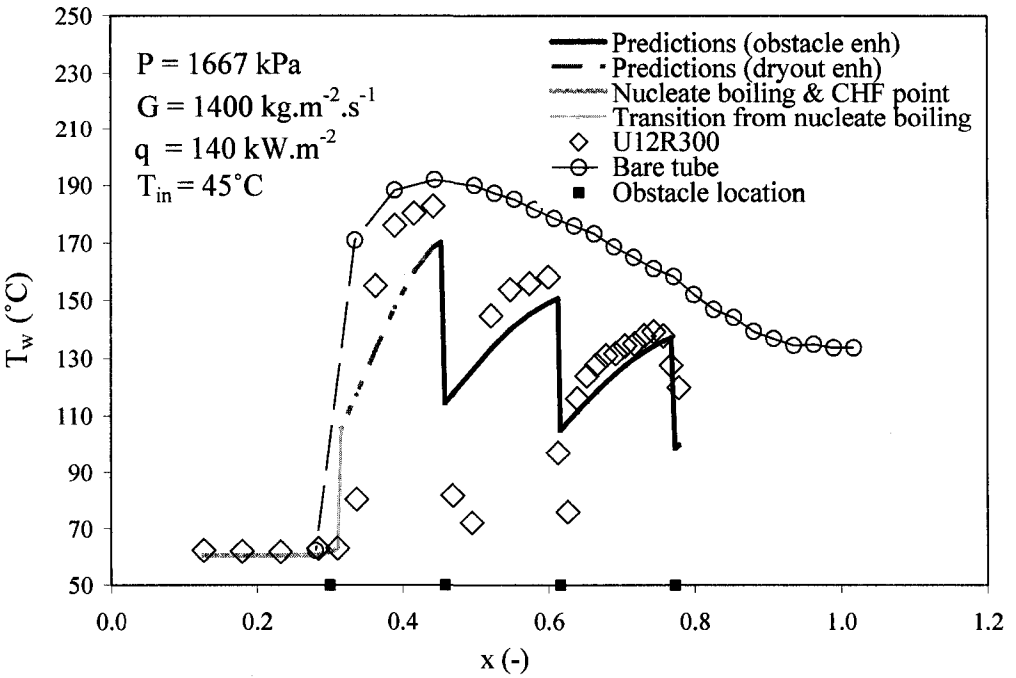

Figure 6.21 Comparison of predicted and measured temperature profiles for U12R300 at low P and G.

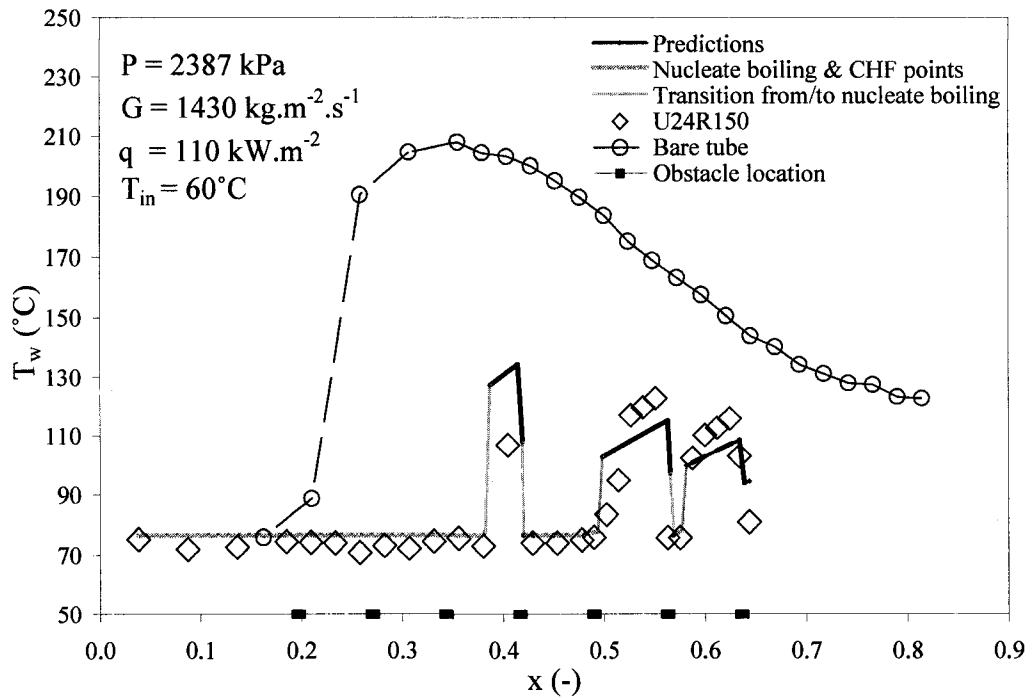

Figure 6.22 Comparison of predicted and measured temperature profiles for U24R150 at high P and low G.

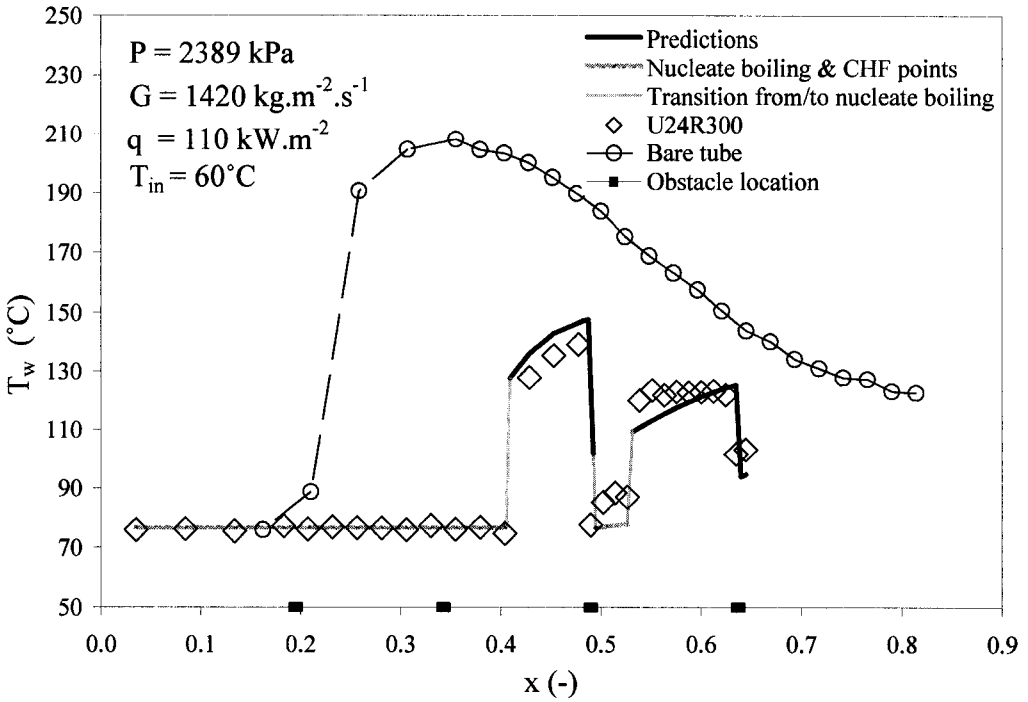

Figure 6.23 Comparison of predicted and measured temperature profiles for U24R300 at high P and low G.

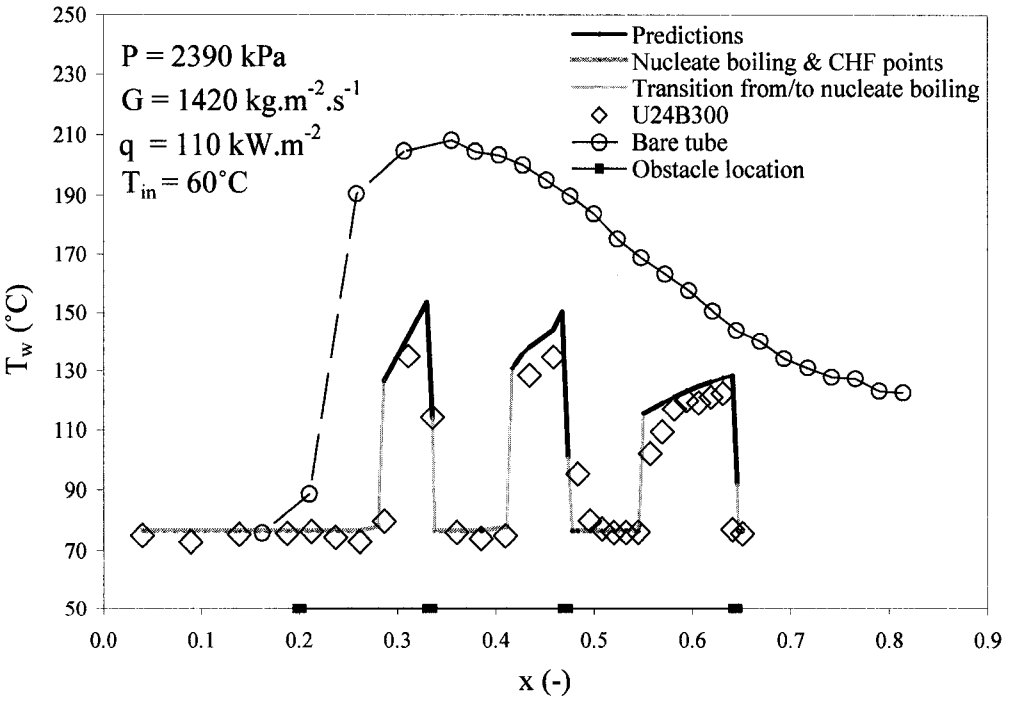

Figure 6.24 Comparison of predicted and measured temperature profiles for U24B300 at high P and low G.

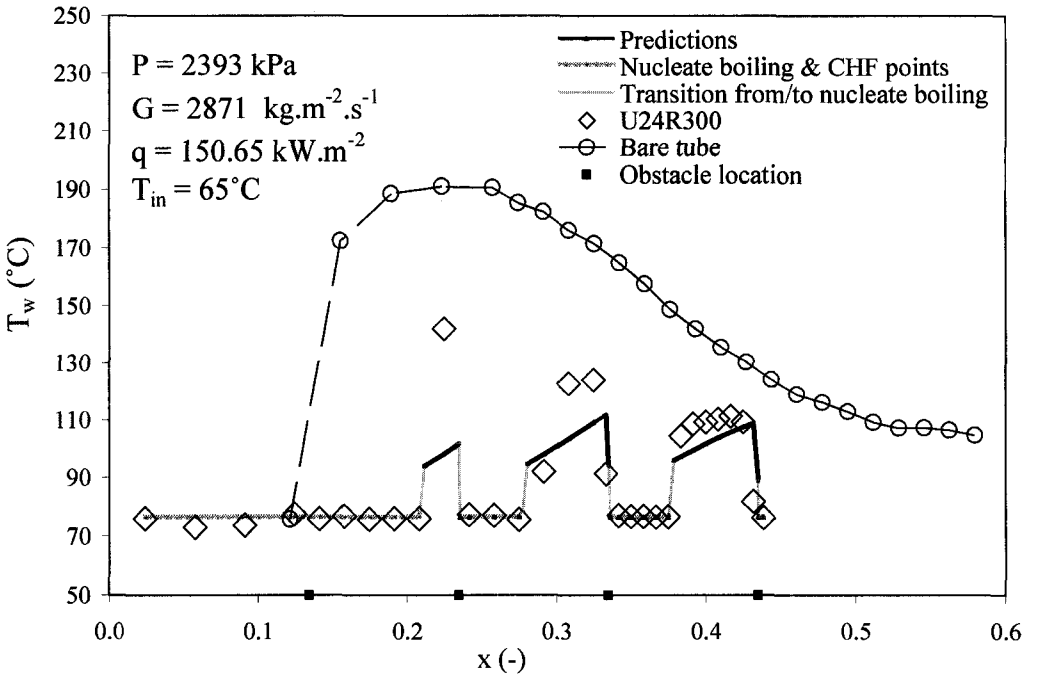

Figure 6.25 Comparison of predicted and measured temperature profiles for U24R300 at high P and G.

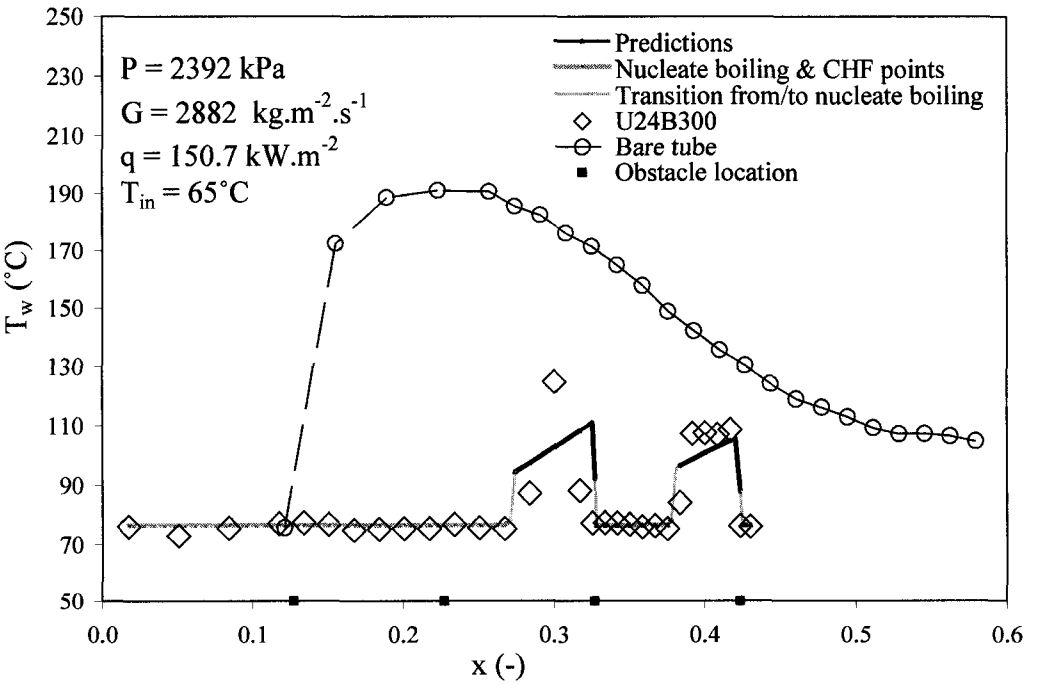

Figure 6.26 Comparison of predicted and measured temperature profiles for U24B300 at high P and G.

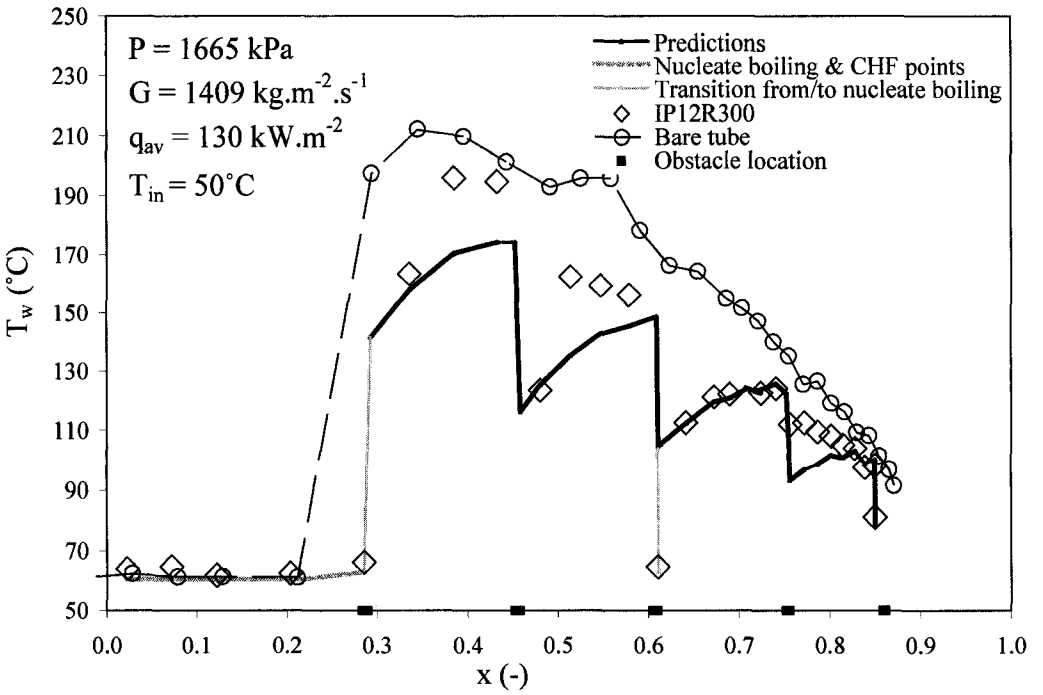

Figure 6.27 Comparison of predicted and measured temperature profiles for IP12R300 at low P and G.

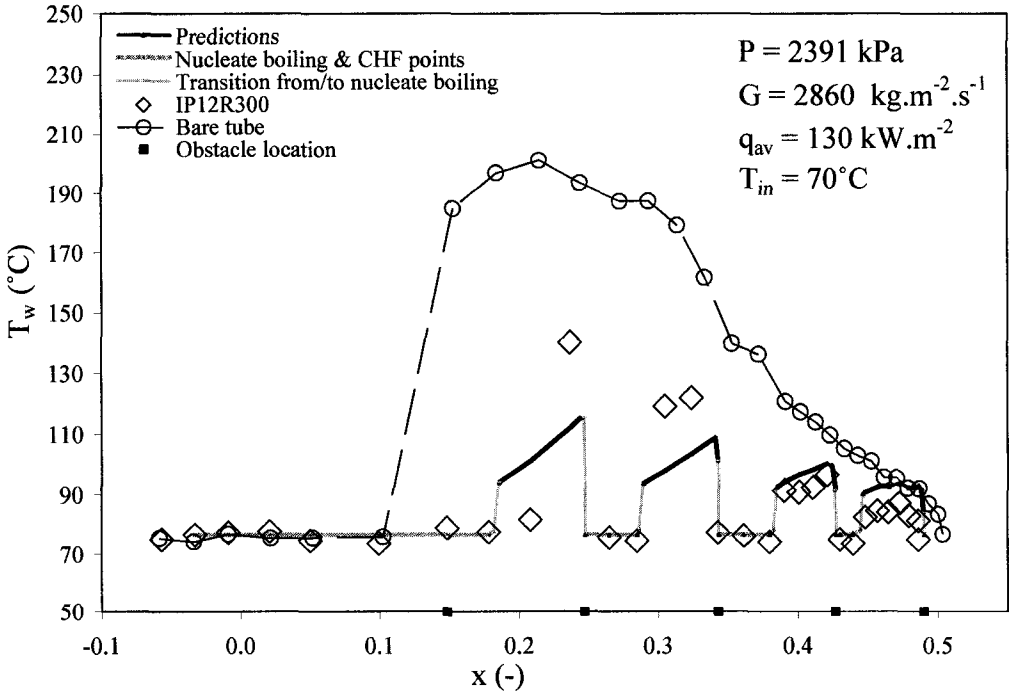

Figure 6.28 Comparison of predicted and measured temperature profiles for IP12R300 at high P and G.

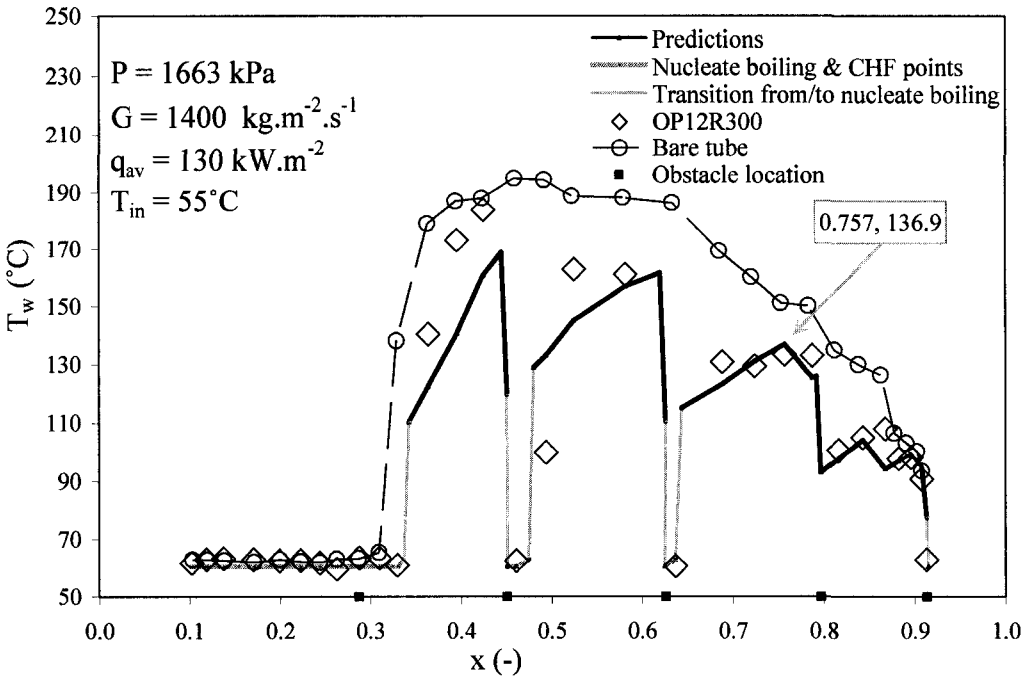

Figure 6.29 Comparison of predicted and measured temperature profiles for OP12R300 at low P and G.

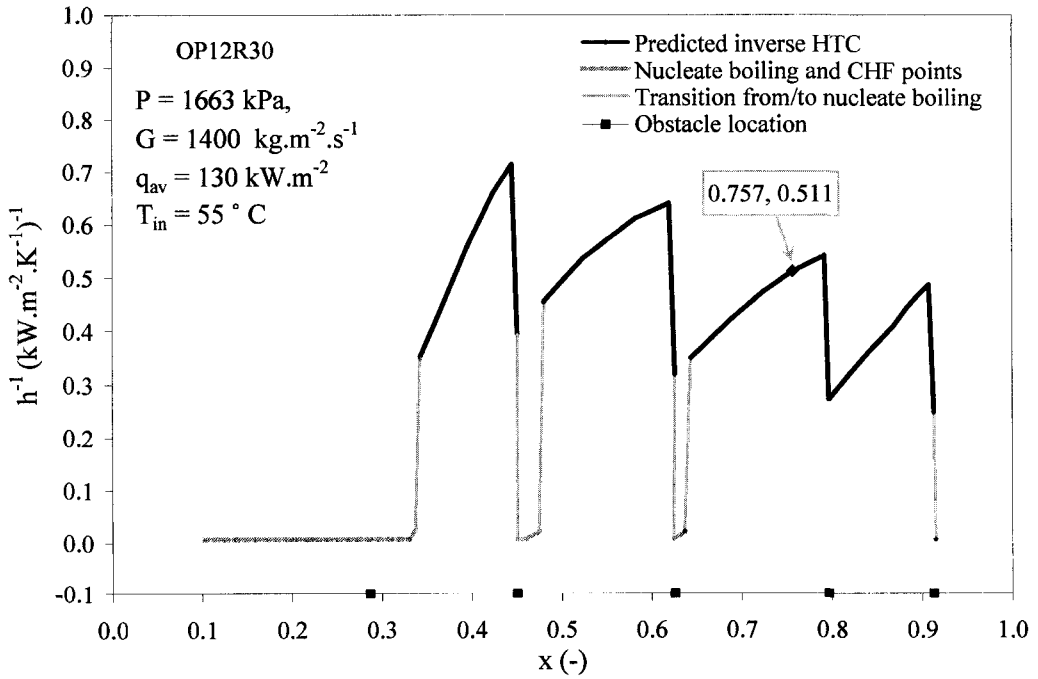

Figure 6.30 Predicted inverse HTC distribution for OP12R300 at low P and G.

6.7 Discussion

6.7.1 Comparison of the Proposed Prediction Method and Previous Methods

The proposed correlation shows that the overall heat-transfer enhancement is strongly affected by (i) distance from the nearest upstream obstacle, (ii) distance from the nearest upstream dryout front, (iii) local quality x, (iv) obstacle flow-blockage coefficient (K_{ob}) and (v) vapour Reynolds number (Re_V). Previous prediction methods for FB heat-transfer enhancement, discussed in Chapters 2 and 5, also showed the significance of these parameters in correlating the FB heat-transfer enhancement.

The proposed prediction method has been applied to uniform AFD and non-uniform AFD tubes; the results show reasonable agreement between measured and predicted wall temperature profiles. The parameters of the prediction method are dimensionless and can therefore be applied to predict the FB wall temperatures distribution for obstacle-equipped channels cooled by water. However the validity of applying the proposed method to water needs to be validated against water-based FB data obtained on obstacle-equipped test sections. For the fully developed FB region, the use of the film boiling look-up table (Groeneveld et al., 2003) is recommended.

A comparison of the proposed prediction method with previous prediction methods and with the measured wall temperatures are presented in Figures 6.31–6.34, where the experimental bare-tube Nu_0 was used for the Leung et al. and Yao et al. predictions. Figures 6.31 and 6.32 show the comparison for uniform-AFD tube with 4 streamlined obstacles having a 12% flow-blockage ratio, while Figures 6.33 and 6.34 show the comparison for the uniform-AFD tube with 4 streamlined obstacles having a 24% flow-blockage ratio. Both the Leung et al. and the Yao et al. prediction methods could not predict the present data, although the wall temperature profile predicted by Leung et al. (2005) results in slightly more reasonable predictions compared to the predictions of Yao et al. (1982) which overpredicted the measured wall temperatures significantly (Figure 6.31). This overprediction was expected since the Yao et al. correlation is derived for single-phase flow and therefore does not include droplet enhancement effects. Figure

6.32 shows the same temperature profiles as in Figure 6.31, except for the application of the nucleate boiling correction factor to Leung et al. (2005) predictions (see Section 5.5.4). Figure 6.33 shows the predicted temperature profile by Leung et al. (2005), the predicted profile is significantly higher than the measured temperatures. Even when the correction factor for $h_{Chen,nb}$ was applied, the predicted temperature profile is still clearly too high as can be seen in Figure 6.32 and especially in Figure 6.34.

6.7.2 Asymptotic Values of $(Nu/Nu_0)_{do}$ and $(Nu/Nu_0)_{ob}$

The asymptotic values of $(Nu/Nu_0)_{do}$ and $(Nu/Nu_0)_{ob}$, were calculated at x = 0 and 1, and respectively at Re_V = 73341 and 520960 for the test section configuration U24R300 (with the higher single-phase-pressure-loss coefficient, K_{ob} = 0.3227) and are shown in Table 6.4. The table shows that the predicted dryout effect by Equation (6.1) (5th column) has a value of 1.015 at x = 1.0 and $(L/D)_{do}$ = 30. However at x = 0 and $(L/D)_{do}$ = 30, $(Nu/Nu_0)_{do}$ = 8.24 — this much higher value reflects the experimental trend (see Figure 6.4 and 6.5) at lower qualities. Sergeev et al. (1990) observed the same increasing FB heat-transfer enhancement trend with decreasing quality.

The predicted $(Nu/Nu_0)_{do}$ has a value of 1.00 at $(L/D)_{do}$ = 100 and x = 1.0; however at $(L/D)_{do}$ = 100 and x = 0, $(Nu/Nu_0)_{do}$ has a value of 1.62. The value at x = 1.0 represents a smooth transition from PDO to single-phase heat-transfer. Additional experimental data are required to confirm the rather high $(Nu/Nu_0)_{do}$ value at x = 0.

Similar asymptotic values were also calculated for Equation (6.5), where K_{ob} = 0.3227 for streamlined obstacles with 24% flow-blockage ratio and 300 mm pitch. The obstacle-enhanced film boiling predicted by Equation (6.5) has a value of 3.8 at Re = 520960 and $(L/D)_{ob}$ = 0; however at Re_V = 73341 and $(L/D)_{ob}$ = 0, $(Nu/Nu_0)_{ob}$ = 4.29, this trend reflects the experimental trend (Figures 6.8 and 6.9). Equation (6.5) predicts $(Nu/Nu_0)_{ob}$ = 1.08 at x = 1.0, $(L/D)_{ob}$ = 100, and Re_V = 520960 and a value of 1.1 at x = 0.0, $(L/D)_{ob}$ = 100, and

Re_V = 73341. These values are somewhat higher than what is expected for obstacle heat-transfer enhancement in single-phase flow.

Table 6.4 Asymptotic values for Equation (6.1) and (6.5), U24R300.

x	Re_V	$(L/D)_{do}$	$(L/D)_{ob}$	$(Nu/Nu_0)_{do}$	$(Nu/Nu_0)_{ob}$
0	73341	30	0	8.24	4.29
1	520960	30	0	1.015	3.8
0	73341	100	100	1.62	1.1
1	520960	100	100	1.00	1.08

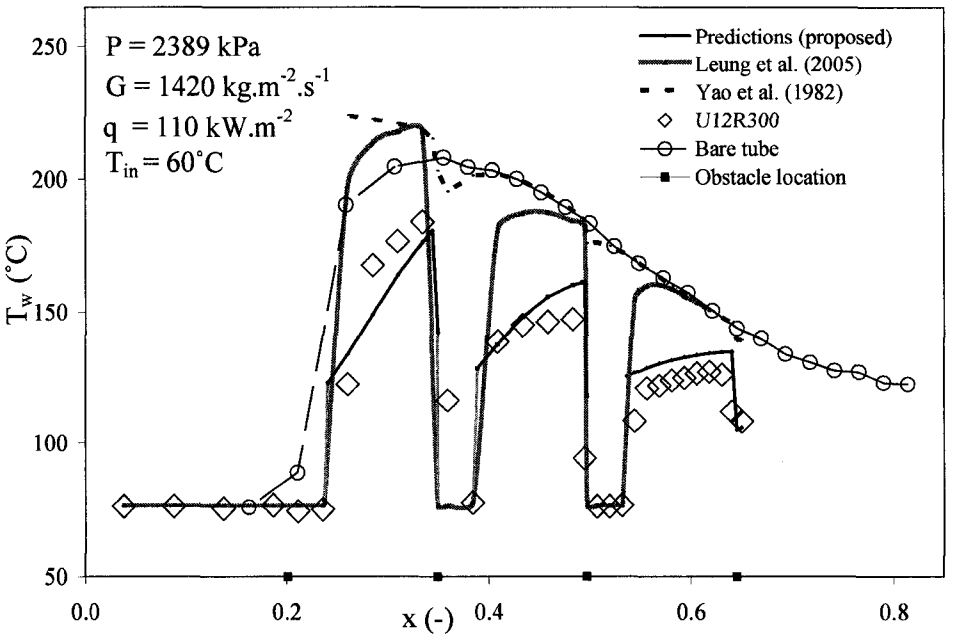

Figure 6.31 Comparison of the predicted temperature profiles of the proposed correlation, Yao et al. (1982), Leung et al. (2005) and the measured temperature profile for U12R300.

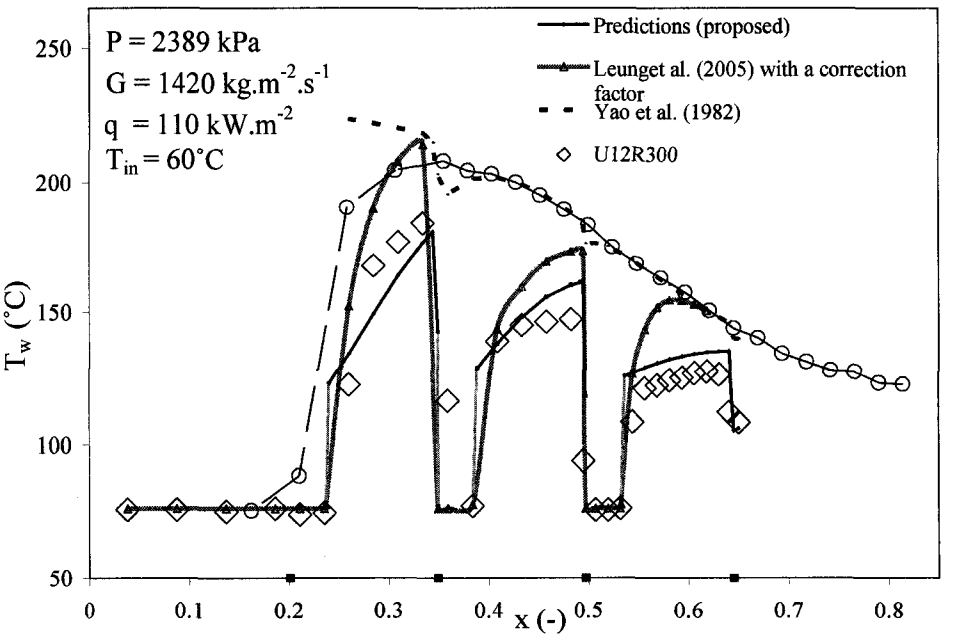

Figure 6.32 Comparison of the predicted temperature profiles of the proposed correlation, Yao et al. (1982), Leung et al. (2005) with a correction factor and the measured temperature profile for U12R300.

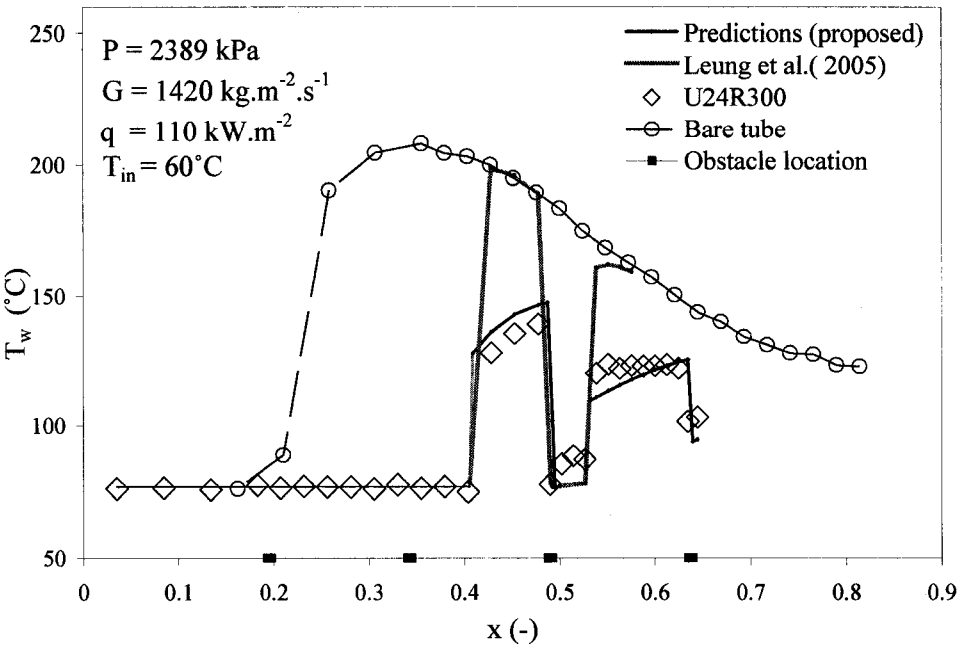

Figure 6.33 Comparison of the predicted temperature profiles of the proposed correlation, Yao et al. (1982), Leung et al. (2005) and the measured temperature profile for U24R300.

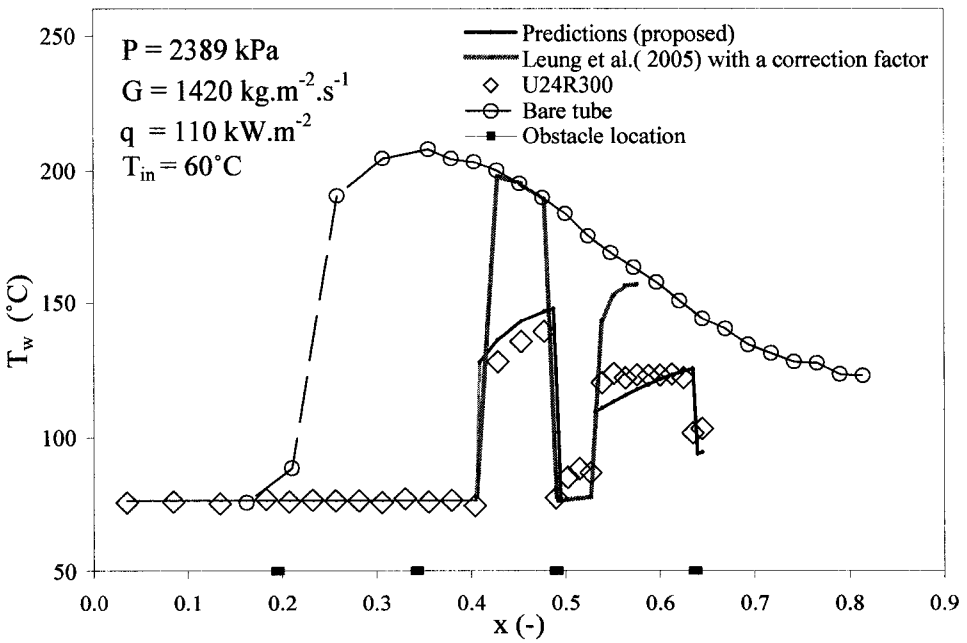

Figure 6.34 Comparison of the predicted temperature profiles of the proposed correlation, Yao et al. (1982), Leung et al. (2005) with a correction factor and the measured temperature profile for U24R300.

CHAPTER 7

CONCLUSIONS AND FINAL REMARKS

1. A unique experimental study has been performed to examine the impact of obstacle and axial power profile on film boiling heat transfer in tubes. The experiment covered a sufficiently wide range of flow conditions, and provided a vast amount of information and experimental data.

2. For the same flow conditions and power, flow obstacles significantly decrease the film-boiling wall temperatures and delay the occurrence of CHF to a downstream location.

3. As expected, film-boiling wall temperatures for obstacle-equipped test sections having a 150-mm obstacle pitch are lower than those for a 300-mm pitch. At low-mass fluxes, the wall temperatures almost coincide at locations just upstream of an obstacle.

4. Film-boiling wall temperatures for the 24% obstruction-ratio obstacle are slightly lower than those for the 12% obstruction-ratio obstacle, especially at locations closer to the outlet. However, the 24% obstruction-ratio obstacle tends to suppress CHF occurrence at low qualities and can result in a large temperature variations in the vicinity of the obstacle.

5. Film-boiling wall temperatures for obstacle-equipped tubes of inlet-peak and outlet-peak profiles converge with those for the bare tube at the downstream end of the test section.

6. The presence of blunt obstacles leads to a delay in the onset of CHF occurrence and a slightly lower film-boiling wall temperatures, compared to streamlined obstacles of the same size at similar flow conditions.

7. This thesis presents an improved prediction method for film-boiling heat-transfer enhancement due to flow obstacles. The proposed prediction method is simple, has the right asymptotic trends, and does not include complex parameters to be estimated.

8. Existing correlations correctly identified the important parameters (exp (-CL/D), x, x_{do}, K_{ob}) but did not adequately predict the observed trends.

9. The proposed prediction method predicts the measured temperature profiles for the developing FB region in both uniform and non-uniform AFD test sections covered in the experiment.

10. The new prediction method contains only dimensionless parameters and can therefore be applied to water. However, its applicability has only been demonstrated at water-equivalent pressures[5] of 10 and 14 MPa. Further validation with relevant water data is strongly recommended.

11. CHF predictions in presence of obstacles can be improved, but ideally we need more CHF data in obstacle-equipped tubes to get the optimum prediction.

12. Current prediction methods do not adequately represent the impact of the flow obstructions on the CHF magnitude and on CHF locations. This was found to be due to (i) the strong impact of the limiting quality region, and (ii) the difficulty in accurately predicting this region.

[5] See Table 3.1

REFERENCES

Anglart, H., Persson, P., and Hedberg, S., (2005), "Experimental Investigation of Stationary and Transient post-Dryout Heat-transfer in 22.1×10 mm Annulus with Spacers", Proceedings of the International Meeting on Nuclear Reactor Thermal-Hydraulics (NURETH-11), Avignon, France, October 2–6.

Azzopardi, B.J., (1996), "Prediction of Dryout, and Post-Burnout Heat-transfer with Axially non-Uniform Heat Input by Means of Annular Flow Model", *Nuclear Engineering and Design*(*NED*), Vol. 163, pp. 51–57.

Becker, K.M., Askeljung, P., Hedberg, S., Soderquist, B., and Kahlbom, U., (1992), "An Experimental Investigation of the Influence of Axial Heat Flux Distribution on Post Dryout Heat-transfer for Flow of Water in Vertical Tubes", Department of Nuclear Reactor Engineering, Royal Institute of Technology, KTH-NEL-54, Sweden.

Chen, J.C., (1963), "A Correlation for Boiling Heat-transfer to Saturated Fluids in Convective Flow", *American Society of Mechanical Engineers* (*ASME*), Vol. 63-HT-34.

Chilton, T.H., and Colburn, A.P., (1934), "Mass Transfer (Absorption) coefficients Prediction from Data on Heat Transfer and Fluid friction" *Industrial and Engineering Chemistry (I & EC)*, Vol. 26 (11), pp. 1183–1187.

Cluss, J.R., (1978), "Post critical Heat Flux Heat-transfer in a Vertical Tube Including Spacer Grid Effects", Master Thesis, Massachusetts Institute of Technology, Cambridge, MA.

Collier, J.G., and Thome, J.R., (1994), "Convective Boiling and Condensation", 3rd ed., Claredon Press, Oxford.

Colburn, A., P., (1933), "A Method of Correlating Forced Convective Heat Transfer Data and a Comparison with Fluid Friction", *Transactions of American Institute of Chemical Engineers (AIChE)*", Vol. 29, p. 174.

Dittus, F.W., and Boelter, L.N.K., (1930), Heat Transfer in Automobile Radiators, Int. Comm. HMT, Vol. 12, pp. 3–22.

El Nakla, M.A., (2007), "Experimental and Analytical Study of Inverted Annular Flow Film Boiling Heat Transfer in a Vertical Tube Using R-134a", Ph-D Thesis, University of Ottawa.

El Nakla, M.A., Groeneveld, D.C., Cheng, S.C., Tanase, A., and Zahlan, A., (2006), "Film Boiling Heat-transfer: Impact of Axial Power Profile and Flow Obstacle, Part I, Experimental and Analytical Study of the Impact of Axial Power Profile", Technical Report, UO-MCG-TH-01, March.

Ergun, S., (2006), "Modeling of Dispersed Flow Film Boiling with Two Flow, Five Field Eulerian- Eulerian Approach and Effects of Spacer Grids on Heat-transfer", Ph-D Thesis, The Pennsylvania State University.

Galchenko et al., (1984), *Teploenergetika*, Vol. 10, pp. 44–46.

Ganic, E.N., and Rohsenow, W.M., (1976), "Post Critical Heat Flux Heat-transfer", MIT Report No. 82672-97.

Gonin, A.I., and Sergeev, V.V., "Dispersed Flow Film Boiling Heat-transfer in Channels with Spacer Elements". Source and year of publication are unknown.

Groeneveld, D.C., (1992), "Inverted Annular and Low Quality Film Boiling: a State-of-the-Art Report", Presented in "Post-Dryout Heat Transfer" Book edited by Hewitt, G.F., Delhaye, J.M., and Zither, N.

Groeneveld, D.C., Doeffer, S., Tain, R.M., Hammouda, N., and Cheng, S.C., (1997), "Fluid-to-fluid modeling of the CHF and PDO Heat-transfer", *Experimental Heat-transfer, Fluid Mechanics and Thermodynamics.*

Groeneveld, D.C., and Fung, K.K., (1976), "Forced Convective Transition Boiling: Review of Literature and Comparison of Predictive Methods", Atomic Energy of Canada Limited, Report AECL-5543.

Groeneveld, D.C., Leung, L.K.H., Vasic, A., Guo, Y.J., and Cheng, S.C., (2003), "A Look-up Table For Fully Developed Film-Boiling Heat-transfer", *Nuclear Engineering and Design* (*NED*), Vol. 225, pp. 83–97.

Groeneveld, D.C., Leung, L.K.H., Zhang, J., Cheng, S.C., and Vasic, A.Z., (1999), "Effect of Appendages on Film Boiling Heat-transfer in Tubes", Proceedings of the Ninth International Topical Meeting on Nuclear Reactor Thermal-Hydraulics (NURETH-9), San Francisco, CA, October 3–8.

Groeneveld, D.C., Pioro, I.L., Guo, Y., Cheng, S.C., Antoshko, Yu.V., Doeffer, S.S., and Vasic, A., (2001), "An Experimental and analytical study of the effect of flow obstacles on the CHF", AECL-12104, FFC-FCT-333.

Groeneveld, D.C., Shan, J.E., Vasic, A.Z., Durmayaz, A., Yang, J., Cheng, S.C., and Tanase, A., (2005), "The 2005 CHF Look-Up Table", log166, Proceedings of the Nuclear Reactor Thermal-Hydraulics (NURETH-11), Avignon, France, October 2–6.

Groeneveld, D.C., and Stewart, J.C., (1982), "The Minimum Film Boiling Temperature for Water during Film Boiling Collapse", Proceedings of the 7th International Heat-Transfer Conference, Munich, West Germany, September, 6–19.

Groeneveld, D.C., and Yousef, W.W., (1980), "Spacing Devices for Nuclear Fuel Bundles: A Survey of their Effect on CHF, Post CHF Heat-Transfer and Pressure Drop", Proceedings of the ANS/ASME/NRC International Topical Meeting on Nuclear Reactor Thermal-Hydraulics, Vol. 2, Saratoga Springs, New York, NY, October 5–8, pp. 1111–1125.

Guo, Y., Groeneveld, D.C., and Cheng, S.C., (2001), "Prediction of CHF Enhancement Due to Flow Obstacles", *International Journal of Heat and Mass Transfer* (*IJHT*), Vol. 44, pp. 4557–4561.

Guo, Y., and Leung, L.K.H, (2005), "Developing Film-Boiling Heat-transfer in Tubes", log 485, Proceedings of the Nuclear Reactor Thermal-hydraulics (NURETH-11), Avignon, France, October 2–6.

Hassan, M.I., and Rehme, K., (1981), "Heat-transfer near Spacer Grids in Gas-Cooled Rod Bundles", *Nuclear Technology*, Vol. 52, pp. 401–414.

Hewit, G. F., and Govan, A. H., (1990), "Phenomenological Modeling of Non-equilibrium Flows with Phase Change", *International Journal of Heat and Mass Transfer* (*IJHT*), Vol. 33, pp. 229–242.

Holloway, M.V., McClusky, H.L., and Beasley, D.E., (2004), "The Effect of Support Grid Features on Local Single-Phase Heat-transfer Measurements in Rod Bundles", *Journal of Heat-transfer*, Vol. 126, pp. 43–53.

Hoyer, N., (1998), "Calculation of Dryout and Post-Dryout Heat-transfer for Tube Geometry", *International Journal of Multiphase Flow*, Vol. 24, No. 2, pp. 319–334.

Incropera, F.P, DeWitt, D.P., Bergman, T.L., Lavine, A.S., (2007), "Fundamentals of Heat and Mass Transfer", 6th ed., John Wiley and Sons.

Isachenko, V.P., Osipova, V.P., and Sukomel, A.S., (1969), *Teploenergetika*, 2nd ed., Moscow: Energy.

Karoutas, Z., Gu, C.Y., and Scholin, B., (1995), "3-D Flow Analyses for Design of Nuclear Fuel Spacer" Proceedings of the 7th International Meeting on Nuclear Reactor Thermal-Hydraulics (NURETH-7), 1, pp. 3153–3174.

Kim, I.G., and Korol'kov, B.P., (1991), "Enhancement of Steady-State post Dryout Heat-transfer in an Annulus with Spacers", *Heat-transfer Soviet Res.,* Vol. 23 (5), pp. 649–657.

Kirrillov, and Groeneveld, D.C., (1999), "General Film Boiling Heat-Transfer Prediction Methods for Advanced Water Cooled Reactors", unknown source.

Krauss et al., (1993), "HFC-134a Transport Properties".

Kreith, F., (1973), "Principles of Heat Transfer", 3rd ed., Intext Educational Publishers, New York.

Leung, L.K.H., Groeneveld, D.C. and Zhang, J., (2005), "Prediction of the Obstacle Effect on Film-Boiling Heat-transfer", *Nuclear Engineering and Design* (*NED*), Vol. 235 (6), pp. 687–700.

Marek, J., and Rehme, K., (1979), "Heat-transfer in Smooth and Roughened Rod Bundles near Spacer Grids"' Presented at the *American Society of Mechanical Engineers (ASME)* Winter Annual Meeting, Dec. 2–7, pp. 163–170.

Nagler, A., (2000), "An Eulerian Lagrangian Simulation of the Dispersed Flow Film Boiling Regime During Reflood Including the Spacer Grid Effects", Ph-D Thesis, Pennsylvania State University.

Peng, S.W., Revellin, R., Groeneveld, D.C., Vasic, A.Z., Shang, , D., and Cheng, S.C., (2003), "Effects of Flow Obstacles on Film Boiling Heat-transfer", *Nuclear Engineering And Design* (*NED*), Vol. 222, pp. 89–95.

Pioro, I.L., Groeneveld, D.C., Cheng, S.C., Doerffer, S., and Vasic, A.Z., (2000), " Effect of Flow Obstruction Shape on the Critical Heat Flux", Proceedings of the International Conference on Nuclear Engineering (ICONE-8), Baltimore, MD, April 2–6, (paper #8350).

Pioro, I.L., Groeneveld, D.C., Doerffer, S.S., Guo, Y., Cheng, S.C., and Vasic, A., (2002), "Effects of Flow Obstacles on The CHF in a Vertical Tube Cooled with upward Flow of R-134a", *International Journal of Heat and Mass Transfer* (*IJHT*), Vol. 45 pp. 4417– 4433.

Pioro, I. L., Cheng, S. C., Vasic, A. Z., and Salah, I., (1999), "Experimental Evaluation of the Limiting Critical Quality Values in Circular and Non-circular Flow Geometries", *Nuclear Engineering and Design* (*NED*), Vol. 190, pp. 317–339.

Rehme, K., and Trippe, G., (1979), "Pressure Drop and Velocity Distribution in Rod Bundles with Spacer Grids", *Nuclear Engineering Design* (*NED*), Vol. 62 (1980), pp. 349–359.

Rehme, K., (1973), "Pressure Drop Correlations for Fuel Element Spacers", *Nuclear Technology*, Vol. 17, pp. 15–23.

Sergeev, V.V., (2005), "One-Dimensional Model of post-Dryout Heat-transfer", Proceedings of the 11th International Meeting on Nuclear Reactor Thermal-Hydraulics (NURETH-11), Avignon, France, October 2–6.

Sergeev, V.V., Gonin, A.I., and Remizov, O.V., (1990), "Super Critical Heat Exchange in Channels with Spacer Elements", *Atomnaya Energiya (Soviet Res.)*, Vol. 68 (6), pp. 445–447.

Stewart, J.C., and Groeneveld, D.C., (1982), "Low Quality and Subcooled Film Boiling at Elevated Pressures", *Nuclear Engineering and Design,* Vol. 67, pp. 259–272.

Stosic, Z., (1995), "The Rod Bundle Spacer Effects on Post-Dryout Heat-transfer Augmentation Analyzed by the Model HECHAN 2.1", American Society of Mechanical Engineers (ASME)/Japanese Society Of Mechanical Engineers (JSME) Thermal Engineering Conference: Volume 2.

Tanase, A., Groeneveld, D.C., Zahlan, H.Z., and Cheng, S.C., (2008), "Experimental Investigation of the Obstacles Effect On Single-Phase Heat Transfer", 29th Annual Conference of the Canadian Nuclear Society (CNS), Toronto, ON, CANADA, June 1–4.

Tavoularis, S., (2005), "Measurement in Fluid Mechanics", Cambridge University Press.

Tillner-Roth and Baehr, (1994), "Thermodynamic Properties of HFC-134a", International Standard Formulation for HFC-134a.

Uchida, H., and Kono, N., (1999), "An Experimental Investigation of Grid Spacer Effect on post DNB Heat-transfer", 7th International Conference on Nuclear Engineering, Tokyo, Japan, April 19–23.

Windecker, U., and Gu, C.Y., (1999), "Droplet Deposition in the Annular Flow Regime with and without the Influence of a Spacer", Ninth International Topical Meeting on Nuclear Reactor Thermal-Hydraulics (NURETH-9), San Francisco, California.

Yang, J., Shang, D., El Nakla, M.A., Cheng, S.C., and Groeneveld, D.C., (2003), "An Investigation of the Effect of Axial Heat-Flux Distribution on CHF in Tubes", Technical Report, UO-MCG-TH-02.

Yang, J., Cheng, S. C., and Groeneveld, D. C, (2005), "An Investigation of the Effect of Axial Heat-Flux Distribution on CHF in Tubes in the Presence of Flow Obstruction, UO-MCG-TH-001.

Yao, S.C., Hochreiter, L.E., and Leech, W.J., (1982), "Heat-transfer Augmentation in Rod Bundles near Grid Spacers", Heat-transfer, Vol. 104 (1), pp. 76–81.

Whalley, P.B, Hutchinson, P., and Hewitt, G.F., (1974), " The Calculation of Critical Heat flux for Forced Convection Boiling. 5th Int. Heat-transfer Conf. Tokyo, paper B6.11.

Zahlan, H., Groeneveld, D.C., Leung, L.K.H., Tanase, A., and Cheng, S.C, (2008), "Investigation of the Combined Effect of Appendages and Axial Power Profile on Post-Dryout Heat-transfer in Tubes", 29th Annual Conference of the Canadian Nuclear Society (CNS), Toronto, ON, CANADA, June 1–4.

Zhang, J., (1997), "Geometry Effect on Post-Dryout Heat-transfer", M.A.Sc. Thesis, University of Ottawa.

APPENDIX A

QUALITY ASSURANCE OF THE EXPERIMENTS

The experimental program at the University of Ottawa follows a strict quality assurance (Q/A) protocol to ensure that the data are accurate and reliable. The following Q/A tests and procedures were adhered to:

A.1 Leakage detection

Leakage detection was performed by filling the whole test loop with nitrogen at 400 psi. All of the potential leakage sites were checked using soap and water mixture. Nitrogen remained in the loop for 24 hours after the soap water checking. The system is considered leak-proof if no pressure change is detected during this period.

A.2 Heat loss test

Heat loss tests were performed by applying power to the test section without insulation after evacuating the test loop. After all readings of the thermocouples installed at the test section indicated that the surface temperatures had stabilized, the power supplied to the test section was recorded. In this case the power supplied to the test section was assumed to be equal to the heat loss from the outside tube surface to the environment in the PDO test for the same heated length and the same average outer surface temperature. Heat loss tests were performed at average outer surface temperatures of 91°C and 96°C, which approximately correspond to the maximum average outer surface temperature in the runs of pressures 1665 and 2389 kPa. The results of heat loss test are shown in Figure A1. The

heat loss without insulation on the test section was very small (0.0685 kW for an average thermocouple temperature reading of 96°C).

A.3 Heat balance tests

Heat balance tests were conducted by supplying the power to the uniform, inlet-peak and outlet-peak test sections, with single-phase liquid flowing through the test section. The power supplied to the test section was compared with the enthalpy rise of the fluid. The heat balance results are shown in Figures A2a-f. The difference between the power supplied to the test section and the enthalpy rise of the working fluid ("heat balance error") was less than 2%. For the powers of interest in this experiment (range 3–5 kW) the heat balance error is less than 1%.

Figure A2f shows 2 points with negative heat loss; this is primarily caused by higher errors in the RTDs at certain temperatures as was found from RTD checks described below.

A.4 Calibration of RTD'S

RTDs for measuring inlet and outlet fluid temperatures were calibrated by using calibrated mercury thermometer (1°C subdivision). The thermometer accuracy was checked against boiling temperature of distilled water under atmospheric pressure at the day of calibration (P_{atm} = 100.85 kPa). The temperature reading at 99.8°C was close to the predicted boiling temperature using the NIST properties code of 99.843°C at saturation. A correction factor was applied to outlet RTD reading of the (data acquisition system) DAS based on the calibrated data over the range of interest (i.e., 35°C to 100°C). Other reference points than the boiling water were taken using an insulated copper block, the results of the RTD calibration are shown in Figures A3a-c. The discrepancies between the mercury thermometer and the RTDs were less than 0.54%.

A.5 Calibration of thermocouples

The thermocouples calibration was carried out using an insulated copper block mentioned above by employing a reference temperature reading of the thermometer for temperatures below 111°C, above 111°C calibrated RTDs readings were taken as reference points. The calibration results are shown in Figures A4a-f. For temperatures between 75°C to 200°C, the discrepancies between the mercury thermometer, RTDs and thermocouples were within 1.3 K.

A.6 Calibration of pressure

The accuracy of the pressure gauges was checked while the loop was filled with nitrogen. Two pressure gauges were used as standard (calibrated), one digital, and the other is mechanical (Bourdon tube), which can be read accurately. The values of the inlet and outlet pressures indicated by the DAS were recorded and compared with the values of the pressure gauges. The results are shown in Figures A5a, b. The discrepancies between the reading from the pressure gauges and the DAS pressure readings are less than 0.8% and for the pressure range of interest are less than 0.4%. During experimental work, pressure readings were verified against saturation temperature with 2- phase inlet fluid, the results show good agreement (better than 0.8%) between saturation pressure and DAS reading of pressure. The agreement was better than 0.8%.

A.7 Q/A repeatability tests

Good repeatability is important in any experimental study, and is demonstrated by close agreement between the results of successive measurements of the same parameter performed under the same measurement conditions.

In this investigation, Q/A repeatability tests were performed for uniform, inlet-peak and outlet-peak test sections; the results (Figures A6a-k) show good agreement between experimental data and repeated points. For the uniform test section, repeat tests were carried out with a replacement test section.

For the outlet-peak test section, repeatability tests were performed twice: the results at three heat flux levels were analyzed by two methods: (i) to show agreement in outside wall temperature, and (ii) to show agreement in heat transfer coefficient in the form (1/h vs. local quality).

The results are shown in Figures A6f-k. Figures A6g, A6i and A6k demonstrate the repeatability of the inverse HTC vs. x (-), it is clear that the repeat points and the original data are in excellent agreement.

A.9 Calibration of voltage and current

The readings of voltage and current from DAS were compared with measured values by calibrated Voltmeter and Ammeter (Figures A7a and A7c). The results of calibration show very good agreement expressed as relative error between readings of the DAS and measurements by Voltmeter and Ammeter (Figure A7b and A7d).

Heat loss test, Figure A1

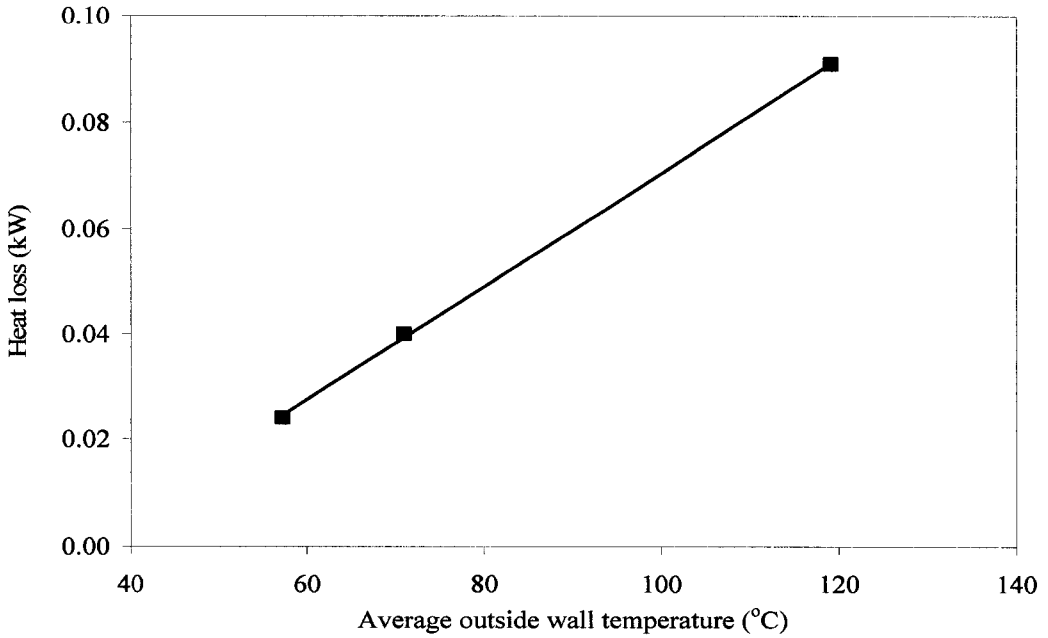

Figure A1 Heat loss test.

Heat balance tests, Figures A2a-f

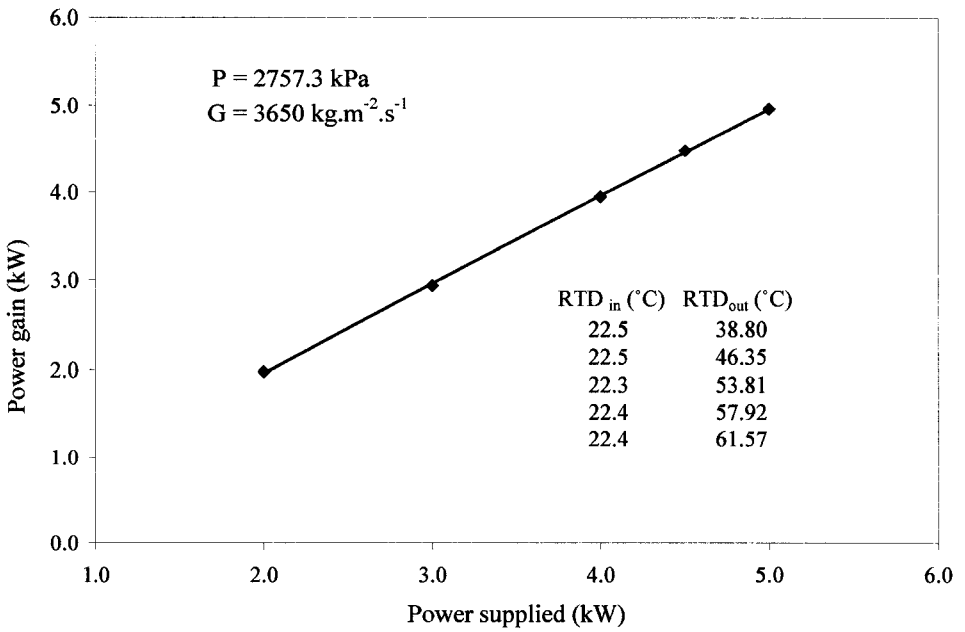

Figure A2a Heat balance test, uniform test section.

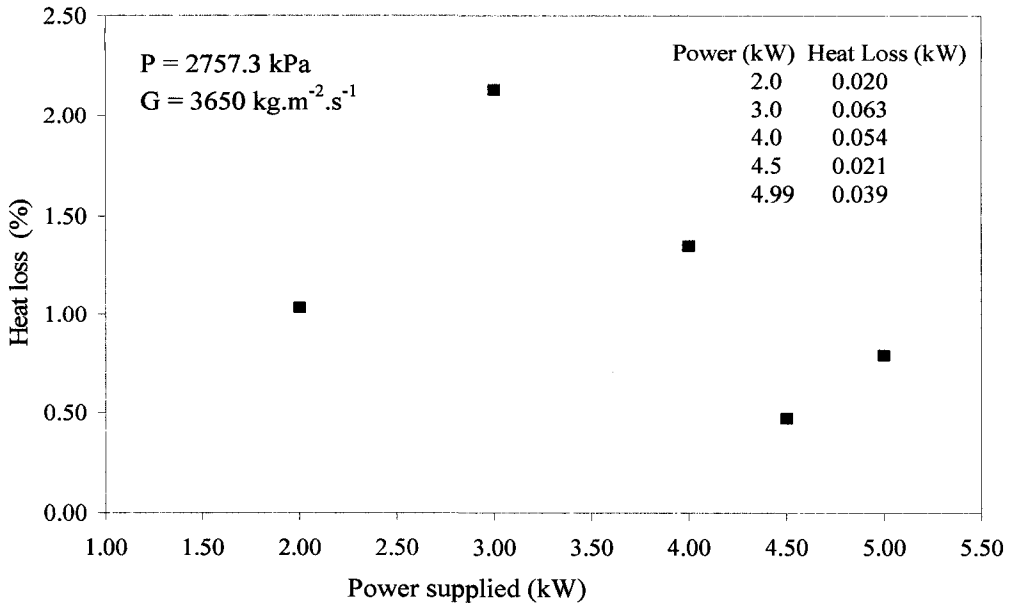

Figure A2b Results heat balance test, uniform test section.

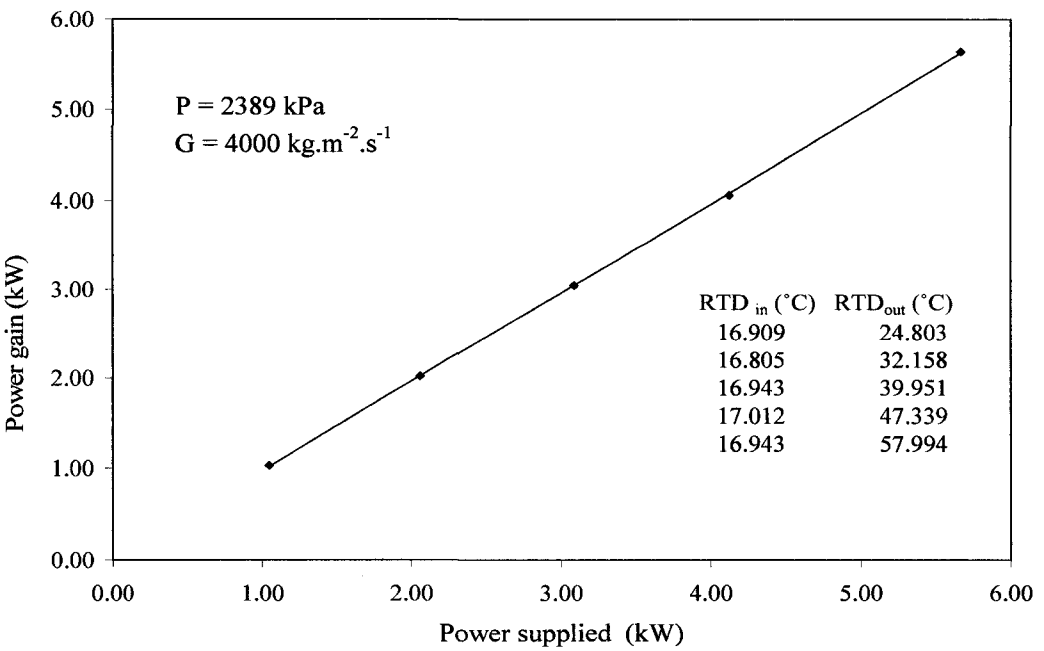

Figure A2c Heat balance test, inlet-peak test section.

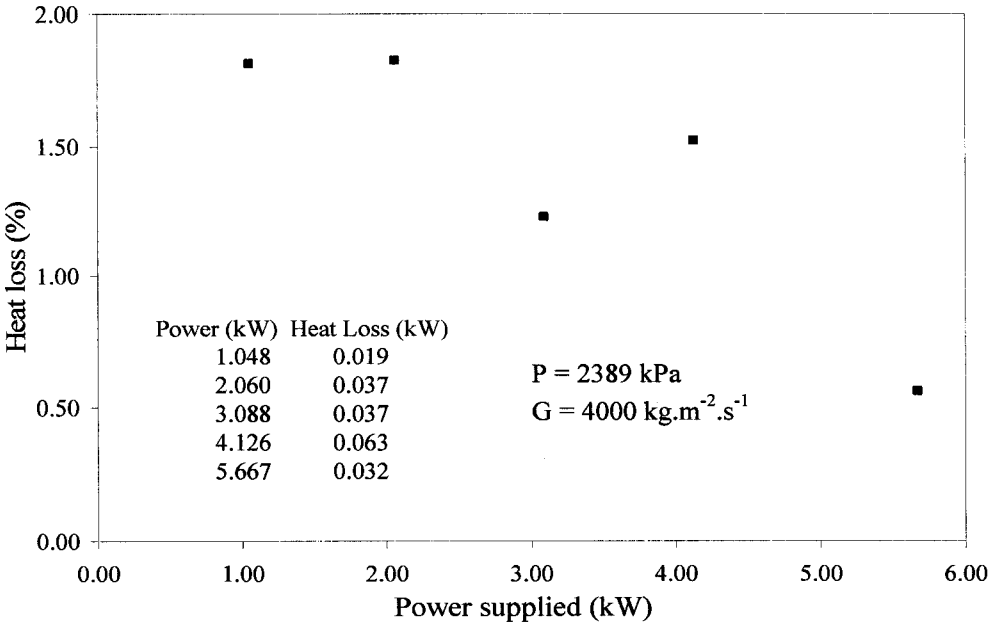

Figure A2d Results heat balance test, inlet-peak test section.

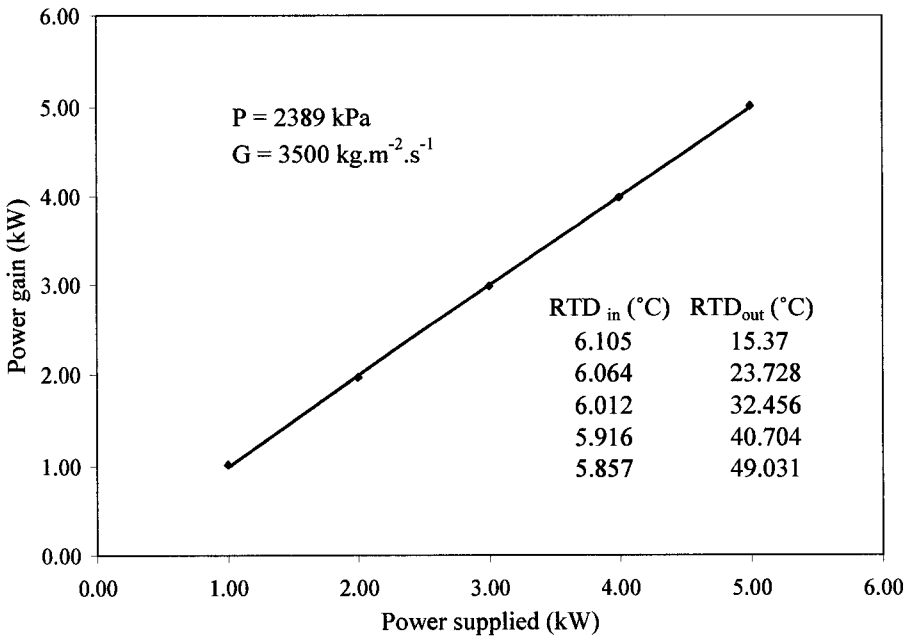

Figure A2e Heat balance test, outlet-peak test section.

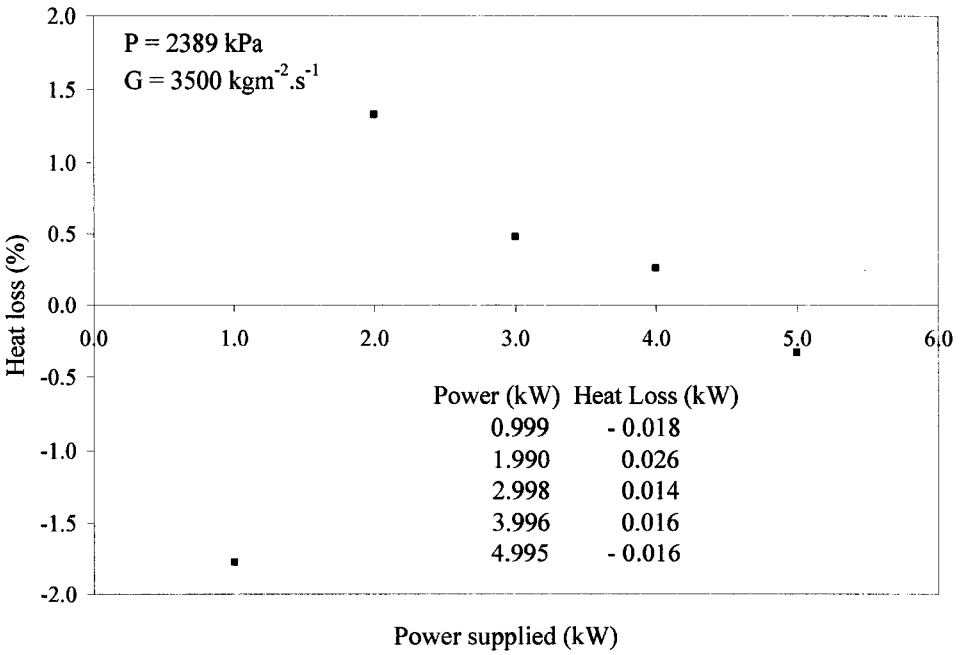

Figure A2f Results heat balance test, outlet-peak test section.

Calibration of RTDs, Figures A3a-c

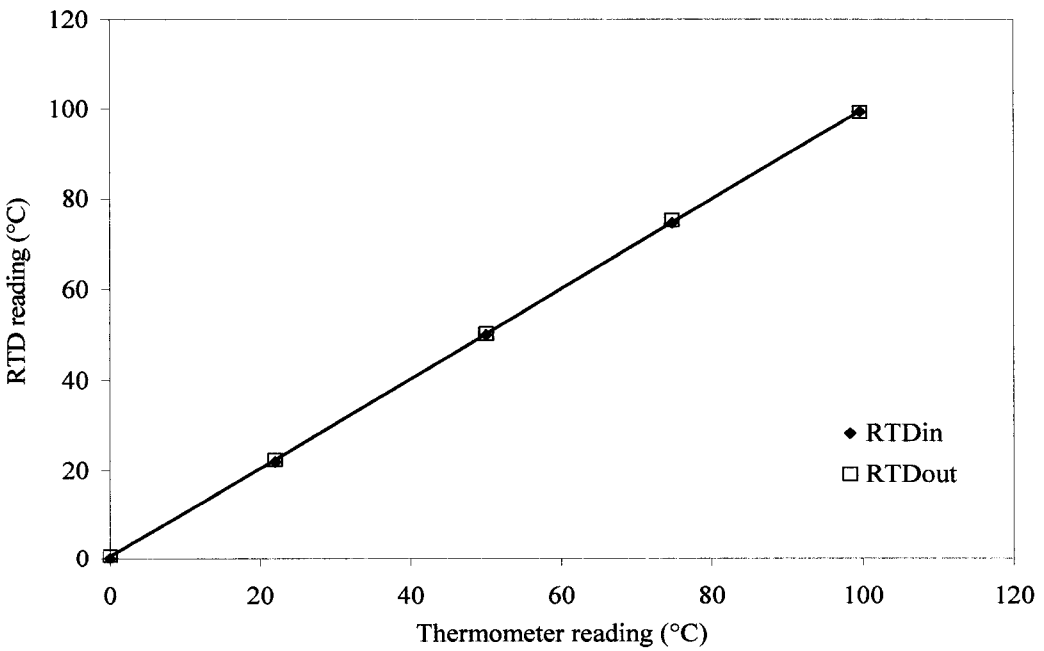

Figure A3a Calibration of RTDs.

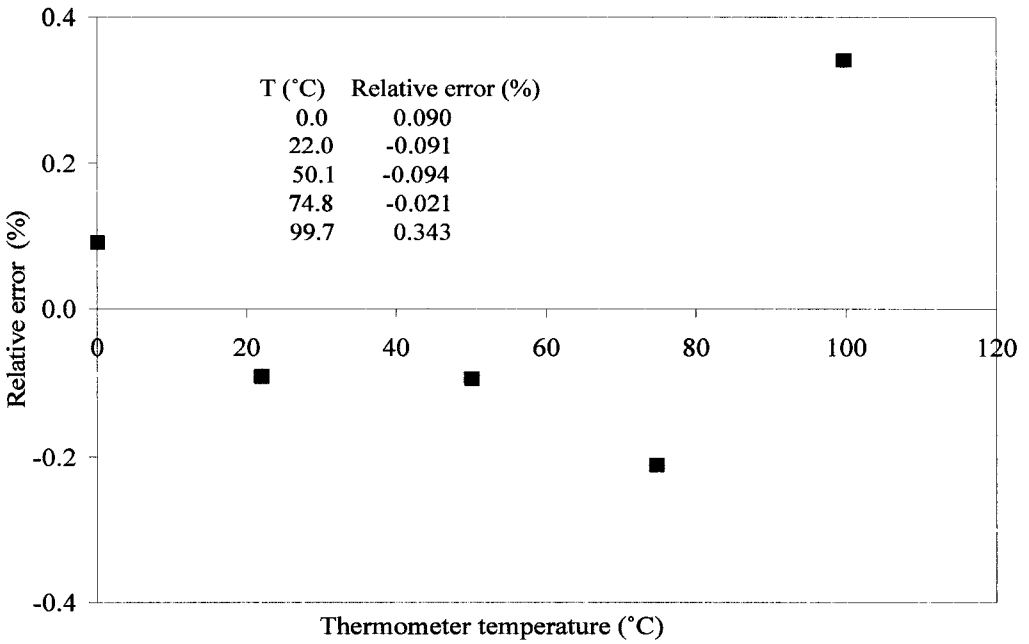

Figure A3b Results of calibration of RTD_{in}.

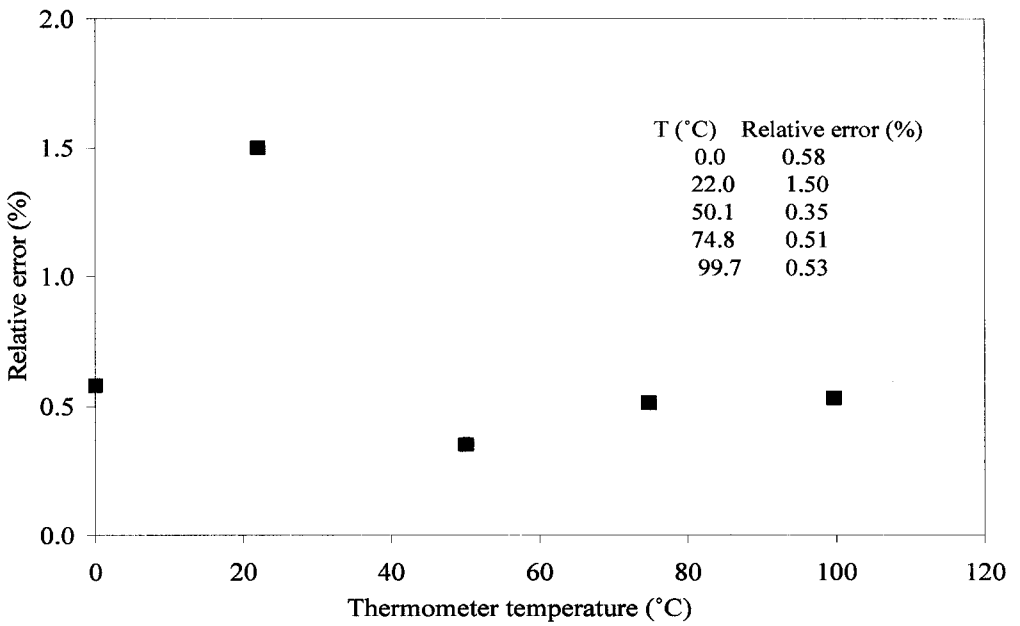

Figure A3c Results of calibration of RTD_{out}.

Calibration of thermocouples, Figures A4a-f

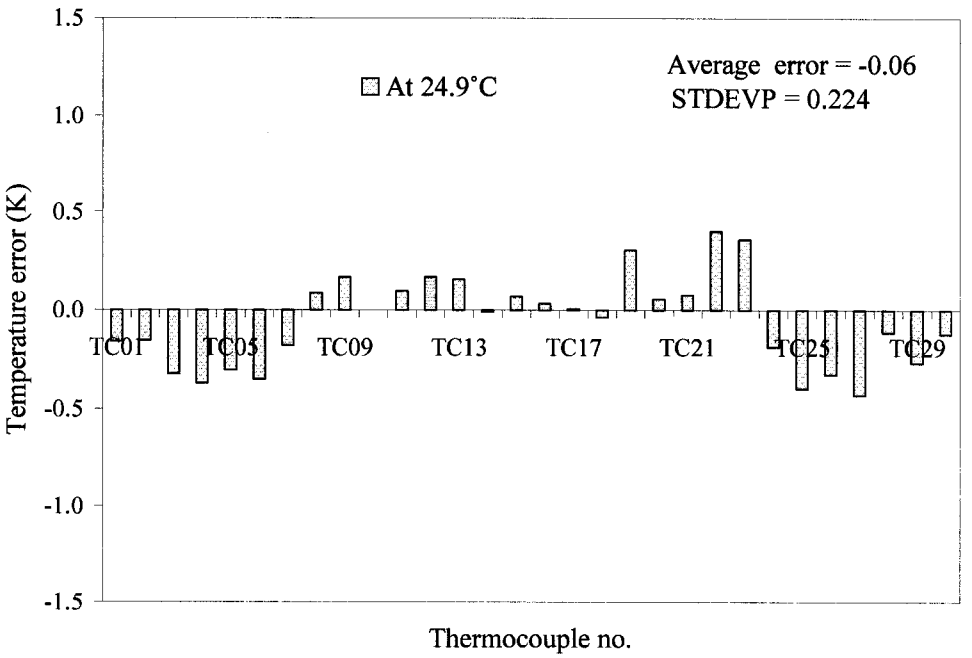

Figure A4a Calibration of thermocouples using a copper block, T = 24.9°C.

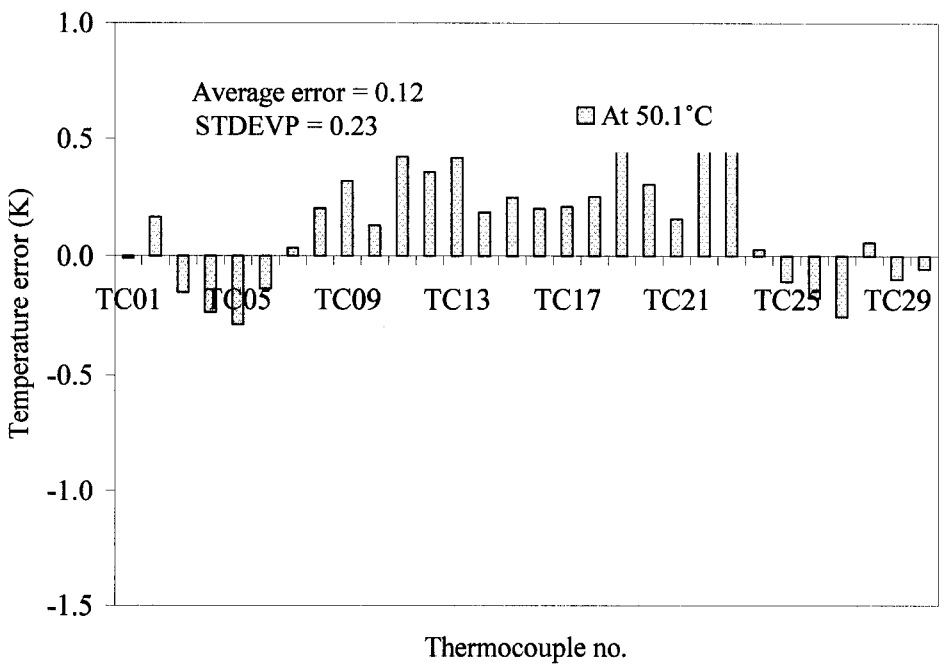

Figure A4b Calibration of thermocouples using a copper block, T = 50.1°C.

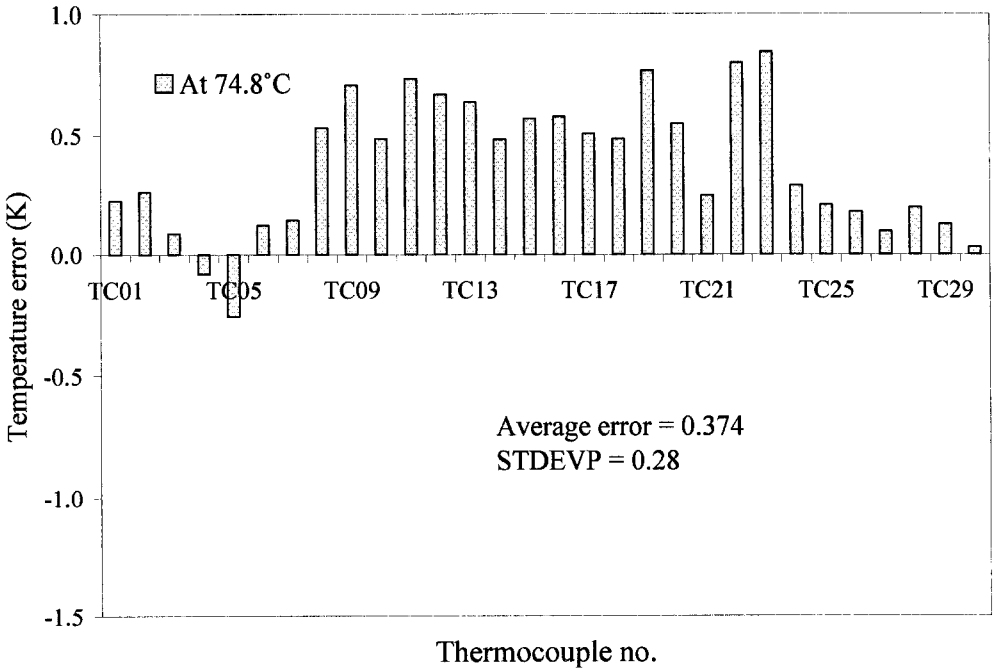

Figure A4c Calibration of thermocouples using a copper block, T = 74.8°C.

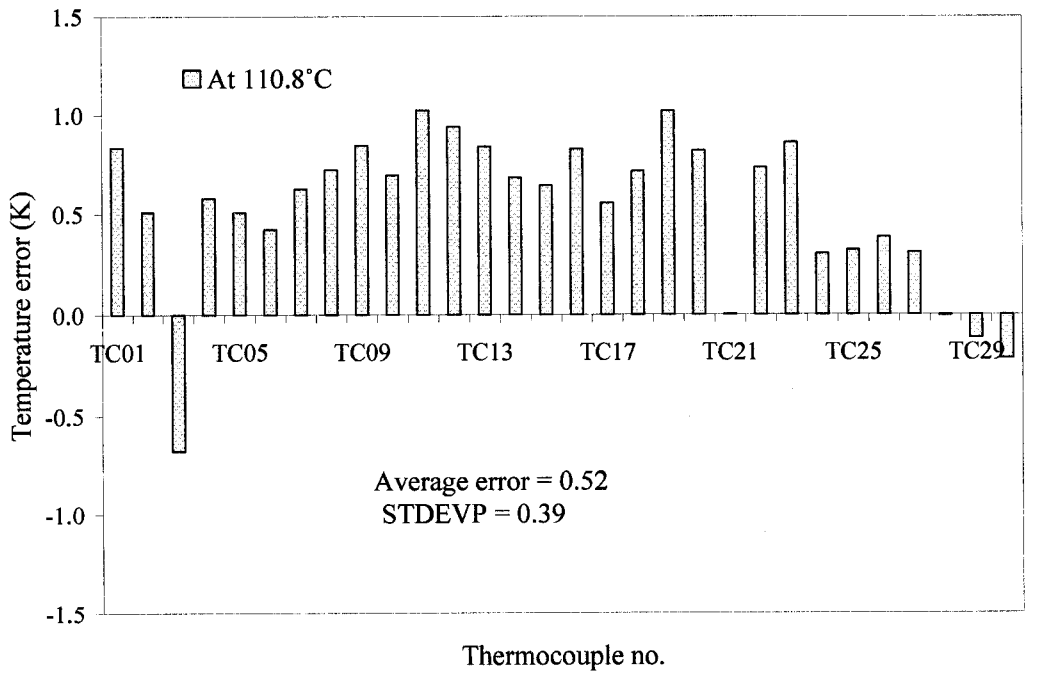

Figure A4d Calibration of thermocouples using a copper block, T = 110.8°C.

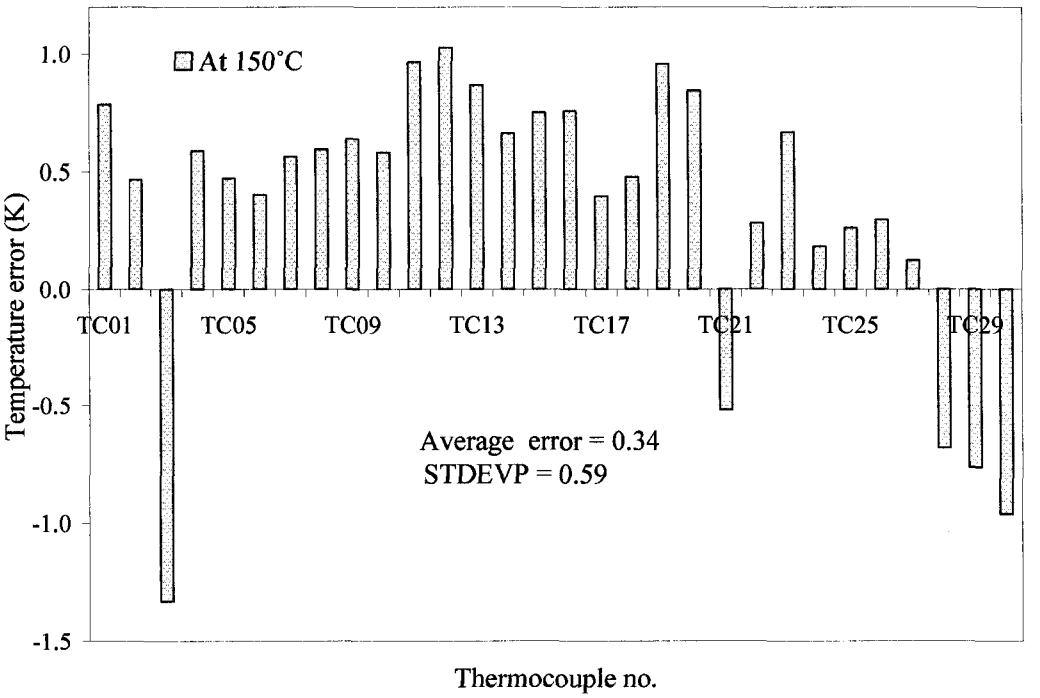

Figure A4e Calibration of thermocouples using a copper block, T = 150°C.

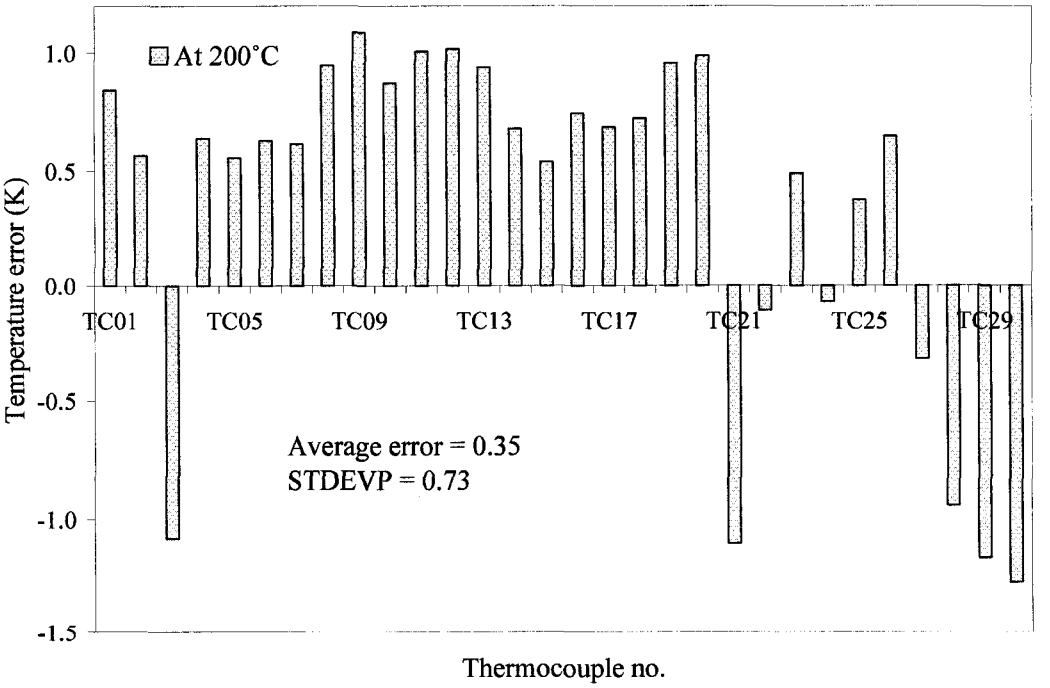

Figure A4f Calibration of thermocouples using a copper block, T = 200°C.

Calibration of pressure, Figures A5a, b

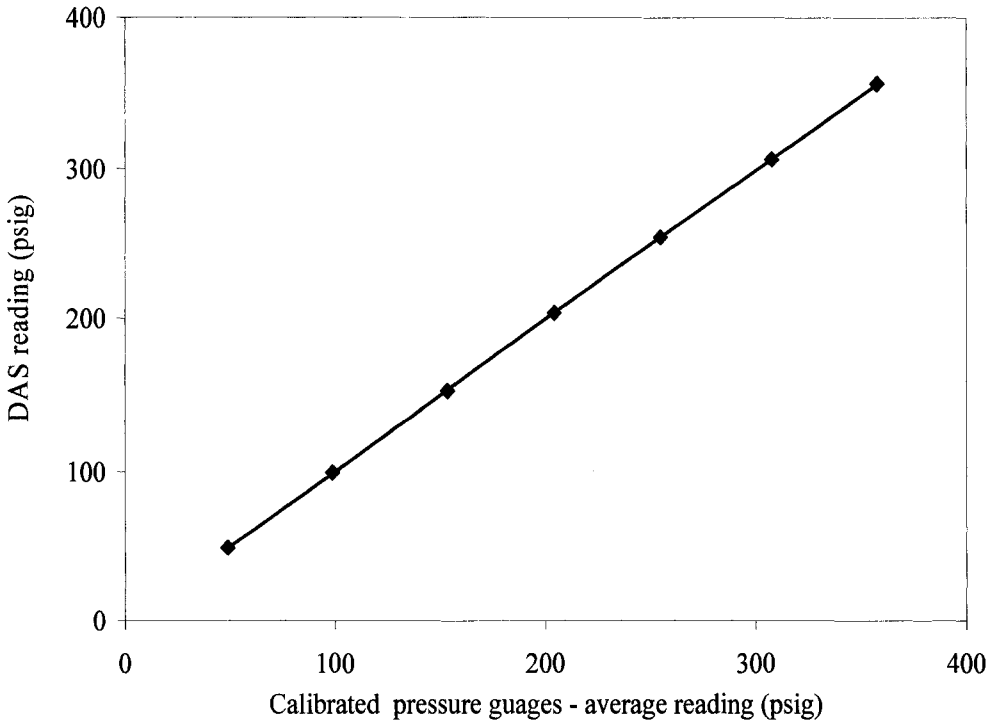

Figure A5a Calibration of pressure.

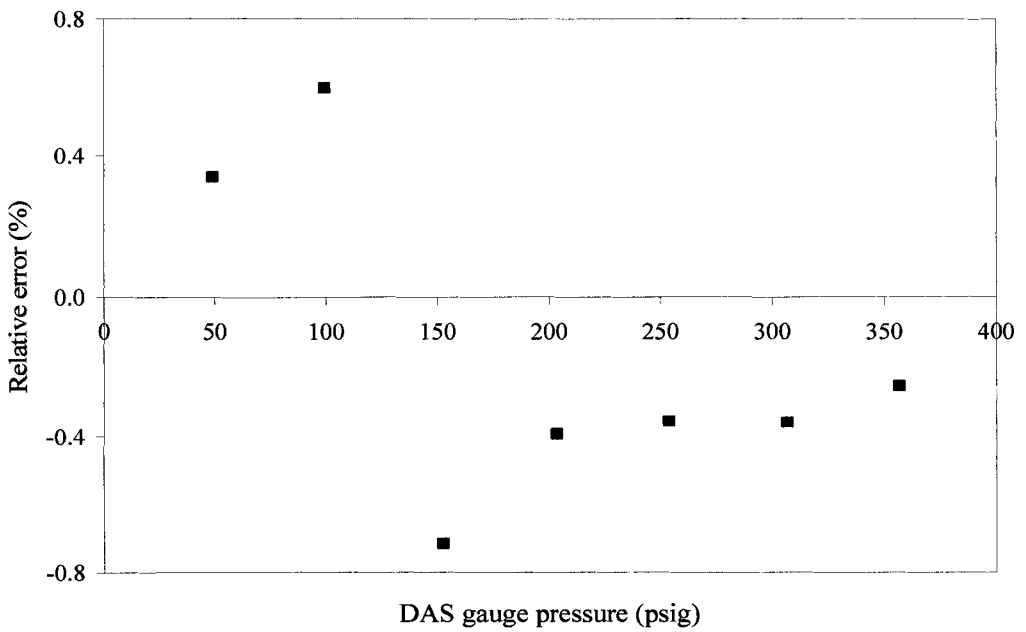

Figure A5b Results of calibration of pressure.

Repeatability test, Figures A6a-k

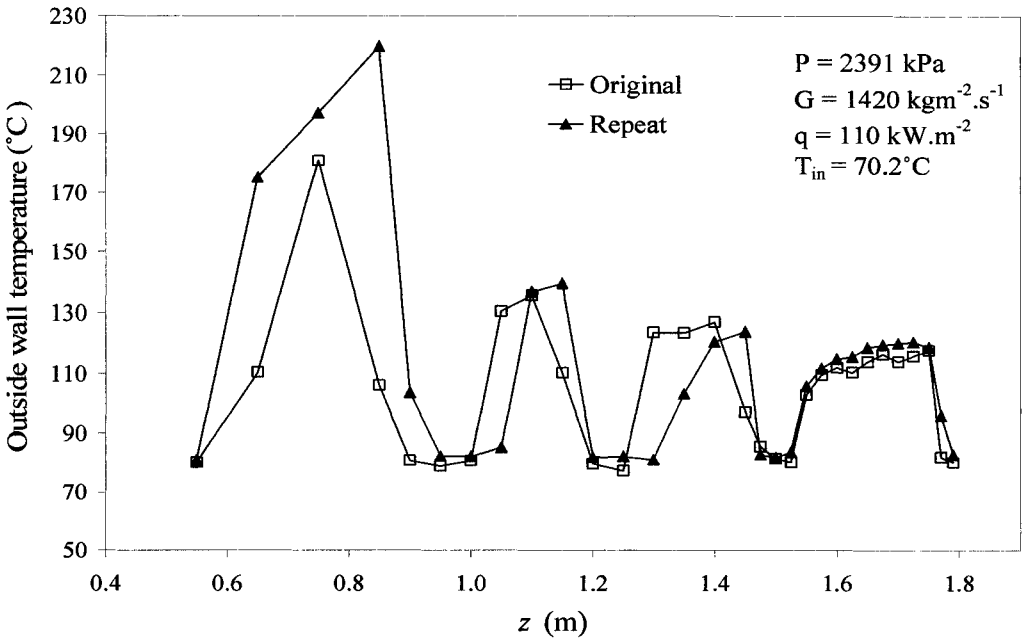

Figure A6a Repeatability test, uniform test section (high-pressure and low-mass flux).

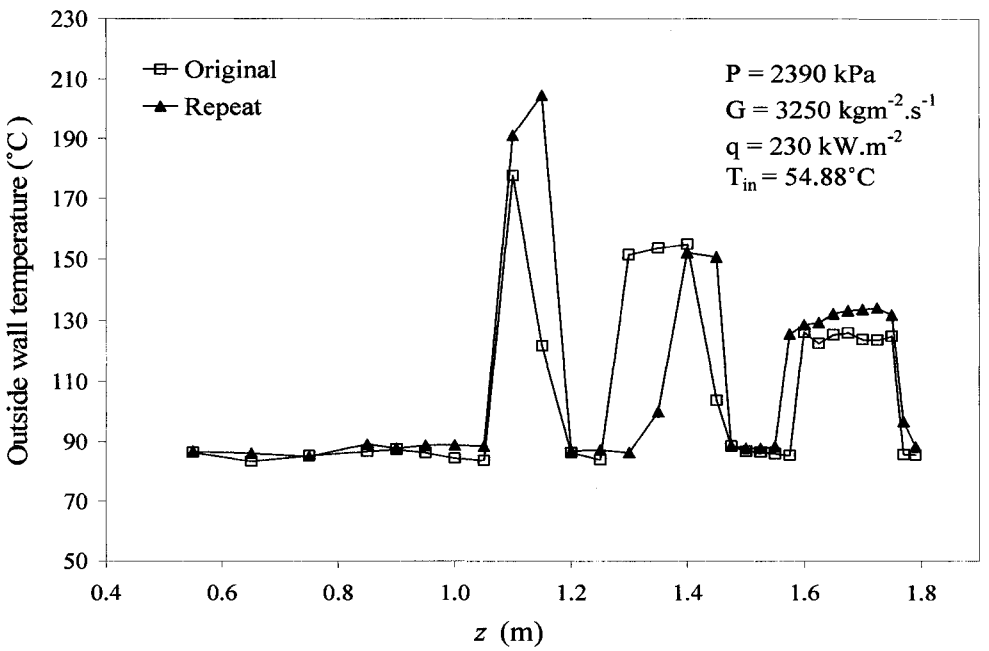

Figure A6b Repeatability test, uniform test section (high-pressure and high-mass flux).

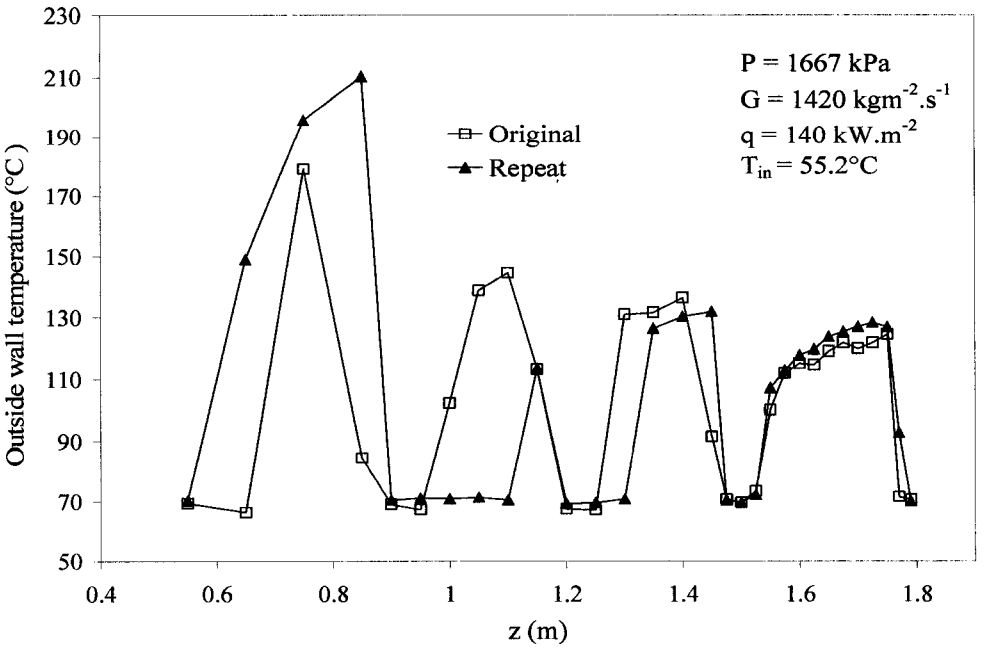

Figure A6c Repeatability test, uniform test section (low-pressure and low-mass flux).

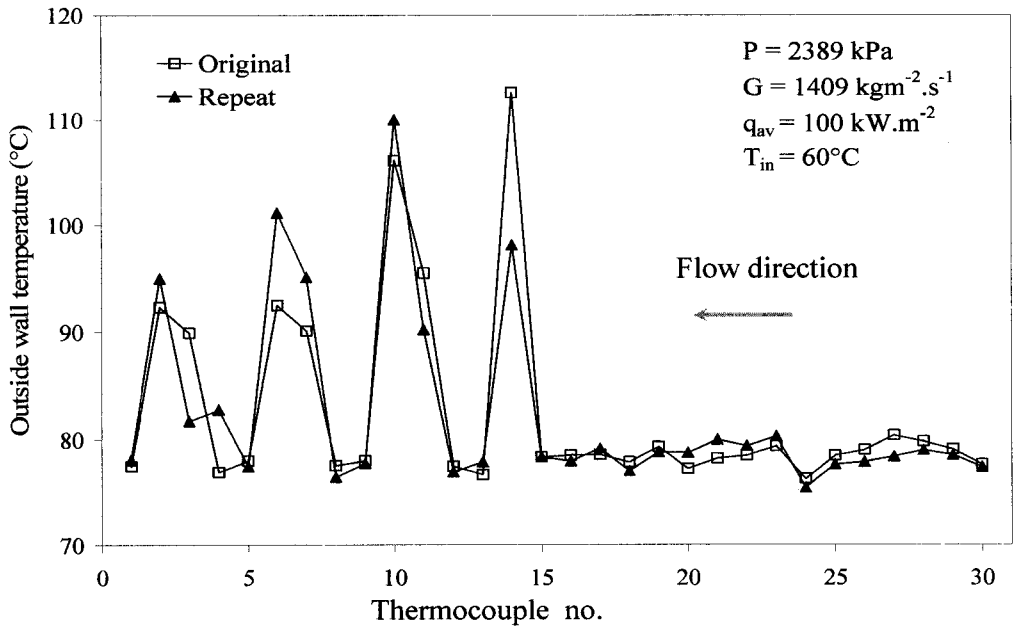

Figure A6d Repeatability test, inlet-peak test section (high-pressure and low-mass flux).

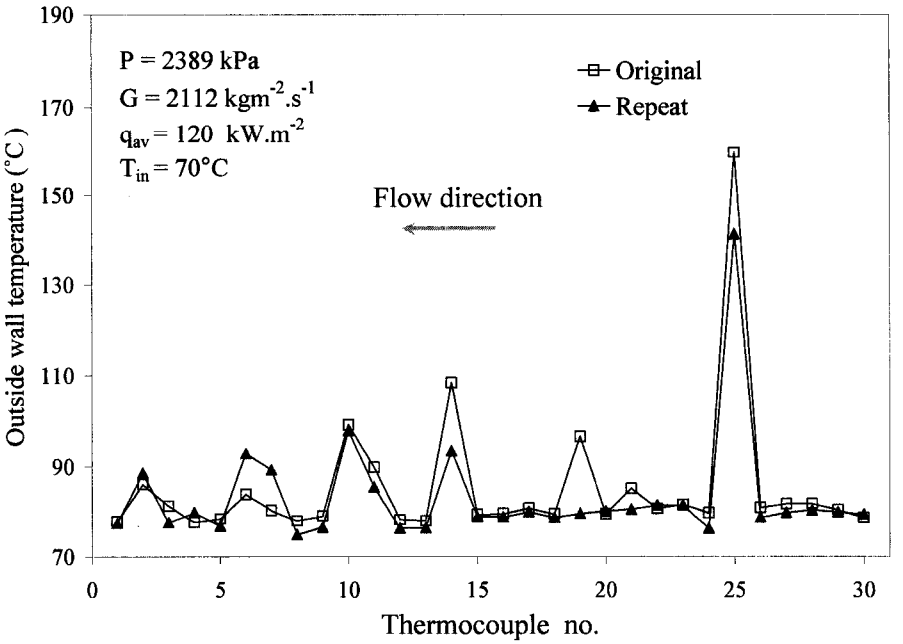

Figure A6e Repeatability test, inlet-peak test section (high-pressure and moderate-mass flux).

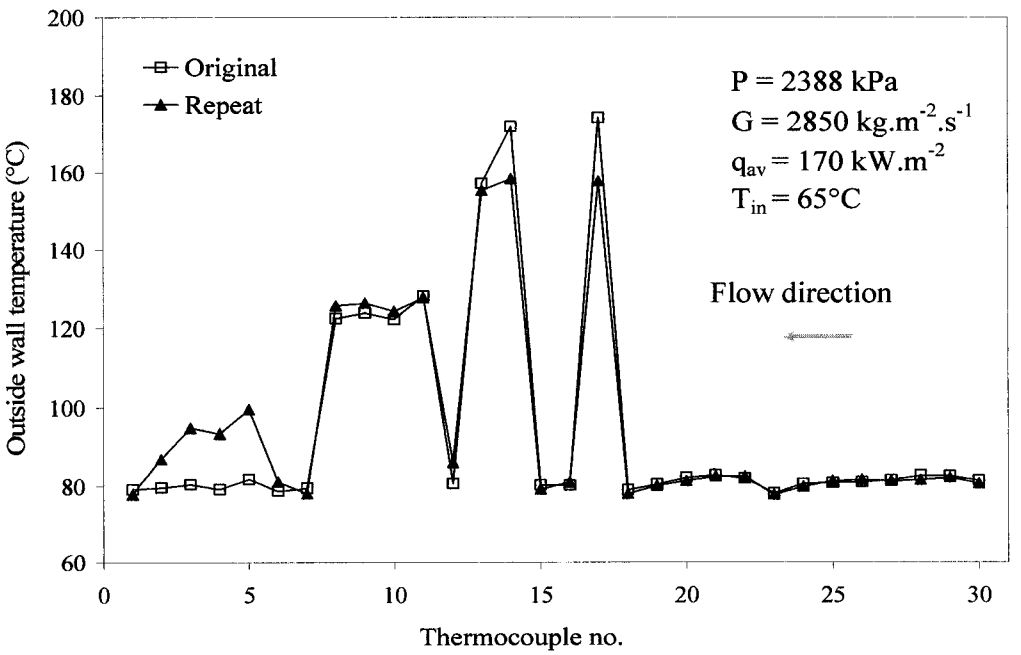

Figure A6f Repeatability test, outlet-peak test section (high-pressure and high-mass flux).

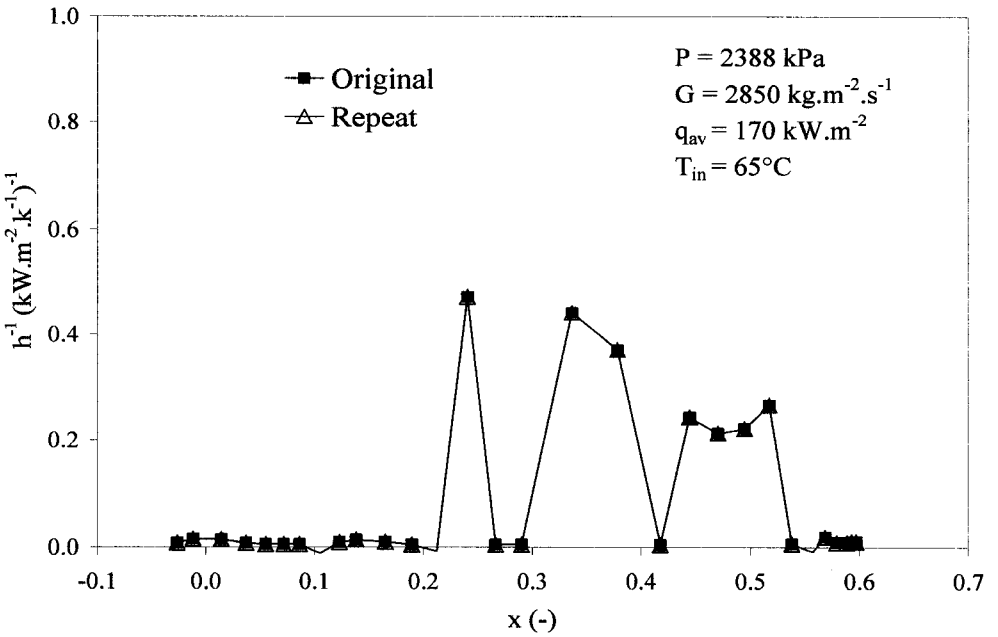

Figure A6g Repeatability test, outlet-peak test section (inverse of HTC vs. local quality, high-pressure and low-mass flux).

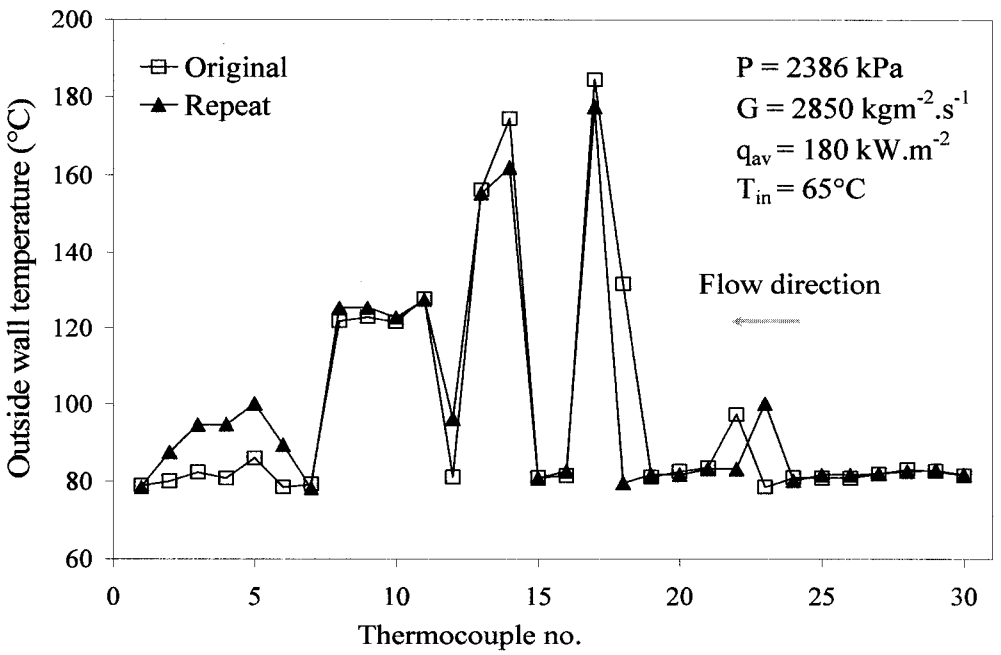

Figure A6h Repeatability test, outlet-peak test section (high-pressure and high-mass flux).

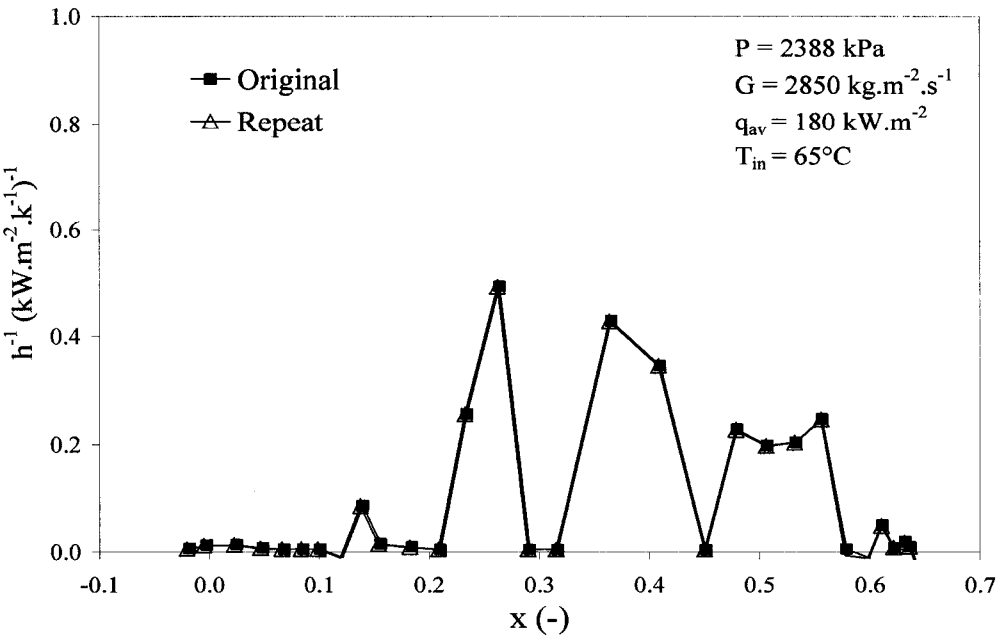

Figure A6i Repeatability test, outlet-peak test section (inverse of HTC vs. local quality, high-pressure and low-mass flux).

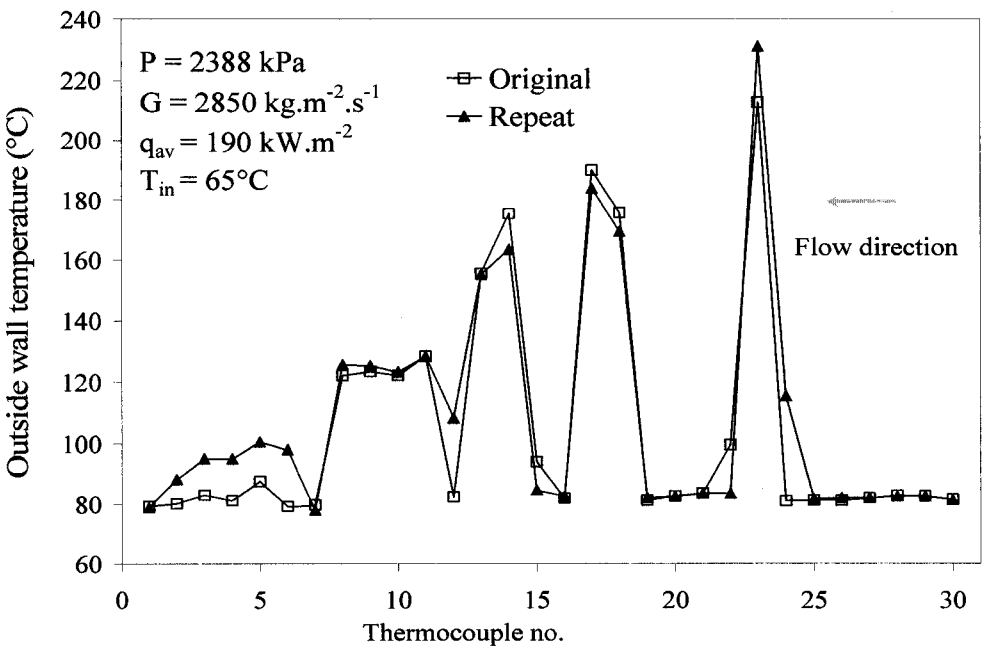

Figure A6j Repeatability test, outlet-peak test section (high-pressure and high-mass flux).

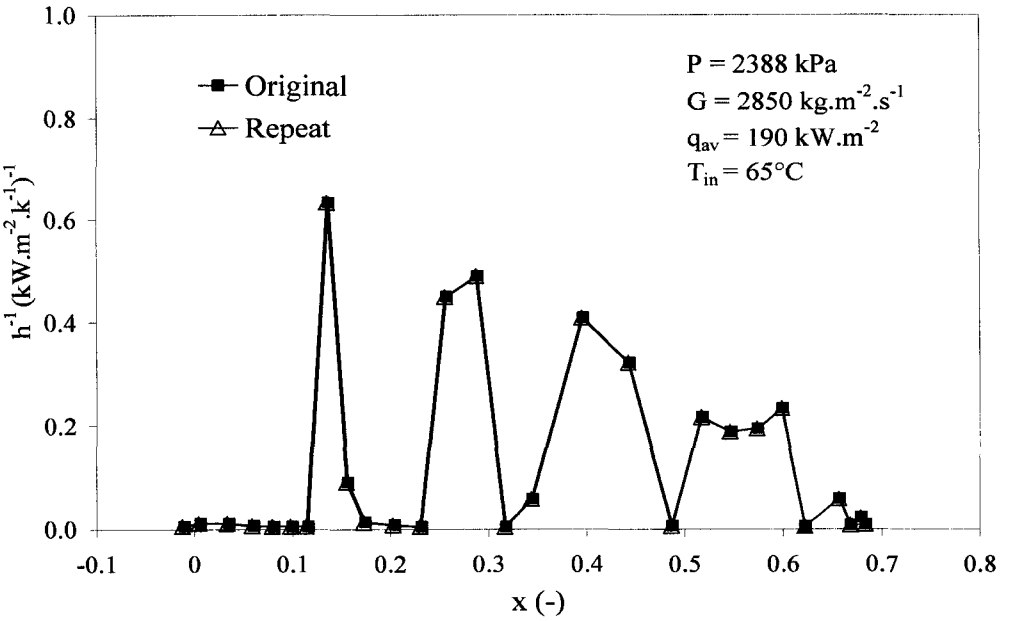

Figure A6k Repeatability test, outlet-peak test section (inverse of HTC vs. local quality, high-pressure and low-mass flux).

Calibration of voltage and current, Figures A7a-d

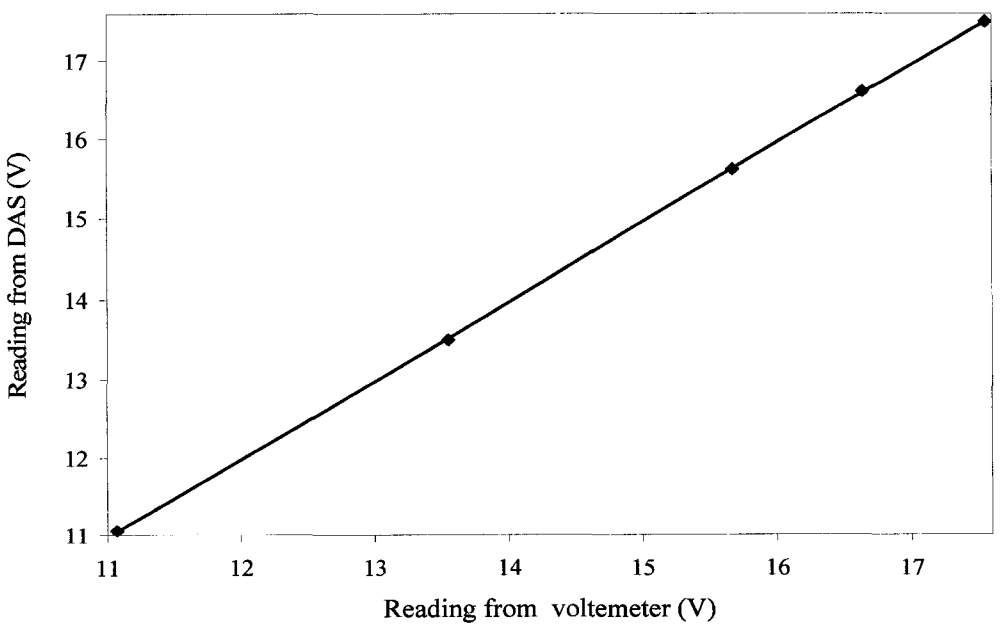

Figure A7a Calibration of voltage.

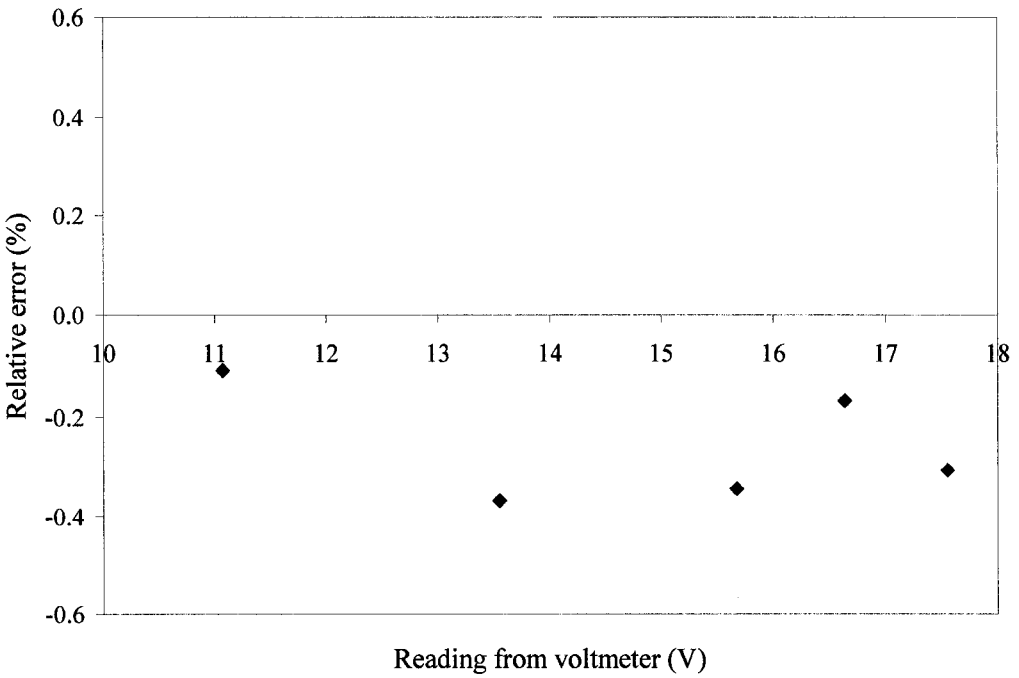

Figure A7b Results of calibration of voltage.

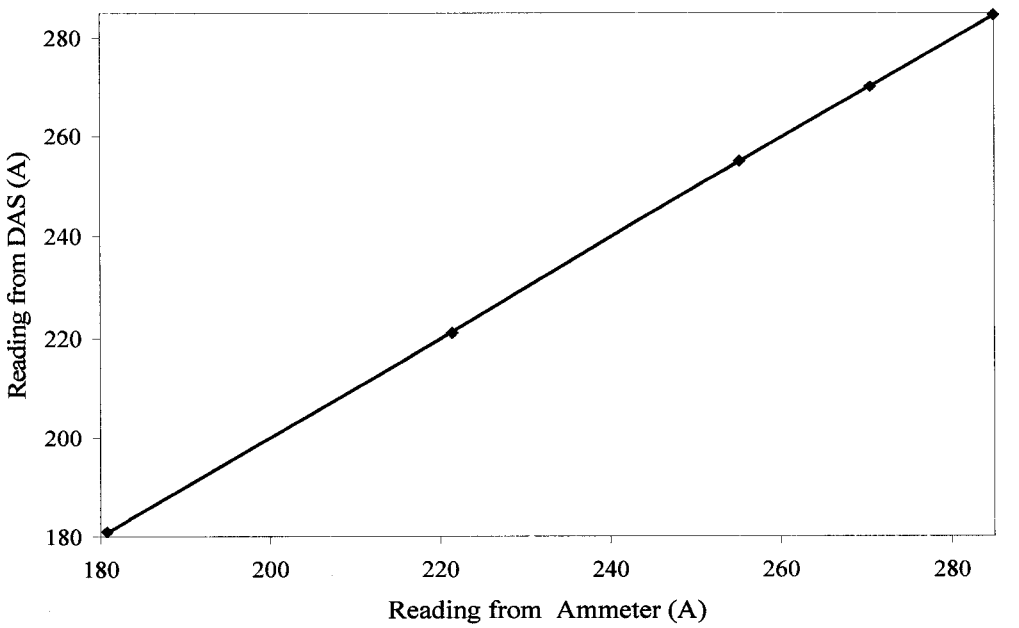

Figure A7c Calibration of current.

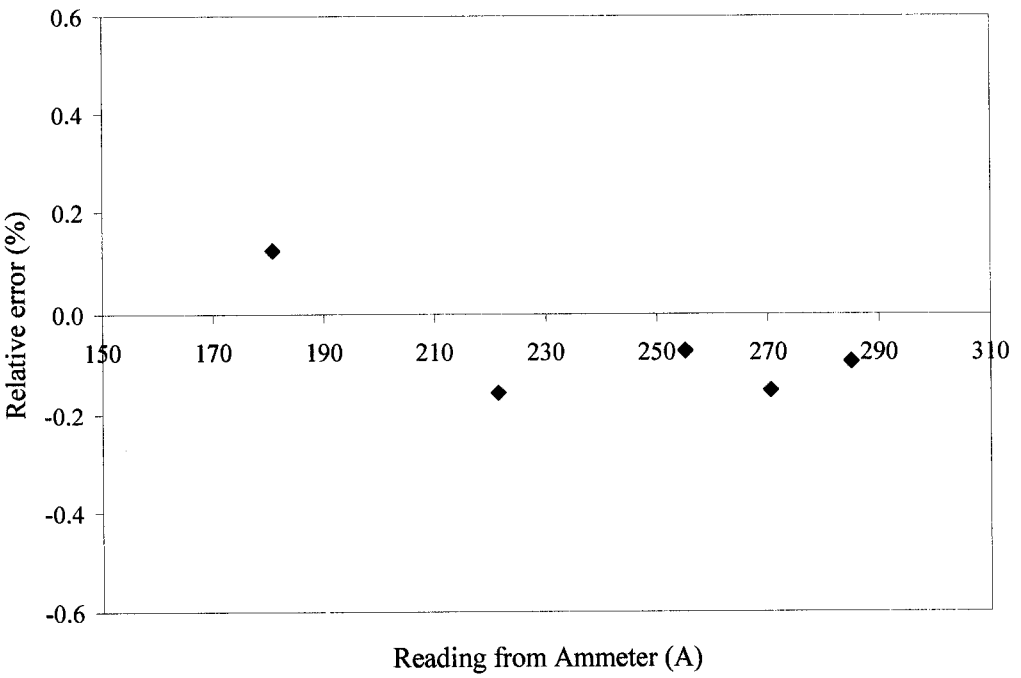

Figure A7d Results of calibration of current.

APPENDIX B

ANALYSIS OF MEASUREMENT UNCERTAINTIES

Tavoularis (2005) reviewed measurement uncertainty definitions and estimation methods, the methodology used in this analysis is from Tavoularis (2005).

When uncertainties (U) are introduced by i = m different components (v_i) in a process of measurement, the total relative uncertainty (U_T/V) of the resultant variable (V) is determined from:

$$\frac{U_T^2}{V^2} = \sum_{i=1}^{m} \left(\frac{U_{v_i}}{v_i} \right)^2 \tag{B.1}$$

The uncertainty in a derived property (U_R) is a function of the uncertainty in each of the subsidiary measurements used in calculating that result. The used methodology can be summarized:

Assuming R is a function of a number of independent variable, v_i, i = 1, 2..., n, then:

$$R = f(v_1, v_2, ..., v_n) \tag{B.2}$$

The uncertainty of the result, U_R, becomes:

$$U_R = \sqrt{\left(\frac{\partial R}{\partial v_1} \right)^2 U_1^{\,2} + \left(\frac{\partial R}{\partial v_2} \right)^2 U_2^{\,2} + \cdots + \left(\frac{\partial R}{\partial v_n} \right)^2 U_n^{\,2}} \tag{B.3}$$

where U_1, U_2, ..., U_n are the corresponding uncertainties of the v_1, v_2, ..., v_n, and has the non-dimensional form:

$$\frac{U_R^2}{R^2} = \sum_{i=1}^{n} \left(\frac{v_i}{R} \frac{\partial R}{\partial v_i} \right)^2 \left(\frac{U_i}{v_i} \right)^2 \tag{B.4}$$

The uncertainties in directly measured variables (assessed by Eqn. (B.1)) are shown in Table B.1. The evaluation of the uncertainties in calculated results are described in detail in the following subsections.

Uncertainty in mass flux

The mass flux is calculated as follows:

$$G = \frac{4\dot{m}}{D^2 \pi} \tag{B.5}$$

Applying Eqn. (B.4) upon Eqn. (B.5) (taking partial derivatives of Eqn. (B.5) with respect to independent variables $\dot{m}$ and D), and using Eqn. (B.1), the measurement uncertainty in G becomes:

$$\frac{U_G}{G} = \sqrt{\left(2\frac{U_D}{D}\right)^2 + \left(\frac{U\dot{m}}{\dot{m}}\right)^2}$$

$$= \sqrt{\left(2\frac{0.0254}{5.461}\right)^2 + (0.006)^2 + (0.0006)^2 + \left(\frac{0.000666}{\dot{m}}\right)^2}$$

which ranged: 0.0238 – 0.0136 in this experiment for G: 1350 – 3575 $kg.m^{-2}.s^{-1}$, respectively.

Uncertainty in power

The power is calculated as follows:

$$Power = U \times I$$

The uncertainty is given by:

$$\frac{U_{Power}}{Power} = \sqrt{\left(\frac{U_U}{U}\right)^2 + \left(\frac{U_I}{I}\right)^2}$$

$$= \sqrt{(0.006)^2 + (0.006)^2} = 0.0085$$

Uncertainty in saturation temperature

Saturation temperature is calculated from property subroutine based on outlet pressure at the exit of the test section.

$$\frac{U_{T_{sat}}}{T_{sat}} = \sqrt{(\frac{U_{pressure}}{pressure})^2 + (\frac{U_{propert}}{property})^2} = \sqrt{(0.0018)^2 + (0.005)^2} = 0.005314$$

Uncertainty in inside wall temperature

The outside wall temperature is measured by K-type thermocouples and the inside wall temperature is obtained by the analytical solution:

$$T_{wi} = T_o + \frac{2 q_{loss}\, r - q_v r_o^2}{2k} \ln \frac{r_o}{r_i} + \left(r_o^2 - r_i^2\right)\frac{q_v}{4k}$$

where $q_v = power / \pi(r_o^2 - r_i^2)L_h$

Performed analysis on uncertainty of the power density revealed that:

$$(\frac{U_{q_v}}{q_v}) = \sqrt{(\frac{U_{power}}{power})^2 + (2\frac{U_{r_o}}{r_o})^2 + (2\frac{U_{ri}}{r_i})^2 + (\frac{U_{Lh}}{L_h})^2} = 0.024$$

The relative uncertainty of inside wall temperature (T_{wi}) is:

$$\frac{U_{T_{wi}}}{T_{wi}} = \sqrt{(\frac{\partial T_{wi}}{\partial T_o}\frac{T_o}{T_{wi}})^2(\frac{U_{To}}{T_o})^2 + (\frac{\partial T_{wi}}{\partial q_v}\frac{q_v}{T_{wi}})^2(\frac{U_{qv}}{q_v})^2 + (\frac{\partial T_{wi}}{\partial r_o}\frac{r_o}{T_{wi}})^2(\frac{U_{ro}}{r_o})^2 + (\frac{\partial T_{wi}}{\partial r_i}\frac{r_i}{T_{wi}})^2(\frac{U_{ri}}{r_i})^2}$$

$$\frac{U_{T_{wi}}}{T_{wi}} = \sqrt{(\frac{T_o}{T_{wi}})^2 + (-\frac{q_v r_o \ln(r_o)}{K})^2(\frac{U_{ro}}{T_{wi}})^2 + \left(-\frac{q_v}{2KT_{wi}}(r_o^2 + r_i^2)\right)^2(\frac{U_{ri}}{r_i})^2 + (A)^2(\frac{U_{q_v}}{T_{w_i}})^2}$$

where $A = \frac{r_o^2}{2K}\ln(r_o / r_i) + \frac{(r_o^2 - r_i^2)}{4K}$, and

$$\frac{U_{T_{wi}}}{T_{wi}} = 0.02.$$

Uncertainty in heat transfer coefficient

The heat transfer coefficient (h) is calculated by:

$$h = \frac{q}{\Delta T_{sat}} = \frac{Power}{\pi D L_h (T_{wi} - T_{sat})}, \text{ and}$$

The uncertainty is given by:

$$\frac{U_h}{h} = \sqrt{(\frac{U_{power}}{power})^2 + (\frac{U_D}{D})^2 + (\frac{U_{Lh}}{L_h})^2 + (\frac{U_{T\,w}}{T_w})^2 + (\frac{U_{T\,sat}}{T_{sat}})^2}$$

$$\frac{U_h}{h} = \sqrt{(0.0085)^2 + (0.0254/5.461)^2 + (1/1800)^2 + (0.0204)^2 + (0.005314)^2}$$

$= 0.023$

Table B.1 Evaluation of uncertainties for the directly measured variables.

Measured variable	Symbol	Units	Error source	Device range	Used range	Uncertainties
Test section inside diameter	D	mm	Measuring device accuracy ± 0.001" => ± 0.0254 mm.	5.461	5.461	$U_D = 0.0254$ mm
Test section heated length	L_h	m	Measuring device accuracy ± 1mm.	2.5	1.8 – 2.0	$U_{Lh} = 0.001$ m
Pressure	P	kPa	Viatran pressure transducer Model 245 0 - 500 psi, 0 –3447 kPa, output 0 – 5 V accuracy ± 0.1% FSO (Full Scale Output), (3447 kPa => ± 3.447 kPa) connected to National Instrument DAS AT-MIO-16E-1 with SCXI-1121 and terminal block SCXI-1320 accuracy ±0.15% of full scale reading, (3447 kPa => ± 5.171 kPa).	0–3447	1662 – 2389	$(U_P)_{max}$=4.31 kPa $\frac{U_P}{P} = 0.0018$
Mass flow rate	$\dot{m}$	$Kg.s^{-1}$	Micro Motion mass flow sensor DS040S119SC with RFT9739 Transmitter, 0 - 20 $kg.min^{-1}$ (0.333 $kg.s^{-1}$), output 4 – 20 mA accuracy ± 0.2% FSO (Full Scale Output), (0.333 $kg.s^{-1}$ => ± 0.000666 $kg.s^{-1}$) connected to National Instrument DAS AT-MIO-16E-1 with SCXI-1120 accuracy ± 0.6% of reading and terminal block SCXI-1327 accuracy ± 0.06% of reading (the range of mass flux during experiments are from 1350 $kg.m^{-2}.s^{-1}$ => 0.03162 $kg.s^{-1}$ to 3575 $kg.m^{-2}.s^{-1}$ => 0.08374 $kg.s^{-1}$).	0 –0.333	0.03162 – 0.083736	$(U_{\dot{m}})_{max}$=0.00084 $kg.s^{-1}$ $\frac{U_{\dot{m}}}{\dot{m}} = \sqrt{(0.006)^2 + (0.0006)^2 + \left(\frac{0.000666}{\dot{m}}\right)^2}$

Table B.1 Evaluation of uncertainties for the directly measured variables (continued).

Measured variable	Symbol	Units	Error source	Device range	Used range	Uncertainties
Test section electrical voltage	U	V	Sorensen power supply DCR 40 −300, 0 −40 V, output 0 −5 V, connected to National Instrument DAS AT-MIO-16E-1 with SCXI-1120 accuracy ± 0.6% of reading and terminal block SCXI-1327 accuracy ± 0.06% of reading.	0 − 40	0 −40	$(U_U)_{max}$ = 0.241 V $\frac{U_U}{U} = 0.006$
Test section electrical current	I	A	Sorensen power supply DCR 40 −300, 0 −320 A, remote current monitor (pins no. 11 and no. 17) output 0 − 2.24 V scaled with Labview to current 0 − 320 A, connected to National Instrument DAS AT-MIO-16E-1 with SCXI-1120 accuracy ± 0.6% of reading and terminal block SCXI-1327 accuracy ± 0.06% of reading.	0 −320	0 −320	$(U_I)_{max}$ =1.93 A $\frac{U_I}{I} = 0.006$
Inlet temperature	Tin	°C	OMEGA 3-wire platinum RTD 1/8" probe accuracy ± 0.8°C connected to National Instrument DAS AT-MIO-16E-1 with SCXI-1121 and terminal block SCXI-1320 accuracy ± 0.15% of full scale reading (100°C => ± 0.15°C).	0 −100	0 −76	$(U_{Tin})_{max}$ = 0.813°C $\frac{U_{Tin}}{Tin} = \sqrt{\left(\frac{0.8}{Tin}\right)^2 + \left(\frac{0.15}{Tin}\right)^2}$
HFC-134a property	–	–	Uof O property code for HFC-134a based on Tillner-Roth and Baehr (1994) formulation accuracy ± 0.5%.	–	–	$\frac{U_{Prop}}{Prop} = 0.005$

Table B.1 Evaluation of uncertainties for the directly measured variables (concluded).

Measured variable	Symbol	Units	Error source	Device range	Used range	Uncertainties
Outside wall temperature	T_o	°C	Thermocouples K-type, narrow range of application, the accuracy = ± 0.5°C, connected to National Instrument DAS AT-MIO-16E-1 with SCXI-1102 and terminal block SCXI-1303. Cold junction accuracy = ± 0.5°C, offset error =± 0.375°C, and resolution error =± 0.3 °C.	0-1250	55-240	$(U_{To})_{max} = 0.855°C$ $\frac{U_{T_O}}{T_o} = \sqrt{(0.5/240)^2 + (0.5/240)^2 + (0.375/240)^2 + (0.3/240)^2}$